2002-06-07

# Design and Characterization of a High-resolution Cardiovascular Imager

Srinivasan Vedantham
*Worcester Polytechnic Institute*

**DESIGN AND CHARACTERIZATION OF A HIGH-RESOLUTION CARDIOVASCULAR IMAGER**

A dissertation submitted to the faculty of the

WORCESTER POLYTECHNIC INSTITUTE

in partial fulfillment of the requirements for the

Degree of Doctor of Philosophy in Biomedical Engineering

by

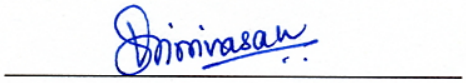

Srinivasan Vedantham

June 2002

APPROVED:

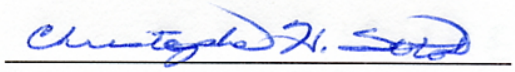

Christopher H. Sotak, Ph.D.
Professor and Head, Academic Advisor
Biomedical Engineering Department
Worcester Polytechnic Institute

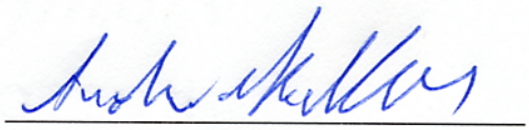

Andrew Karellas, Ph.D.
Professor of Radiology, Major Advisor
University of Massachusetts Medical
School and UMass Memorial Healthcare

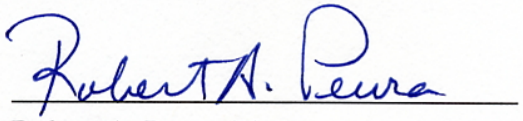

Robert A. Peura, Ph.D.
Professor
Biomedical Engineering Department
Worcester Polytechnic Institute

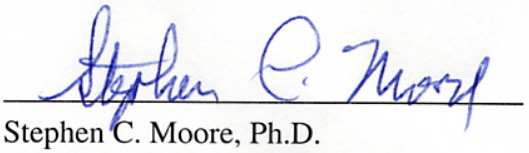

Stephen C. Moore, Ph.D.
Associate Professor of Radiology
Harvard Medical School and Brigham
and Women's Hospital

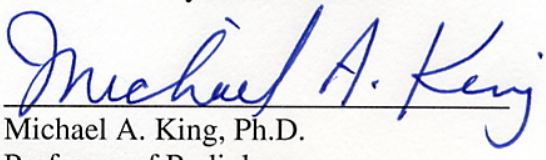

Michael A. King, Ph.D.
Professor of Radiology
University of Massachusetts Medical
School and UMass Memorial Healthcare

## ABSTRACT

Fluoroscopic imaging devices for interventional radiology and cardiovascular applications have traditionally used image-intensifiers optically coupled to either charge-coupled devices (CCDs) or video pick-up tubes. While such devices provide image quality sufficient for most clinical applications, there are several limitations, such as loss of resolution in the fringes of the image-intensifier, veiling glare and associated contrast loss, distortion, size, and degradation with time.

This work is aimed at overcoming these limitations posed by image-intensifiers, while improving on the image quality. System design parameters related to the development of a high-resolution CCD-based imager are presented. The proposed system uses four 8 x 8-cm three-side buttable CCDs tiled in a seamless fashion to achieve a field of view (FOV) of 16 x 16-cm. Larger FOVs can be achieved by tiling more CCDs in a similar manner. The system employs a thallium-doped cesium iodide (CsI:Tl) scintillator coupled to the CCDs by straight (non-tapering) fiberoptics and can be operated in 78, 156 or 234-microns pixel pitch modes.

Design parameters such as quantum efficiency and scintillation yield of CsI:Tl, optical coupling efficiency and estimation of the thickness of fiberoptics to provide reasonable protection to the CCD, linearity, sensitivity, dynamic range, noise characteristics of the CCD, techniques for tiling the CCDs in a seamless fashion, and extending the field of view are addressed. The signal and noise propagation in the imager

was modeled as a cascade of linear-systems and used to predict objective image quality parameters such as the spatial frequency-dependent modulation transfer function (MTF), noise power spectrum (NPS) and detective quantum efficiency (DQE).

The theoretical predictions were compared with experimental measurements of the MTF, NPS and DQE of a single 8 x 8-cm module coupled to a 450-microns thick CsI:Tl at x-ray beam quality appropriate for cardiovascular fluoroscopy. The measured limiting spatial resolution (10% MTF) was 3.9 cy/mm and 3.6 cy/mm along the two orthogonal axes. The measured DQE(0) was ~0.62 and showed no dependence with incident exposure rate over the range of measurement. The experimental DQE measurements demonstrated good agreement with the theoretical estimate obtained using the parallel-cascaded linear-systems model. The temporal imaging properties were characterized in terms of image lag and showed a first frame image lag of 0.9%.

The imager demonstrated the ability to provide images of high and uniform spatial resolution, while preserving and potentially improving on DQE performance at dose levels lower than that currently used in clinical practice. These results provide strong support for potential adaptation of this type of imager for cardiovascular and pediatric angiography.

## ACKNOWLEDGEMENTS

This work was supported in part by Grant Number R01 HL65551 from the National Heart, Lung and Blood Institute (NHLBI), National Institutes of Health (NIH), to the University of Massachusetts Medical School (Principal Investigator: Andrew Karellas, Ph.D.).

I would like to thank my research advisor and mentor Dr. Karellas, for his professional support and scientific and technical guidance. I would like to express my sincere gratitude to my advisors and committee members, Dr. Sotak, Dr. Peura, Dr. King and Dr. Moore for their advice and scientific expertise, which greatly enhanced the quality of this work. I also wish to extend my sincere gratitude to Dr. Stephen J. Glick, University of Massachusetts Medical School, and colleagues in our research laboratory, Mr. Sankararaman Suryanarayanan and Ms. Hetal Ved, for their valuable input during scientific discussions. I also wish to thank Ms. Patricia Belanger, UMass Memorial Health Care, for her assistance with some of the experimental measurements. I also thank members of our collaborating company, Fairchild Imaging, Milpitas, CA.

Most importantly, I would like to thank my parents, my brother, Ramanuja, and my wife, Manju, for being a constant source of inspiration and encouragement.

## DISCLAIMER

This work addresses the design and evaluation of a specific laboratory prototype device and may not be representative of any particular current or future commercially available product.

The contents of this work are solely the responsibility of the author and do not necessarily represent the official views of the National Heart, Lung and Blood Institute (NHLBI) or the National Institutes of Health (NIH).

## TABLE OF CONTENTS

## LIST OF FIGURES

## LIST OF TABLES

# 1. INTRODUCTION – PROBLEM IDENTIFICATION

The term fluoroscopy refers to the use of x-ray imaging techniques for the real-time, typically 30 frames/sec (fps), visualization of internal anatomy for diagnostic and therapeutic purposes. The power of x-ray fluoroscopic techniques is in their ability to visualize anatomy and function simultaneously. Physiologic functions such as peristalsis and flow, and real-time image feedback for the placement of devices, such as catheters, or intravascular stents are typical examples of fluoroscopic imaging. However, fluoroscopy alone is of limited use without a spot image "snapshot" capability and in many applications acquisition of rapid sequences of spot images is essential. In this mode, the fluoroscopic system operates in a rapid sequence radiographic mode where the exposure per frame at the entrance of the image-intensifier is increased from the typical 1 - 3 μR per frame (fluoroscopy mode) to about 300 μR per frame (radiographic mode). In fluoroscopy, the ability to change the spatial resolution during the examination enables physicians to "focus" on a smaller area and visualize with greater detail. Although the traditional role of fluoroscopy provides enough justification of the importance of maintaining and improving image quality at a reduced radiation dose, in the past five years the role of fluoroscopy has greatly expanded to cover many more diagnostic and therapeutic applications. More interventional procedures are performed today in younger patients as a minimally invasive alternative to surgery.

## 1.1. CARDIAC IMAGING APPLICATIONS

In spite of recent developments in non-invasive diagnostic cardiac procedures, x-ray fluoroscopy remains the "gold-standard" for procedures such as diagnostic percutaneous coronary angiography, angioplasty, stent placement, pacemaker placement, electrophysiology, and peripheral vascular procedures. In recent years the volume of cardiovascular x-ray procedures has increased dramatically partly due to the high success rate of angioplasty, stent placement and electrophysiology techniques. The success of these procedures is making a major impact not only in the survival rate of patients from cardiovascular disease, but also on the overall quality of life. As these procedures become more effective, younger patients are increasingly becoming candidates for such procedures. It is now common for young patients and children to undergo radiofrequency ablation procedures [1]. In several parts of the US, elective diagnostic percutaneous coronary angiography is now commonly performed in mobile trailers, which attach to the hospital on a planned schedule. There are also clinical situations such as the evaluation of coronary artery patency following thrombolysis or in the operating room to assess graft patency where compact bedside angiographic equipment can be extremely useful [2]. This work is aimed at developing technology capable of improving the image quality at full-function fixed or mobile equipment for invasive cardiovascular procedures.

## 1.2. CURRENT STATE-OF-THE-ART

Tube-based image-intensifiers for fluoroscopy were invented in about 1940 [3]. The first patent on this technology was awarded to Langmuir from GE Corporate Research in

1940 [3]. The development of a practical device did not materialize for several years after Langmuir's inception of the concept. The landmark "Carman Lecture" on fluoroscopes and fluoroscopy at the Radiological Society of North America (RSNA) in 1941 by W. E. Chamberlaine is considered as the first awakening call for the need of image intensification.

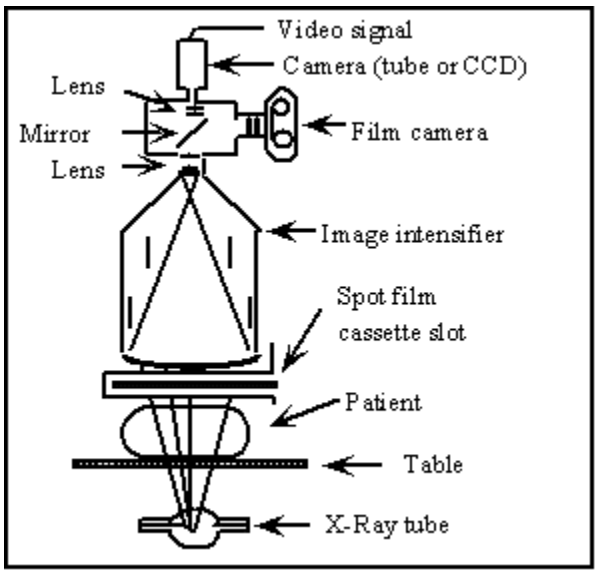


*Figure 1.1 Schematic showing a conventional image-intensifier-based fluoroscopic system.*

It was not until 1948 that John Coltman built the first practical image-intensifier at Westinghouse Research Laboratories [4]. The development of the image-intensifier represents one of the major technological landmarks in radiological imaging. Now, image-intensifiers are a standard and essential component of fluoroscopic systems. Although several aspects of the design of this technology have evolved over the years, the basic approach of detection remains the same. Image-intensifier technology with

video tube-based cameras [5] and more recently charge-coupled devices (CCDs) [6, 7] has had a major impact in this field for the past fifty years. In Figure 1.1, a schematic of a conventional image-intensifier-based fluoroscopic system is shown. A typical system is a combination of image-intensifier, spot film cassette device, film camera and video camera. Typically for cardiac applications, which require acquisition at high frame rates, the spot film cassette is not used.

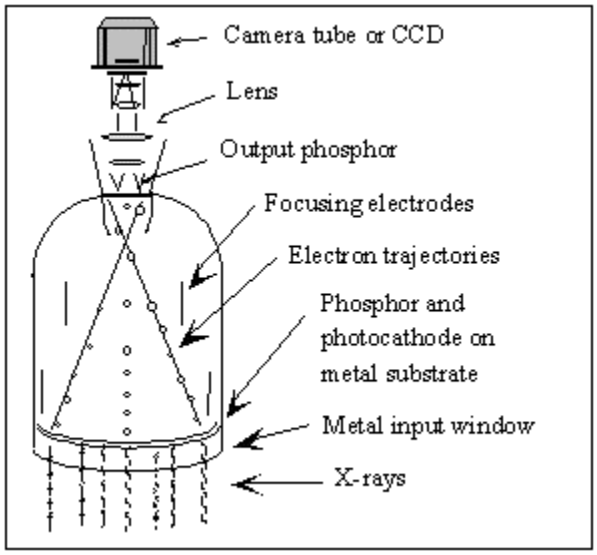


*Figure 1.2 Schematic showing the internal details of detection and amplification in an image-intensifier.*

In Figure 1.2, a schematic of the internal details of the detection and amplification process in an image-intensifier is shown. X-rays after transmitting through the patient travel through the metal window and interact with the scintillator deposited on the metal substrate. The light from the scintillator is converted to electrons and accelerated through the electric field. The focusing electrodes orient the accelerated electrons to the output

phosphor, which upon interaction produces light. The light is coupled to a video pickup tube or CCD camera by relay lenses.

## 1.3. LIMITATIONS OF IMAGE-INTENSIFIER

While image-intensifier technology has progressed since its inception, this technology has several inherent limitations described in detail below, such as veiling glare and contrast loss, S-type distortions, pincushion and barrel type distortions, scattering and absorption due to the high vacuum window, size and complexity, and degradation with time.

### *1.3.1. Veiling Glare and Associated Contrast Loss*

This is one of the most important problems, inherent in the electro-optic design of the image-intensifier. After conversion of the light from the scintillator to electrons by the photocathode, these electrons are accelerated in a field potential of about 30 kV. During this stage a fraction of the electrons undergo scatter within the tube. At the output stage, after conversion from electrons to photons, the light scatters within the optical elements of the output [8]. This long-range light scatter is referred to as veiling glare and causes degradation of the image contrast. This phenomenon is best described in Figures 1.3 and 1.4. In Figure 1.3, the image-intensifier is subjected to uniform x-ray incidence. The oscilloscope trace of the video signal through the center of the image-intensifier shows a pronounced decrease in signal intensity at the periphery compared to the center.

In Figure 1.4, a lead (*Pb*) disc covering approximately 10% of the image-intensifier surface area is placed at the center. The *Pb* disc is thick enough to provide complete attenuation of the incident x-rays. Ideally, the signal intensity below the area attenuated by the *Pb* disc should reach the baseline. However, as shown in the oscilloscope trace through the center of the image-intensifier, the signal intensity under the *Pb* disc is above the baseline, resulting in degradation of image contrast.

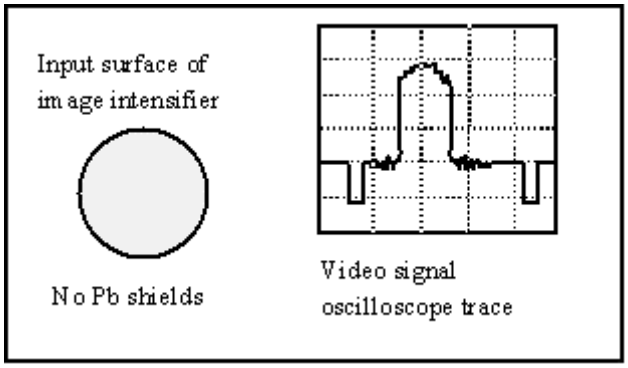


*Figure 1.3 Schematic showing the pronounced decrease in signal intensity at the periphery with uniform x-ray incidence as observed by the oscilloscope trace through the center of the image-intensifier.*

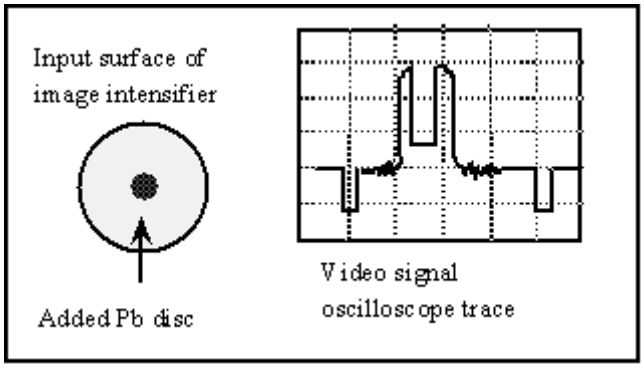


*Figure 1.4 Schematic showing the effect of veiling glare and the resultant contrast loss as observed by the oscilloscope trace. The signal intensity under the Pb disc is above the baseline resulting in loss of image contrast.*

### *1.3.2. S-type Distortion*

This is also a well-known phenomenon, which makes imaging of a straight object to appear having an S-shape. It is caused by the influence of earth's magnetic field on the trajectories of electrons within the image-intensifier tube. Shielding of the image-intensifier with a material called "mu-metal" is essential but in most cases a significant amount of s-type distortion is still present. This type of distortion may not compromise the diagnosis but can be bothersome during treatment procedures requiring high spatial accuracy and precision. Most troublesome is the fact that the s-type distortion changes spatially as the intensifier is moved around the patient. Therefore, a mathematical correction for the distortion becomes unreliable.

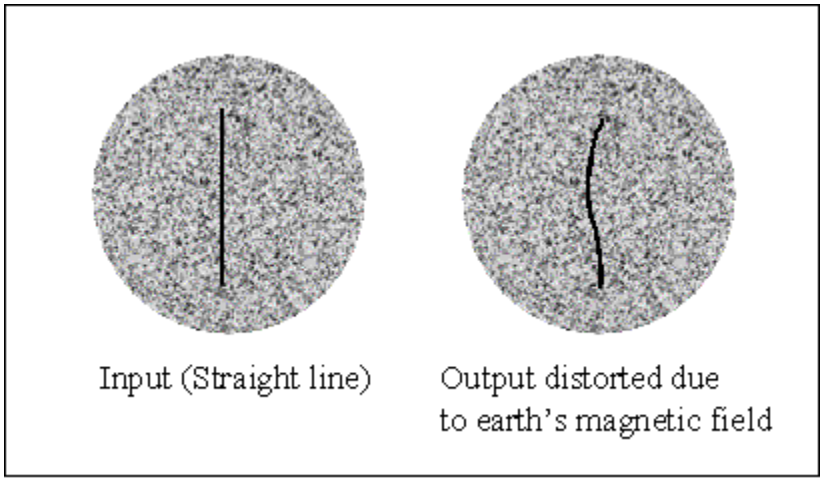


*Figure 1.5 Illustration of the S-type distortion. The image of a straight-line object appears distorted at the output of the image-intensifier due to the influence of the earth's magnetic field.*

### *1.3.3. Pincushion and Barrel-type Distortions*

These are caused by the inherent limitations of the electron focusing optics. The degradation of the geometric integrity due to these effects is also well known to practitioners in this field. Pincushion and barrel distortions are tolerable in many instances but they present a hindrance in the proper visualization of anatomy [9, 10]. Similar effects, but for different physical reasons are well known to arise from the lens coupling [11].

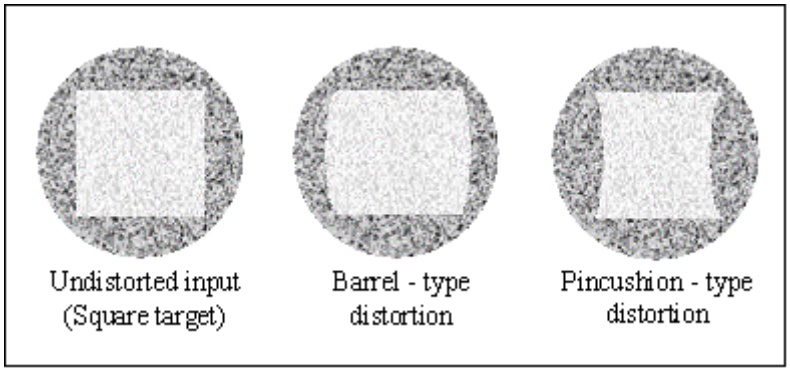


*Figure 1.6 Illustration of the barrel and pincushion-type distortions.*

### *1.3.4. Effect of Input High Vacuum Window*

The glass input window, which traditionally has been the input window of image-intensifiers (typically 1-3 mm thick), absorbs useful x-rays and produces forward scatter, has now been replaced with a thickness of 0.7 - 1.2 mm of aluminum [12]. While this represents a significant improvement, the input window itself absorbs about 20 to 30% of the useful x-ray beam depending on the photon energy. The high vacuum of the

intensifier requires a relatively thick metal window for maintaining the mechanical integrity of the tube. In addition to this aluminum layer of the input window, x-rays must pass through another 0.5-mm thick aluminum, the scintillator substrate, before they reach the scintillator [12].

### *1.3.5. Size and Complexity*

The current image-intensifier-video camera chain occupies too much space in a x-ray examination room, which could be particularly problematic in bi-planar installations. Even in simple fluoroscopic installations, the camera tower frequently interferes with the overhead radiographic x-ray tube and other structures.

### *1.3.6. Degradation with Time*

The gain of all image-intensifiers is known to degrade with time and much of this degradation occurs in the first year of operation. This degradation is caused in part by the out-gassing of components in the vacuum chamber and degradation of the photocathode. The image quality of these systems is noticeably lower after three years of operation, and their useful lifetime if good image quality is to be maintained is about 3-5 years [13].

## 1.4. CLINICAL SIGNIFICANCE

The use of cardiac fluoroscopy has increased dramatically in the past twenty years. The major reason for this increase is the creativeness of physicians in developing new

interventional techniques for diagnostic and therapeutic procedures. The rapid proliferation of these procedures has resulted in a small but alarming number of non-stochastic radiation effects on patients [14-16]. These include epilation, erythema and tissue necrosis in a number of patient cases brought to the attention of the United States Food and Drug Administration (FDA). Cardiac angiography produces one of the highest radiation exposures of any commonly used diagnostic x-ray procedure. Recently, chronic radiodermatitis has been reported after repeated therapeutic interventional procedures using prolonged fluoroscopic imaging [17]. Radiation exposure to patients during diagnostic and interventional cardiac procedures has increased as a result of the increased complexity of the angiographic procedures performed in current clinical practice [18]. It is particularly curious to witness such a trend in an era of increasing sophistication in electronics and better-than-ever computer-controlled x-ray equipment. An examination of the 1948 article on image-intensifiers by Coltman reveals that little has changed in the basic design concept of this technology. The technology has evolved significantly over the years and the image quality of today's modern image-intensifier with CCD readout is far superior to the earlier approaches. However, the current image-intensifier technology has reached a plateau and major improvements beyond the current state-of-the art are unlikely. This technology was not designed for the application it is forced to perform today. Even with the most advanced equipment, the potential for over exposure to the patient and even epilation and erythema are significant risks, and appropriate precautions must be taken during these procedures. A significant part of the problem with excessive radiation to the patient is related to proper training and good fluoroscopic habits.

However, many physicians find that practicing these "good habits" can be difficult at times when they must focus all their attention on a stent placement or angioplasty in a difficult high-risk case. For example, in electrophysiology procedures, long fluoroscopic times are common by the nature of the procedure. Therefore, the equipment must provide excellent image quality at a minimum radiation dose.

## 1.5. OVERVIEW

Development of an optimized imaging system involves several tasks. These include, design of the system, development of a prototype, characterization of the prototype, and task-specific optimization. This work addresses the design aspects, development of models to predict system performance, description of the developed prototype, and experimental characterization of the developed prototype. Task-specific optimization of the system is yet to be performed and is included in the section addressing future work as one of the tasks. Chapter 2 addresses the specific aims of the project and chapter 3 addresses the specific hypotheses that are tested in this work. Chapter 4 provides the background on various detector technologies that are currently being investigated.

Chapter 5 addresses the methods and material uses in this work. Description of the system, and design aspects are presented in this chapter. Further, techniques to extend the imaging area from the 16 x 16-cm field of view (FOV) to larger area and a method to correct for the seam due to tiling of several modules are addressed. Chapter 5 also addresses the two linear-system-based models – serial and parallel cascades.

Parallel-cascaded linear-systems-based model is an improvement in describing the signal and noise processes in the system compared to the serial-cascaded linear-systems-based model. The accuracy of the results predicted by the parallel-cascaded linear-systems-based model may be further improved by incorporating Monte-Carlo simulation technique to accurately estimate the K-fluorescent reabsorption fraction and the K-fluorescent blur, corresponding to the imaging geometry specific to this system. Inclusion of such a simulation technique is identified as one of the tasks that need to be performed in the section addressing future work. Chapter 5 also addresses the experimental techniques used for characterizing the single module prototype. Chapter 6 addresses the results of the theoretical and experimental studies. Chapter 7 provides a discussion of the observed results and the significance of the observed results to the stated specific hypotheses. Chapters 8 and 9 provide the conclusions and the future work that need to be performed, respectively.

## 2. SPECIFIC AIMS

This research is aimed at:

- Exploring new technological approaches for performing cardiovascular fluoroscopic x-ray examinations using a large-area imager based on charge-coupled devices (CCDs), which will cover an area of 16 cm x 16 cm.
- Developing a theoretical model to describe the signal and noise transfer characteristics of the imager and using the results of this computational study to develop a prototype detector system comprised of a structured CsI:Tl scintillator coupled to four CCDs by a straight (non-tapering) fiberoptic plate, and tiled in a seamless fashion.
- Performing comprehensive evaluation of the electrical characteristics of the detector and evaluating the system though objective and universally accepted metrics such as the frequency-dependent modulation transfer function (MTF), and the frequency-dependent detective quantum efficiency (DQE).

## 3. SPECIFIC HYPOTHESES

The specific hypotheses are that the new fluoroscopic CCD-based system:

- Will be x-ray quantum-noise-limited, and will exhibit higher quantum efficiency than current image-intensifier-based fluoroscopic technology.
- Will be free of geometric distortion effects (barrel, pincushion and S-type distortions), often observed with image-intensifier-based systems.
- Will be free of veiling glare effects, which cause significant loss of contrast in image-intensifier-based systems.
- Will exhibit higher spatial resolution than current fluoroscopic imaging systems without loss of contrast.
- Will deliver better detective quantum efficiency (DQE) than existing image-intensifier-based systems.

# 4. BACKGROUND

The need for replacing conventional image-intensifiers has been recognized for several years and attempts have been made to develop alternate technologies. Such attempts have focused on flat-panel intensifiers typically using microchannel plates or solid-state detectors [19], but did not succeed in replacing the image-intensifier, which is still considered the "gold standard". In the past seven years, pioneering research with a new amorphous silicon based flat-panel technology from the University of Michigan in collaboration with Xerox Corporation has had a major impact on fluoroscopic imaging [20]. Independent research and development by GE Medical Systems on the amorphous silicon technology has resulted in a commercially available cardiac fluoroscopic system [21]. Another technological approach that is being actively investigated for potential application in cardiac fluoroscopy is the amorphous selenium based flat-panel imager [22, 23]. These detection technologies can be broadly classified into two distinct types, indirect and direct-detection, based on the method of signal generation.

## 4.1. INDIRECT TYPE DETECTORS

In general any technology, which uses at least one intermediate step to convert incident x-rays to electrons is considered an indirect type detector. Typically, such detectors use a scintillator for conversion from x-rays to light, followed by subsequent

detection of light by either a CCD or a flat-panel amorphous silicon (a-Si) array. Commonly used scintillators are CsI:Tl and gadolinium oxysulfide. An illustration of the detection process in an a-Si based detector is shown in Figure 4.1. X-rays interact with the scintillator and the generated light is detected by the a-Si photodiode array.

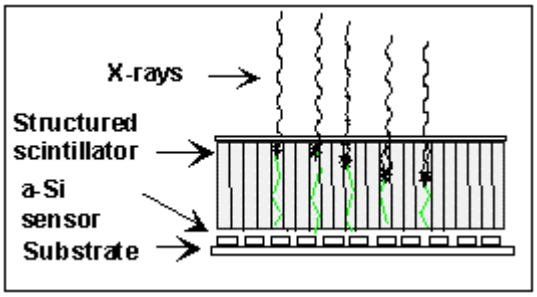


*Figure 4.1 Illustration of the detection process in an amorphous silicon based detector.*

While this technology has excellent prospects, concerns with respect to the relatively high electronic noise from the thin-film transistor (TFT) based readout, and the loss of fill factor due to the finite space occupied by the TFT, bias and data lines in each pixel, continue to persist. Moreover, the current technology is geared to a single resolution mode with a fixed pixel size (typically 200-μm). In spite of these limitations, currently in the United States, the a-Si based technology is the only commercially available alternative to an image-intensifier-based system for cardiac fluoroscopy. The detection process in a CCD based detector is similar, except that the scintillator is coupled to the CCD by a fiberoptic plate.

## 4.2. DIRECT TYPE DETECTORS

In contrast to the indirect type detector, direct type detectors do not use an intermediate conversion step and the incident x-ray photons are converted to electrons by the photoconductive layer. Typical examples of such direct conversion material are amorphous selenium (a-Se), lead iodide ($PbI_2$), mercuric iodide ($HgI_2$) and cadmium zinc telluride (CdZnTe). Among these materials, a-Se has been the object of several investigations, in particular by the research group at the University of Toronto, Canada. The use of a-Se was first introduced in the 1970s for xeroradiography, but this technique was limited by the powder cloud method, which reduced image quality in the developed image. Since then, substantial progress has been made in a-Se readout methods [22, 24, 25]. Current readout approaches use a TFT-array similar to that used with a-Si detectors [22]. An illustration of the detection process in an amorphous selenium based detector is shown in Figure 4.2. A bias voltage typically on the order of 5-kV is applied between the electrodes, such that an electric field of 10-V/μm for a 500-μm thick a-Se layer is maintained [22]. When x-rays interact in the material, electron-hole pairs are generated and the charges are collected and read out using the TFT-array. Since the intermediate scintillator layer is eliminated, a-Se detectors can provide an improvement in spatial resolution compared to indirect detectors [26]. This technology is commercially available for radiography and its adaptation for fast readout suitable for cardiac fluoroscopy is currently in progress. It may appear intuitive that direct detection may be preferable because of the lack of the photo-conversion step resulting in a larger signal with high spatial resolution. However, the TFT-readout suffers from the same

deficiencies addressed with the a-Si detector, such as reduction in geometric fill factor and the high electronic noise associated with the readout electronics.

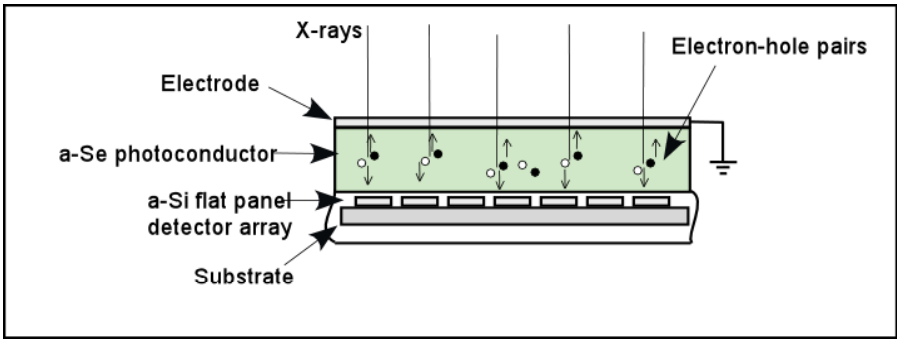


*Figure 4.2 Illustration of the detection process in an amorphous selenium based imager.*

Further, isolating the signal (a few mV) in the presence of the high bias voltage (~5kV) is technically challenging and this problem is further accentuated with increasing x-ray energies, which require a thicker layer of a-Se, resulting in a need for higher bias voltages, to maintain a constant electric field. This problem is amplified when such signal isolation has to be performed at fast readout speeds suitable for cardiac fluoroscopy. Another major issue concerning this technology is the possibility of significant noise aliasing [27] due to the high modulation transfer function (MTF). As with the a-Si detector, this technology is geared for a single resolution mode with a fixed pixel size. However, this technology with either a-Se or other direct conversion materials is evolving and has potential for cardiac fluoroscopy.

While several technological approaches are being investigated, there is no single technology that addresses all the issues. The technology of choice depends on several criteria such as quantum and energy absorption efficiency, detective quantum efficiency (DQE), spatial resolution (MTF), fast readout, high dynamic range, image correction and display capabilities, and acceptable cost. While there may be applications where one type of technology is preferable to the other, at this time the body of knowledge is too limited to allow drawing prudent and general conclusions.

### 4.3. CCD-BASED IMAGING SYSTEM

There is ample evidence that CCD-based detection technology is feasible for mammographic and radiographic applications [28-33]. The research group at the University of Massachusetts was one of the first to propose, conduct research, and publish their results on the use of CCD technology for stereotactic localization and spot views [28, 29, 33]. This research has yielded a digital mammographic cassette using a 61 mm x 61 mm CCD suitable for stereotactic localization and spot views, and is commercially available through GE Medical systems. Comprehensive evaluation of this digital cassette [33] has shown good spatial resolution and a detective quantum efficiency of about 40% under realistic mammographic conditions. This cassette employs a gadolinium oxysulfide scintillator coupled to a 15-μm pixel CCD (2 x 2 binned to operate in the 30-μm mode). A straight (non-tapering) fiberoptic plate with a thickness of about 4 mm is used between the scintillator and the CCD. This mammographic CCD is being described, as its general design resembles that of the fluoroscopic imager and the results

with mammographic imaging serve as a guide for its adaptation to other applications. At the time of its inception, the concept of a mammographic CCD-based cassette was considered a high-risk engineering venture. However, improved CCD-processing techniques and creative electronic engineering have yielded very favorable results. Now, single CCD modules with dimensions of 8.0 x 8.0 cm are being manufactured. Moreover, this new generation of CCDs will be three-side buttable, thus enabling the tiling of several CCD modules into one large sensor. Four of these CCD modules can be combined in a seamless fashion to form a sensor with 16 cm x 16 cm (6.3" x 6.3") field of view. The adaptation of this technology for cardiac x-ray imaging involves a number of challenging tasks, and appropriate precautions should be taken to provide an imager with desirable characteristics.

### 4.4. BACKGROUND ON CASCADED LINEAR-SYSTEMS MODELING

A cascaded linear-systems-based model was developed to analyze the processes that govern the output image quality of the CCD-based fluoroscopic system. With the assumptions that the proposed system is linear and shift-invariant, the model was developed to describe the output image quality in terms of the objective measure, detective quantum efficiency (DQE). Cascaded linear-systems-based modeling techniques have been used to predict imaging performance of systems developed for x-ray imaging [6, 34-37]. Such models have been used to investigate key objective parameters of image quality such as the Wiener spectrum or noise power spectrum (NPS) [38-40], noise equivalent quanta (NEQ) [39, 41] and detective quantum efficiency (DQE)

[39, 41-42]. Over the past several years, many aspects detailing the development of the theory and modeling techniques have been described [43-49].

The imaging chain is represented as a serial cascade of amplifying and scattering mechanisms. In order to apply such a model to describe the image formation process, the system has to be linear and shift invariant [39, 44]. Since CCD-based imaging systems demonstrate a linear dependence with incident exposure over much of their dynamic range, the assumption of linearity can be supported. This assumption breaks down at high exposure levels where the CCD saturates as well as at very low exposure levels where the electronic noise is a dominant factor. The assumption of shift-invariance is valid only up to the point that the image is sampled; hence much of the discussion will be restricted to the presampling signal and noise. Further, the assumption that the system is spatially and temporally stationary has to be made to facilitate representation of image noise in terms of the Wiener spectrum (NPS). While such an assumption is not truly valid in the spatial domain, as pixel and scintillator nonuniformities exist, the process of background subtraction and flat-field correction does allow for such an assumption at least in the widest sense. For fluoroscopic applications, image lag caused by trapping and slow release of signal to subsequent frames also limits the validity of such an assumption in the temporal domain. Hence, the description of image noise in terms of the spatio-temporal NPS, which incorporates the image lag, has been sought [50]. Cunningham et al [50] have shown experimentally and theoretically that the spatial component of the spatio-temporal DQE of a system operating in the fluoroscopic mode is the same as the conventional DQE of the same system operating in the radiographic mode under

quantum-noise-limited conditions. The model makes use of this finding so that a single frame of the fluoroscopic mode is considered as essentially a radiographic mode of operation with an exposure level corresponding to that typically used in fluoroscopy.

# 5. METHODS AND MATERIAL

## 5.1. SYSTEM DESCRIPTION

The proposed system consists of four, three-side buttable, 8 x 8-cm large area interlined CCDs, coupled to a structured CsI:Tl scintillator by a straight (non-tapering) fiberoptic plate. An illustration of the four-module imager prior to optical coupling with the CsI:Tl scintillator is shown in Figure 5.1. Illustrations of the single and the four module imager after coupling to the CsI:Tl scintillator are shown in Figure 5.2.

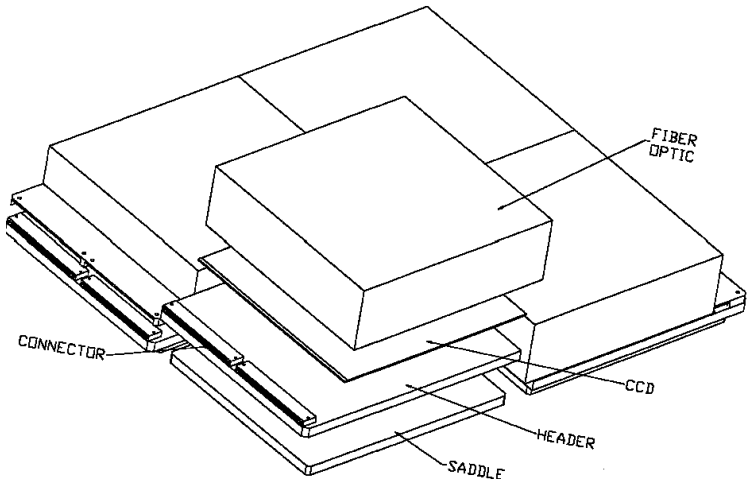


*Figure 5.1 Illustration of the four-module imager. The CsI:Tl scintillator (not shown) is placed on top of the fiberoptic. (Courtesy: Fairchild Imaging, Milpitas, CA.)*

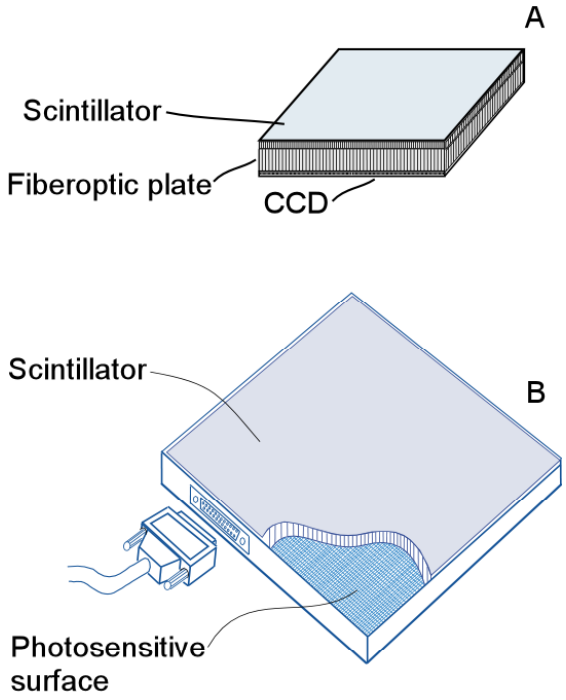


*Figure 5.2 Illustrations of the single module imager (A) and the four module imager (B) after coupling the CsI:Tl scintillator to the CCD(s) by a straight fiberoptic plate.*

Each CCD has a 2048 x 2048 pixel matrix with a fundamental pixel pitch of 39-μm. The CCDs are capable of being operated in 3 different pixel pitch modes of 78, 156 and 234-μm, resulting in Nyquist limits of 6.4, 3.2 and 2.1 cycles/mm (cy/mm) respectively. The variable pixel pitch is achieved by grouping (binning) 2 x 2, 4 x 4 and 6 x 6 adjacent pixels respectively, prior to readout. The interlined CCD (CCD incorporating data lines along one direction of the pixel matrix) has been proposed for this application, in order to facilitate frame rates of up to 30 frames per second (fps).

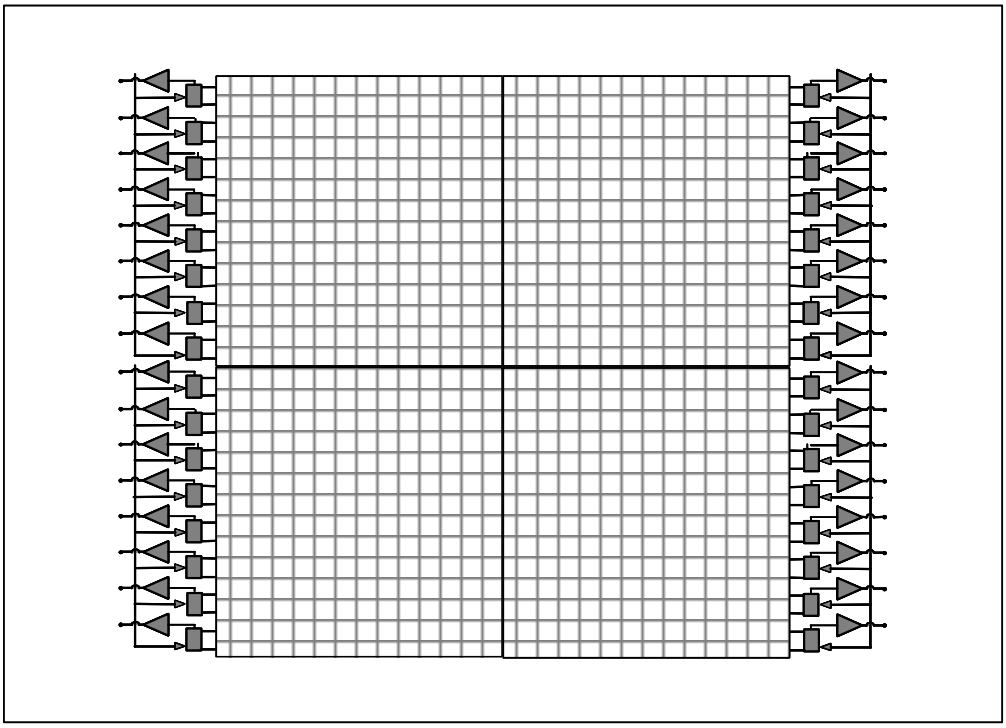

*Figure 5.3 Schematic showing the orientation of the readout ports in the four-module imager. Each CCD has eight readout ports.*

In addition, since the proposed system is an interlined CCD, in principle, the x-ray source can be continuously on, as the time taken for transfer from the active area of the pixel (photosite) to the data line (interline mask) is extremely short (5-μs) and would not contribute to smearing. This would also allow use of these systems with cost efficient fluoroscopic devices, which may not employ a pulsed fluoroscopic source, such as some mobile C-arms. The interline mask is opaque to light resulting in degradation of the fill factor. The width of the interline mask is 11-μm and traverses the length of the pixel, resulting in an active area of 28 x 39-μm for each fundamental pixel. This results in a fill factor of ~72%. The charge readout process for a single CCD module operating in the 2

x 2-binned (78-μm) mode is described below. Each CCD module has 8 output ports as shown in Figure 5.3 and the charge readout is illustrated in Figure 5.4.

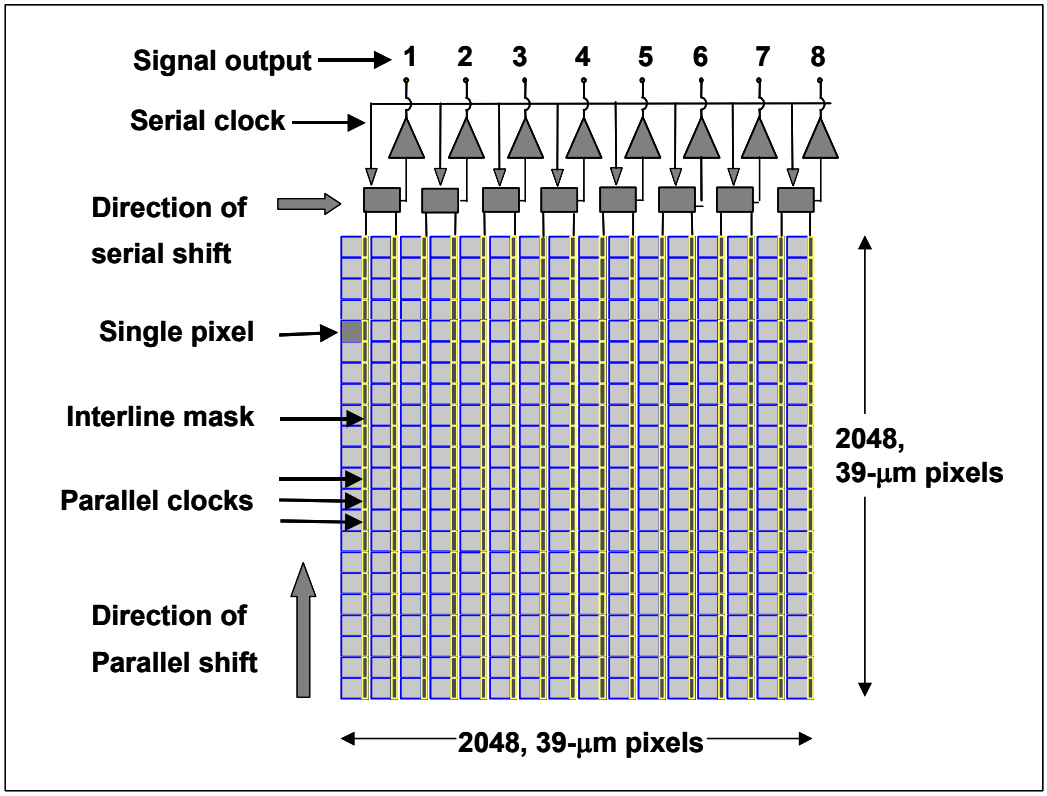


*Figure 5.4 Schematic showing the charge readout process in a single CCD module.*

During the 5-μs period when the charges are transferred from the photosites to the interline mask, there is no shifting of charges along the direction of parallel shift. This period is referred to as the vertical blanking time. Once the charges are transferred to the interline mask, it takes 15-μs to transfer one row of 2048 pixels of 39 x 39-μm to the serial registers. Vertical binning is achieved by transferring two or more rows at the same instant. The clock rate of the serial register is 25 MHz, which corresponds to 40-ns

for transferring one charge packet (vertically binned pixel) to the summing well of the output port. Horizontal binning is achieved by transferring two or more vertically binned pixels to the summing well at the same instant. Since the proposed readout uses 8 ports, the entire contents of the serial register are transferred in 5.12-μs $\left(= \frac{2048 \text{ pixels/row}}{2\,(\text{binning}) \times 8 \text{ ports} \times 25 \text{ MHz}}\right)$. Hence, the contents of a single frame from a single CCD module are transferred in 20.61-ms $\left(= 5\,\mu\text{s} + \left[(15\,\mu\text{s} + 5.12\,\mu\text{s}) \times 1024 \text{ vertically binned rows}\right]\right)$. Thus the proposed system is designed to achieve frame rates of up to 30 fps, even in the 78μm pixel mode. An important characteristic of this readout scheme is that the x-ray source could be operated in the continuous mode without affecting the readout process as the interline mask and the horizontal register are opaque to light.

However, it is not always desirable to operate in a continuous mode. For example, in pulsed fluoroscopy, the CCD readout can be synchronized with the x-ray pulse to further reduce motion blur. The pulse-width of commercially available x-ray generators typically is in the range of 1 to 13-ms, depending upon the manufacturer. At a frame rate of 30 fps, the time taken per frame is 33.33-ms. During this period, the x-ray source is active for at the most 13-ms. Hence, at the termination of the x-ray pulse, the charges on the photosites are transferred to the data line in 5-μs, and the imager is ready to integrate charges for the next frame immediately after this period. However, an additional delay of 2-ms from the termination of the x-ray pulse to the start of charge transfer has been provided to account for the fall-time characteristics of the x-ray source

due to the capacitance of the high-tension cable for systems not equipped with grid-controlled x-ray tubes. The timing diagram for a single CCD module is shown in Figure 5.5.

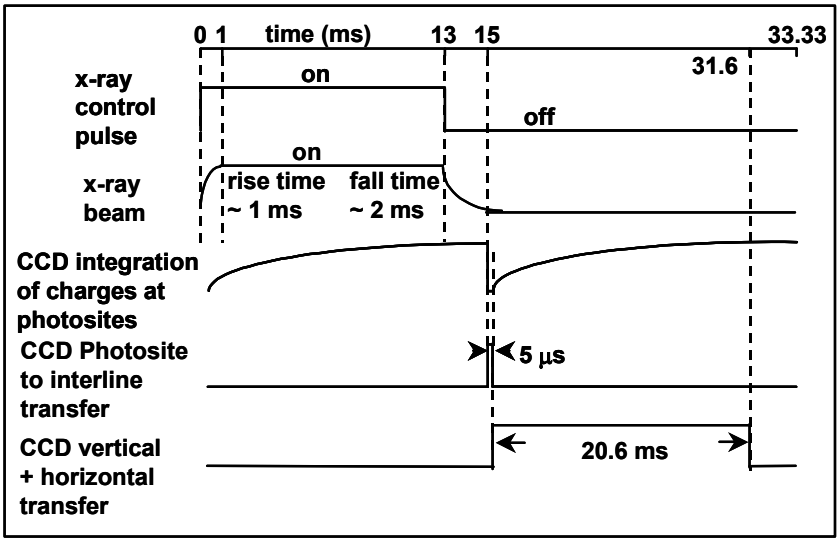


*Figure 5.5 Timing diagram for a single CCD module.*

A schematic illustrating the interface between the CCD imager and the pulsed fluoroscopy x-ray source for synchronization is shown in Figure 5.6.

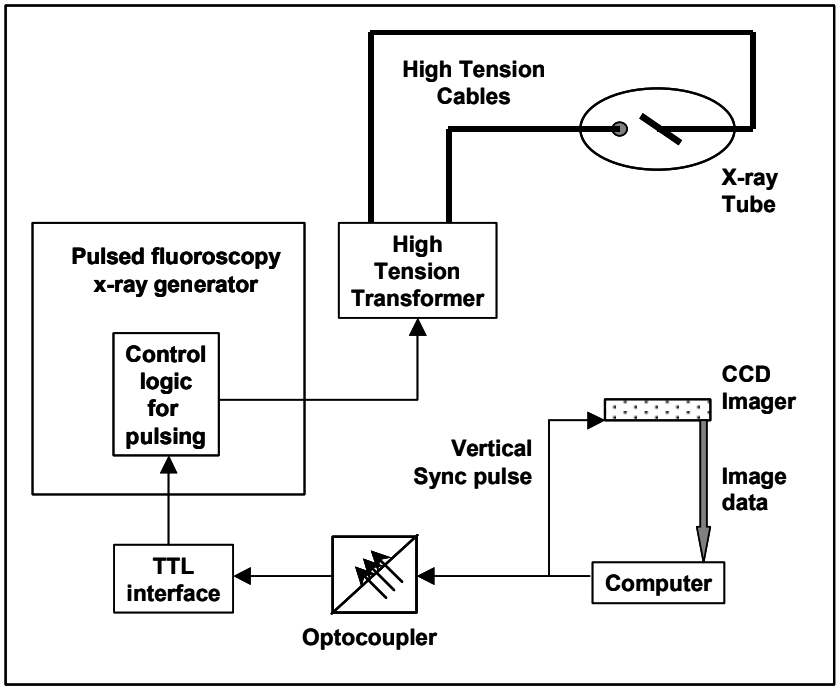


*Figure 5.6 Schematic illustrating the interface between the CCD imager and the pulsed fluoroscopy x-ray source for synchronization.*

## 5.2. DESIGN PARAMETERS

Thallium-doped Cesium Iodide (CsI:Tl) has been selected as the scintillator of choice, as it has the capability to maintain high spatial resolution due to its structured columnar arrangement. Such scintillators have been successfully used with flat-panel systems using amorphous silicon for mammography [51, 52], radiography [53, 54] and fluoroscopy [21]. Also, such scintillators have been used with CCD-based imaging devices for mammography [32]. In addition, the spectral emission of CsI:Tl scintillators is in the wavelength range of 400 to 700-nm, which matches well with the peak absorption range of the silicon photosites [54]. The scintillator design parameters

addressed are quantum efficiency and scintillation yield. The fiberoptic design parameters presented are optical coupling efficiency and estimation of the fiberoptic length (fiberoptic plate thickness). The system parameters addressed in this work are CCD read noise, sensitivity, dynamic range, and spatial resolution characteristics. Techniques for seamless tiling of the CCDs and extending the field of view for larger coverage are also addressed. All computations were performed with a 72-kVp x-ray beam from a tungsten (*W*) source, with 1-inch of added aluminum (*Al*) in the beam path, to provide a first half-value layer (HVL) of 7.0-mm *Al*, corresponding to the post-patient beam quality typically observed during cardiac fluoroscopy, and used by other investigators [21]. The x-ray spectrum, denoted as $q(E)$, was simulated using the software provided by the Institute of Physics and Engineering in Medicine (IPEM), United Kingdom, based on the report number 78, catalogue of diagnostic x-ray spectra and other data [55]. The simulation was performed with an anode target angle of 12 degrees and is shown in Figure 5.7. To verify the accuracy of the simulation, experimental measurement of the first HVL was performed with an x-ray tube (Model: A192, tungsten target, target angle of 12°, inserted in B-150 tube housing, Varian medical systems, Salt Lake City, UT) powered by a commercially available general purpose 50-kW radiographic and fluoroscopic generator (Model: Indico 100, Communications & Power Industries, CPI, Canada). The measured first HVL was 7.02-mm of *Al*, demonstrating good agreement with the simulation. The same x-ray generator and tube is used for all experimental measurements addressed in future sections.

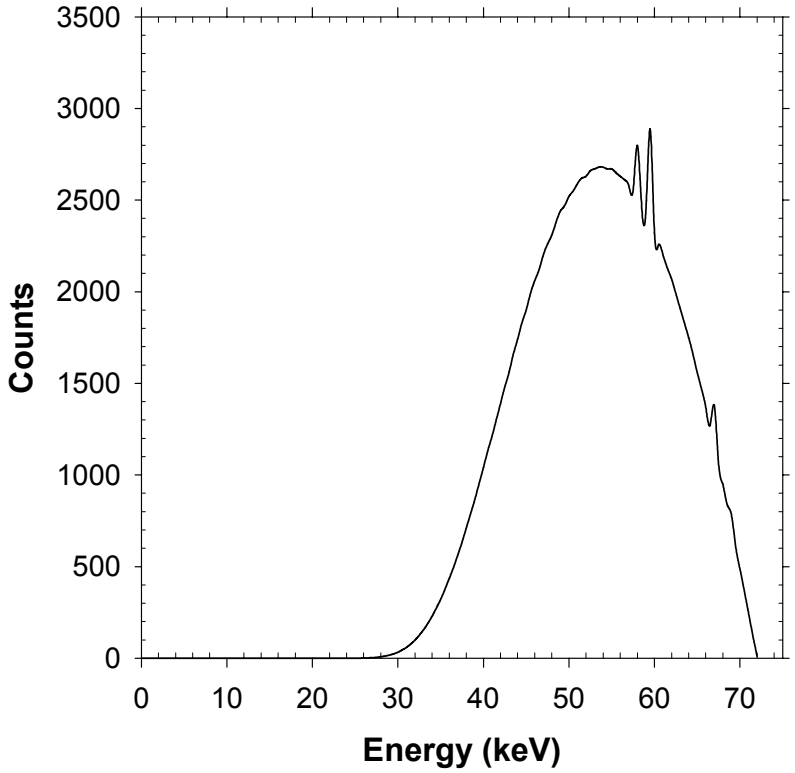


*Figure 5.7 Plot of the simulated post-patient 72-kVp x-ray spectrum with a first half-value layer of 7-mm of Al.*

It is often convenient to represent the incident spectrum $q(E)$, as a normalized spectrum $q_{norm}(E)$ and is expressed as:

$$q_{norm}(E) = \frac{q(E)}{\sum q(E)} \qquad 5.1$$

The photon fluence per μR represented as $\frac{\overline{q_0}}{X}$ calculated for this x-ray spectrum is 291 x-ray photons/(mm$^2$.μR). While all calculations that have a direct impact on image quality were performed with the 72-kVp x-ray spectrum shown above, for estimation of fiberoptic plate thickness needed to provide reasonable protection to the CCD

monoenergetic 60-keV x-ray photons, corresponding to an energy slightly above the average spectral energy, have been used for simplicity.

### *5.2.1. Quantum Efficiency*

The quantum efficiency ( $g_1(E)$ ) for various scintillator thicknesses, ranging from 300 to 525-μm thick in steps of 75-μm, was calculated as per equation 5.2, using published energy-dependent mass attenuation coefficient values [56].

$$g_1(E) = 1 - e^{-\mu_m(E)\cdot\rho_s} \qquad 5.2$$

where $g_1(E)$ is the quantum efficiency, $\mu_m(E)$ is the energy-dependent mass attenuation coefficient and $\rho_s$ is the surface density (phosphor concentration, coverage) of the scintillator. The phosphor concentration provided by the manufacturer (Hamamatsu corporation, Bridgewater, NJ) for the 300, 375, 450 and 525-μm thick (nominal, $\pm 10\%$ tolerance) CsI:Tl scintillators grown on an amorphous carbon substrate (to maximize transmittance) and the resultant packing fraction are shown in Table 5.1.

The quantum efficiency for various thickness of CsI:Tl for the 72-kVp x-ray spectrum was computed as per equation 5.3.

$$\overline{g_1} = \sum g_1(E) \cdot q_{norm}(E) \cdot \Delta E \qquad 5.3$$

*Table 5.1 Scintillator thickness, phosphor concentration and their corresponding packing fraction used in the study*

| Scintillator thickness (μm) | Phosphor concentration (mg/cm$^2$) | Packing fraction |
|---|---|---|
| 300 | 103 | 0.758 |
| 375 | 126 | 0.742 |
| 450 | 148 | 0.726 |
| 525 | 175 | 0.736 |

### *5.2.2. Scintillation Yield (Quantum Gain)*

Holl [57] measured the scintillation yield of CsI:Tl scintillators to be 52,000 optical quanta per absorbed 1-MeV x-ray photon. Recently, researchers at the Lawrence Berkeley Laboratories [54, 58] have reported scintillation yield of up to 64,000 optical quanta per absorbed 1-MeV x-ray photon. Hence, a mean value between the two measurements of 58,000 optical quanta per absorbed 1-MeV x-ray photon, corresponding to conversion energy of 17.24 eV, has been used. The number of optical quanta emitted per absorbed x-ray photon of energy $E$ at a distance $z$ from the output side (towards the CCD) of the scintillator, represented as $g_2(E,z)$, for various x-ray photon energies was calculated as:

$$\begin{aligned} g_2(E,z) &= 58 \cdot E \cdot \eta_{esc}(z) && \text{for } E < E_K \text{ and} \\ g_2(E,z) &= 58 \cdot E \cdot \eta_{esc}(z) \cdot \left(1 - \frac{E_K \cdot K_f}{E}\right) && \text{for } E \geq E_K \end{aligned} \qquad 5.4$$

where $E$ indicates the energy of the incident x-ray photon expressed in keV, $E_K$ indicates the K-edge of the CsI:Tl scintillator (approximated to 33.5 keV), $K_f$ is the escape fraction of $K$-fluorescent x-rays, and $\eta_{esc}(z)$ is the escape probability for a light photon

generated at a distance $z$ from the output port of the scintillator to be emitted in the direction of the fiberoptic (and the CCD). Rowlands and Taylor [59] measured the $K$-fluorescent escape fraction for a cesium iodide scintillator used in image-intensifiers to be constant above the $K$-edge. A mathematical model developed by Dance and Day also reported similar findings [60]. As noted by Swank [61], $K_f$ varies with scintillator surface density. The escape probability of a light photon, $\eta_{esc}(z)$, has been modeled analytically by Lubinsky [62], as well as estimated through Monte-Carlo simulation techniques [63-65]. The depth dependent escape probability ($\eta_{esc}$) was determined from the results of Hillen et al [65]. Modeling was performed by considering a scintillator of thickness *t*, to be composed of fractional layers of thickness $\Delta t$. A schematic of the model used for computing the scintillation yield is shown in Figure 5.8. For a fractional layer of thickness $\Delta t$, located at a distance z from the exit side of the scintillator (towards the CCD), the combined effects of x-ray attenuation within that fractional layer and optical quanta generation and emission from that layer towards the CCD can be written as:

$$g_1(E)\cdot g_2(E,z) = e^{-\mu_m\cdot\rho\cdot P_f\cdot(t-z)}\cdot(1-e^{-\mu_m\cdot\rho\cdot P_f\cdot\Delta t})\cdot g_2(E,z) \qquad 5.5$$

where the term $e^{-\mu_m\cdot\rho\cdot P_f\cdot(t-z)}$ represents the fraction of x-ray photons transmitted past the layer of thickness t-z and the term $(1-e^{-\mu_m\cdot\rho\cdot P_f\cdot\Delta t})$ represents the fraction of x-ray photons attenuated by the fractional layer of thickness $\Delta t$. Thus the number of optical quanta generated for an incident photon of energy $E$ is computed as:

$$g_1(E) \cdot g_2(E) = \int_{z=t}^{0} g_1(E) \cdot g_2(E,z) \cdot dz \qquad 5.6$$

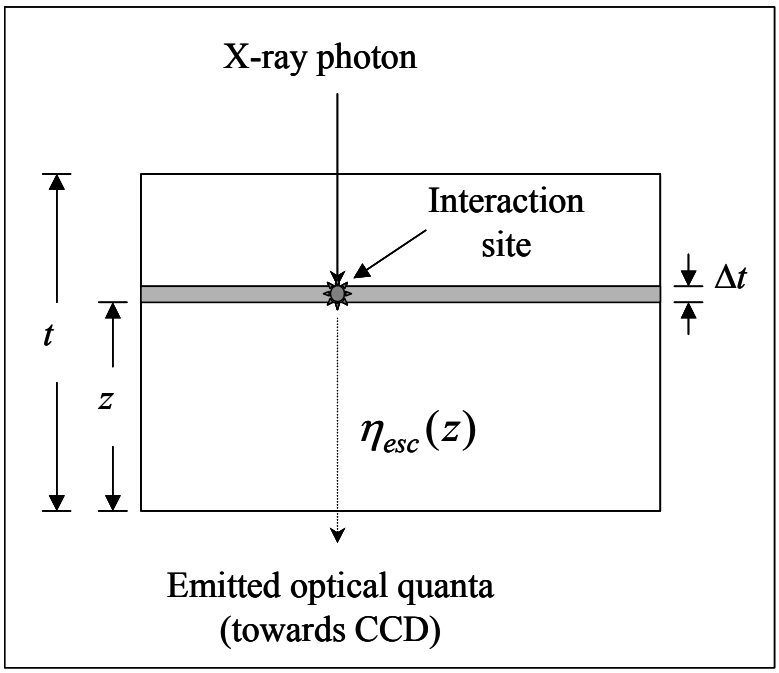


*Figure 5.8 Schematic of the model used for determining the scintillation yield (quantum gain) of CsI:Tl.*

The energy-dependent quantum gain of the scintillator, $g_2(E)$, was computed as per equation 5.7.

$$g_2(E) = \frac{g_1(E) \cdot g_2(E)}{g_1(E)} \qquad 5.7$$

The mean number of optical quanta emitted in the direction of the fiberoptic (and the CCD) for the specified spectrum, referred to as the quantum gain of the scintillator, and represented as $\overline{g_2}$, is calculated as:

$$\overline{g_2} = \frac{\int q_{norm}(E) \cdot g_1(E) \cdot g_2(E) \cdot dE}{\overline{g_1}} \qquad 5.8$$

The quantum gain, $\overline{g_2}$, was calculated for various thickness of CsI:Tl. It is known that structured CsI:Tl scintillators yield better light output compared to traditional gadolinium oxysulfide screens [54].

### *5.2.3. Swank Factor Estimation*

The Swank factor [61] represented as $A_S$, is a measure of the quantum-gain variance represented as $\sigma^2_{g_2}$. Quantum-gain variance is also referred to as conversion noise. It is related to the quantum-gain variance by:

$$A_S = \frac{1}{1 + \frac{\sigma^2_{g_2}}{\overline{g_2}^2}} \qquad 5.9$$

The Swank factor is determined from the moments of the absorbed energy distribution (AED). As noted by Swank [61], it is incorrect to average the Swank factor directly over the spectrum. The moments of the AED have to be weighted by the spectrum and then the Swank factor should be calculated as shown by the equations 5.10 and 5.11 below.

$$A_S = \frac{m_1^2}{m_0 \cdot m_2} \qquad 5.10$$

where

$$m_0 = \int q_{norm}(E) \cdot g_1(E) \cdot dE$$
$$m_1 = \int q_{norm}(E) \cdot g_1(E) \cdot \left[\left(1 - K_f(E)\right) \cdot E \cdot g_2(E) + K_f(E).\left(E - E_K\right) \cdot g_2(E)\right] \cdot dE \qquad 5.11$$
$$m_2 = \int q_{norm}(E) \cdot g_1(E) \cdot \left[\left(1 - K_f(E)\right) \cdot \left(E \cdot g_2(E)\right)^2 + K_f(E).\left(\left(E - E_K\right) \cdot g_2(E)\right)^2\right] \cdot dE$$

The Swank factor is an important parameter as the DQE of an imaging system cannot exceed the product of the $\overline{g_1} \cdot A_S$. It is also often convenient to represent the quantum-gain variance by Poisson excess (factor by which the quantum-gain variance exceeds the Poisson variance, $\overline{g_2}$), represented as $\varepsilon_{g_2}$ and is related to the Swank factor by:

$$\varepsilon_{g_2} = \overline{g_2} \cdot \left(\frac{1}{A_S} - 1\right) - 1 \qquad 5.12$$

*5.2.4. Scintillator Blur*

The columnar arrangement of CsI:Tl scintillators restricts spatial spreading and hence, exhibits improved spatial resolution characteristics compared to gadolinium oxysulfide scintillators. In order to study the impact of CsI:Tl thickness on the spatial resolution characteristics, system presampling modulation transfer function ($MTF_{pre,sys}$) measurements were performed for four thicknesses of CsI:Tl. A 1-inch x 1-inch, back-illuminated CCD operating at a pixel pitch of 96-μm was used. The presampling MTF was measured using the slanted-slit technique [50]. The experimental procedure for these measurements has been described in detail [33, 51]. Specifically, an image of a 10-mm long, 10-μm wide (±1-μm) slit was acquired. The image was corrected for minor variations in slit width. The finely sampled line spread function (LSF) was obtained

based on the angulation of the slit and normalized to a peak value of one. The finely sampled LSF was extrapolated from 1% down to 0.01% of the peak amplitude using an exponential fit to avoid truncation errors. The Fourier transform of the finely sampled LSF was performed and then deconvolved for the finite dimension of the slit (10-μm) by a *sinc* function in the frequency domain to obtain the system presampling MTF ($MTF_{pre,sys}$). The obtained $MTF_{pre,sys}$ includes the effects of scintillator blur ($MTF_{CsI:Tl}$), focal spot blur ($MTF_{fs}$), and the pixel-presampling MTF ($MTF_{pre,pix}$).

$$MTF_{pre,sys} = MTF_{CsI:Tl} \cdot MTF_{fs} \cdot MTF_{pre,pix} \qquad 5.13$$

Since the slit was placed in contact with the scintillator, the slit image acquired using the small focal spot size of 0.6-mm, and the source-to-imager distance was sufficiently large (195-cm), the effect of focal spot blur can be ignored $\left(MTF_{fs} = 1\right)$. In order to determine the $MTF_{CsI:Tl}$, the $MTF_{pre,pix}$ has to be deconvolved from the measured $MTF_{pre,sys}$. While the $MTF_{pre,pix}$ can be represented as a *sinc* function for imaging systems that use discrete pixels such as amorphous silicon photodiodes, such an assumption needs to be verified for CCD-based imaging systems. Hence, the $MTF_{pre,sys}$ was also measured for the 300-μm CsI:Tl with the CCD operating at 24-μm. If the assumption that the $MTF_{pre,pix}$ can be represented by the *sinc* function were to be true, then the $MTF_{CsI:Tl}$ obtained by deconvolving the *sinc*(24μm) from the $MTF_{pre,sys}$ acquired with the CCD operating at 24-μm should be identical to that obtained by deconvolving the *sinc*(96μm) from the measured $MTF_{pre,sys}$ with the CCD operating at

96-μm. It is often convenient to represent the scintillator MTF by a single parameter. For gadolinium oxysulfide scintillators, the scintillator MTF can be adequately represented by a single parameter ( $H$ ) with a Lorentzian fit of the form:

$$MTF_{Gd_2O_2S}(f) = \frac{1}{1 + H \cdot f^2} \qquad 5.14$$

However for CsI:Tl scintillators, the Lorentzian fit did not yield favorable results. For the CsI:Tl scintillators used in the study, the best fit to $MTF_{CsI:Tl}$ was obtained by using an equation of the form:

$$MTF_{CsI:Tl}(f) = \frac{1}{1 + B \cdot (f + f^2)} \qquad 5.15$$

where, $B$ is the fit-parameter and $f$ is the spatial frequency in cy/mm.

### *5.2.5. Optical Coupling Efficiency*

The optical coupling efficiency of lens-coupled CCD-based systems has been reported [29]. Hejazi and Trauernicht [31] have provided an analysis of the optical coupling efficiency of lens-coupled and fiberoptic-coupled CCD-based systems. The study also addresses the effect of tapered fiberoptics in CCD-based systems. A straight fiberoptic plate (non-tapering, 1:1 fiber) provides better optical coupling between the scintillator and the CCD with minimal loss of spatial resolution [28, 31]. The optical coupling efficiency ( $\eta_{FO}$ ) of the fiberoptics, which is the fraction of light captured and transmitted by a fiber pressed against a Lambertian source, can be given as [31]:

$$\eta_{FO} = \overline{g_4} = n^2 \cdot \sin^2\theta_1 \cdot e^{-u \cdot l} \cdot (1 - L_R) \cdot F_c \qquad 5.16$$

where, $n$ is the refractive index of the material before the fiber entrance, $\theta_1$ is the entrance angle such that the total internal reflection condition at the core-cladding interface is satisfied, $u$ is the absorption coefficient of the fiber, $l$ is the length of the fiber, $L_R$ is the loss at the surface due to Fresnel reflection, and $F_c$ is the fill factor of the fiber core. The terms $n\sin\theta_1$, and $e^{-ul}$ are often referred to as the numerical aperture of the fiberoptic, and the fiber core transmission efficiency, respectively. The fiber core transmission efficiency is ~0.8 [31]. Since it is difficult to model the effect of Fresnel reflections and there are means to decrease the loss associated with Fresnel reflection by anti-reflection (AR) coating or using a medium with matching index, the losses associated with Fresnel reflections ($L_R$) has been assumed to be ~10%. In order to satisfy the total internal reflection condition at the core-cladding interface, the entrance angle $\theta_1$ should be such that, $\sin\theta_1 < \frac{\sqrt{n_2^2 - n_3^2}}{n}$, where, $n_2$ is the index of refraction of the core, $n_3$ is the index of refraction of the cladding and $n$ is the refractive index of the material before the fiber entrance. For the fiberoptic plate proposed with this system (Type 47A, Schott Fiberoptics, Sturbridge, MA), the fibers have a circular cross-section and the diameter of the clad and core are 12-μm and 10-μm respectively. Also, the refractive index of the core and clad are 1.8 and 1.5, respectively.

### *5.2.6. Estimation of Fiberoptic Length*

In addition to optically coupling the scintillator with the CCD, the fiberoptics also perform an important role of protecting the CCD from direct x-ray photon interactions. Exposure to high-energy radiation over long duration might damage and degrade detector sensitivity [67-69], and could be the primary cause of system failure. Other possible sources of defects that could limit lifetime are related to CCD manufacturing techniques, such as bond-wire breakage, particularly when CCDs are subjected to temperature cycling. However, considering that this system operates at room temperature with no external cooling mechanism this is not likely to be a source of failure. Hence, it is important to estimate the fiberoptic length needed to provide adequate shielding to the CCD but without attenuating too much light. Measurements of the x-ray linear attenuation coefficient of various commercially available fiberoptic plates have been presented in the past [70]. These fiberoptic plates are doped with non-scintillating high-atomic number (Z) material to efficiently attenuate the incident x-ray beam. Based on these attenuation measurements [54], type 47A (Schott Fiberoptics, Sturbridge, MA) was used for estimation of the fiberoptic length. In addition, this type of fiberoptic plate was selected as the optical characteristics of this plate were found to be suitable for digital mammography and has been successfully used with a CCD-based system developed for spot compression views and stereotactic localization [33]. For simplicity, a mono-energetic 60-keV x-ray beam was used for estimation of fiberoptic length. Also, the scintillator thickness was assumed to be 450-μm. The number of x-ray photons incident on the entire CCD as a function of time for various fiberoptic plate thickness was

calculated based on an exposure rate of 2-μR/frame, 30 fps, 30 minutes of fluoroscopic usage each hour, 10 hours of usage per day, 300 days of usage per year and 10 years of usage. Hence, the projected lifetime of this system is 10 years, which far exceeds the useful lifetime of image-intensifiers.

### *5.2.7. CCD Quantum Efficiency*

It is known that the emission wavelength of CsI:Tl matches well with the absorption wavelength of the silicon pixels in the CCD [42]. In general, the wavelength-dependent quantum efficiency of the CCD ($g_5(\lambda)$) is weighted with the normalized emission spectrum of CsI:Tl ($g_{2_{norm}}(\lambda)$), as shown in equation 5.17 below, to obtain the average quantum efficiency of the CCD ($\overline{g_5}$).

$$\overline{g_5} = \int g_5(\lambda) \cdot g_{2_{norm}}(\lambda) \cdot d\lambda \qquad 5.17$$

The geometrical fill factor ($F_f$) is defined as the ratio of the active area (photosensitive area) of the pixel ($a_x \cdot a_y$) to the pixel area ($A_{pix,x} \cdot A_{pix,y}$) as shown in equation 5.18.

$$F_f = \frac{a_x \cdot a_y}{A_{pix,x} \cdot A_{pix,y}} \qquad 5.18$$

where, $a_x$ and $a_y$ represent the dimensions of the active region of the pixel along the *x* and *y* directions, and, $A_{pix,x}$ and $A_{pix,y}$ represent the dimension of the pixel along the *x*

and *y* directions. For a system with a square pixel pitch matrix, which is the case with this system, $A_{pix,x} = A_{pix,y} = A_{pix}$.

### *5.2.8. Sensitivity*

The sensitivity (Γ) of the system in units of electrons/μR can be theoretically computed as:

$$\Gamma = \frac{\overline{q_0}}{X} \cdot \overline{g_1} \cdot \overline{g_2} \cdot \overline{g_4} \cdot \overline{g_5} \cdot F_f \cdot A_{pix}^2 \qquad 5.19$$

where, $\frac{\overline{q_0}}{X}$ is the photon fluence in units of photons/(mm$^2$.μR), $\overline{g_1} \cdot \overline{g_2}$ are the quantum efficiency and quantum gain of the CsI:Tl scintillator, $\overline{g_4}$ is the fiberoptic coupling efficiency, $\overline{g_5} \cdot F_f$ is the quantum efficiency of the CCD including the loss due to the geometrical fill factor, and $A_{pix}^2$ is the pixel area in units of mm$^2$.

### *5.2.9. CCD Electronic Noise*

The total electronic noise ($\sigma_T$) associated with a CCD-based system can be classified into noise arising from within the CCD ($\sigma_{CCD}$) such as dark noise, noise from the on-chip output node ($\sigma_{op}$) such as read noise and reset noise, and that arising from external sources ($\sigma_{ext}$) such as analog-to-digital converter (ADC) quantization noise. Since these noise sources are uncorrelated, the total electronic noise then can be stated as:

$$\sigma_T = \sqrt{\sigma_{CCD}^2 + \sigma_{op}^2 + \sigma_{ext}^2} \qquad 5.20$$

The primary sources of noise arising from within the CCD ($\sigma_{CCD}$) are dark noise due to thermally generated electrons, trapping-state noise, and charge-transfer noise. The trapping-state noise arises from the uncertainty in the quantity of charge due to trapping and slow release of charges either by surface or bulk states. Buried-channel operation prevents such noise from the surface states and material control during fabrication can reduce the bulk trapping-state density to negligible levels [55]. The charge-transfer noise is due to the finite efficiency of the charge transfer process. The high charge transfer efficiency that is routinely being achieved by modern CCDs makes this source of noise relatively unimportant [55]. Hence for this analysis, trapping-state noise and charge-transfer noise are ignored. Thus, the CCD noise ($\sigma_{CCD}$) can been stated as:

$$\sigma_{CCD} = \sqrt{t \cdot q_d \cdot A_{pix}^2} \qquad 5.21$$

where, $q_d$ is the dark charge generated per unit time per unit area, $t$ is frame integration period, and $A_{pix}^2$ is the area of a pixel. The dark current is typically around 15 pA/cm$^2$, and for the system operating at a frame rate of 30 frames/second (fps), the integration time per frame is 33.3 ms.

The primary sources of noise arising from the on-chip output amplifier are the read noise and the reset noise. Reset noise is due to the uncertainty in voltage to which the output node is reset after a charge packet is read out. This noise can be removed very effectively using correlated double sampling techniques [71]. Hence for this analysis, the reset noise has been assumed to be negligible. Low noise CCD detectors [28] have been

known to exhibit much lower read noise than amorphous-silicon (a-Si) based flat-panel detectors [34]. Increased noise observed with a-Si based detectors is primarily due to the thin-film transistor (TFT) readout. The read noise estimated by the manufacturer (Fairchild Imaging, Inc., Milpitas, CA) is in the range of 15-20 electrons rms. Hence, the noise arising from on-chip output node can be stated as:

$$\sigma_{op} = \sigma_r \tag{5.22}$$

where, $\sigma_r$ is the on-chip output amplifier read noise.

Primary external noise sources ($\sigma_{ext}$) include ADC quantization noise, clock-jitter noise and electromagnetic interference (EMI). Proper shielding of the CCD imager can reduce EMI to negligible levels [72]. Jitter on the master clock can introduce noise referred to as clock-jitter noise. This could be a significant source for systems using phase-lock-loop clocks and can be almost eliminated by using crystal oscillators [71]. ADC quantization noise ($\sigma_{ADC}$) arises from the uncertainty in its value due to digitization and can be stated as:

$$\sigma_{ADC} = \frac{\Delta}{\sqrt{12}} \tag{5.23}$$

where, $\Delta$ is the step size in units of electrons/digital unit (DU) and is also often referred to as the camera gain constant. For the system operating in the fluoroscopic mode, the camera gain constant is set to be 2.2 electrons/DU, to provide improved sensitivity. This results in $\sigma_{ADC} < 1$ electron rms for the fluoroscopic mode of operation. However, if the camera gain constant is adjusted to provide a wide dynamic range, then $\sigma_{ADC}$ could become significant. The maximum $\sigma_{ADC}$ would occur when the camera gain constant is

adjusted to accommodate the summing-well capacity, which is 1 x $10^6$ electrons for this system. This would result in a camera gain constant of ~61 electrons/DU and $\sigma_{ADC}$ of 17.6 electrons rms.

Thus, the total electronic noise of the CCD imager can be stated as:

$$\sigma_T = \sqrt{t \cdot q_d \cdot A_{pix}^2 + \sigma_r^2 + \sigma_{ADC}^2} \qquad 5.24$$

*5.2.10. Dynamic Range*

Yaffe and Rowlands [73] have provided an alternate definition of the dynamic range, which they refer to as 'effective dynamic range' ( $DR_{eff}$ ) and is defined as:

$$DR_{eff} = \frac{k_2 \cdot X_{\max}}{k_1 \cdot X_{noise}} \qquad 5.25$$

where, $k_1$ is the factor by which minimum signal must exceed the noise for reliable detection, $X_{\max}$ is the x-ray fluence providing the maximum signal that the detector can accommodate, and $X_{noise}$ is the fluence that provides a signal equivalent to $\sigma_T$. The constant $k_2$ is the factor by which the signal-to-noise ratio (SNR) improves due to integration over multiple pixels. The CCD is designed to have a summing well capacity and hence saturation limit of 1 x $10^6$ electrons. Assuming $k_1$ to be 5 based on the work of Rose [74], the system is capable of providing signal response in the range of $5 \times \sigma_T$ to 1 x $10^6$ electrons. The corresponding exposure levels ( $X$ ) can be calculated from the sensitivity ( $\Gamma$ ) of the system as

$$X = \frac{Signal}{\Gamma} \qquad 5.26$$

## 5.3. SEAMLESS TILING OF CCDS

Seamless tiling of CCDs using tapered fiberoptics has been achieved for the spatial resolution demanding application of mammography [75] and is used in a commercially available digital mammography system. Such tiling can be achieved using techniques, which are currently used for defect correction in CCDs. Specifically, by treating the seams as defective columns, corrections can be performed based on linear interpolation from surrounding pixels. Since the seam of the proposed system is expected to be approximately 40-μm, which corresponds well with the fundamental pixel size, it is easy to correct for this seam. An artificial column is created at the location of the seam by providing the mean values of the adjacent columns. In order to verify the effectiveness of such a scheme, a preliminary study was conducted where two 6 x 6-cm CCDs operating at a pixel pitch of 30-μm were tiled. The seam between the two CCDs was approximately 30-μm. A photograph of the tiled system is shown in Figure 5.9. The CCDs were coupled to a MinR 2000™ scintillator (Eastman Kodak Company, Rochester, NY) by a straight fiberoptic plate.

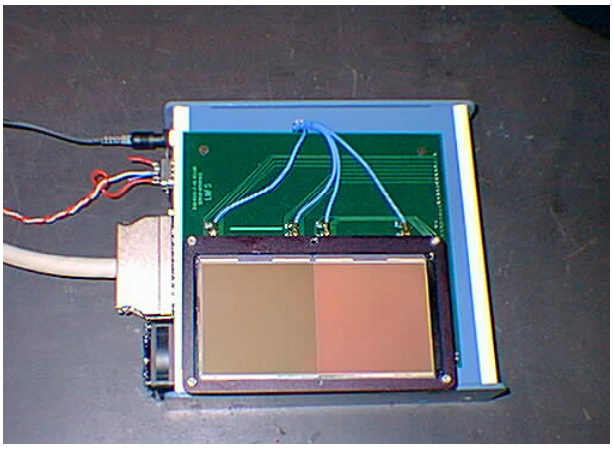

*Figure 5.9 Photograph of two 6 cm x 6 cm CCDs tiled to illustrate the seam suppression technique.*

An image of a spoke wheel phantom was acquired. The image clearly indicated a seam at the junction between the two CCDs. The acquired image was subjected to the seam suppression algorithm. The resultant image indicates successful suppression of the seam. Since, the tiled CCD-based system used for this study was designed for the more spatial resolution demanding application of mammography, successful suppression of the seam artifact would indicate an overwhelming possibility of effectively suppressing the seam for the fluoroscopic applications. More recently, several algorithms for tiling multiple detector modules were investigated [76] and the effectiveness and suitability of these algorithms with this system is yet to be explored.

## 5.4. EXTENDING FOV

The proposed system provides a FOV at the image plane of 16 x 16-cm. The 6-inch diameter FOV of the image-intensifier is used for most cardiac angiography examination

including coronary angiograms. The 16 x 16-cm (6.3 x 6.3–inch) FOV of the CCD-based system is sufficient to provide adequate coverage for these examinations. However, for certain applications such as ventriculograms, a larger FOV (such as the 9-inch diameter FOV of image-intensifier) may be preferred. Hence, this section addresses a technique to tile additional CCD modules to provide larger FOV. As each of the CCD-modules is three-side buttable, extending the FOV in either of the two directions can be easily accomplished by tiling additional modules. For example, tiling 2 x 3 modules can achieve a 16 x 24-cm imager. However, extending the FOV in both directions requires considerable adaptation, as the readout pins of the central module cannot be easily accessed. In order to overcome this issue, the height (length) of the fiberoptic plate for the inaccessible CCD(s) have been increased to provide sufficient clearance, such that the readout pins are accessible. This staggered fiberoptic arrangement can be achieved in several ways. One such technique, which can be implemented with ease, is shown in Figure 5.10.

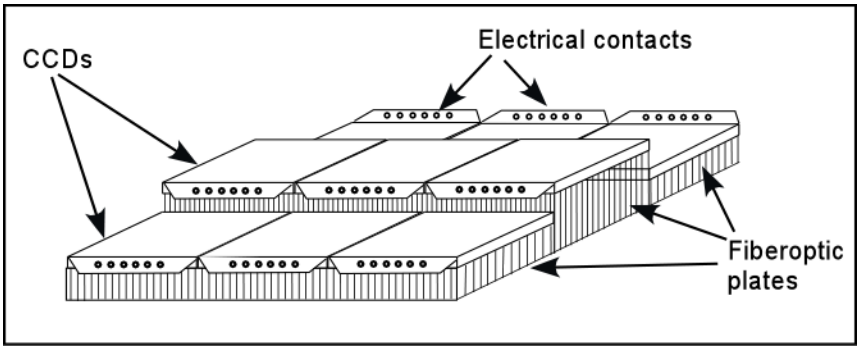


*Figure 5.10 Illustration of the staggered fiberoptic arrangement to overcome the difficulty associated with accessing the readout pins of the central CCD. This staggered approach can be achieved in several ways.*

## 5.5. SERIAL-CASCADED LINEAR-SYSTEMS MODEL

Modeling was performed with a 72-kVp x-ray beam hardened with 1-inch of *Al*, such that the first half-value layer (HVL) of the beam was 7-mm of *Al*. The proposed system is considered a serial cascade of discrete stages, which can be represented by one of the following processes: quantum gain, stochastic blurring or deterministic blurring. A quantum gain stage affects the mean number of image quanta and the blurring stage affects the spatial distribution of image quanta. The signal and noise transfer characteristics from the input to the output of each process is distinct. For any given stage *i*, the image quanta distribution of the output signal is represented as $q_i(x,y)$ in the spatial coordinates of $(x,y)$, and the output Wiener spectrum (NPS) is represented as $W_i(u,v)$ in its orthogonal spatial frequency coordinates of $(u,v)$. Based on the work of Rabbani, Shaw and Van Metter [45], for a quantum gain stage '*i*' where the input signal is represented as $q_{i-1}$ and the output signal is represented as $q_i$ the signal transfer from the input to the output can be stated as:

$$q_i = q_{i-1} \cdot \overline{g_i} \tag{5.27}$$

where, $\overline{g_i}$ is the average quantum gain of that stage. The NPS transfer from the input to the output is expressed as:

$$W_i(u,v) = W_{i-1}(u,v) \cdot \overline{g_i}^2 + \overline{q_{i-1}} \cdot \sigma_{g_i}^2 + W_{add\,i}(u,v) \tag{5.28}$$

where, $\overline{q_{i-1}}$ represents the average input signal, $\sigma_{g_i}^2$ represents the variance in the quantum gain of that stage and $W_{add\,i}(u,v)$ represents any additive noise imparted by that stage. Quantum gain stages can be classified into stages where there is a loss in image quanta such as attenuation of the incident radiation by the scintillator, self-absorption of the generated optical quanta within the scintillator medium, and fiberoptic coupling, and quantum amplification stages such as generation of optical quanta in the scintillator. Further, some gain stages can be described by a known probability distribution such as Poisson, Binomial or deterministic, where the relationship between the average gain $\overline{g_i}$ and the gain-variance $\sigma_{g_i}^2$ can be expressed analytically. The gain variance can also be expressed in terms of the Poisson excess, $\varepsilon_{g_i}$, or in terms of the Swank factor [61], $A_S$.

For a stochastic blurring stage *i*, such as the redistribution of image quanta in a scintillator, with a normalized point spread function (PSF) represented as $p_i(x,y)$ and the corresponding modulation transfer function (MTF) represented as $T_i(u,v)$, the signal transfer can be written as:

$$q_i(x,y) = q_{i-1}(x,y) \,**_s\, p_i(x,y) \tag{5.29}$$

where, $**_s$ represents the stochastic convolution operator. The noise transfer for the stochastic blurring stage can be expressed as:

$$W_i(u,v) = \left[W_{i-1}(u,v) - \overline{q_{i-1}}\right] \cdot T_i^2(u,v) + \overline{q_{i-1}} \tag{5.30}$$

The above equation indicates that for a stochastic blurring stage, the uncorrelated component $\overline{q_{i-1}}$ is unaffected, and the correlated component $\left[W_{i-1}(u,v) - \overline{q_{i-1}}\right]$ is

modulated by the square of the MTF, $T_i^2(u,v)$. For a deterministic blurring stage *i*, such as integration over the pixel aperture, with a MTF represented as $T_i(u,v)$, the signal transfer is written as:

$$q_i(u,v) = q_{i-1}(u,v) \cdot T_i(u,v) \qquad 5.31$$

The noise transfer for a deterministic blurring stage is expressed as:

$$W_i(u,v) = W_{i-1}(u,v) \cdot T_i^2(u,v) \qquad 5.32$$

The system was modeled by dividing the imaging chain into the following elementary stages:

0. Incident image quanta
1. Attenuation of x-rays by the CsI:Tl scintillator
2. Generation and emission of optical quanta by the CsI:Tl scintillator
3. Stochastic blurring by the CsI:Tl scintillator
4. Coupling of the optical quanta by straight (non-tapering) fiberoptics
5. Absorption of optical quanta by the CCD
6. Deterministic blurring by the pixel presampling MTF and effect of pixel fill factor
7. Additive noise

The model encompasses elementary stages up to the aliasing stage, thus providing the presampling signal and the presampling NPS. While most of the objective parameters of image quality can be addressed adequately by the presampling signal and the presampling NPS, in reality, DQE measurements performed on digital imaging systems are based on the presampling signal (MTF) and the aliased NPS. Hence, an additional section illustrating the effects of noise aliasing has been provided. This is of particular

importance to this imager as the system can be operated in any of the three pixel pitch modes and hence, their impact on the aliased NPS need to be addressed. Modeling of system performance was performed for the three pixel pitch modes of 78, 156 and 234-μm and for four CsI:Tl scintillator thicknesses of 300, 375, 450 and 525-μm.

### *5.5.1. Stage 0: Incident X-ray Quanta*

The system was modeled using the polyenergetic 72-kVp x-ray beam filtered by 1-inch of *Al* from a 12° tungsten (W) target, with a first half-value layer (HVL) of 7.0-mm of *Al*, and represented by the normalized spectrum $q_{norm}(E)$ as per equation 5.1. A plot of this spectrum is also shown in Figure 5.7. The photon fluence per μR of exposure $\left(\frac{\overline{q_0}}{X}\right)$ for this beam was calculated to be 291 x-ray photons/(mm$^2$.μR) based on the definition of Roentgen provided by Johns and Cunningham [77] and the technique described by Siewerdsen et al [34]. Since the incident x-ray quanta are Poisson distributed the signal and NPS can be stated as:

$$\overline{q_0} = \overline{q_0} \tag{5.33}$$

$$W_0(u,v) = \overline{q_0} \tag{5.34}$$

### *5.5.2. Stage 1: Attenuation of X-rays by the Scintillator*

This is a stochastic gain stage that follows the binomial process, where the probability that an incident x-ray photon is attenuated by the CsI:Tl scintillator is given

by the average quantum efficiency, $\overline{g_1}$. The variance of this binomial gain stage is given by:

$$\sigma_{g_2}^2 = \overline{g_1} \cdot \left(1 - \overline{g_1}\right) \tag{5.35}$$

The signal and the NPS at the output of stage 1, after simplification, can be written as:

$$\overline{q_1} = \overline{q_0} \cdot \overline{g_1} \tag{5.36}$$

$$W_1(u,v) = \overline{q_0} \cdot \overline{g_1} \tag{5.37}$$

### *5.5.3. Stage 2: Generation and Emission of Optical Quanta by Scintillator*

This stage is a stochastic gain stage that describes the generation and emission of optical quanta by the CsI:Tl scintillator. The variance in the quantum gain ($\sigma_{g_2}^2$) was computed from the Swank factor $A_S$ addressed in section 5.2.3, and expressed in terms of the Poisson excess ($\varepsilon_{g_2}$). The signal and NPS at the output of stage 2, after simplification, can be written as:

$$\overline{q_2} = \overline{q_0} \cdot \overline{g_1} \cdot \overline{g_2} \tag{5.38}$$

$$W_2(u,v) = \overline{q_0} \cdot \overline{g_1} \cdot \overline{g_2} \cdot \left(\overline{g_2} + 1 + \varepsilon_{g_2}\right) \tag{5.39}$$

### 5.5.4. *Stage 3: Stochastic Blurring by the Scintillator*

This is a stochastic blurring stage, where the incident quanta are randomly displaced (redistributed) through convolution by the normalized point spread function (PSF) in the spatial domain. In the spatial frequency domain the PSF ( $p_i(x,y)$ ) can be represented by the scintillator blur, which is the Fourier transform of the PSF. The scintillator blur represented as $T_3(u,v)$ is identical to the $MTF_{CsI:Tl}$ discussed in section 5.2.4. The signal and NPS at the output of stage 3 can be written as:

$$q_3(u,v) = \overline{q_0} \cdot \overline{g_1} \cdot \overline{g_2} \cdot T_3(u,v) \tag{5.40}$$

$$W_3(u,v) = \overline{q_0} \cdot \overline{g_1} \cdot \overline{g_2} \cdot \left[1 + T_3^2(u,v) \cdot \left(\overline{g_2} + \varepsilon_{g_2}\right)\right] \tag{5.41}$$

### 5.5.5. *Stage 4: Coupling of Optical Quanta by Fiberoptics*

This is a stochastic gain stage that follows the binomial process, where the probability that an incident quantum is coupled to the CCD is given by the average fiberoptic coupling efficiency, $\overline{g_4}$. The signal and the NPS at the output of stage 4 is written as:

$$q_4(u,v) = \overline{q_0} \cdot \overline{g_1} \cdot \overline{g_2} \cdot \overline{g_4} \cdot T_3(u,v) \tag{5.42}$$

$$W_4(u,v) = \overline{q_0} \cdot \overline{g_1} \cdot \overline{g_2} \cdot \overline{g_4} \cdot \left[1 + \overline{g_4} \cdot T_3^2(u,v) \cdot \left(\overline{g_2} + \varepsilon_{g_2}\right)\right] \tag{5.43}$$

### 5.5.6. *Stage 5: Absorption of Optical Quanta by the CCD*

This is a stochastic gain stage that follows the binomial process, where the probability that the CCD absorbs an incident quantum is given by the average CCD quantum efficiency, ( $\overline{g_5}$ ). The signal and NPS at the output of stage 5 is written as:

$$q_5(u,v) = \overline{q_0} \cdot \overline{g_1} \cdot \overline{g_2} \cdot \overline{g_4} \cdot \overline{g_5} \cdot T_3(u,v) \tag{5.44}$$

$$W_5(u,v) = \overline{q_0} \cdot \overline{g_1} \cdot \overline{g_2} \cdot \overline{g_4} \cdot \overline{g_5} \cdot \left[1 + \overline{g_4} \cdot \overline{g_5} \cdot T_3^2(u,v) \cdot \left(\overline{g_2} + \varepsilon_{g_2}\right)\right] \tag{5.45}$$

### 5.5.7. *Stage 6: Deterministic Blurring by the Pixel and Effect of Fill Factor*

This is a deterministic stage as there is no variance associated with the pixel dimension. The pixel presampling MTF is represented as $T_6(u,v)$ and expressed as:

$$T_6(u,v) = \left| \frac{\sin(\pi \cdot a_x \cdot u) \cdot \sin(\pi \cdot a_y \cdot v)}{(\pi \cdot a_x \cdot u) \cdot (\pi \cdot a_y \cdot v)} \right| \tag{5.46}$$

where, $a_x$ and $a_y$ represent the dimensions of the pixel that is sensitive to light (active dimension) in the *x* and *y* directions, respectively. For the proposed CCD architecture, the active dimension along the *x* and *y* directions are not identical, as the interline channel is opaque to light. Hence, the pixel presampling MTF along the *u* and *v* – axes are represented as:

$$\begin{aligned} T_6(u) &= \left| \frac{\sin(\pi \cdot a_x \cdot u)}{(\pi \cdot a_x \cdot u)} \right| \\ T_6(v) &= \left| \frac{\sin(\pi \cdot a_y \cdot v)}{(\pi \cdot a_y \cdot v)} \right| \end{aligned} \tag{5.47}$$

Thus the extension of the model from symmetric pixel geometry to asymmetric pixel geometry is straightforward. The signal and NPS at the output of stage 6 is written as:

$$q_6(u,v) = \overline{q_0} \cdot \overline{g_1} \cdot \overline{g_2} \cdot \overline{g_4} \cdot \overline{g_5} \cdot A_{pix}^2 \cdot F_f \cdot T_3(u,v) \cdot T_6(u,v) \qquad 5.48$$

$$W_6(u,v) = \overline{q_0} \cdot \overline{g_1} \cdot \overline{g_2} \cdot \overline{g_4} \cdot \overline{g_5} \cdot A_{pix}^4 \cdot F_f^2 \cdot T_6^2(u,v) \cdot \left[1 + \overline{g_4} \cdot \overline{g_5} \cdot T_3^2(u,v) \cdot \left(\overline{g_2} + \varepsilon_{g_2}\right)\right] \qquad 5.49$$

The signal and NPS represented in above equations are the presampling signal and the presampling NPS. However, DQE measurements reported in literature [21-22, 33, 37, 51, 54, 75, 78] for digital imaging (sampled) systems are based on the presampling MTF and the aliased NPS. The aliased NPS represented as $W_6^a(u,v)$ is expressed as:

$$W_6^a(u,v) = W_6(u,v) ** III(u,v) \qquad 5.50$$

where *III(u,v)* is the Fourier transform of a rectangular array of $\delta$ -functions representing the pixel matrix with a spacing of $A_{pix}$. While most of the analysis addressed in this work is based on the presampling NPS; due to the various pixel sizes (78, 156 and 234-μm) afforded by the system, the effect of aliasing becomes relevant. Hence, this effect is addressed in section 5.5.11.

*5.5.8. Stage 7: Additive Noise*

The total additive electronic noise ($\sigma_T$) associated with a CCD-based system is addressed in section 5.2.9. The presampling signal and the presampling NPS at the output of stage 7 is written as:

$$q_7(u,v) = \overline{q_0} \cdot \overline{g_1} \cdot \overline{g_2} \cdot \overline{g_4} \cdot \overline{g_5} \cdot A_{pix}^2 \cdot F_f \cdot T_3(u,v) \cdot T_6(u,v) \tag{5.51}$$

$$W_7(u,v) = \overline{q_0} \cdot \overline{g_1} \cdot \overline{g_2} \cdot \overline{g_4} \cdot \overline{g_5} \cdot A_{pix}^4 \cdot F_f^2 \cdot T_6^2(u,v) \cdot \left[1 + \overline{g_4} \cdot \overline{g_5} \cdot T_3^2(u,v) \cdot \left(\overline{g_2} + \varepsilon_{g_2}\right)\right] + W_{add}(u,v) \tag{5.52}$$

where the variance ($\sigma_T^2$) is related to the additive noise power [$W_{add}(u,v)$] by:

$$\sigma_T^2 = \iint W_{add}(u,v) \cdot du \cdot dv \tag{5.53}$$

For the case where the electronic noise is 'white' (independent of spatial frequency), equation 6.26 can be simplified to:

$$\sigma_T^2 = \int_{-V_{Nyq}}^{+V_{Nyq}} \int_{-U_{Nyq}}^{+U_{Nyq}} K \cdot du \cdot dv \tag{5.54}$$

where, $K$ is the amplitude of the 'white' noise power. Hence, $K$ can be estimated as:

$$K = \frac{\sigma_T^2}{4 \cdot U_{Nyq} \cdot V_{Nyq}} \tag{5.55}$$

where, $\sigma_T$ is the estimated electronic noise, $U_{Nyq}$ and $V_{Nyq}$ are the Nyquist sampling limits along the two orthogonal directions.

*5.5.9. Detective Quantum Efficiency*

The detective quantum efficiency, which is defined as the ratio of the square of the output signal-to-noise ratio to the square of the input signal-to-noise ratio can be calculated from the above equations as:

$$DQE(u,v) = \frac{\overline{g_1} \cdot \overline{g_2} \cdot \overline{g_4} \cdot \overline{g_5} \cdot T_3^2(u,v)}{1 + \overline{g_4} \cdot \overline{g_5} \cdot T_3^2(u,v) \cdot \left(\overline{g_2} + \varepsilon_{g_2}\right) + \frac{W_{add}(u,v)}{\left(\frac{q_0}{X}\right) \cdot X \cdot \overline{g_1} \cdot \overline{g_2} \cdot \overline{g_4} \cdot \overline{g_5} \cdot A_{pix}^4 \cdot F_f^2 \cdot T_6^2(u,v)}} \qquad 5.56$$

where, $\left(\frac{q_0}{X}\right)$ is the photon fluence per μR of incident exposure and $X$ is the incident exposure in μR. As noted by Siewerdsen [36], many of the important signal and transfer properties can be adequately described by the zero-frequency DQE. Following his work, the $DQE(0)$ is written as:

$$DQE(0) = \frac{\overline{g_1} \cdot \overline{g_2} \cdot \overline{g_4} \cdot \overline{g_5}}{1 + \overline{g_4} \cdot \overline{g_5} \cdot \left(\overline{g_2} + \varepsilon_{g_2}\right) + \frac{\sigma_T^2}{\left(\frac{q_0}{X}\right) \cdot X \cdot \overline{g_1} \cdot \overline{g_2} \cdot \overline{g_4} \cdot \overline{g_5} \cdot A_{pix}^2 \cdot F_f}} \qquad 5.57$$

*5.5.10. Effect of Image Lag*

For fluoroscopic applications, in addition to the spatial characteristics, the temporal characteristics of the imager also need to be addressed. Of particular importance is image lag, which is a result of a fraction of the generated electrons from a particular frame being trapped and released into subsequent frames. Primary sources that

contribute to image lag in pulsed fluoroscopic systems include the decay characteristics of the scintillator, decay characteristics of the x-ray source primarily due to the capacitance of the high-tension cables and charge traps within the CCD. Measurements of the CsI:Tl scintillator decay characteristics at room temperature by Valentine et al [79] have found two primary decay time constants of $679 \pm 10$ ns and $3.34 \pm 0.14$ μs, which contribute to 63.7% and 36.1% of the emission. The system design addressed in section 5.1 includes a delay of 2-ms after the termination of the x-ray pulse, which is sufficient to allow for almost complete integration of the emitted optical quanta within a particular frame. Also, scientific-grade CCDs are routinely used for fast-framing applications. Hence, image lag is not expected to be significant with this system. However the designed system uses a large-area interline-transfer CCD, which may be the largest such device ever manufactured, and may manifest charge-traps. Hence, the effect of charge trapping on the performance of the system was studied. Based on the deterministic model of Matsunaga et al [80] and under conditions of signal equilibrium, Siewerdsen et al [34] have derived the pixel variance after readout from the $n^{\text{th}}$ frame ($\sigma^2_{R_{(n)}}$) as a function of the fraction of trapped charge (electrons) [$f_{trap}$] as:

$$\sigma^2_{R_{(n)}} = \left(\frac{1 - f_{trap}}{1 + f_{trap}}\right) \cdot \left(\sigma^2_{G_{(n)}} + \sigma^2_{N_{\text{int}(n)}}\right) + \sigma^2_{N_{ext(n)}} \qquad 5.58$$

where $\sigma^2_{G_{(n)}}$ is the variance in the number of electrons generated, $\sigma^2_{N_{\text{int}(n)}}$ is the additive noise generated within the active area of the pixel, and $\sigma^2_{N_{ext(n)}}$ is the additive noise generated external to the pixel, in the $n^{\text{th}}$ frame. Since all the additive noise sources

addressed in section 5.2.9 occur external to the active area of the pixel (i.e., $\sigma^2_{N_{\text{int}(n)}} = 0$ and $\sigma^2_{N_{ext(n)}} = \sigma^2_T$), the pixel variance including the effects of charge trapping ($\sigma^2_{trap,n}$) is written as:

$$\sigma^2_{trap,n} = \left(\frac{1-f_{trap}}{1+f_{trap}}\right)\cdot\frac{\overline{q_0}}{X}\cdot X\cdot\overline{g_1}\cdot\overline{g_2}\cdot\overline{g_4}\cdot\overline{g_5}\cdot A^2_{pix}\cdot F_f \times\left[1+\overline{g_4}\cdot\overline{g_5}\cdot s\cdot\left(\overline{g_2}+\varepsilon_{g_2}\right)\right]+\sigma^2_T \tag{5.59}$$

where, *s* is the sharpness factor defined by:

$$s = A^2_{pix}\cdot F_f\cdot\iint T^2_3(u,v)\cdot T^2_6(u,v)\cdot du\cdot dv \tag{5.60}$$

In terms of the signal, under conditions of signal equilibrium, Siewerdsen et al [34] have also derived the mean number of electrons readout in the $n^{\text{th}}$ frame ($\overline{R_n}$) to be equal to the mean number of electrons generated by x- ray photon interaction in the $(n+1)^{\text{th}}$ frame ($\overline{G_{n+1}}$). In a fluoroscopic sequence with uniform exposure over successive frames, $\overline{G_{n+1}} = \overline{q_7}$. Hence, zero-frequency DQE including the effects of charge trapping [$DQE^{trap}(0)$] can be easily derived with $\overline{g} = \overline{g_4}\cdot\overline{g_5}$ to be:

$$DQE^{trap}(0) = \frac{\overline{g_1}\cdot\overline{g_2}\cdot\overline{g}}{\left(\frac{1-f_{trap}}{1+f_{trap}}\right)\cdot\left(1+\overline{g}\cdot\left(\overline{g_2}+\varepsilon_{g_2}\right)+\frac{\sigma^2_T}{\left(\frac{1-f_{trap}}{1+f_{trap}}\right)\cdot\left(\frac{q_0}{X}\right)\cdot X\cdot\overline{g_1}\cdot\overline{g_2}\cdot\overline{g}\cdot A^2_{pix}\cdot F_f}\right)} \tag{5.61}$$

*5.5.11. Frequency-dependent DQE*

The above sections address only the zero-frequency DQE [$DQE(0)$] and the frequency-dependent DQE [$DQE(f)$] would provide additional insight into the imaging performance of the system. The two-dimensional (2-D) $DQE(u,v)$ addressed in equation 5.56 is based on the presampling signal and the presampling NPS. For simplicity and as an approximation, the one-dimensional (1-D) is used in these simulations. The notation $W_7(u)$ and $DQE(u)$ are used to indicate the 1-D presampling NPS and 1-D presampling DQE along the *u*-axis. The notation $W_7^a(u)$ is used to represent the aliased NPS along the *u*-axis, where $W_7^a(u)$ is computed from equations 5.50 and 5.52 as:

$$W_7^a(u) = \left[W_6(u) * III(u)\right] + W_{add}(u) \qquad 5.62$$

The 1-D DQE computed using the aliased NPS along the *u*-axis $W_7^a(u)$, is represented as $DQE^a(u)$. Similar notations are used to represent these parameters along the *v*-axis. The axes, *u* and *v* correspond to active pixel dimensions $a_y$ and $a_x$, respectively in the spatial domain. In order to illustrate the effect of aliasing on the NPS, $W_6(u)$ was compared with $W_6^a(u)$. This effect is illustrated by a simulation using a nominal fluoroscopic exposure rate of 2-μR/frame with the imager operating at 30-fps in the 156-μm pixel mode and prior to the addition of the electronic noise. The scintillator thickness used in this simulation is 450-μm.

The effect of CsI:Tl thickness on the frequency-dependent DQE was studied. Simulations of the frequency-dependent DQE [$DQE^a(u)$] were performed at a nominal

fluoroscopic exposure rate of 2-μR/frame and with the imager operating at 30-fps in the 78-μm pixel mode.

The effect of pixel size on the frequency-dependent DQE was analyzed in terms of the presampling DQE [$DQE(u)$] and the DQE computed using the aliased NPS [$DQE^a(u)$]. The simulations of the $DQE(u)$ and $DQE^a(u)$ of the system were performed with the imager operating at 30-fps and employing a 450-μm CsI:Tl scintillator at a nominal fluoroscopic exposure rate of 2-μR/frame.

The effect of incident exposure on the frequency-dependent DQE computed with the aliased NPS [$DQE^a(u)$] was studied. For simplicity, the system using the 450-μm thick CsI:Tl scintillator alone is reported. Similar trends were observed for all thicknesses of CsI:Tl. The incident exposure rate was varied from 1 to 10-μR/frame and the simulations were performed for all pixel sizes.

*5.5.12. Comparison of DQE along u and v-axes*

All the computations of the frequency-dependent DQE addressed so far are along the *u*-axis in the spatial frequency domain, which corresponds to the active dimension that is unaffected by the fill factor in the spatial domain. However, along the *v*-axis there is degradation of the active dimension due to interline channel. Hence, it is pertinent to compare the DQE performance along the two orthogonal axes. Simulations of the $DQE^a(u)$ and $DQE^a(v)$ were performed with the imager operating at 30-fps and 156-μm pixel size, with a 450-μm CsI:Tl and a nominal exposure rate of 2-μR/frame.

## 5.6. PARALLEL-CASCADED LINEAR-SYSTEMS MODEL

The serial-cascaded linear-systems-based model addressed in section 5.5 does not take into account the reabsorption of the K-fluorescent x-rays within the scintillator medium in the quantum gain stage addressed in sections 5.2.2 and 5.5.3. The model assumes that all of the K-fluorescent x-rays escape the scintillator medium, which in reality is not the case. A fraction of the K-fluorescent x-rays are reabsorbed either in the same location or at a secondary location within the scintillator medium. Reabsorption of K-fluorescent x-rays cause a spatial blur and results in spatial correlation between the primary interaction site shown as A, and the reabsorption site shown as B, in Figure 5.11. This results in parallel pathways for signal and noise transfer within the scintillator medium. Cunningham et al [48] used the term 'parallel cascade' to describe this process in his model. The modeling technique used by Yao [81] and Zhao [82] address the case of monoenergetic incident x-rays and for a deterministic quantum gain stage (the gain variance of the stage is zero). In this work, their model was extended to a more clinically representative polyenergetic x-ray spectrum and by considering the variance in the quantum gain stage through the Swank factor [61]. It should be noted that this effect only affects the quantum gain stage addressed in sections 5.2.2 and 5.5.3 and hence, the other stages that contribute to the system NPS and DQE are not addressed as they are identical to that described in section 5.5.

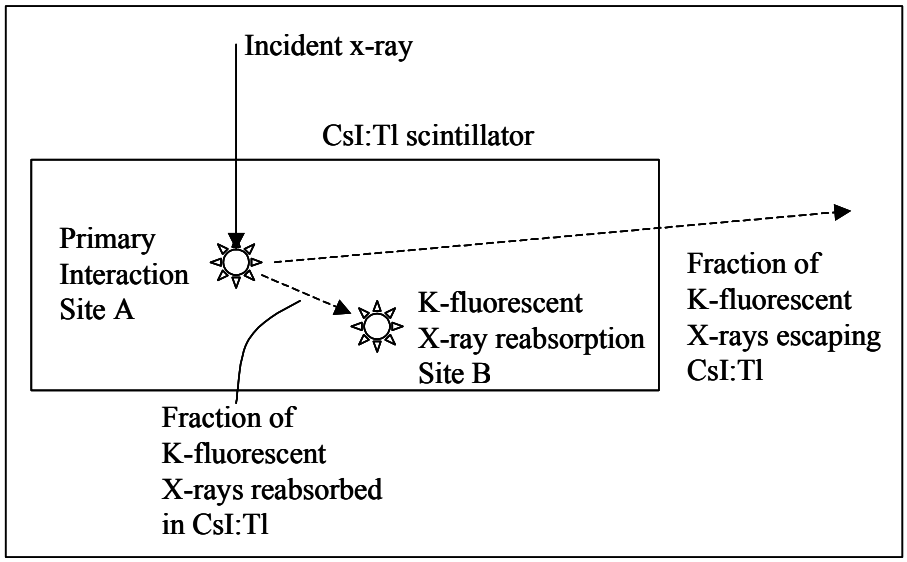


*Figure 5.11 Schematic illustration of the K-fluorescent x-ray reabsorption in the CsI:Tl scintillator. The reabsorption process causes a spatial blur and results in spatial correlation between the primary interaction site A and the reabsorption site B.*

The model is best described by a schematic illustration of the stages 0 through 3 shown in Figure 5.12, which involve the incident x-ray quanta, quantum efficiency of CsI:Tl, quantum gain of CsI:Tl, and the stochastic blur of CsI:Tl, respectively.

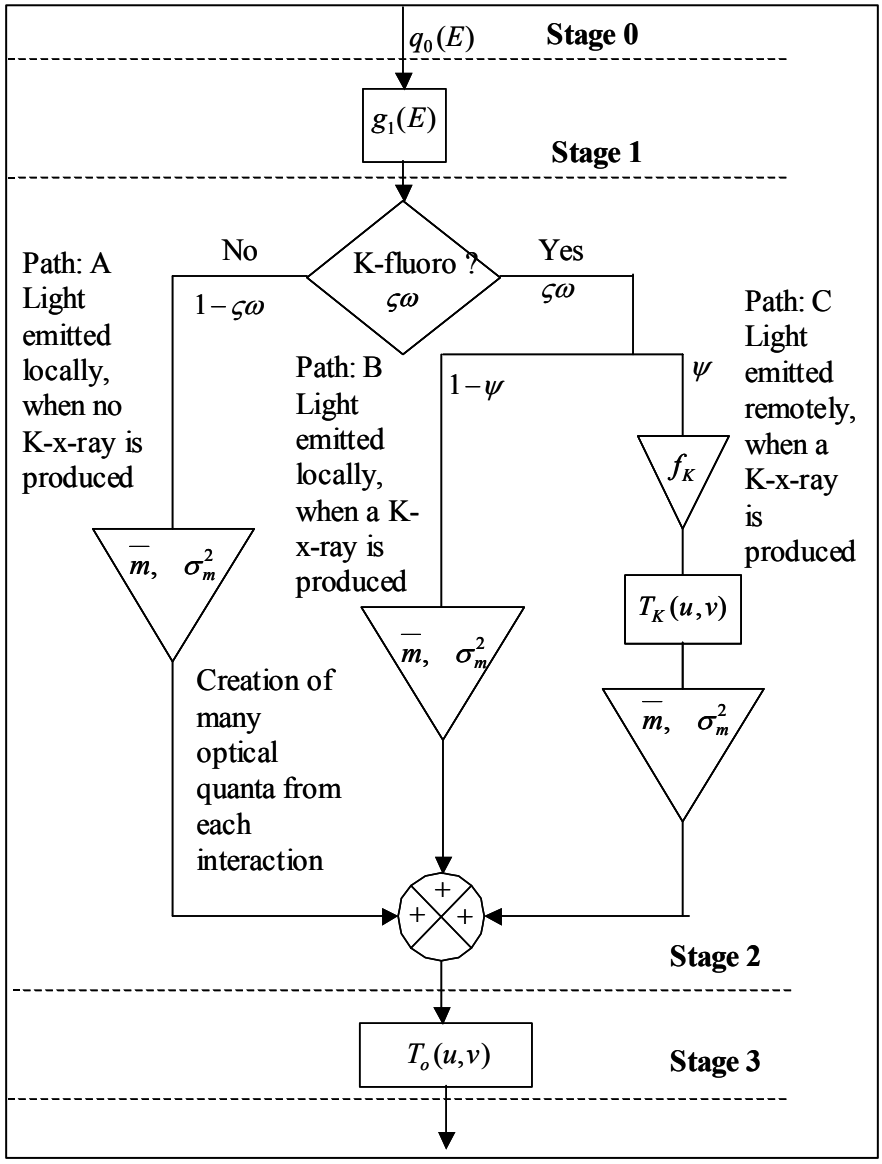


*Figure 5.12 Flowchart illustrating the parallel pathways in the CsI:Tl scintillator.*

An incident photon $q_0(E)$ with energy $E$ is attenuated by the CsI:Tl scintillator with a probability given by $g_1(E)$. Upon interaction, depending on the energy, K-fluorescent x-rays may be produced. If $\varsigma$ is the probability of photoelectric interaction and $\omega$ is the probability that such an interaction occurs at the K-shell, then the

probability a K-fluorescent x-ray is produced is given by $\varsigma\omega$. It should be noted that for incident photon energies less than the K-edge of CsI:Tl, $\omega = 0$, indicating that all of the incident photon energy is used for conversion to optical quanta via the path A. For incident photon energies greater than the K-edge of CsI:Tl (~33.5 keV and represented as $E_K$), $1-\varsigma\omega$ indicates the probability that all of the incident photon energy is used for conversion to optical quanta. This is path A shown in Figure 5.12. Let $\overline{m}$ represent the mean number of optical quanta generated per x-ray interaction and $\sigma_m^2$ represent the variance in $\overline{m}$. The number of optical quanta generated per interacting x-ray of energy $E$ is given by:

$$m(E) = 58 \cdot E \cdot \eta_{esc}(z) \tag{5.63}$$

which is identical to equation 5.4. The variance in $\overline{m}$ is represented in terms of the Poisson excess $\varepsilon_m$ as:

$$\sigma_m^2 = \overline{m} \cdot (1 + \varepsilon_m) \tag{5.64}$$

Thus the mean signal and NPS contribution to the summing stage through path A represented as $\overline{q_{2A}}$ and $W_{2A}(u,v)$ respectively, after simplification can be written as:

$$\overline{q_{2A}} = \overline{q_0} \cdot \overline{g_1} \cdot \overline{m} \cdot (1 - \varsigma\omega) \tag{5.65}$$

$$W_{2A}(u,v) = \overline{q_0} \cdot \overline{g_1} \cdot \overline{m} \cdot (1 - \varsigma\omega) \cdot \left[\overline{m} + 1 + \varepsilon_m\right] \tag{5.66}$$

For incident photon energies greater than the K-edge of CsI:Tl (~33.5 keV and represented as $E_K$), $\varsigma\omega$ indicates the probability that a K-fluorescent x-ray would be produced. When a K-fluorescent x-rays is produced they deposit an energy of $E - E_K$ at the primary interaction site (locally), which is converted to optical quanta and is

represented as path B in Figure 5.12. Thus the mean signal and NPS contribution to the summing stage through path B represented as $q_{2B}$ and $W_{2B}(u,v)$ respectively, after simplification can be written as:

$$\overline{q_{2B}} = \overline{q_0} \cdot \overline{g_1} \cdot \overline{m} \cdot \varsigma\omega \cdot (1-\psi) \tag{5.67}$$

$$W_{2B}(u,v) = \overline{q_0} \cdot \overline{g_1} \cdot \overline{m} \cdot \varsigma\omega \cdot (1-\psi) \cdot \left[\overline{m} + 1 + \varepsilon_m\right] \tag{5.68}$$

where, $\psi = \frac{E_K}{E}$. The generated K-fluorescent x-ray carries on energy of $E_K$. This K-fluorescent x-ray may be reabsorbed within the scintillator medium. The probability that a generated K-fluorescent x-ray is reabsorbed is given by $f_K$. Further, this reabsorption might occur locally or at a secondary interaction site (remotely), resulting in a stochastic blur represented by $T_K(u,v)$. This is path C shown in Figure 5.12. Thus the frequency-dependent signal, mean signal and NPS contribution to the summing stage through path C represented as $q_{2C}(u,v)$, $\overline{q_{2C}}$ and $W_{2C}(u,v)$ respectively, after simplification can be written as:

$$q_{2C}(u,v) = \overline{q_0} \cdot \overline{g_1} \cdot \overline{m} \cdot \varsigma\omega \cdot \psi \cdot f_K \cdot T_K(u,v) \tag{5.69}$$

$$\overline{q_{2C}} = \overline{q_0} \cdot \overline{g_1} \cdot \overline{m} \cdot \varsigma\omega \cdot \psi \cdot f_K \tag{5.70}$$

$$W_{2C}(u,v) = \overline{q_0} \cdot \overline{g_1} \cdot \overline{m} \cdot \varsigma\omega \cdot \psi \cdot f_K \cdot \left[\overline{m} + 1 + \varepsilon_m\right] \tag{5.71}$$

The total signal available to the summing stage through the three paths can be stated as:

$$\overline{q_2} = \overline{q_{2A}} + \overline{q_{2B}} + \overline{q_{2C}} \tag{5.72}$$

After substitution and simplification, the average signal at output of stage 2 is given by:

$$\overline{q_2} = \overline{q_0} \cdot \overline{g_1} \cdot \overline{m} \cdot \left[1 - \varsigma\omega \cdot \psi \cdot \left(1 - f_K\right)\right] \tag{5.73}$$

The spatial frequency-dependent signal at the output of stage 2 is given by:

$$q_2(u,v) = \overline{q_0} \cdot \overline{g_1} \cdot \overline{m} \cdot \left[1 - \varsigma\omega \cdot \psi \cdot \left(1 - f_K \cdot T_K(u,v)\right)\right] \tag{5.74}$$

In terms of the NPS, the correlation between paths B and C result in cross-spectral density. The cross-spectral density $W_{2BC}$ can be stated as:

$$W_{2BC}(u,v) = \overline{q_0} \cdot \overline{g_1} \cdot \varsigma\omega \cdot \left(1 - \psi\right) \cdot \overline{m} \cdot \psi \cdot f_K \cdot \overline{m} \cdot T_K^*(u,v) \tag{5.75}$$

where, $T_K^*(u,v)$ is the complex conjugate of $T_K(u,v)$. Similarly, the cross-spectral density $W_{2CB}$ can be stated as:

$$W_{2CB}(u,v) = \overline{q_0} \cdot \overline{g_1} \cdot \varsigma\omega \cdot \left(1 - \psi\right) \cdot \overline{m} \cdot \psi \cdot f_K \cdot \overline{m} \cdot T_K(u,v) \tag{5.76}$$

Since, $T_K(u,v) + T_K^*(u,v) = 2 \cdot \mathrm{Re}\{T_K(u,v)\}$, combining the two cross-spectral density terms yields,

$$W_{2BC}(u,v) + W_{2CB}(u,v) = 2 \cdot \overline{q_0} \cdot \overline{g_1} \cdot \varsigma\omega \cdot \psi \cdot f_K \cdot \left(1 - \psi\right) \cdot \overline{m}^2 \cdot \mathrm{Re}\{T_K(u,v)\} \tag{5.77}$$

Thus the total NPS at the output of summing stage can be stated as:

$$W_2(u,v) = W_{2A}(u,v) + W_{2B}(u,v) + W_{2C}(u,v) + W_{2BC}(u,v) + W_{2CB}(u,v) \tag{5.78}$$

Upon substitution and simplification, the total NPS at the output of summing stage can be stated as:

$$\begin{aligned} W_2(u,v) = {} & \overline{q_0} \cdot \overline{g_1} \cdot \overline{m} \cdot \left(\overline{m} + 1 + \varepsilon_m\right) \cdot \left[1 - \varsigma\omega\psi \cdot \left(1 - f_K\right)\right] \\ & + 2 \cdot \overline{q_0} \cdot \overline{g_1} \cdot \varsigma\omega \cdot \psi \cdot f_K \cdot \left(1 - \psi\right) \cdot \overline{m}^2 \cdot \mathrm{Re}\{T_K(u,v)\} \end{aligned} \tag{5.79}$$

The mean gain of stage 2 can be stated as:

$$\overline{g_2} = \frac{\overline{q_2}}{\overline{q_1}} \tag{5.80}$$

where, $\overline{q_2}$ is the mean signal at the output of stage 2 determined according to equation 5.73 and $\overline{q_1}$ is the input to stage 2 and can be stated as:

$$\overline{q_1} = \overline{q_0} \cdot \overline{g_1} \tag{5.81}$$

Substituting equations 5.73 and 5.81 in equation 5.80 yields the mean gain of stage 2 as:

$$\overline{g_2} = \overline{m} \cdot [1 - \varsigma\omega \cdot \psi \cdot (1 - f_K)] \tag{5.82}$$

Substituting equation 5.82 in the first term of equation 5.79 yields:

$$W_2(u,v) = \overline{q_0} \cdot \overline{g_1} \cdot \overline{g_2} \cdot (\overline{m} + 1 + \varepsilon_m) + 2 \cdot \overline{q_0} \cdot \overline{g_1} \cdot \varsigma\omega \cdot \psi \cdot f_K \cdot (1 - \psi) \cdot \overline{m}^2 \cdot \mathrm{Re}\{T_K(u,v)\} \tag{5.83}$$

It is preferable to express the term $(\overline{m} + 1 + \varepsilon_m)$ in terms of the Swank factor [61] to facilitate easy analysis. The gain variance $\sigma_{g_2}^2$ of a stage with a mean gain $\overline{g_2}$ can be stated in terms of the Poisson excess $\varepsilon_{g_2}$ as:

$$\sigma_{g_2}^2 = \overline{g_2} \cdot (1 + \varepsilon_{g_2}) \tag{5.84}$$

where, the Poisson excess can be related to the Swank factor $A_S$ by:

$$\varepsilon_{g_2} = \overline{g_2} \cdot \left( \frac{1}{A_S} - 1 \right) - 1 \tag{5.85}$$

If one considers the quantum gain stage as a gain stage with a mean gain of $\overline{g_2}$ and ignoring the cross spectral density terms, yields an NPS at the output of stage 2 as:

$$W_{2A}(u,v) + W_{2B}(u,v) + W_{2C}(u,v) = \overline{q_0} \cdot \overline{g_1} \cdot \overline{g_2} \cdot (\overline{g_2} + 1 + \varepsilon_{g_2}) \tag{5.86}$$

Equating the above result with the first term of equation 5.83 yields:

$$\overline{m} + 1 + \varepsilon_m = \overline{g_2} + 1 + \varepsilon_{g_2} \tag{5.87}$$

Using equations 5.85 and 5.87 in equation 5.83 yields the NPS at the output of stage 2 in term of the Swank factor as:

$$W_2(u,v) = \overline{q_0} \cdot \overline{g_1} \cdot \overline{g_2} \cdot \left( \frac{\overline{g_2}}{A_S} \right) + 2 \cdot \overline{q_0} \cdot \overline{g_1} \cdot \varsigma\omega \cdot \psi \cdot f_K \cdot (1-\psi) \cdot \overline{m}^2 \cdot \mathrm{Re}\{T_K(u,v)\} \quad 5.88$$

Propagating the signal through stage 3, which is a stochastic blurring stage describing the optical blur with the transfer function represented as $T_o(u,v)$, yields:

$$q_3(u,v) = \overline{q_0} \cdot \overline{g_1} \cdot \overline{m} \cdot T_o(u,v) \cdot \left[1 - \varsigma\omega \cdot \psi \cdot (1 - f_K \cdot T_K(u,v))\right] \quad 5.89$$

It should be noted that the measurement of $MTF_{CsI:Tl}$ in section 5.2.4 and the stochastic blurring stage with transfer function $T_3(u,v)$ in section 5.5.4 for incident photon energies greater than $E_K$ includes the combined effects of $T_o(u,v)$ and $T_K(u,v)$. However, when these measurements are performed at incident photon energies lower than $E_K$, the measured scintillator blur in only due to the optical blur $T_o(u,v)$. This describes one possible technique to determine $T_o(u,v)$. The stochastic blur due to K-fluorescent x-ray reabsorption $T_K(u,v)$ can be deduced by combining the measured $T_o(u,v)$ and by performing similar measurement at photon energies greater than $E_K$. However, such a measurement can be affected, as with increasing incident x-ray photon energies, $T_o(u,v)$ tends to improve as the scintillations are produced closer to the output side (towards the fiberoptic and CCD) of the phosphor. The NPS at the output of the stage 3 represented as $W_3(u,v)$ can be stated after simplification as:

$$\begin{aligned} W_3(u,v) = {} & \overline{q_0} \cdot \overline{g_1} \cdot \overline{g_2} \cdot \left[ 1 + T_o^2(u,v) \cdot \left( \frac{\overline{g_2}}{A_S} - 1 \right) \right] \\ & + 2 \cdot \overline{q_0} \cdot \overline{g_1} \cdot \varsigma\omega \cdot \psi \cdot f_K \cdot (1-\psi) \cdot \overline{m}^2 \cdot T_o^2(u,v) \cdot \mathrm{Re}\{T_K(u,v)\} \end{aligned} \quad 5.90$$

Propagating the signal through the subsequent stages results in a signal at the output of stage 7 represented by $q_7(u,v)$ as:

$$q_7(u,v) = \overline{q_0} \cdot \overline{g_1} \cdot \overline{g_4} \cdot \overline{g_5} \cdot \overline{m} \cdot A_{pix}^2 \cdot F_f \cdot T_o(u,v) \cdot T_6(u,v) \times \left[1 - \varsigma\omega \cdot \psi \cdot \left(1 - f_K \cdot T_K(u,v)\right)\right] \tag{5.91}$$

The presampling NPS prior to the inclusion of the additive noise at the output of stage 6 represented by $W_6(u,v)$ can be stated as:

$$W_6(u,v) = \overline{q_0} \cdot \overline{g_1} \cdot \overline{g_2} \cdot \overline{g_4} \cdot \overline{g_5} \cdot A_{pix}^2 \cdot F_f \cdot T_6^2(u,v) \cdot \left[1 + \overline{g_4} \cdot \overline{g_5} \cdot T_o^2(u,v) \cdot \left(\frac{\overline{g_2}}{A_S} - 1\right)\right] + 2 \cdot \overline{q_0} \cdot \overline{g_1} \cdot \overline{g_4}^2 \cdot \overline{g_5}^2 \cdot A_{pix}^2 \cdot F_f \cdot \varsigma\omega \cdot \psi \cdot f_K \cdot (1 - \psi) \cdot \overline{m}^2 \cdot T_o^2(u,v) \cdot T_6^2(u,v) \cdot Re\{T_K(u,v)\} \tag{5.92}$$

where, $\overline{g_2} = \overline{m} \cdot \left[1 - \varsigma\omega \cdot \psi \cdot \left(1 - f_K\right)\right]$. The aliased NPS at the output of stage 6 represented by $W_6^a(u,v)$ can be written as

$$W_6^a(u,v) = W_6(u,v) ** III(u,v) \tag{5.93}$$

The NPS at the output of stage including the additive noise $W_{add}(u,v)$ can be stated as:

$$W_7^a(u,v) = \left[W_6(u,v) ** III(u,v)\right] + W_{add}(u,v) \tag{5.94}$$

The DQE computed using the aliased NPS represented by $DQE^a(u,v)$ is computed as:

$$DQE^a(u,v) = \frac{\left[q_7(u,v)\right]^2}{q_0 \cdot W_7^a(u,v)} \tag{5.95}$$

In order to compute the DQE, the individual parameters need to be determined. The parameters $\overline{q_0}, \overline{g_1}, \overline{g_4}, \overline{g_5}, A_{pix}^2, F_f, T_6(u,v),$ and $W_{add}(u,v)$ were determined as per sections 5.2 and 5.5. The parameters for $\varsigma$ and $\omega$ published by Hillen et al [65] was

used. The K-fluorescence reabsorption fraction $f_K$ was obtained from Boone et al [83]. The optical blur parameter $T_o(u,v)$ was obtained as an approximate measure through $T_3(u,v)$ as per the technique addressed in section 5.2 using incident x-ray photon energies less than the K-edge of CsI:Tl. This measured scintillator MTF is represented as $T_{3,E<E_K}(u,v)$ to denote the incident x-ray photon energy was below the K-edge of CsI:Tl. The measurement was performed using a polyenergetic 28-kVp, *Mo* anode *Mo* filtration mammographic x-ray source, which contains energies below 33.5 keV, the K-edge of CsI:Tl. The blur due to K-fluorescence reabsorption $T_K(u,v)$ was obtained as an approximate measure from the $T_3(u,v)$ measurement performed according to section 5.2.4 using an 80-kVp x-ray beam, and represented as $T_{3,E>E_K}(u,v)$. Thus, the measurements can be stated as:

$$T_{3,E<E_K}(u,v) \approx T_o(u,v) \tag{5.96}$$

$$T_{3,E>E_K}(u,v) \approx T_o(u,v) \cdot \left[1 + f_K \cdot T_K(u,v)\right] \tag{5.97}$$

The parameters $m$ and $\psi$ are energy-dependent. Hence $q_3(u,v)$ was calculated as:

$$\begin{aligned} q_3(u,v) = {} & \overline{q_0} \cdot T_o(u,v) \cdot \int q_{norm}(E) \cdot g_1(E) \cdot m(E) \cdot dE \\ & - \overline{q_0} \cdot \varsigma\omega \cdot \left(1 - f_K \cdot T_K(u,v)\right) \cdot T_o(u,v) \cdot \int q_{norm}(E) \cdot g_1(E) \cdot m(E) \cdot \psi(E) \cdot dE \end{aligned} \tag{5.98}$$

The output signal of stage 7 $q_7(u,v)$ was calculated as:

$$q_7(u,v) = q_3(u,v) \cdot \overline{g_4} \cdot \overline{g_5} \cdot A_{pix}^2 \cdot F_f \cdot T_6(u,v) \tag{5.99}$$

In order to determine the first term of $W_6(u,v)$, the terms $\overline{g_2}$ and $A_S$ need to determined. $\overline{g_2}$ was determined as:

$$\overline{g_2} = \frac{\int q_{norm}(E) \cdot g_1(E) \cdot m(E) \cdot \left[1 - \varsigma\omega \cdot \psi(E) \cdot (1 - f_K)\right] \cdot dE}{\overline{g_1}} \qquad 5.100$$

The Swank factor $A_S$ was determined according to section 5.2.3. The second term of $W_6(u,v)$ was determined as:

$$2 \cdot \overline{q_0} \cdot \overline{g_4}^2 \cdot \overline{g_5}^2 \cdot A_{pix}^2 \cdot F_f \cdot \varsigma\omega \cdot f_K \cdot T_o^2(u,v) \cdot T_6^2(u,v) \cdot \mathrm{Re}\{T_K(u,v)\} \times \int q_{norm}(E) \cdot g_1(E) \cdot \psi(E) \cdot [1 - \psi(E)] \cdot m^2(E) \cdot dE \qquad 5.101$$

The NPS at the output of stage 7 was computed as per equation 5.94. For determination of these parameters, the scintillator was decomposed into fractional layers of thickness $\Delta t$, similar to that used in Figure 5.8 and described in section 5.2.2. It should be noted that the K-fluorescence reabsorption fraction $f_K$ used [83] is for a 150 mg/cm$^2$ (~ 450-μm thick) CsI:Tl. Hence all the computations are restricted for the system using the 450-μm CsI:Tl. Monte-Carlo simulation could be a useful technique for the determination of $f_K$ [83]. The laboratory is currently in the process of acquiring an appropriate Monte-Carlo simulation package to study x-ray photon transport within the CsI:Tl.

The DQE performance of the imaging system was simulated using the parallel cascade model for the system operating at 156-μm pixel size and using a 450-μm CsI:Tl scintillator for exposure rates from 1 to 10-μR/frame.

## 5.7. EXPERIMENTAL CHARACTERIZATION OF SINGLE MODULE PROTOTYPE

The theoretical model addressed in the previous sections serve as a useful tool to understand the processes involved in image formation and provide an estimate of the

performance. These predictions need to be verified through experimental characterization. Our partners in this research, Fairchild Imaging, Inc., Milpitas, CA, fabricated an 8 x 8-cm CCD. The CCD was coupled to a 450-μm thick CsI:Tl scintillator through a 1-inch thick straight (1:1) fiberoptic plate. The prototype system currently operates at a fixed pixel size of 156-μm. Future versions of the imager would be capable of multiple resolution modes addressed in the previous chapters. The imaging system was coupled to an x-ray source capable of radiographic and fluoroscopic (continuous and pulsed) modes of operation. Description of the x-ray tube and the x-ray generator were stated earlier. The x-ray source was synchronized with the CCD for pulsed fluoroscopy according to the scheme described in chapter 5. The acquired images were digitized to 14-bits [84] with a conversion gain optimized for sensitivity and transferred to a workstation. Important observer-independent objective image quality parameters such as linearity, sensitivity, electronic noise, presampling MTF, and NPS were measured. The DQE of the imaging system was computed from the measured signal, presampling MTF and the NPS at various exposure rates suitable for fluoroscopy. The entire experimental characterization involving x-ray exposure was performed using a 72-kVp x-ray beam after transmitting through 1-inch of *Al* to provide a first HVL of 7.0-mm of *Al*. The source-to-imager distance (SID) was maintained at a constant 192.3-cm. Prior to describing the experimental methodology, it is important to address some of the basic image corrections, such as dark-image subtraction and flat-field correction that are normally performed in all electronic x-ray imaging systems.

### *5.7.1. Dark-image Subtraction and Flat-field Correction*

Dark-image subtraction and flat-field correction is also often referred to as offset and gain correction, respectively. X-ray based imaging systems under the condition of no incident x-ray exposure to the detector exhibit thermionic charge generation, resulting in a dark signal. This dark signal is integrated along with the charges generated during exposure resulting in increased amplitude. Hence, the acquired images need to be corrected for this increase. If $I(x,y)$ represents the image acquired prior to dark-image subtraction, then the dark-image subtracted image can be stated as:

$$I_{ds}(x,y) = I(x,y) - \langle D(x,y) \rangle \tag{5.102}$$

where, $\langle D(x,y) \rangle$ represents the average dark image obtained by pixel-by-pixel averaging of several dark images. In addition, there may be a pixel-to-pixel variation in gain. This can be corrected through the process of flat-field correction. The dark-image subtracted, flat-field corrected image represented as $I_C(x,y)$ is obtained by:

$$I_C(x,y) = \frac{I_{ds}(x,y)}{\langle F(x,y) \rangle} \times \overline{\langle F(x,y) \rangle} \tag{5.103}$$

where, $\langle F(x,y) \rangle$ is the average dark-image subtracted flat-field image acquired at approximately the midpoint of the operating range and $\overline{\langle F(x,y) \rangle}$ represents the spatial mean of the image $\langle F(x,y) \rangle$.

*5.7.2. Linearity and Sensitivity*

The linearity and sensitivity of the system was measured using the technique addressed in prior publications [33, 51]. Specifically, varying the pulse width or the tube current of the pulsed fluoroscopic x-ray source changed the incident exposure to the detector, while maintaining a constant beam quality. Table 5.2 provides the image acquisition technique factors used to achieve various exposure rates in the fluoroscopic range of 1 to 10-μR/frame.

*Table 5.2 Image acquisition technique factors used to achieve various exposure rates to the imaging system.*

| Pulse width (ms) | Tube current (mA) | Exposure rate (μR/frame) |
|---|---|---|
| 2 | 12 | 0.99 |
| 4 | 12 | 2.51 |
| 6 | 12 | 3.96 |
| 5 | 20 | 5.25 |
| 10 | 20 | 10.49 |

A pulsed fluoroscopic sequence of 500 images at each exposure rate was acquired. The acquired images were dark-image subtracted and flat-field corrected. The mean and the variance in the central 256 x 256 region-of-interest (ROI) of each image were computed. The average signal in units of DU/pixel at each exposure rate of $X$ μR/frame was computed as the average of the mean computed from the 500 ROIs and represented as $S_X$. The *rms* variance was computed from the variance in each of the 500 ROIs. Plotting the average signal vs. the incident exposure per frame generated the

linearity plot. The slope of the linearity plot provided the sensitivity of the imager in units of DU/(pixel μR). The sensitivity of the system was also calculated in units of electrons/($mm^2$ μR), based on the manufacturer provided conversion gain in electrons/DU and the pixel area computed as $A_{pix}^2$, where $A_{pix} = 0.156$ mm.

### *5.7.3. Measurement of Electronic Noise*

The electronic noise was measured as the spatial mean of the temporal standard deviation image obtained from a sequence of 500 dark images, prior to any correction. The imager was operated in the 30-fps fluoroscopic mode. These measurements were performed at discrete time points from the initialization of the imager at room temperature, to study the time (and temperature) dependence of the electronic noise. These measurements provided the electronic noise in DU/pixel, which were scaled by the manufacturer provided conversion gain, to facilitate comparison with the theoretical estimations.

### *5.7.4. Measurement of Electronic NPS*

The technique for measurement of the spatial-frequency dependence of the electronic noise through the NPS has been addressed in prior publications [33, 51]. Specifically, a dark sequence of 500 images was acquired with the imager operating at 30-fps after the imager reached temperature stabilization. All the images were converted to floating point numbers. The central 256 x 256 region-of-interest (ROI) from each

image, represented as $DROI_i(x,y)$, was extracted and the average amplitude of the ROI, represented as $\overline{DROI_i(x,y)}$, subtracted to provide the autocorrelation ROI. The ensemble average of the magnitude of the Fourier transform of these autocorrelation ROIs scaled as shown below provided the two-dimensional (2-D) electronic NPS, represented as $W_E(u,v)$.

$$W_E(u,v) = \frac{\left\langle \left| FT\left[ DROI_i(x,y) - \overline{DROI_i(x,y)} \right] \right|^2 \right\rangle}{N_x \cdot N_y} \Delta x \cdot \Delta y \qquad 5.104$$

where, $N_x$ and $N_y$ represent the number of elements in the ROI ($N_x = N_y = 256$), and $\Delta_x$ and $\Delta_y$ are the pixel pitch along the $x$ and $y$ directions, respectively ($\Delta_x = \Delta_y = 0.156$ - mm). From the $W_E(u,v)$, the 1-D electronic NPS along the $u$ and $v$-axes were determined as $W_E(u,0)$ and $W_E(0,v)$. The NPS determined through the above technique also includes any structural electronic noise component (also referred to as fixed-pattern noise in literature) that may be present in the imager.

### *5.7.5. Measurement of Electronic NPS without Structured-noise*

The same dark sequence used in the previous section was used to determine the electronic NPS without the structured (fixed-pattern) noise component. The central 256 x 256 ROI from each image, represented as $DROI_i(x,y)$, was extracted and the average image from these ROIs, represented as $\langle DROI_i(x,y) \rangle$, subtracted to provide the autocorrelation ROI without the presence of structured-noise component. These ROIs

were Fourier transformed and scaled as shown below to obtain the electronic NPS without the presence of any structured-noise component represented as $W_E^{NS}(u,v)$.

$$W_E^{NS}(u,v) = \frac{\left\langle \left| FT\left[ DROI_i(x,y) - \left\langle DROI_i(x,y) \right\rangle \right] \right|^2 \right\rangle}{N_x \cdot N_y} \Delta x \cdot \Delta y \qquad 5.105$$

The resultant $W_E^{NS}(u,v)$ was scaled by a factor of $\frac{500}{499}$ to account for the loss in variance due to the subtraction of the average dark ROI, $\left\langle DROI_i(x,y) \right\rangle$. From the $W_E^{NS}(u,v)$, the 1-D electronic NPS along the *u* and *v*-axes were determined in a manner similar to that used in the previous section.

### *5.7.6. Presampling MTF Measurement*

The presampling modulation transfer function (MTF) was determined using the technique described by Fujita et al [66]. A detailed description of the methodology used has also been published [33, 51]. Specifically, a long pulsed fluoroscopic sequence consisting of dark-subtracted, flat-field corrected image frames was acquired using a 72-kVp x-ray beam with a 10-μm slit placed on top of the imager at a slight angle ($<4^0$) to the detector matrix. The source-to-imager distance (SID) was sufficiently large (192.5-cm) compared to the distance between the slit and the CsI:Tl scintillator (~1.5-cm), so that magnification effects could be ignored. The fluoroscopic frames were converted from the original 14-bit digitization to floating point values. An average of 100 consecutive frames was used to compute the finely sampled line-spread function (LSF),

so that the tails of the LSF were not overtly affected by noise. The finely sampled LSF was normalized to the peak value and had equally spaced data points 4-μm apart. The finely sampled LSF was Fourier transformed and deconvolved of the finite width of the slit [ $\mathrm{sinc}(10\mu m)$ ], to provide the presampling MTF. Measurements of the presampling MTF were performed along two orthogonal directions and represented as $T_{pre}(u,0)$ and $T_{pre}(0,v)$.

### *5.7.7. Fluoroscopic NPS Measurement*

A dark-image subtracted, flat-field corrected fluoroscopic sequence of 500 images was acquired with the imager operating at 30-fps after the imager reached temperature stabilization at each of the exposure rates shown in Table 5.2. All the images were converted to floating point numbers. The central 256 x 256 region-of-interest (ROI) from each image, represented as $ROI_i(x,y)$, was extracted and the average amplitude of the ROI, represented as $\overline{ROI_i(x,y)}$, subtracted to provide the autocorrelation ROI. The ensemble average of the magnitude of the Fourier transform of these autocorrelation ROIs scaled as shown below provided the two-dimensional (2-D) NPS at an exposure rate of $X$ μR/frame, represented as $W_X(u,v)$.

$$W_X(u,v) = \frac{\left\langle \left| FT\left[ ROI_i(x,y) - \overline{ROI_i(x,y)} \right] \right|^2 \right\rangle}{N_x \cdot N_y} \Delta x \cdot \Delta y \qquad 5.106$$

where, $N_x$ and $N_y$ represent the number of elements in the ROI ( $N_x = N_y = 256$ ), and $\Delta_x$ and $\Delta_y$ are the pixel pitch along the *x* and *y* directions, respectively. From the $W_X(u,v)$, the 1-D electronic NPS along the *u* and *v*-axes were determined as $W_X(u,0)$ and $W_X(0,v)$. The NPS determined through the above technique also includes any structural noise component (electronic or due to x-rays) that may be present in the imager.

### *5.7.8. Fluoroscopic NPS Measurement without Structured-noise*

The same fluoroscopic sequences used in the previous section were used to determine the fluoroscopic NPS without the structured-noise (fixed-pattern) component. The central 256 x 256 ROI from each image, represented as $ROI_i(x,y)$, was extracted and the average image from these ROIs, represented as $\langle ROI_i(x,y)\rangle$, was subtracted to provide the autocorrelation ROI without the presence of structured-noise component. These ROIs were Fourier transformed and scaled as shown below to obtain the fluoroscopic NPS without the presence of any structured-noise component at an exposure rate of $X$ μR/frame, represented as $W_X^{NS}(u,v)$.

$$W_X^{NS}(u,v) = \frac{\left\langle \left| FT\left[ ROI_i(x,y) - \langle ROI_i(x,y)\rangle \right] \right|^2 \right\rangle}{N_x \cdot N_y} \Delta x \cdot \Delta y \qquad 5.107$$

The resultant $W_X^{NS}(u,v)$ was scaled by a factor of $\frac{500}{499}$ to account for the loss in variance due to the subtraction of the average ROI, $\langle ROI_i(x,y)\rangle$. From the $W_X^{NS}(u,v)$, the 1-D

electronic NPS along the *u* and *v*-axes were determined in a manner similar to that used in the previous section.

### *5.7.9. Measurement of Image Lag*

The experimental procedure used for measuring image lag was identical to that used by Granfors [21]. A pulsed fluoroscopic sequence (30-fps) consisting of 100 dark-image subtracted flat-field corrected images was acquired, with the x-ray exposure terminated at the end of the 50$^{th}$ frame. The average signal of the central 256 x 256 ROI of each frame was used to represent the mean signal amplitude of that frame. Image lag was computed as the fraction of the residual signal after the termination of the x-ray exposure to that prior to the termination of the x-ray exposure as shown below [21].

$$Lag_n = \frac{\left|\overline{Signal_n} - \overline{Signal_f}\right|}{\left|\overline{Signal_0} - \overline{Signal_f}\right|} \qquad 5.108$$

where, $Lag_n$ is the image lag in the n$^{th}$ frame after the termination of the x-ray exposure, $\overline{Signal_n}$ is the mean signal computed from the central 256 x 256 ROI of the n$^{th}$ frame after the termination of the x-ray exposure, $\overline{Signal_0}$ is the mean signal computed from the central 256 x 256 ROI of the last exposed frame, and $\overline{Signal_f}$ is the mean signal at equilibrium after the termination of the x-ray exposure. Three such measurements were performed and averaged to improve the estimate.

The lag-correction factor ( $LCF$ ) was computed as [21]:

$$LCF = (1 - Lag_1)^2 + \sum_{n=1}^{\infty} (Lag_n - Lag_{n-1})^2 \qquad 5.109$$

*5.7.10. Lag-corrected Fluoroscopic NPS*

The lag-corrected fluoroscopic NPS at an exposure rate of $X$ μR/frame along the *u*-axis represented as $W_X^{LC}(u,0)$ was obtained by [21]:

$$W_X^{LC}(u,0) = W_E^{NS}(u,0) + \frac{W_X^{NS}(u,0) - W_E^{NS}(u,0)}{LCF} \qquad 5.110$$

where, $W_E(u,0)$ was determined according to section 5.7.4 and $W_X(u,0)$ was determined according to section 5.7.7. Similarly, the lag-corrected fluoroscopic NPS along the *v*-axis was determined.

*5.7.11. Lag-corrected DQE*

The lag-corrected DQE of the imaging system at an exposure rate of $X$ μR/frame along the *u*-axis represented as $DQE_X^{LC}(u,0)$ was obtained by:

$$DQE_X^{LC}(u,0) = \frac{S_X^2 \cdot T_{pre}^2(u,0)}{X \cdot \left(\frac{q_0}{X}\right) \cdot W_X^{LC}(u,0)} \qquad 5.111$$

where, $S_X$ is the mean signal determined according to section 5.7.2, $T_{pre}(u,0)$ is the presampling MTF along the u-axis determined according to section 5.7.6, $W_X^{LC}(u,0)$ is

the lag-corrected fluoroscopic NPS determined according to section 5.7.10, and $\left(\frac{q_0}{X}\right)$ is the incident photon fluence in units of x-ray photons/(mm$^2$ μR) which was determined to be 2.91 x $10^2$ in section 5.2.

## 5.8. QUALITATIVE MEASURES

Qualitative measures that are often used to monitor image quality of clinical systems such as resolution measurements using bar-pattern tool (Model: 07-501, Gammex RMI, Middleton, WI) and distortion measurements using wire-mesh grid (Model: 141, Gammex RMI, Middleton, WI) were performed.

# 6. RESULTS

## 6.1. SYSTEM DESIGN PARAMETERS

The quantum efficiency of the scintillator computed as per equation 5.2 is shown in Figure 6.1.

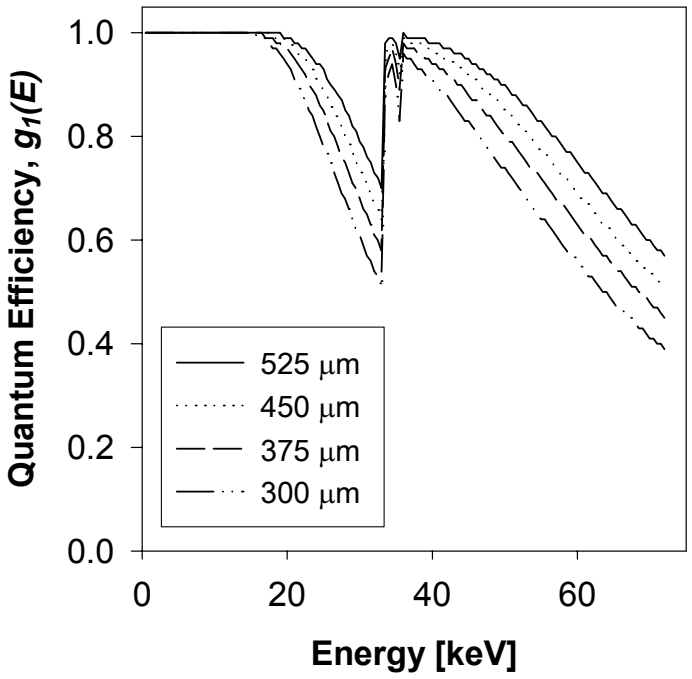


*Figure 6.1 Quantum efficiency as a function of incident photon energy for various thickness of CsI:Tl used.*

The incident spectrum-weighted quantum efficiency computed as per equation 5.3 is shown in Table 6.1.

*Table 6.1 Quantum efficiency as a function of CsI:Tl thickness for the 72-kVp x-ray spectrum.*

| Scintillator thickness (μm) | Quantum Efficiency, $\overline{g_1}$ |
|---|---|
| 300 | 0.672 |
| 375 | 0.737 |
| 450 | 0.786 |
| 525 | 0.833 |

The scintillator quantum gain as a function of incident photon energy calculated as per equation 5.7 is shown in Figure 6.2.

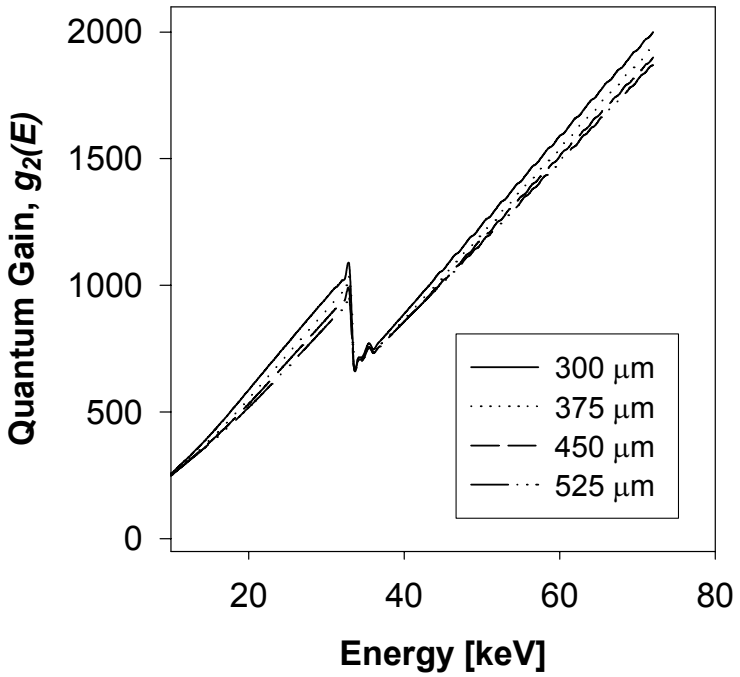


*Figure 6.2 Energy-dependent quantum gain of CsI:Tl for various thickness of the scintillator used.*

The spectrum-weighted average quantum gain for the CsI:Tl scintillator thickness used is summarized in Table 6.2.

*Table 6.2 Quantum gain as a function of CsI:Tl thickness for the 72-kVp spectrum.*

| Scintillator thickness (μm) | Quantum gain, $\overline{g_2}$ |
|---|---|
| 300 | $1.30 \times 10^3$ |
| 375 | $1.27 \times 10^3$ |
| 450 | $1.26 \times 10^3$ |
| 525 | $1.25 \times 10^3$ |

The Swank factor, $A_S$ and the Poisson excess, $\varepsilon_{g_2}$ computed for the various CsI:Tl thickness is shown in Table 6.3.

*Table 6.3 Swank factor and Poisson excess computed for various thickness of CsI:Tl for the 72-kVp x-ray spectrum.*

| Scintillator thickness (μm) | Swank factor, $A_S$ | Poisson excess, $\varepsilon_{g_2}$ |
|---|---|---|
| 300 | 0.771 | 385.1 |
| 375 | 0.786 | 346.7 |
| 450 | 0.798 | 317.8 |
| 525 | 0.811 | 291.0 |

Figure 6.3 shows the $MTF_{CsI:Tl}$ obtained for the 300-μm CsI:Tl with the CCD operating at 24-μm (circles) and 96-μm (solid line).

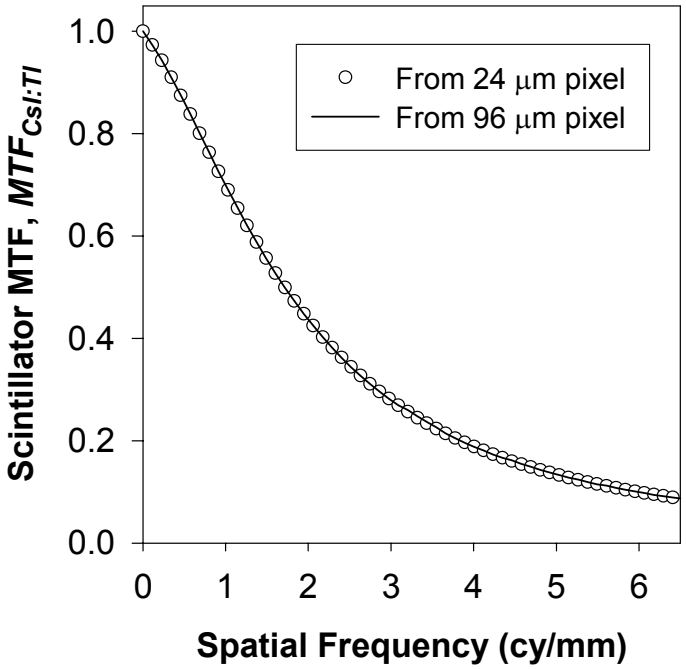


*Figure 6.3 Scintillator blur obtained by deconvolving sinc(96μm) and sinc(24μm) from system presampling MTF measurements performed at 24 and 96-μm, respectively.*

Figures 6.4 through 6.7 show the estimated $MTF_{CsI:Tl}$ for the four thickness of CsI:Tl scintillator used. The experimental data points (shown as circles) were curve-fitted with a Lorentzian fit as per equation 5.14 (shown as dotted line) and also with a blur fit as per equation 5.15 (shown as a solid line).

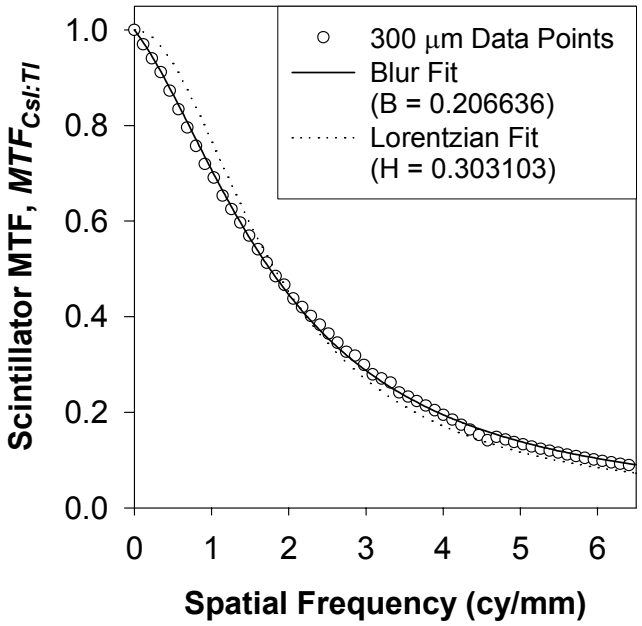


*Figure 6.4 Scintillator MTF obtained by deconvolving the pixel presampling MTF for the 300-μm CsI:Tl.*

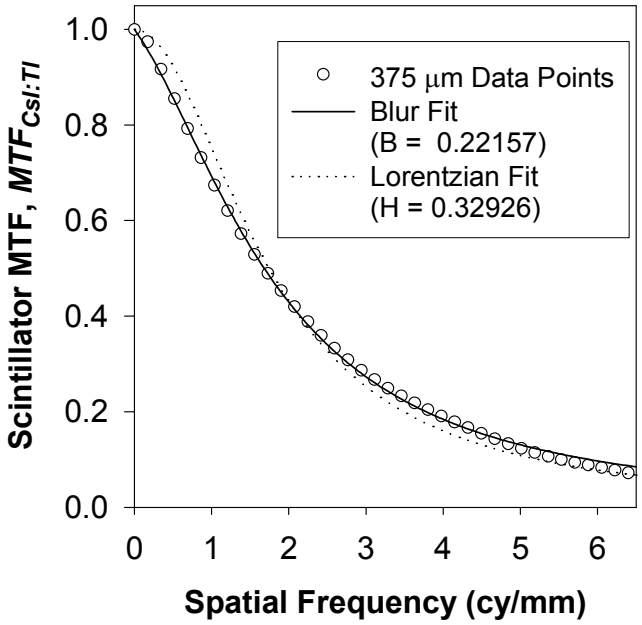


*Figure 6.5 Scintillator MTF obtained for the 375-μm CsI:Tl.*

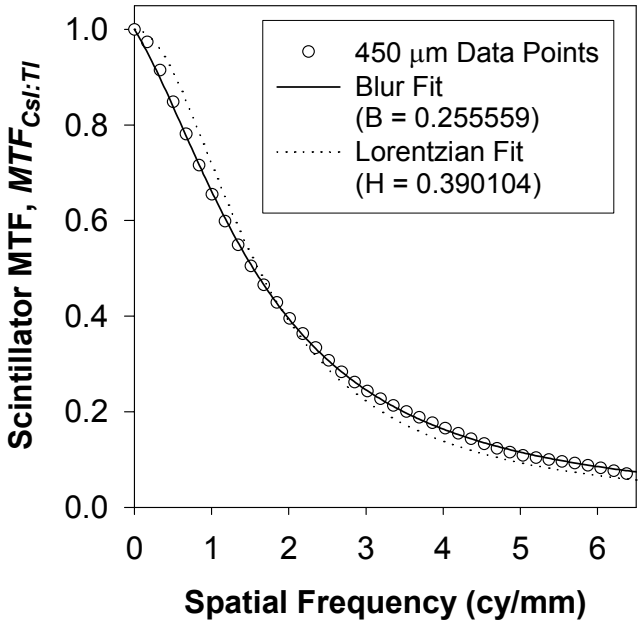


*Figure 6.6 Scintillator MTF for the 450-μm CsI:Tl.*

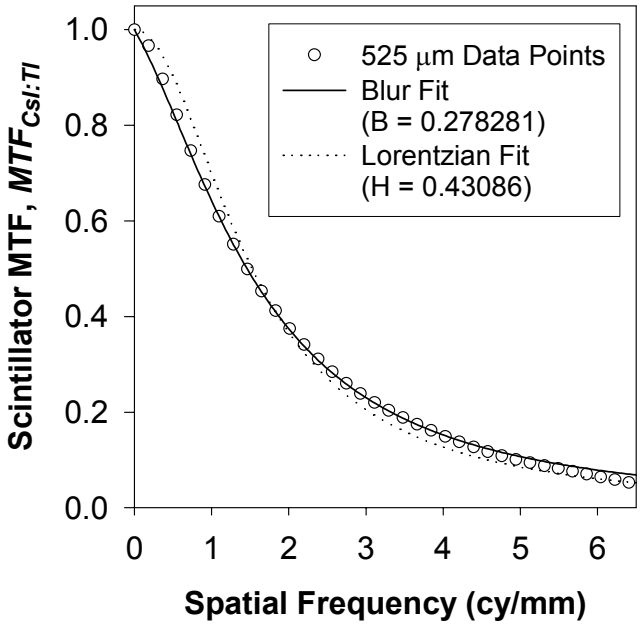


*Figure 6.7 Scintillator MTF for the 525-mm CsI:Tl.*

The calculated optical coupling efficiency of the fiberoptic, represented as $\overline{g_4}$, is 0.5. The calculated results of the fiberoptic length indicate that ~2.5-cm (1-inch) fiberoptic plate of type 47A would provide sufficient protection to the CCD. The average quantum efficiency of the CCD including the loss due to the geometrical fill factor ($\overline{g_5} \cdot F_f$) is estimated to be 0.4. The calculated sensitivity at pixel sizes of 78, 156 and 234-μm for various CsI:Tl thickness are shown in Table 6.4.

*Table 6.4 Calculated sensitivity for the system operating at various pixel sizes and incorporating different thickness of CsI:Tl scintillator.*

| CsI:Tl thickness (μm) | Calculated sensitivity [e-/(pixel.μR)] for various pixel sizes | | |
|---|---|---|---|
| | 78-μm | 156-μm | 234-μm |
| 300 | 241.3 | 965.3 | 2172.0 |
| 375 | 259.2 | 1036.8 | 2332.7 |
| 450 | 272.8 | 1091.1 | 2454.9 |
| 525 | 287.5 | 1150.0 | 2587.4 |

The estimated electronic noise of the CCD imager operating as a 30 fps fluoroscopic imager for the three pixel sizes are shown in Table 6.5.

*Table 6.5 Electronic noise of the system operating at 30 fps fluoroscopy.*

| Pixel size (μm) | Total additive noise, $\sigma_T$ |
|---|---|
| 78 | 24.3 |
| 156 | 34.1 |
| 234 | 45.9 |

The effective dynamic range of the system using a 450-μm CsI:Tl scintillator estimated for the three pixel sizes are shown in Table 6.6.

*Table 6.6 Effective dynamic range using a 450-μm thick CsI:Tl scintillator estimated for the three pixel sizes.* $X_{noise}$ *indicates the exposure at which the signal generated is equivalent to the total electronic noise, and* $X_{\max}$ *indicates the exposure at which the CCD saturates.*

| Pixel size (μm) | $X_{noise}$ (μR) | $X_{\max}$ (μR) | Effective dynamic range, $DR_{eff}$ |
|---|---|---|---|
| 78 | 0.09 | 3666 | 8235:1 |
| 156 | 0.03 | 917 | 5874:1 |
| 234 | 0.02 | 407 | 4356:1 |

## 6.2. SEAMLESS TILING STUDY

The effectiveness of the seam suppression algorithm was studied as per the technique addressed in Chapter 5. Figure 6.8 (A) shows the image of the spoke wheel phantom prior to implementation of the seam suppression algorithm. Figure 6.8 (B) shows the image of the spoke wheel phantom after subjecting the acquired image to the seam suppression algorithm.

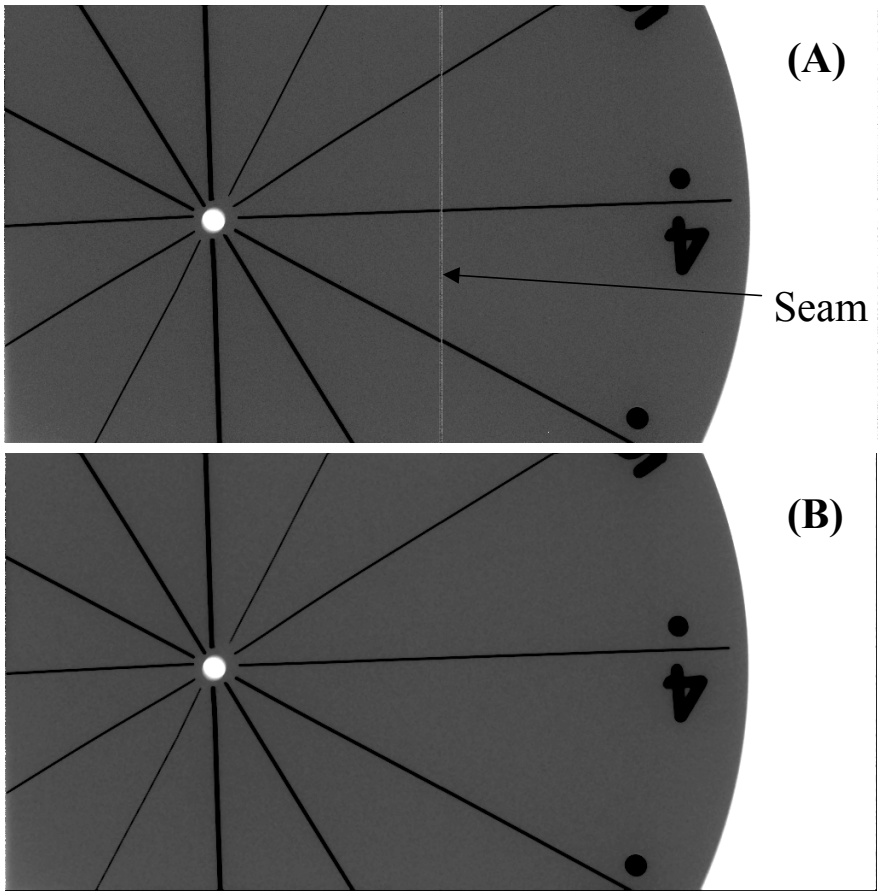


*Figure 6.8 Effectiveness of seam suppression algorithm. (A) An acquired image of a spoke wheel phantom, prior to implementing any seam suppression algorithm. (B) The corrected image after implementation of the algorithm.*

## 6.3. SERIAL-CASCADED LINEAR-SYSTEMS MODEL

### *6.3.1. Zero-frequency DQE*

Figure 6.9 shows the exposure dependence of $DQE(0)$ for the three pixel pitch modes of operation for each of the four scintillators.

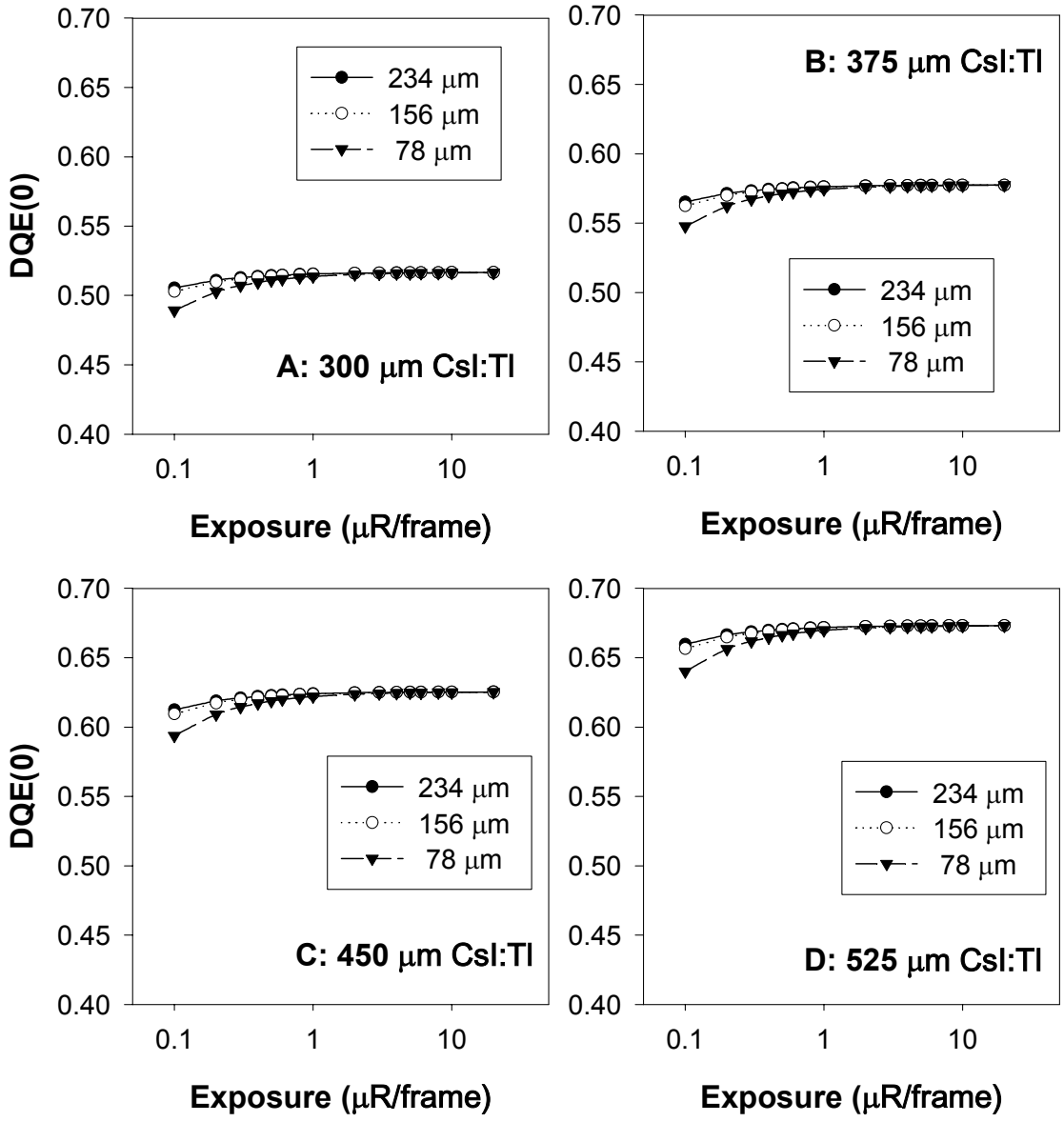


*Figure 6.9 Exposure dependence of DQE(0) for the 78, 156 and 234-μm pixel sizes.*

Figure 6.10 shows the effect of additive noise on the zero-frequency DQE of the system operating at 30-fps fluoroscopy.

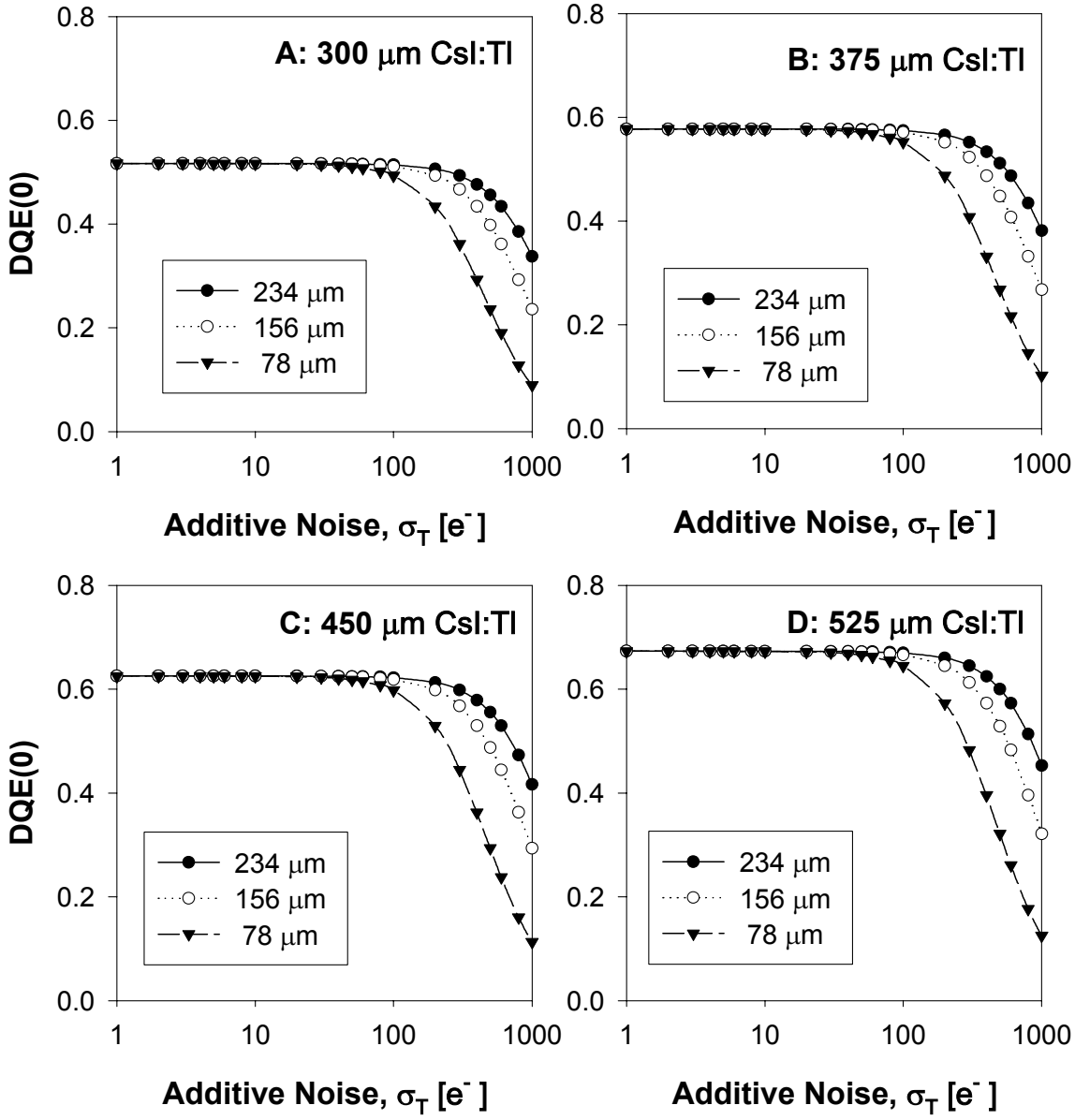


*Figure 6.10 Effect of additive noise on the DQE(0) of the system operating at 30-fps fluoroscopy and a nominal exposure rate of 2-μR/frame.*

Figure 6.11 shows the effect of charge-traps on the zero-frequency DQE performance of the imaging system operating at 30-fps fluoroscopy.

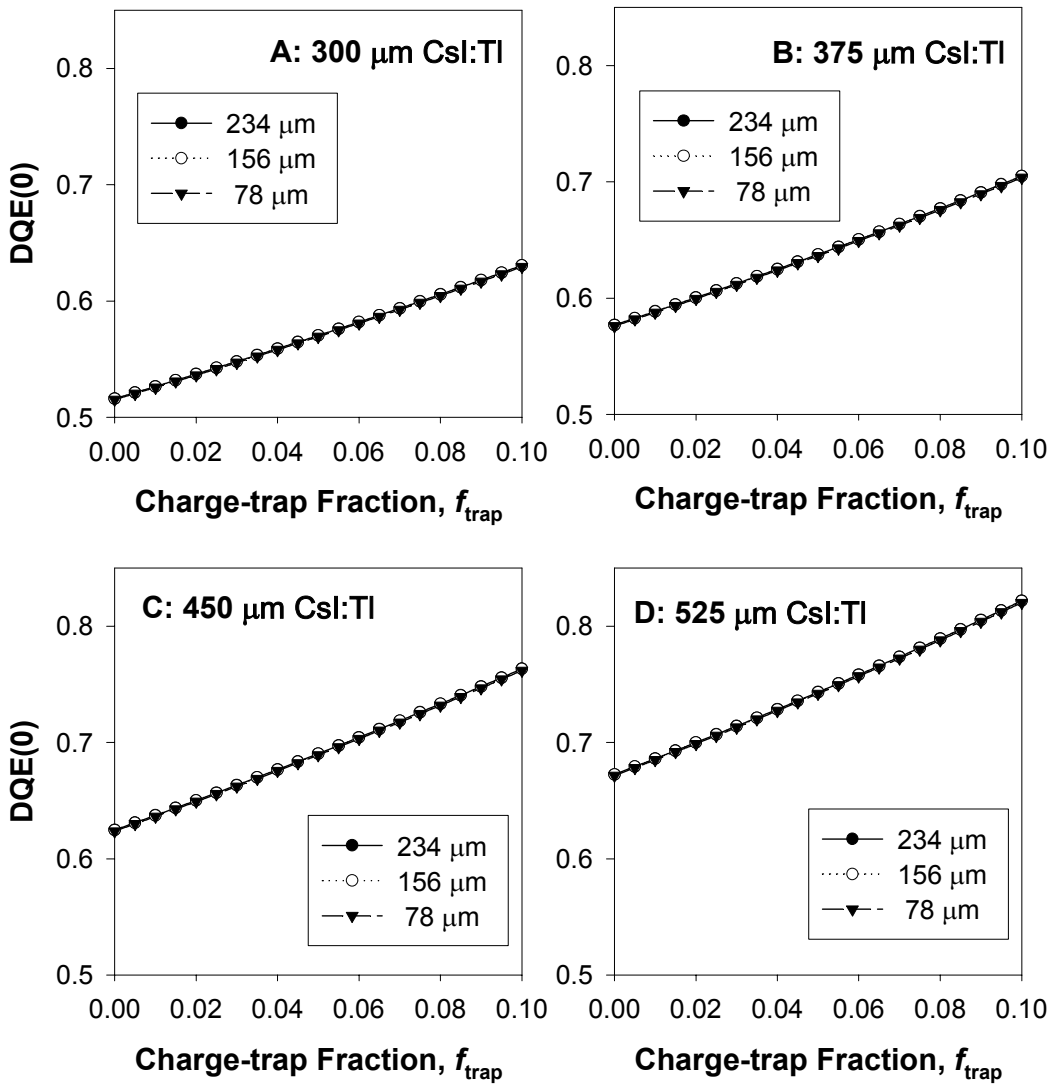


*Figure 6.11 Effect of charge-trap fraction on the DQE(0) for the system operating at 30-fps fluoroscopy and a nominal exposure rate of 2-μR/frame.*

### *6.3.2. Frequency-dependent DQE*

In order to better understand the effect of aliasing, the presampling NPS is compared with the aliased NPS. Figure 6.12 shows the effect of noise aliasing. The

presampling NPS prior to the addition of the electronic noise $W_6(u)$ is plotted up to the cut-off frequency (which is twice the Nyquist limit).

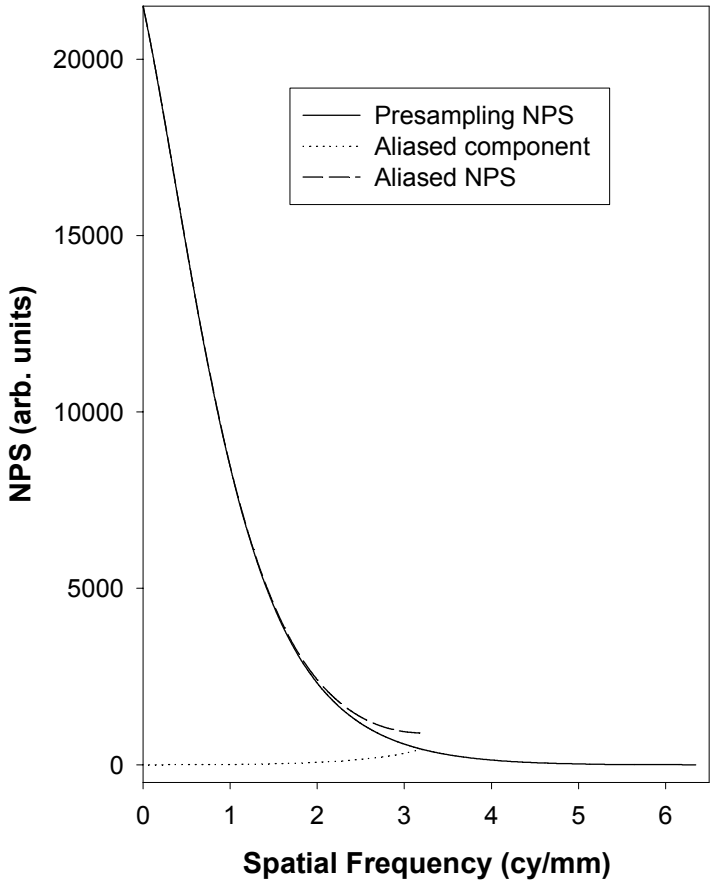


*Figure 6.12 Effect of aliasing on the NPS of the imaging system.*

Figure 6.13 shows the effect of CsI:Tl thickness on the $DQE(f)$ of the system operating at 30-fps and a pixel size of 78-μm. A nominal fluoroscopic exposure rate of 2-μR/frame was used for this simulation. While these simulations were performed for all

pixel sizes and exposure rates from 0.1 to 100-μR/frame, the results of these simulations were not plotted as similar trends were observed.

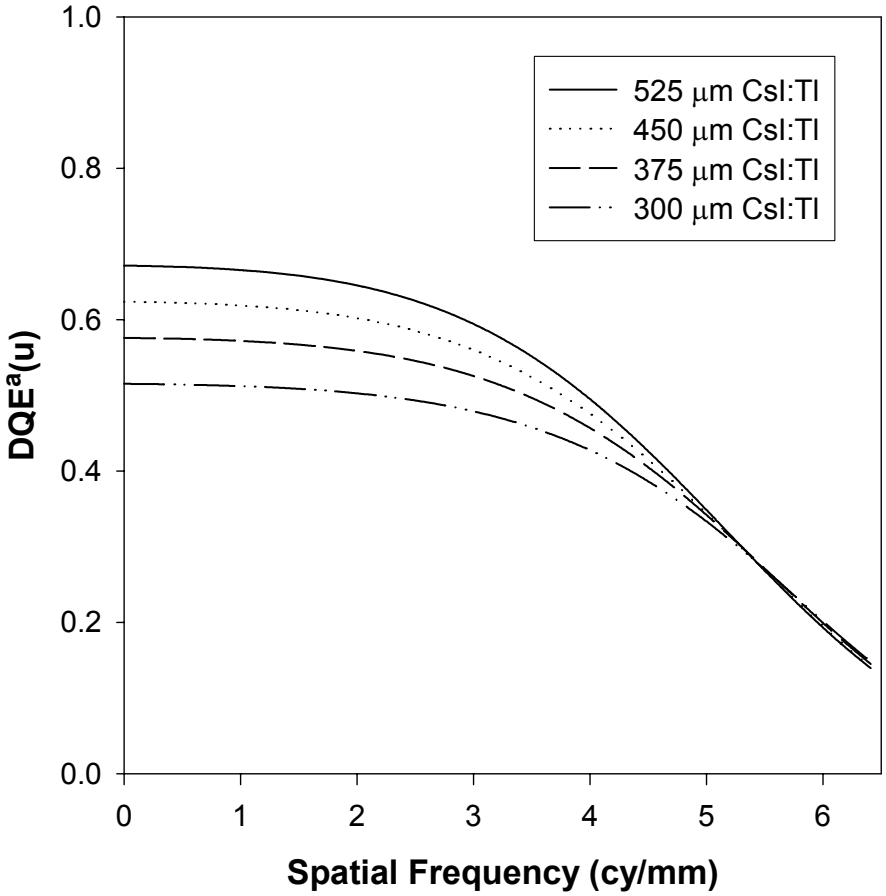


*Figure 6.13 Effect of CsI:Tl thickness on the frequency-dependent DQE of the system. These simulations were performed with the imager operating at 78-μm pixel size and 30-fps fluoroscopy at a nominal fluoroscopic exposure rate of 2-μR/frame.*

Figure 6.14 shows the presampling DQE [ $DQE(u)$ ] estimated for the system operating at 30-fps and employing a 450-μm CsI:Tl scintillator. For each pixel size, the presampling DQE is plotted up to its Nyquist sampling limit.

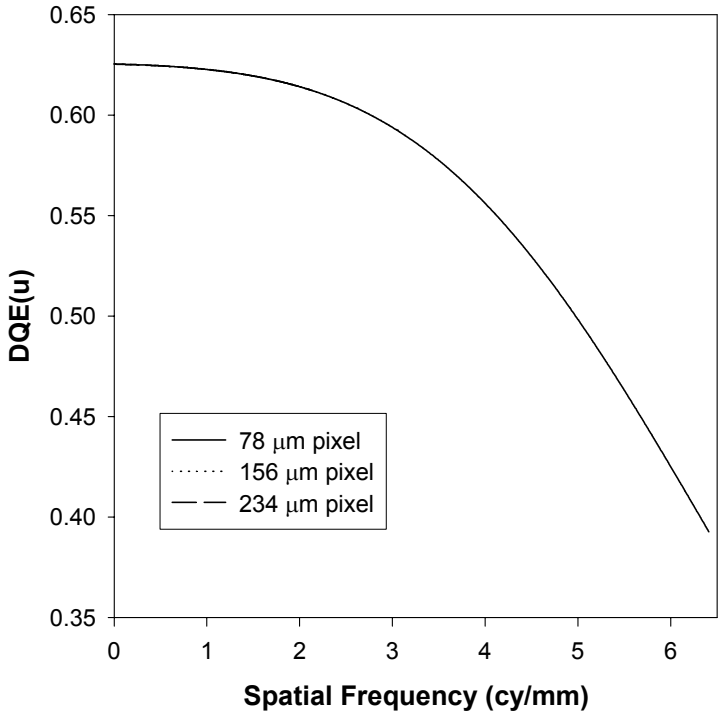


*Figure 6.14 Presampling DQE computed with the imager operating at 30-fps and using a 450-μm CsI:Tl scintillator at a nominal fluoroscopic exposure rate of 2-μR/frame.*

Figure 6.15 shows the frequency-dependent DQE computed with the aliased NPS [ $DQE^a(u)$ ] at conditions identical to that shown in Figure 6.14. For each pixel size, the presampling DQE is plotted up to its Nyquist sampling limit.

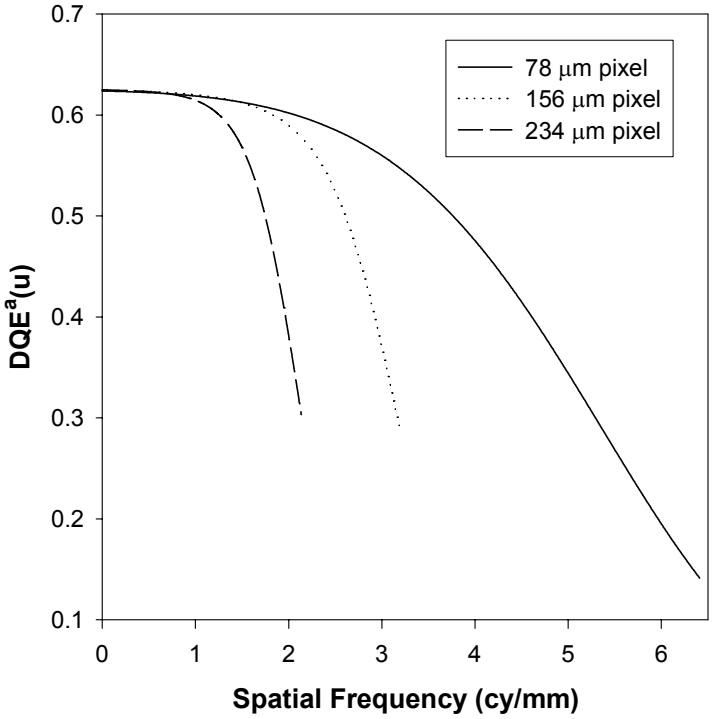


*Figure 6.15 Frequency-dependent DQE computed using aliased NPS for the system operating at 30-fps and using a 450-μm CsI:Tl to study the effect of pixel size.*

The results of the simulation to study the effect of incident exposure on the frequency-dependent DQE computed with the aliased NPS [ $DQE^{a}(u)$ ] for the pixel sizes of 78, 156 and 234-μm are shown in Figures 6.16 through 6.18, respectively. The simulations performed for the system using the 450-μm thick CsI:Tl scintillator alone is reported. Similar trends were observed for all thicknesses of CsI:Tl. The incident exposure rate was varied from 1 to 10-μR/frame.

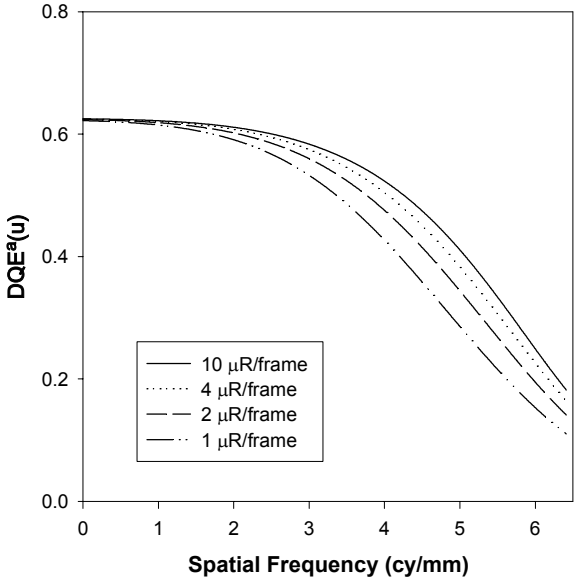


*Figure 6.16 Exposure dependence of frequency-dependent DQE. The results of the simulation for the imager operating at 30-fps fluoroscopy and 78-μm pixel size are shown. The CsI:Tl scintillator used is 450-μm.*

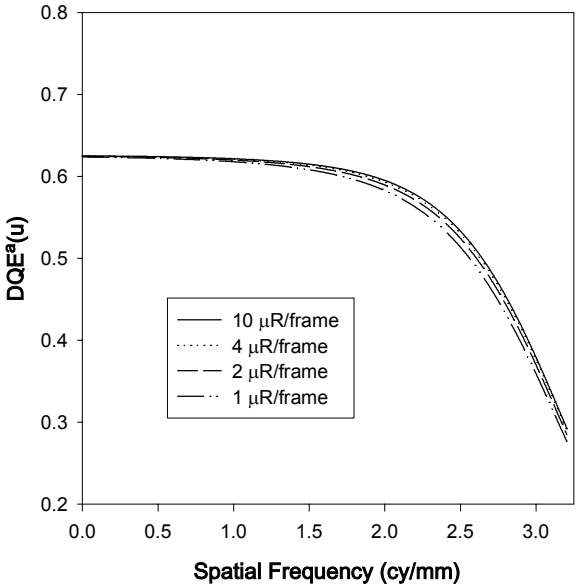


*Figure 6.17 Exposure dependence of frequency-dependent DQE. The results of the simulation for the imager operating at 30-fps fluoroscopy and 156-μm pixel size are shown. The CsI:Tl scintillator used is 450-μm.*

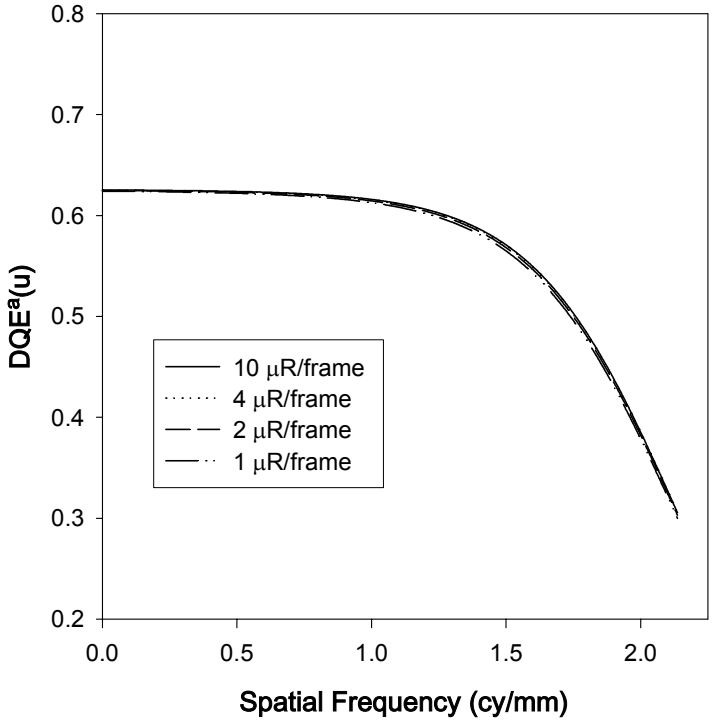


*Figure 6.18 Exposure dependence of frequency-dependent DQE. The results of the simulation for the imager operating at 30-fps fluoroscopy and 234-μm pixel size are shown. The CsI:Tl scintillator used is 450-μm.*

Figure 6.19 shows the estimated DQE along *u* and *v*-axes using the aliased NPS with the imager operating at 30-fps and 156-μm. The simulations were performed at a nominal fluoroscopic exposure rate of 2-μR/frame and with the system using a 450-μm CsI:Tl. The DQE estimated along the *u*-axis, represented as $DQE^a(u)$ and shown as circles in Figure 6.19 corresponds to an active pixel dimension of 156-μm. The DQE estimated along the *v*-axis, represented as $DQE^a(v)$ and shown as a solid line in Figure

6.19 corresponds to an active pixel dimension of 112-μm, which is degraded from the 156-μm due to fill factor.

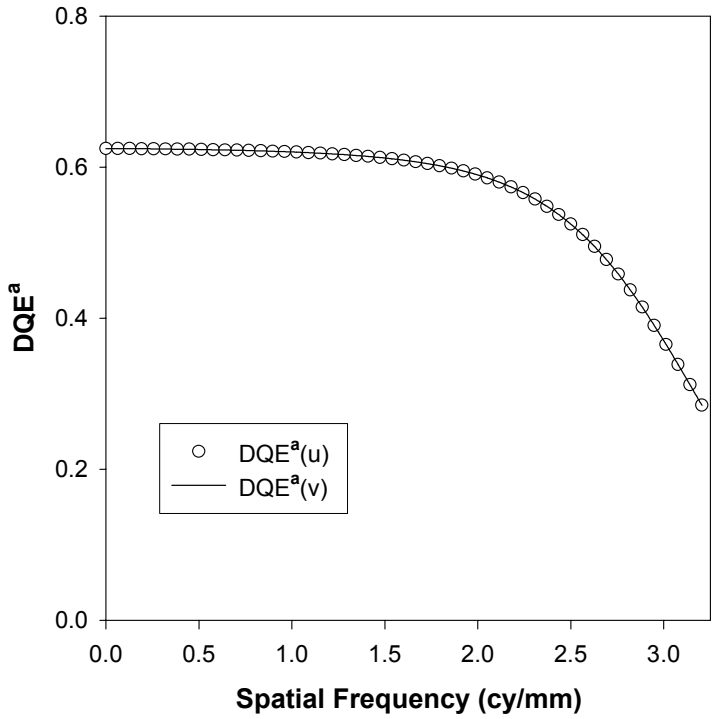


*Figure 6.19 Comparison of frequency-dependent DQE along two orthogonal axes.*

## 6.4. PARALLEL-CASCADED LINEAR-SYSTEMS MODEL

Figure 6.20 shows the estimated DQE along the u-axis computed using the aliased NPS and represented as $DQE_p^a(u)$, where the subscript '$p$' is used to denote the DQE estimated using the parallel-cascaded linear-systems-based model. The system uses a

450-μm CsI:Tl and operates at 156-μm pixel size. The fluoroscopic frame rate is 30-fps. The incident exposure rate is varied from 1 to 10-μR/frame.

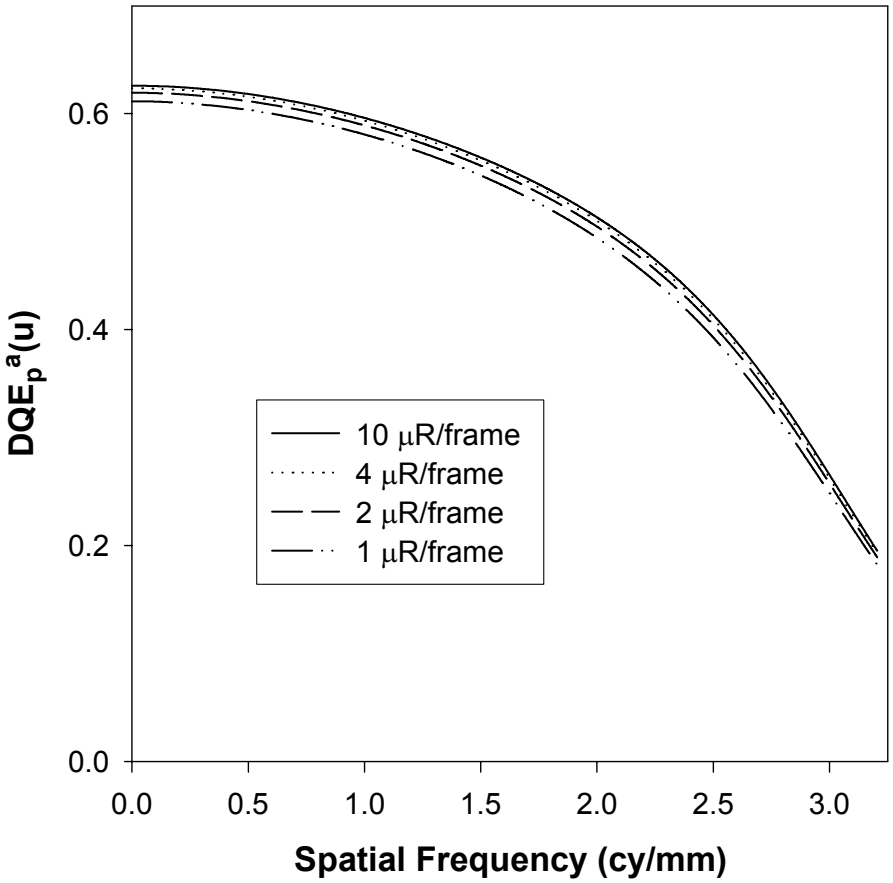


*Figure 6.20 Theoretically computed DQE along the u-axis using the parallel-cascaded linear-systems-based model. The system uses a 450-μm thick CsI:Tl and operates at 156-μm pixel size.*

Figure 6.21 shows the estimated DQE along the *v*-axis computed using the aliased NPS according to the parallel-cascaded linear-systems-based model and represented as

$DQE_p^a(v)$. The $v$-axis corresponds to the active pixel dimension of 112-μm. The scintillator used in this simulation is 450-μm CsI:Tl. The fluoroscopic frame rate is 30-fps. The incident exposure rate is varied from 1 to 10-μR/frame.

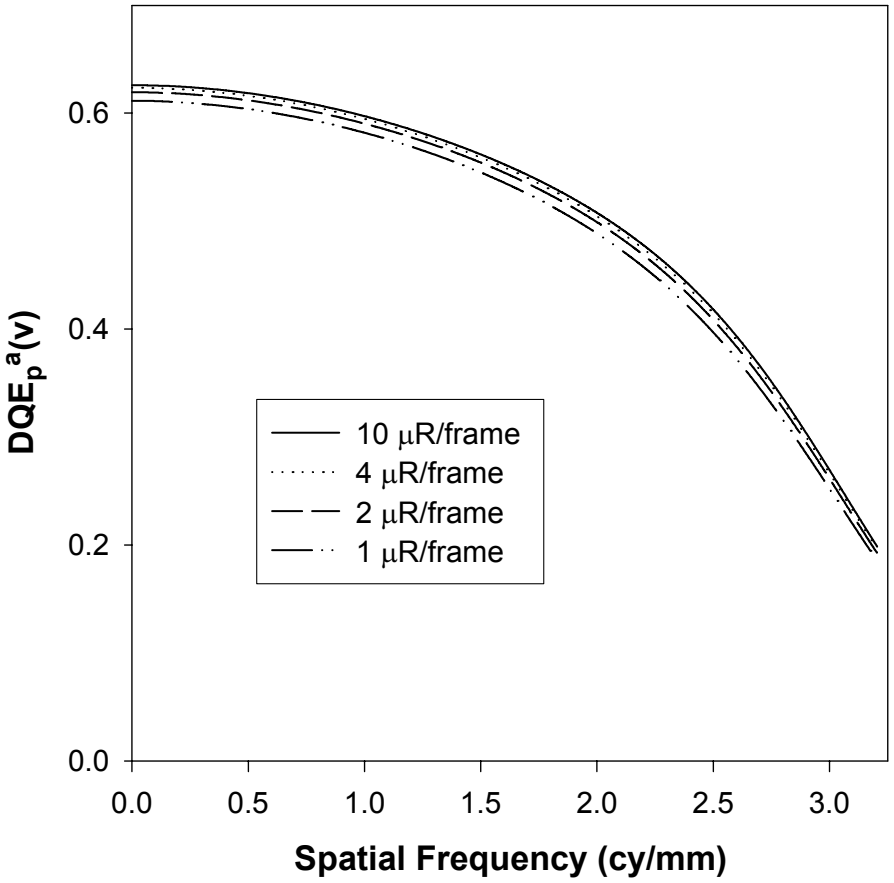


*Figure 6.21 Theoretically computed DQE along the v-axis using the parallel-cascaded linear-systems-based model. The system uses a 450-μm thick CsI:Tl and operates at 156-μm pixel size.*

Figure 6.22 shows the comparison of the DQE estimated along two-orthogonal axes using the aliased NPS according to the parallel-cascaded linear-systems-based model. The DQE along the u-axis is represented as circles and that along the v-axis by a solid line. The system uses a 450-μm CsI:Tl and operates at 156-μm pixel size. A nominal fluoroscopic exposure rate of 2-μR/frame is used in the simulation.

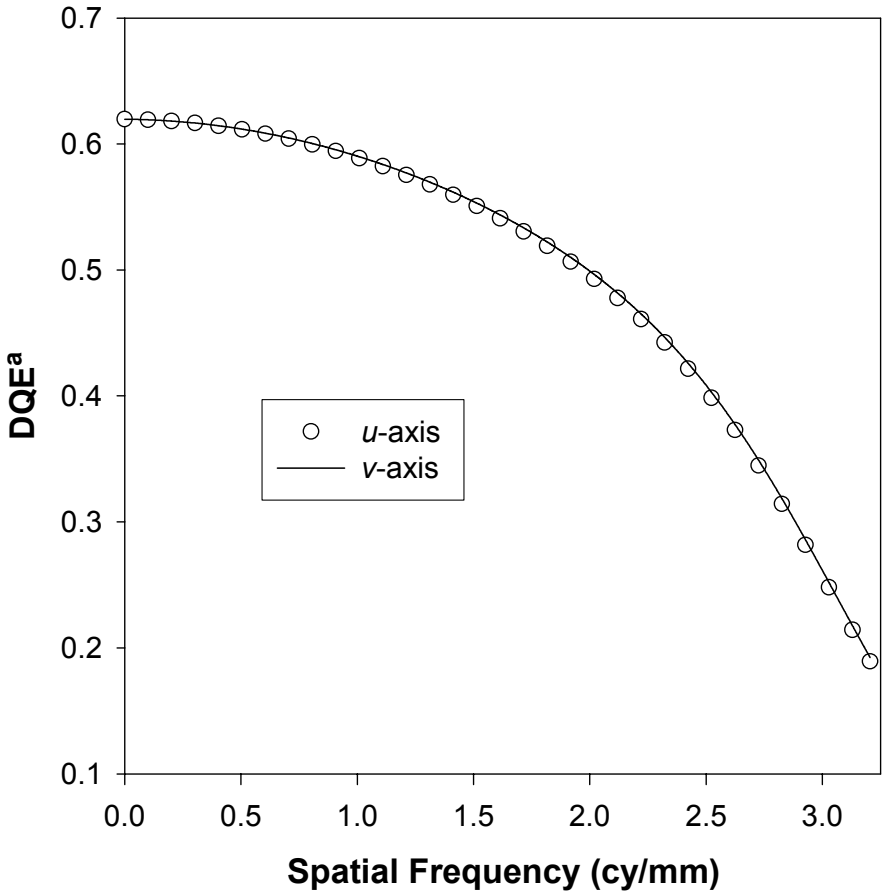


*Figure 6.22 Comparison of the DQE estimated along two-orthogonal axes using the aliased NPS according to the parallel-cascaded linear-systems-based model.*

## 6.5. EXPERIMENTAL RESULTS

Figure 6.23 shows the exposure-signal linearity plot for the system operating at 30-fps. The error bars at each exposure rate represents the *rms* standard deviation computed as the square-root of the *rms* variance. It should be noted that the slope of the linearity plot is dependent on the conversion gain (electrons/digital unit) of the electronics (ADC).

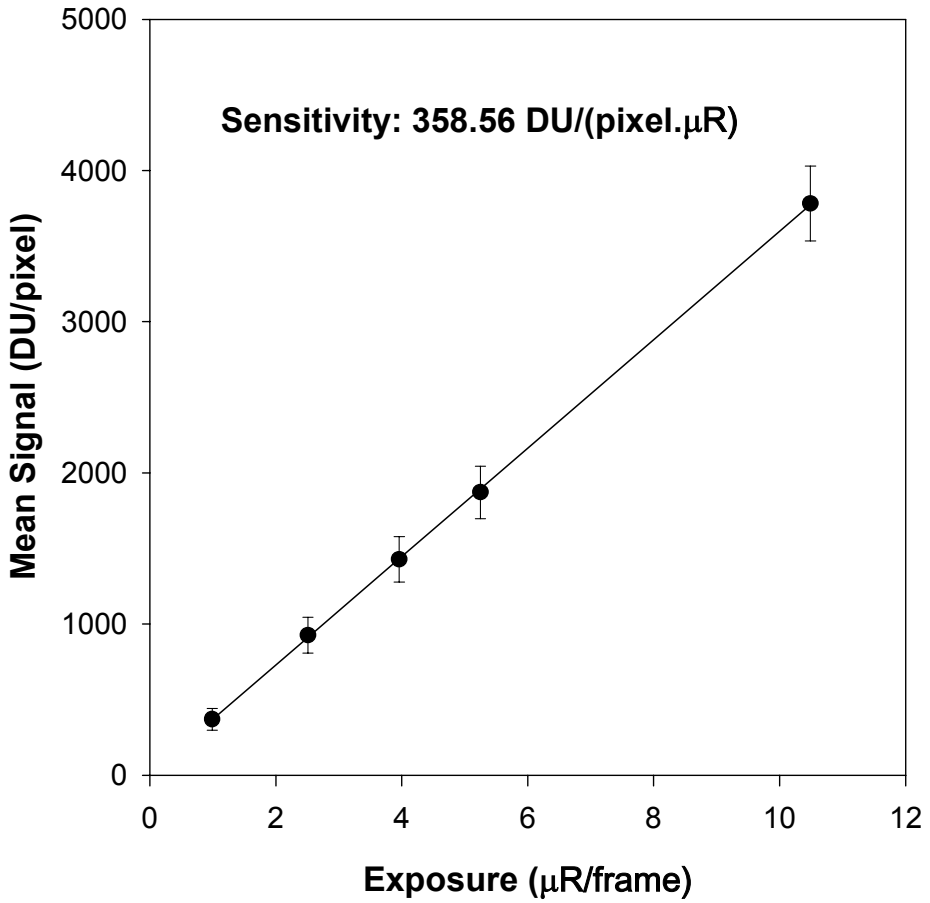


*Figure 6.23 Plot of exposure-signal linearity. The sensitivity calculated as the slope of the linearity plot was 358.56 DU/(pixel.μR).*

Figure 6.24 shows the presampling MTF measured along the $u$ and $v$-axes represented as $T_{pre}(u,0)$ and $T_{pre}(0,v)$, respectively.

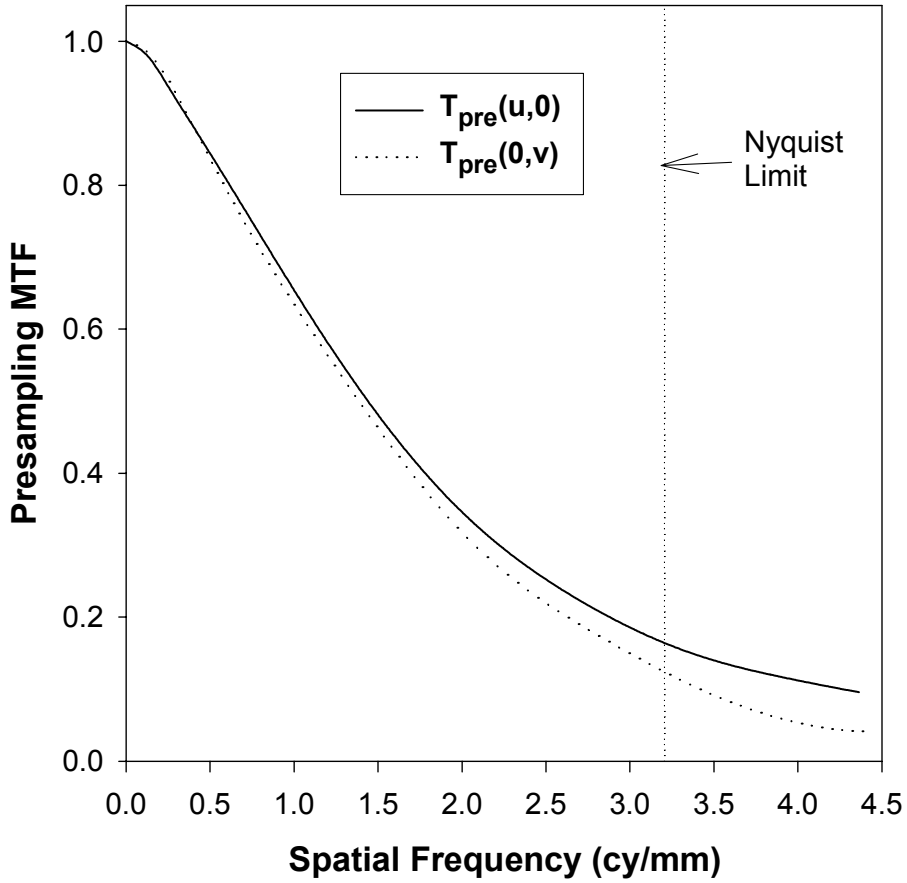


*Figure 6.24 Presampling MTF measured along the two orthogonal axes.*

Figure 6.25 shows the time (and temperature) dependence of the electronic noise from start-up of the imager at room temperature. At $t = 0$ the imager was turned on and the electronic noise was monitored at discrete time points over a period of 3.5 hours.

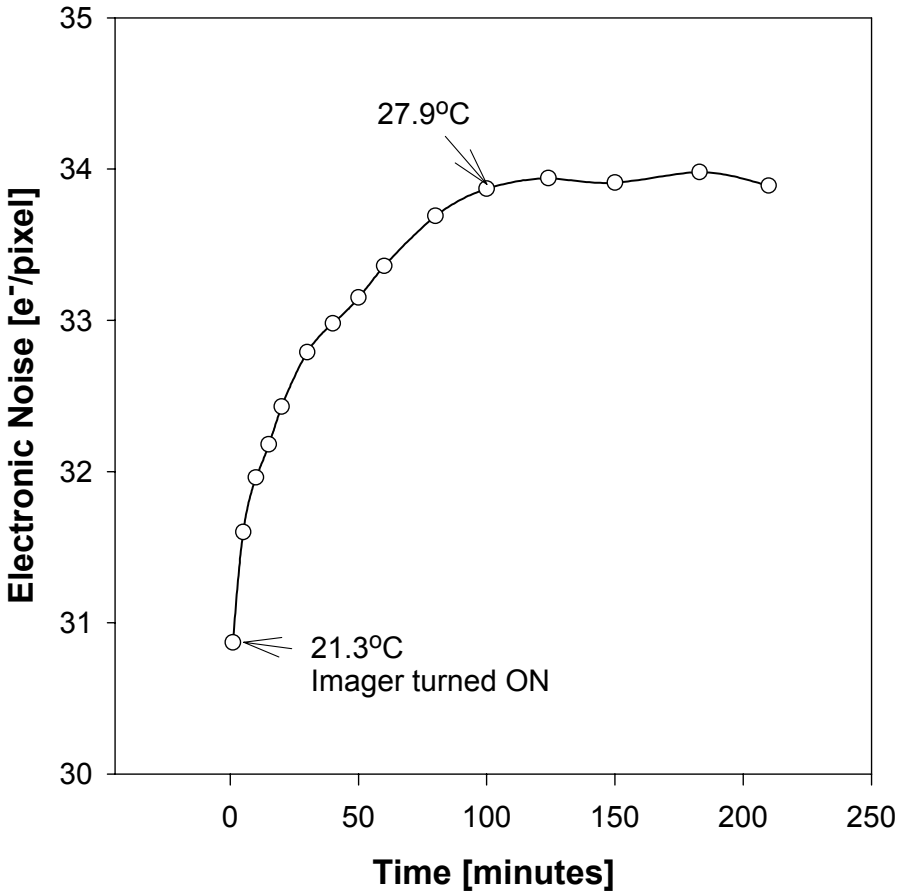


*Figure 6.25 Time (and temperature) dependence of the electronic noise from start-up of the imager at room temperature. At t=0 the imager was turned on and the electronic noise was monitored at discrete time points over a period of 3.5 hours.*

Figure 6.26 shows the 2-D electronic NPS estimated from a sequence of 500 images according to sections 5.7.3 and 5.7.4. The 2-D electronic NPS with the structured (fixed-pattern) noise [$W_E(u,v)$] is shown on the left and the 2-D electronic NPS without the structured-noise [$W_E^{NS}(u,v)$] is shown on the right. Figure 6.27 shows the 1-D electronic NPS estimated along the *u* and *v*-axes estimated according to section 5.7.4.

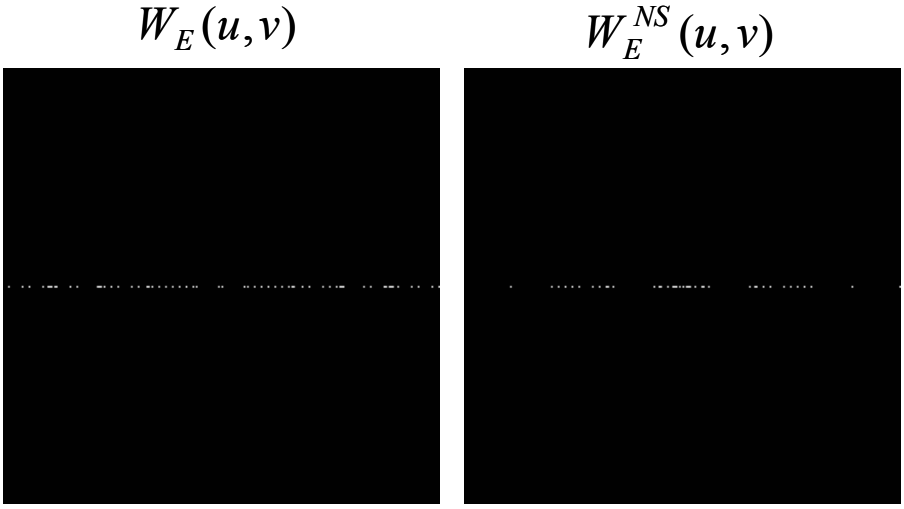


*Figure 6.26 2-D Electronic NPS with the structure noise [$W_E(u,v)$] and without the structured-noise [$W_E^{NS}(u,v)$].*

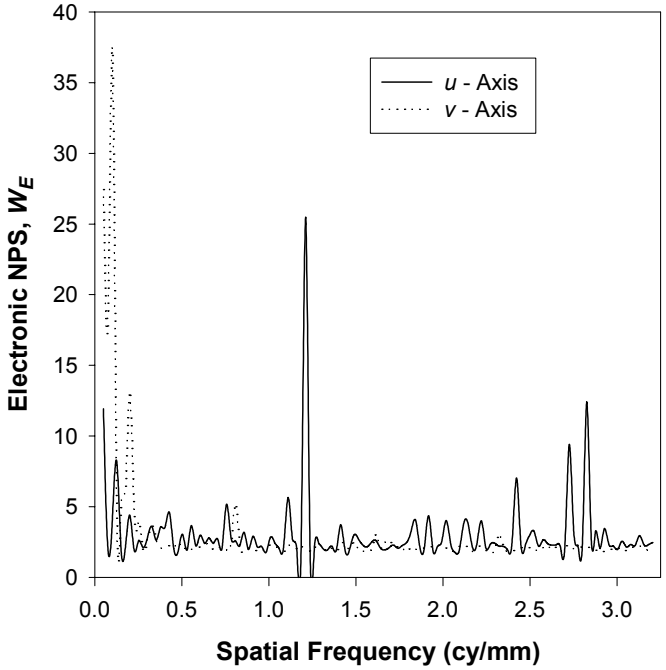


*Figure 6.27 Electronic NPS with the structured-noise component included estimated along the u and v-axes.*

Figure 6.28 shows the electronic NPS without the structured (fixed-pattern) noise component along the *u* and *v*-axes estimated according to section 5.7.5.

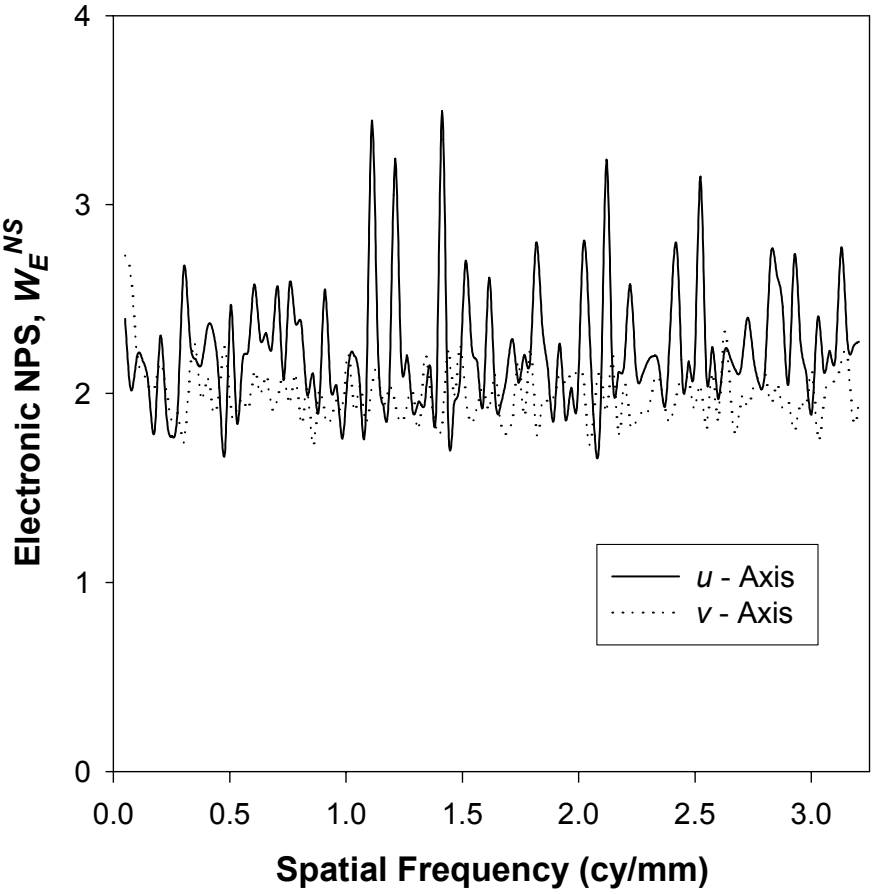


*Figure 6.28 Electronic NPS without the structured (fixed-pattern) noise component along the u and v-axes estimated according to section 5.7.5.*

Figure 6.29 shows the 2-D fluoroscopic NPS measured according to section 5.7.7 with the structured-noise component included at exposure rates of 0.99, 2.51, 3.96 and 10.49-μR/frame. Similar measurement was also performed at 5.25-μR/frame, but is not reported.

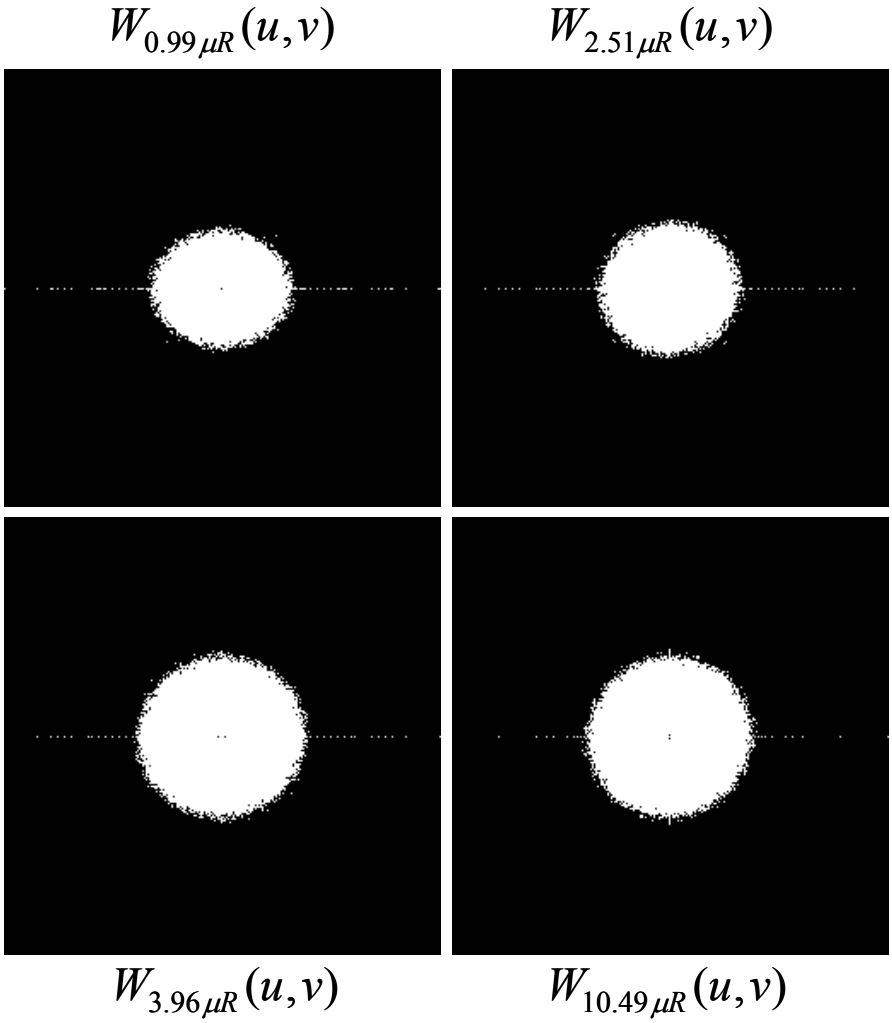


*Figure 6.29 2-D fluoroscopic NPS measured according to section 5.7.7 with the structured-noise component included at exposure rates of 0.99, 2.51, 3.96 and 10.49-μR/frame.*

Figure 6.30 shows the 2-D fluoroscopic NPS measured according to section 5.7.8 without the structured-noise component at exposure rates of 0.99, 2.51, 3.96 and 10.49-μR/frame. Similar measurement was also performed at 5.25-μR/frame, but is not reported.

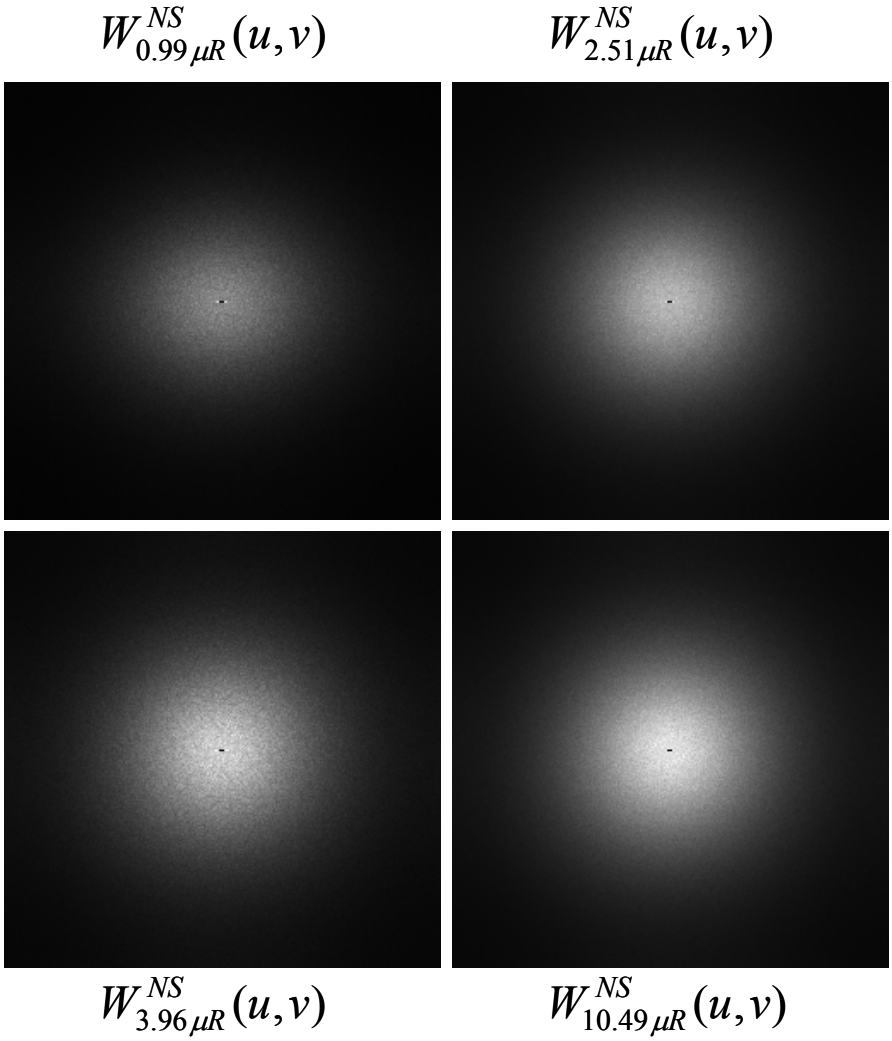


*Figure 6.30 2-D fluoroscopic NPS measured according to section 5.7.8 without the structured-noise component at exposure rates of 0.99, 2.51, 3.96 and 10.49-μR/frame.*

Figure 6.31 shows the measured image lag of the system operating at 30-fps according to the method stated in section 5.7.9 at an exposure rate of 2.51-μR/frame. Measurement of the image lag performed at each of the exposure rates shown in Table

5.2 indicated no exposure dependence. From these measurements, the lag-correction factor ($LCF$) was calculated to be 0.9836.

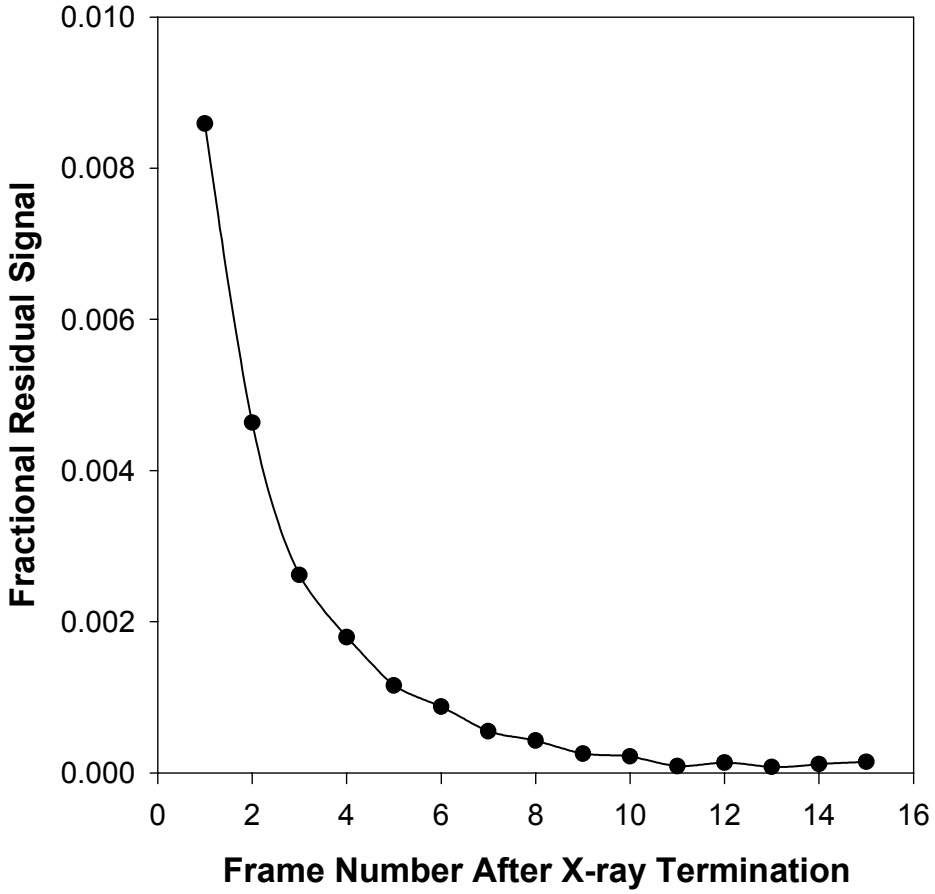


*Figure 6.31 Measured image lag of the system operating at 30-fps.*

Figure 6.32 and Figure 6.33 show the lag-corrected fluoroscopic NPS along the $u$ and $v$-axes represented as $W_X^{LC}(u,0)$ and $W_X^{LC}(0,v)$ calculated according to section 5.7.10 for the five exposure rates shown in Table 5.2. The electronic NPS [$W_E^{NS}$] corresponding to the axes are also plotted to facilitate easy comparison.

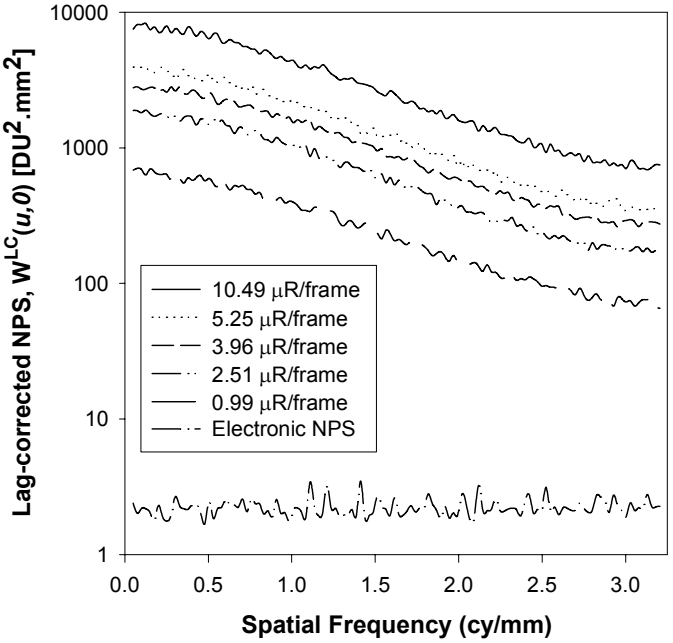


*Figure 6.32 Lag-corrected fluoroscopic NPS along the u-axis.*

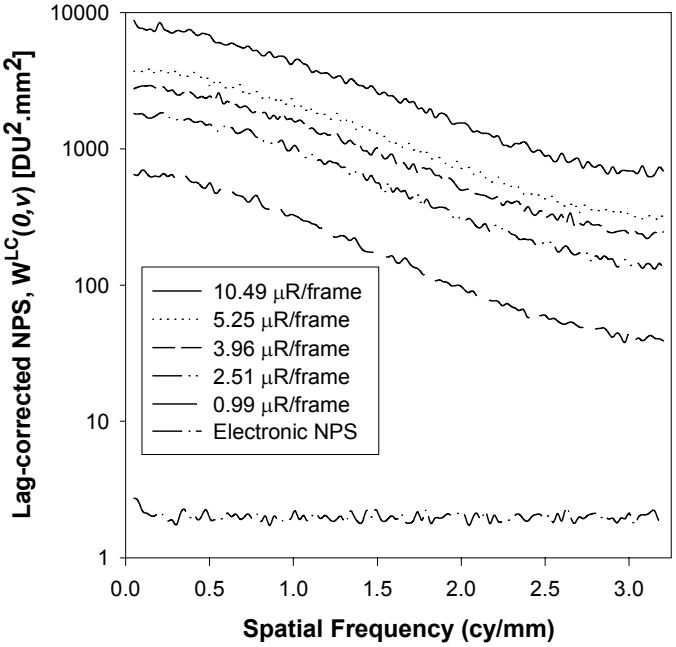


*Figure 6.33 Lag-corrected fluoroscopic NPS along the v-axis.*

Figure 6.34 shows the lag-corrected DQE along the *u*-axis at each of the exposure rates shown in Table 5.2.

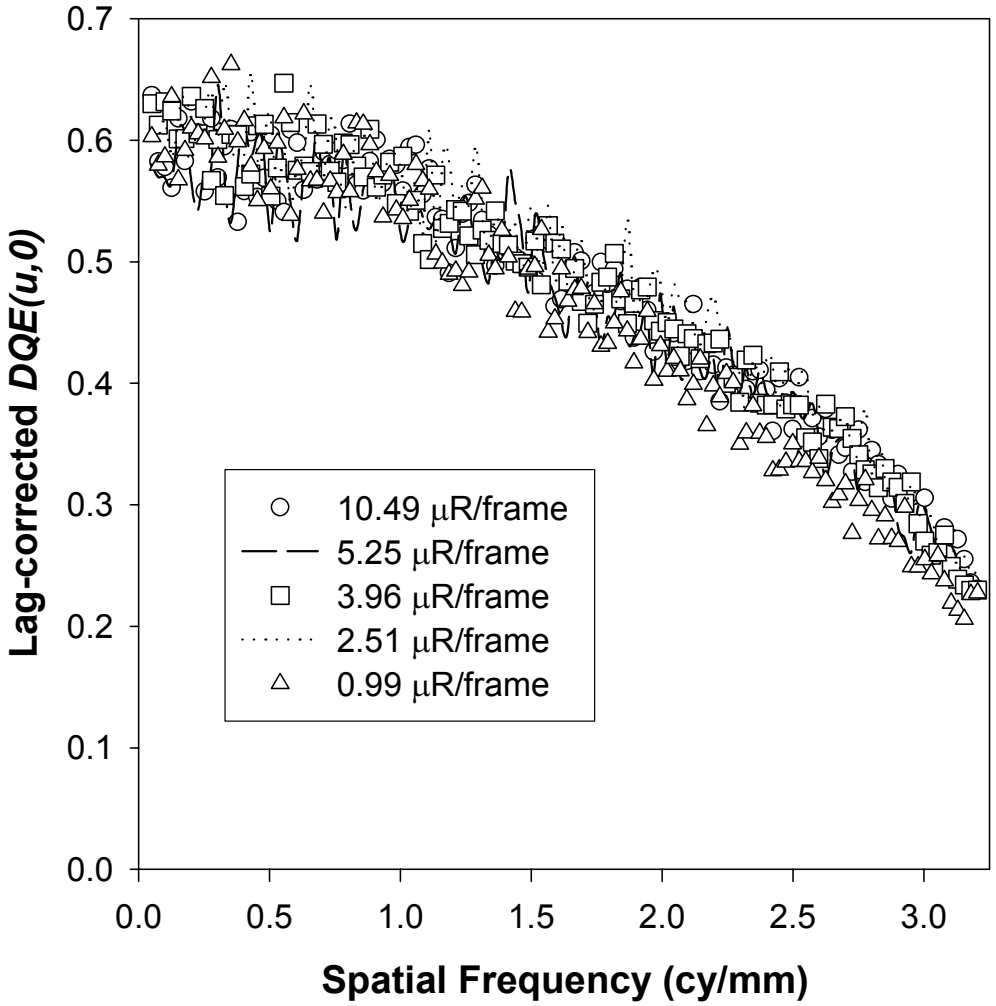


*Figure 6.34 Lag-corrected DQE along the u-axis at various exposure rates.*

Figure 6.35 shows the lag-corrected DQE along the *v*-axis at various exposure rates.

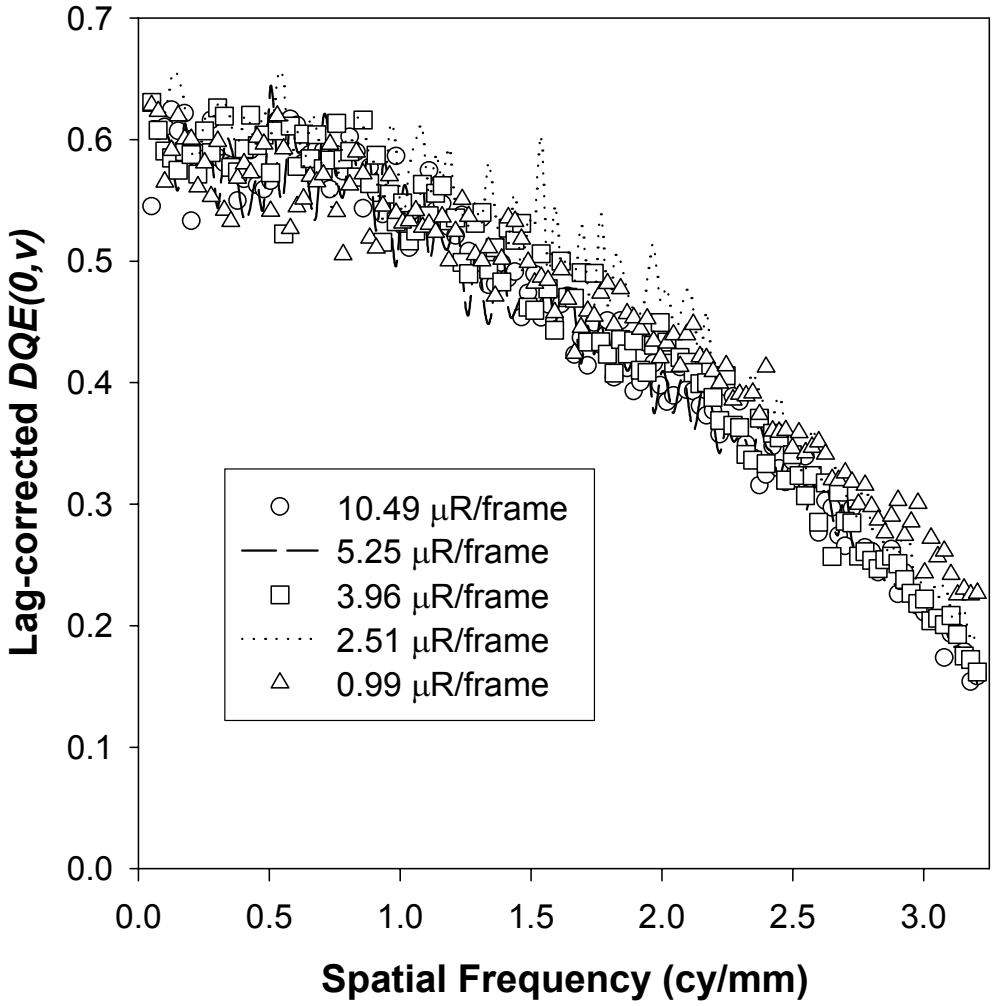


*Figure 6.35 Lag-corrected DQE along the v-axis at various exposure rates.*

## 6.6. QUALITATIVE IMAGES

Images of a bar-pattern test tool and a wire-mesh phantom were acquired to provide qualitative (visual) measure of image quality. The acquired image of the bar-pattern test tool is shown in Figure 6.36.

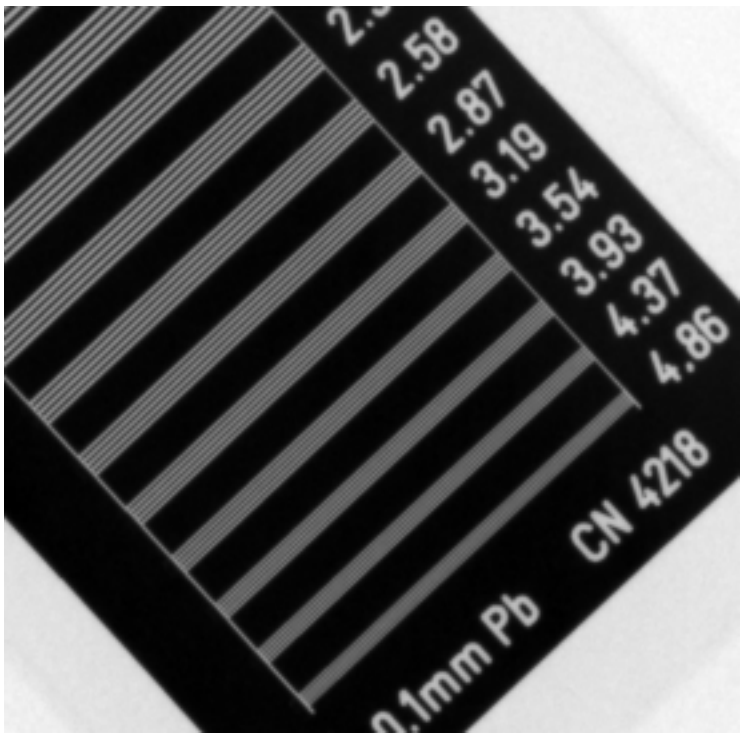


*Figure 6.36 Acquired image of a bar-pattern test tool.*

The acquired image of the wire-mesh phantom to study distortion and uniformity of resolution is shown in Figure 6.37.

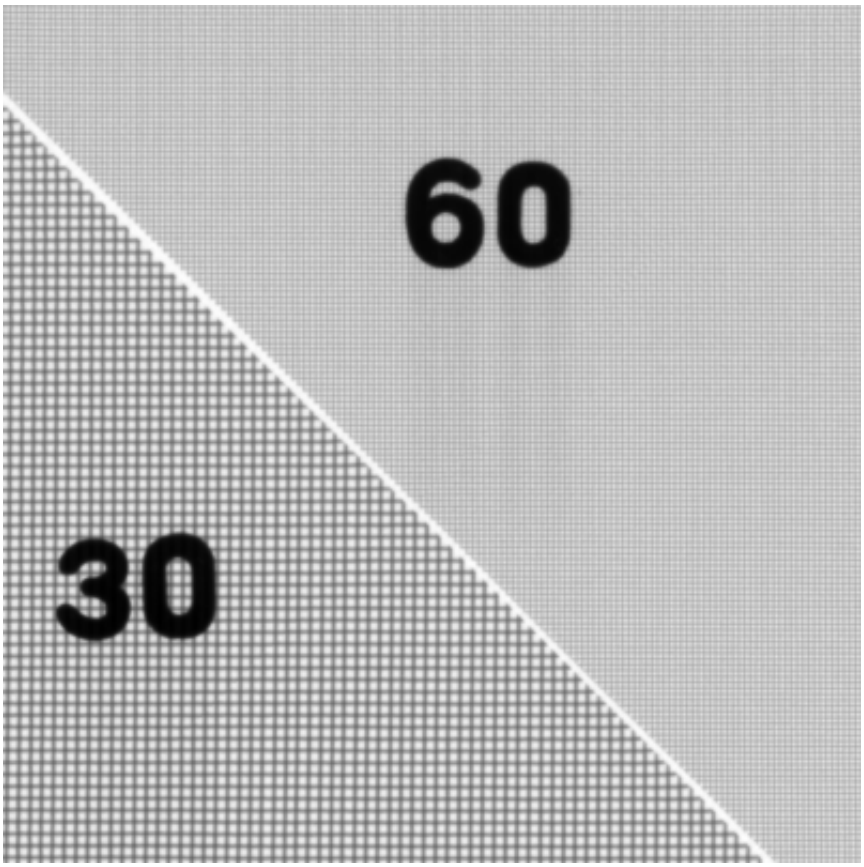


*Figure 6.37 Acquired image of a wire-mesh phantom to study distortion and uniformity of resolution.*

# 7. DISCUSSION

## 7.1. SYSTEM DESIGN PARAMETERS

Figure 6.1 showed the quantum efficiency of various thickness of CsI:Tl as a function of incident x-ray photon energy. A significant increase in quantum efficiency observed at ~33.5 and 35.5 keV, which correspond to energies just above the K-edge of Iodine and Cesium respectively. The incident spectrum-weighted quantum efficiency was shown in Table 6.1. The quantum efficiency of the system, for CsI:Tl thickness greater than 375-μm, can easily exceed 0.7. In comparison, the reported quantum efficiency of a clinical x-ray image-intensifier [59] ranges from 0.256 to 0.682, depending on incident photon energy, with the peak quantum efficiency of 0.682 achieved at 40-keV (slightly above the K-edge of CsI:Tl). The improved quantum efficiency observed provides *strong support* of the *first specific hypothesis* that this new fluoroscopic system will exhibit higher quantum efficiency than current image-intensifier-based fluoroscopic technology.

Figure 6.2 showed the energy-dependence of the quantum gain for various thickness of the CsI:Tl scintillator. A decrease in scintillator gain is observed at ~33.5 keV corresponding to the K-edge (approximate) of CsI:Tl. Thus, it is important to note that while using incident photon energies just above the K-edge improves the quantum efficiency as shown in Figure 6.1, it also causes a decrease in the number of optical

quanta generated (and emitted) at these energies, as a fraction of the absorbed x-rays is lost through K-fluorescent x-rays. The absorbed x-ray spectrum-weighted quantum gain for various thickness of the CsI:Tl scintillator was summarized Table 6.2. The light output ranged from 1300 to 1250 emitted optical quanta per interacting x-ray, depending on CsI:Tl thickness. A slight decrease in light output was observed with increasing thickness of CsI:Tl scintillator as the escape efficiency of the generated optical quanta decreases due to the increased travel path. This is also referred to as self-attenuation of the optical quanta [34, 65].

The calculated Swank factor was shown in Table 6.3. Swank factor is an important parameter as the maximum DQE performance achievable by an imager is limited by the product $\overline{g_1} \cdot A_s$. The Swank factor improved with increased CsI:Tl thickness for the same incident x-ray beam quality, as the K-escape fraction $K_f$ decreases with increasing CsI:Tl thickness [59, 61]. A plot of the K-escape fraction against phosphor thickness is shown in Figure 12 of reference 59, which illustrates this effect. Table 6.3 also contains the computed Poisson excess, used for convenience in DQE calculations, based on the Swank factor and the quantum gain.

Figure 6.4 showed the scintillator blur $MTF_{CsI:Tl}$ obtained by deconvolving *sinc(96μm)* and *sinc(24μm)* from system presampling MTF measurements performed at 24 and 96-μm, respectively. This study was undertaken to verify if the pixel presampling MTF in a CCD-based system, which has a contiguous-pixel architecture, can be approximated by a *sinc* function as used with imaging systems that have discrete pixels. If the scintillator blur obtained at two different pixel sizes were identical, this would

indicate that the pixel presampling MTF could be approximated by the *sinc* function. Figure 6.4 showed that the scintillator blur obtained through presampling MTF measurements at 24 and 96-μm were identical, thus providing verification that the pixel presampling MTF could be approximated by the *sinc* function. Figures 6.4 though 6.7 showed the estimated scintillator MTF for the four thickness of CsI:Tl used. In all cases, the Lorentzian fit to the measured data overestimated at low spatial frequencies and underestimated at high spatial frequencies. The blur fit according to equation 5.15 provided the best fit to the scintillator MTF. The calculated optical coupling efficiency of the fiberoptic is 0.5. In comparison, for an image-intensifier system using relay lenses, the fraction of optical quanta emitted from the output phosphor of the image-intensifier reaching the face of the photomultiplier (PMT) is ~3% [59]. The average quantum efficiency of the CCD including the loss due to the geometrical fill factor ($\overline{g_5} \cdot F_f$) was estimated to be 0.4. The calculated sensitivity at pixel sizes of 78, 156 and 234-μm for various CsI:Tl thickness were shown in Table 6.4. The increase in sensitivity observed with increasing CsI:Tl thickness is due to the increased quantum efficiency as observed in Table 6.1. The increase in sensitivity observed with increasing pixel size is due to the increased signal obtained by the integration over the larger pixel area. As expected, the sensitivity scales by the square of the pixel dimension in Table 6.1. Experimental determination of sensitivity for an image-intensifier-based system indicate that 189 electrons are released by the photocathode of the PMT (video pickup tube) for an absorbed x-ray photon [59]. The sensitivity expressed in the units used above is

independent of pixel size. Hence, the calculated sensitivity was represented in units of electrons/absorbed x-ray photon, by scaling as shown below.

$$\Gamma\left[\frac{e^-}{\text{absorbed x - ray photon}}\right] = \Gamma\left[\frac{e^-}{\text{pixel}.\mu\text{R}}\right] \times \frac{1}{\left(q_0/X\right)\cdot\overline{g_1}\cdot A_{pix}^2} \qquad 7.1$$

where, $A_{pix}^2$ is the pixel area in mm$^2$, $\left(q_0/X\right)$ is the incident photon fluence per μR in units of x-ray photons/(mm$^2$ μR) and $\overline{g_1}$ is the quantum efficiency shown in Table 6.1. It should be noted that the calculated sensitivity is scaled by $\overline{g_1}$ as shown in equation 7.1, so that the sensitivity can be expressed in terms of the absorbed x-ray photon (and not incident x-ray photon) to facilitate direct comparison with the image-intensifier-based system. The calculated sensitivity in units of electrons/absorbed x-ray photon is shown in Table 7.1 below.

*Table 7.1 Calculated sensitivity in units of electrons/absorbed x-ray photon. The percent improvement in sensitivity was computed using the published sensitivity of 189 electrons/absorbed x-ray photon for an image-intensifier-based system [59].*

| CsI:Tl thickness (μm) | Sensitivity ($e^-$/absorbed x-ray photon) | Improvement (%) |
|---|---|---|
| 300 | 202.82 | 7.31 |
| 375 | 198.65 | 5.11 |
| 450 | 196.04 | 3.72 |
| 525 | 194.04 | 3.15 |

From Table 7.1, it is seen that the CCD-based imaging system provides improved sensitivity compared the image-intensifier-based system. Comparing with Table 6.4, which showed an increase in sensitivity with increasing scintillator thickness, Table 7.1 shows a decrease. The values obtained in Table 7.1 were calculated for an absorbed x-ray photon (not an incident x-ray photon), hence does not contain the effect of quantum efficiency $\overline{g_1}$. The decrease in sensitivity with increased CsI:Tl thickness observed is due to self-attenuation of the generated optical quanta [34. 65].

The estimated electronic noise of the system operating at 30-fps for the 78, 156 and 234-μm pixel sizes was shown in Table 6.5. The increase in electronic noise with increasing pixel size is due to the increased contribution of CCD noise ($\sigma_{CCD}$) according to equation 5.21 as $A_{pix}^2$ increases. The effective dynamic range of the system using a 450-μm CsI:Tl for the 78, 156 and 234-μm pixel sizes was shown in Table 6.6. The dynamic range calculations indicate that the imager is capable of operation over three orders of magnitude, and more importantly in the exposure range suitable for fluoroscopy.

## 7.2. SEAMLESS TILING

Figure 6.8 showed images of a spoke wheel phantom prior to seam suppression (A) and after suppression (B). The images indicate that successful seam suppression can be achieved. Recently, several algorithms for seam suppression were investigated [76].

The effectiveness and the suitability of these algorithms for this imaging system will be pursued in future.

## 7.3. SERIAL-CASCADED LINEAR-SYSTEMS MODELING

The serial-cascaded linear-system-based model was used to predict the DQE performance of the imaging system.

### *7.3.1. Zero-frequency DQE*

The parameters that influence the DQE performance of the imaging system were addressed in chapter 5. These parameters were used to provide a theoretical estimate of the zero-frequency DQE. The zero-frequency DQE [$DQE(0)$] can provide vital information about the imager performance. In general, $DQE(0)$ provides the upper limit of the frequency-dependent DQE and hence, studying the limitations of $DQE(0)$ would provide an understanding of the maximum performance that can be achieved by the imager. Within the exposure range considered, $DQE(0)$ improved with increased CsI:Tl thickness as observed in Figure 6.9 This is due to the increase in the scintillator quantum efficiency, $\overline{g_1}$ as observed in Table 6.1. At exposure rates of 0.1 to 0.5-μR, a slight degradation in $DQE(0)$ is observed, in particular with decreasing pixel size, due to the relatively low signal. It should be noted that this effect is observed only at exposure rates that are not used in current clinical practice, which is typically 2-4 μR/frame, and may be irrelevant for the intended application. At fluoroscopic exposure rates of 2-4 μR/frame,

the $DQE(0)$ performance is unaffected by pixel size, indicating that the SNR performance can be maintained even at the high-resolution mode of 78-μm. Most importantly, these plots indicate that the $DQE(0)$ is either comparable or improved, depending on CsI:Tl thickness, to state-of-the-art image-intensifier-based technology, which typically exhibits $DQE(0)$ of ~0.55 [21].

### *7.3.2. Impact of Additive Noise*

The $DQE(0)$ for the various CsI:Tl scintillator thickness shown in Figure 6.9 were calculated using estimated values for the additive noise summarized in Table 6.5. However, at low frame rates, the CCD noise ($\sigma_{CCD}$) will be higher due to the increased frame integration period ($t$), as per equation 5.21. Hence, the impact of additive noise was studied at a nominal fluoroscopic exposure of 2-μR for the three pixel pitch modes of operation for each scintillator thickness and was shown in Figure 6.10. The plots indicate that as the additive noise $\sigma_T$ increases beyond 100 electrons, $DQE(0)$ degrades. Further at the same additive noise level, this degradation is more pronounced with the smaller pixel sizes, as the pixel area over which the signal is integrated decreases with smaller pixel sizes. Most importantly, these results indicate that the imager can maintain the SNR performance even at $\sigma_T$ of 100 electrons. Based on equation 5.21 and the other noise sources addressed in section 5.2.9, $\sigma_T$ of 100 electrons translates to a frame integration period of 1.6-seconds or frame rate of ~1 frame every 2-seconds, which is well-beyond the requirements for any fluoroscopic system.

### 7.3.3. *Effect of Image Lag*

Simulations of $DQE^{trap}(0)$ were performed by varying the fraction of trapped charge ($f_{trap}$) in the range $0 < f_{trap} < 0.1$, using $\sigma_T$ summarized in Table 6.5 for a nominal fluoroscopic exposure rate of 2-μR/frame. The results of these simulations performed for the three pixel pitch modes for each of the scintillator were shown in Figure 6.3. The results indicate that for increasing $f_{trap}$, the individual pixel variance reduces due to increased correlation between frames. This results in inflation of the DQE. These results are consistent with that observed by Cunningham [50], further illustrating the need to measure the 'lag-free' DQE. Several authors have provided techniques for correcting the effect of image lag for DQE measurements performed under fluoroscopic mode of operation [21, 36, 50, 85].

### 7.3.4. *Frequency-dependent DQE*

Aliasing causes a preferential increase in the NPS at higher spatial frequencies as observed in Figure 6.12, as the noise power at spatial frequencies above the Nyquist limit are folded back and added to the presampling NPS. The plot of the CsI:Tl thickness dependence on the $DQE^{a}(u)$ shown in Figure 6.13, indicates that increasing the scintillator thickness improves the DQE at low frequencies and causes a faster roll-off at high frequencies. The improvement in DQE at low frequencies with increased CsI:Tl

thickness is due to the improved quantum efficiency and the faster roll-off at high frequencies with increased CsI:Tl thickness is due to the increased scintillator blur addressed in section 5.2.4. The trends are similar to the measured DQE reported in literature [21].

Simulation of the presampling DQE [ $DQE(u)$ ] for the system operating at 30-fps and employing a 450-μm CsI:Tl scintillator at a nominal fluoroscopic exposure rate of 2-μR/frame shown in Figure 6.14 indicates that the presampling DQE is unchanged with pixel size, as per expectations. Figure 6.15 showed the $DQE^a(u)$ simulation performed with the aliased NPS at identical conditions. The plot indicates a significant drop in DQE at spatial frequencies close to the Nyquist sampling limit due to noise aliasing, addressed previously. In spite of increased noise power at spatial frequencies close to the Nyquist sampling limit, for the 156 and 234-μm pixel sizes DQE of ~0.3 is observed at their corresponding Nyquist sampling limits. In comparison with current image-intensifier-based technology, which exhibit a DQE of ~0.3 at 1.6 cy/mm for the 6-inch field-of-view [21], the CCD-based system is capable of achieving the DQE of 0.3 at spatial frequencies of 5, 3 and 2.1 cy/mm for the 78, 156 and 234-μm pixel sizes, thus providing support to the hypothesis of improved performance.

The $DQE^a(u)$ at various fluoroscopic exposure rates were simulated in Figures 6.16 through 6.18. The results of the simulation performed with the imager operating at the pixel size of 78-μm, shown in Figure 6.16 indicates that the DQE performance at low spatial frequencies is unaffected by increased exposure. However, increasing the

exposure resulted in an increase in DQE performance at the mid and high spatial frequencies. The combined effects of the small pixel size resulting in a relatively low signal integrated by the pixel and the degradation of this signal at mid to high-frequencies due to the scintillator blur and the pixel presampling MTF is sufficiently low for the total additive electronic noise shown in Table 6.5 to cause the degradation of the DQE at mid to high-frequencies for the low exposure rates. However, when the imager is operated at the 156-μm mode, there is a minimal change in the DQE performance with exposure over all spatial frequencies as seen in Figure 6.17, in spite of the slight increase in the additive noise with the larger pixel size as seen in Table 6.5. This suggests that the imager is quantum-noise-limited providing support to the *first hypothesis* stated in chapter 3. When the system is operated in the 234-μm pixel size, similar results are observed as shown in Figure 6.18. Thus for the fluoroscopic exposure range of 1 to 10-μR/frame, quantum-noise-limited operation is expected for the 156 and 234-μm pixel sizes. While for the 78-μm pixel size, degradation of the DQE at mid to high-spatial frequencies is observed with decreased exposure, the DQE performance is still much superior to the current image-intensifier-based technology [21].

Figure 6.19 shows the estimated DQE along *u* and *v*-axes using the aliased NPS with the imager operating at 30-fps and 156-μm. The results of this simulation indicate that there is no difference in the DQE performance along the *u* and *v*-axes. Analyzing equation 6.31, when the additive NPS $[W_{add}(u,v)]$ relative to the signal becomes insignificant (quantum-noise-limited operation), the second term in the denominator that contains $W_{add}(u,v)$ becomes negligible. Since, this is the only term that contains the

effect of fill factor through the terms $T_6$ and $F_f$, the DQE performance along the *u* and *v*-axes are unchanged.

## 7.4. PARALLEL-CASCADED MODEL

The serial-cascaded model does not include the effect of reabsorption of K-fluorescent x-rays. Hence, the parallel-cascaded model was developed to include this effect. The DQE estimated along the *u*-axis using the aliased NPS with the parallel-cascaded model represented as $DQE_p^a(u)$ was shown in Figure 6.20. The simulation was performed with a 450-μm CsI:Tl with the imager operating at 156-μm pixel size. The plot indicates that there is slight exposure dependence within the exposure range examined. Also, the predicted DQE at mid to high spatial frequencies is significantly lower than that predicted using the serial-cascaded model shown in Figure 6.17. This is due to stochastic blur caused by the reabsorption K-fluorescent x-rays represented as $T_K(u,v)$. Analysis of the DQE using the parallel-cascaded model with photoconductive materials have also shown similar trends [82]. Similar trend was also observed in the DQE predicted along the *v*-axis shown in Figure 6.21. Comparison between the predicted DQE along the two orthogonal axes shown in Figure 6.22, shows no significant difference, consistent with the predictions of the serial-cascaded model shown in Figure 6.19.

## 7.5. DISCUSSION ON EXPERIMENTAL RESULTS

The experimentally determined exposure-signal linearity plot for the prototype single module operating at 30-fps and 156-μm pixel size shown in Figure 6.23, indicate that the system response is linear. The error bars at each exposure rate represents the *rms* standard deviation computed as the square-root of the *rms* variance.

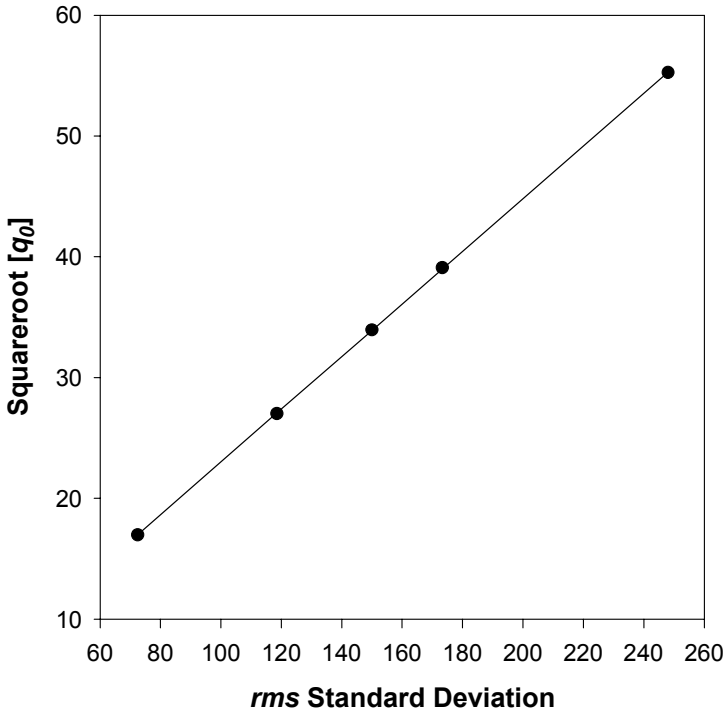


*Figure 7.1 Plot of the rms standard deviation against the square root of the incident photon fluence. The linear relationship indicates that the system is quantum-noise-limited.*

The increase in the *rms* standard deviation observed with increasing exposure in Figure 6.23 is due to the increased quantum-noise. This can be verified by plotting the *rms* standard deviation against the square root of the incident photon fluence, which is the

quantum-noise of the Poisson distributed quanta as shown in Figure 7.1. The plot indicates a linear relationship, which provides *strong experimental support* that the system is x-ray quantum-noise-limited, in support of the *first hypothesis*.

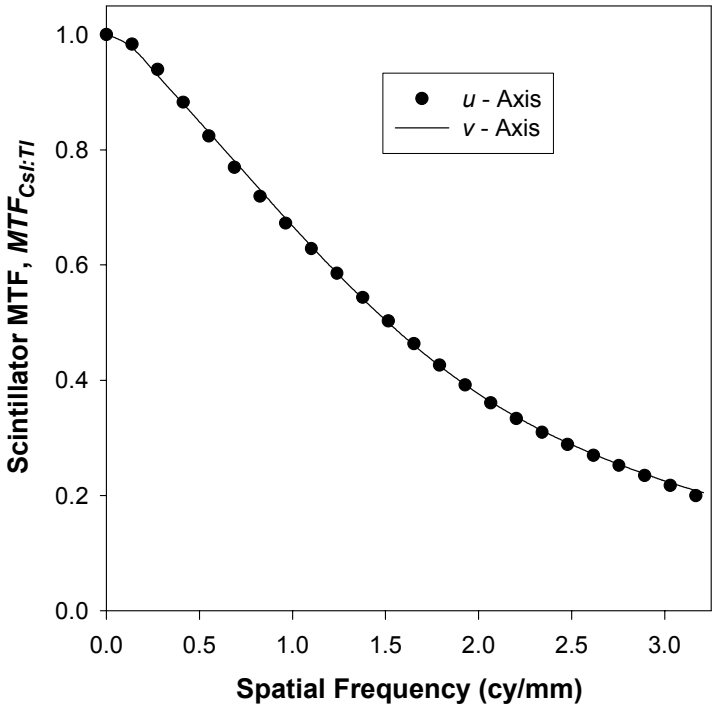


*Figure 7.2 Scintillator MTF obtained by deconvolving the pixel presampling MTF corresponding to the axes from the measured presampling MTF along the u and v-axes.*

Figure 6.24 showed the presampling MTF measured along the *u* and *v*-axes represented as $T_{pre}(u,0)$ and $T_{pre}(0,v)$, respectively. The lack of a low-frequency drop in the measured presampling MTF provides *strong experimental support* of the *third hypothesis* that the imager will be free of veiling glare. $T_{pre}(0,v)$ corresponds to the axis

where the active dimension of the pixel is 156-μm and $T_{pre}(u,0)$ corresponds to the axis where the active dimension of the pixel is 112-μm. Theory predicts that the scintillator blur is isotropic. To verify the theoretical prediction, the pixel presampling MTF corresponding to each axis was deconvolved. Figure 7.2 shows the scintillator MTF obtained along *u* and *v*-axes. Almost identical scintillator MTF along the *u* and *v* –axes indicate that the difference in the presampling MTF is due to the pixel presampling MTF. Figure 7.3 shows the comparison between the measured presampling MTF with the MTF of an image-intensifier-based system [86].

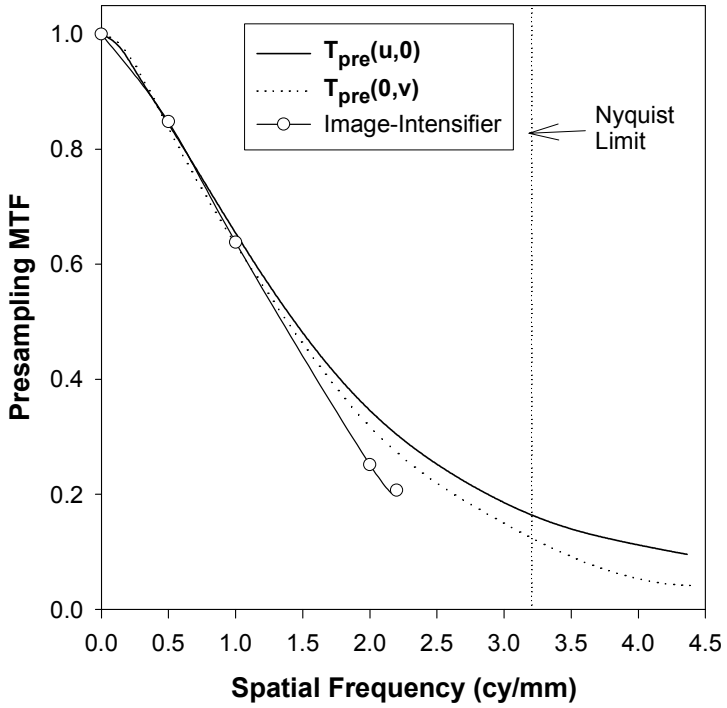


*Figure 7.3 Comparison of the measured presampling MTF with that of an image-intensifier-based system.*

The plot indicates a significant improvement in spatial resolution at mid to high frequencies providing *strong experimental support* of the *fourth hypothesis* of improved spatial resolution compared to image-intensifier-based systems.

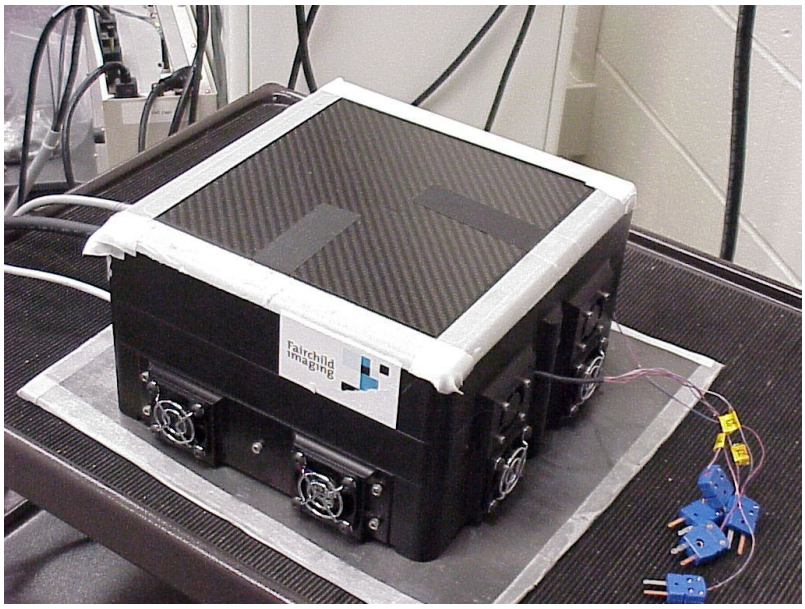


*Figure 7.4 Photograph of the imager.*

The time (and temperature) dependence of the electronic noise from start-up of the imager at room temperature was measured and shown in Figure 6.25. At $t = 0$ the imager was turned on and the electronic noise was monitored at discrete time points over a period of 3.5 hours. The plot indicates that temperature stabilization is achieved in approximately 90 minutes after start-up. While such a characteristic in general may not be a desirable, it is important to note that the increase in electronic noise is ~3.5 electrons from start up to temperature stabilization, which may not have a significant impact on

image quality. Also the measured electronic noise of ~34 electrons is in excellent agreement with the theoretical prediction of 34.1 electrons for the imager operating at 156-μm pixel size as seen in Table 6.5. Temperature stabilization is achieved through air circulation by fans as shown in the photograph of the imager in Figure 7.4. The imager is neither liquid-cooled nor does it use thermoelectric coolers (TECs).

Figure 6.26 showed the 2-D electronic NPS with and without the structured-noise. The Figures indicate that there is no off-axis noise source (which if present, would appear as bright spots in the image at points not on the *u* and *v* axes). However, the images do indicate that there is some significant noise along the *u*-axis. This noise source is due to the readout and appears as vertical lines in the spatial domain as shown in Figure 7.5. The eighth readout port (farthest right) in Figure 7.5 is defective.

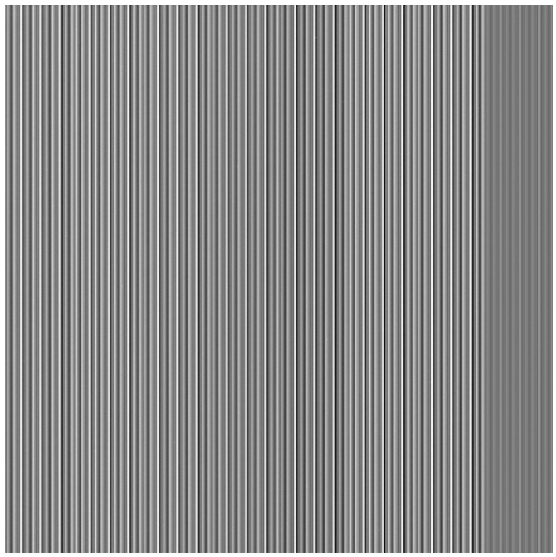

*Figure 7.5 Dark image showing the vertical lines arising from the readout. The eighth readout port (farthest right) is defective.*

While these vertical lines can be suppressed in the signal field through the process of flat-field correction as shown by images of a hand phantom acquired with this system in Figure 7.6, the flat-field correction process cannot eliminate this in the NPS [52].

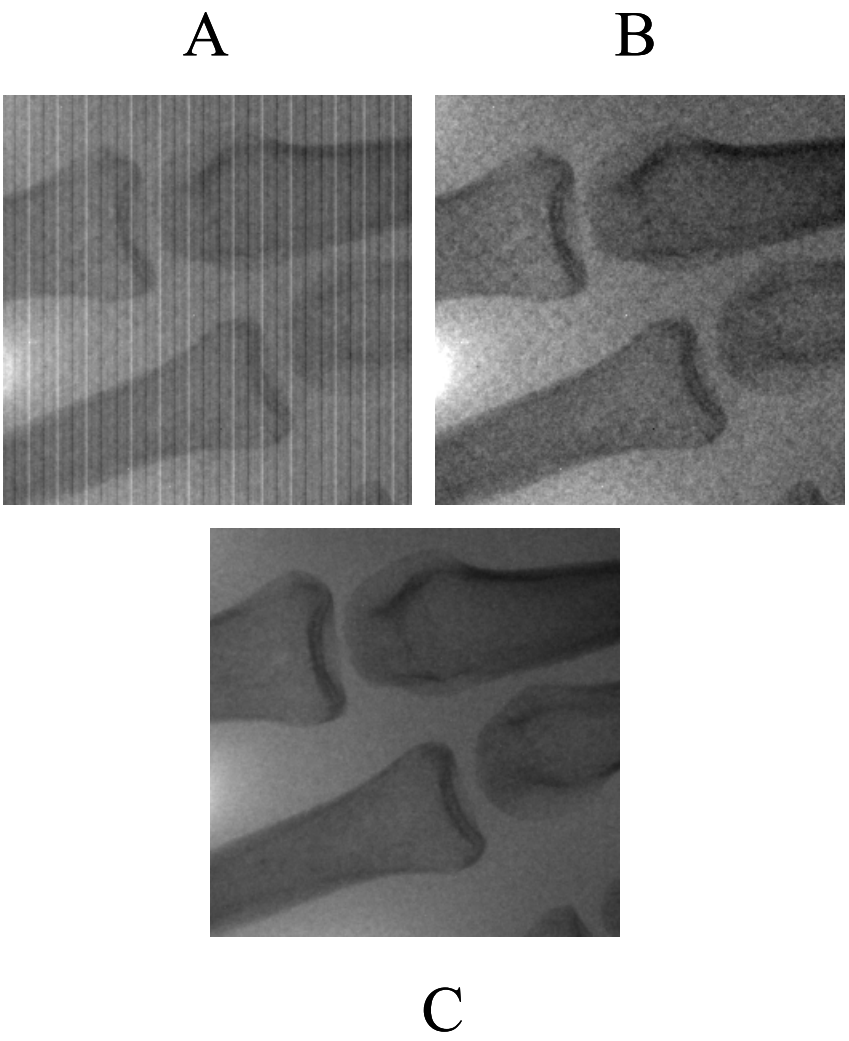


*Figure 7.6 Effect of dark-image subtraction and flat-field correction in signal field. A: Image prior to dark-image subtraction and flat-field correction. B: After dark-image subtraction and prior to flat-field correction. C: After dark-image subtraction and flat-field correction.*

Figure 6.27 showed the 1-D electronic NPS inclusive of the fixed-pattern noise along *u* and *v*-axes. Significant 'spikes' at mid and high spatial frequencies were observed along the *u*-axis and at low spatial frequencies along the *v*-axis. Figure 6.28 showed the 1-D electronic NPS without the structured-noise component along *u* and *v*-axes. The integral of the NPS scaled by the conversion gain indicated electronic noise of 31.5 and 28.2 electrons along *u* and *v*-axis, which is in good agreement with the theoretical predictions. The plot indicates that the NPS is predominantly 'white' (frequency-independent). Also, the NPS along the *u*-axis is slightly elevated in comparison to the NPS along the *v*-axis. The 'spikes' seen in Figure 6.27 are absent in Figure 6.28 indicating that these spikes were due to the structured (fixed-pattern) electronic noise. The structured-noise component along the *u*-axis [$W_E^S(u,0)$] can be estimated by:

$$W_E^S(u,0) = W_E(u,0) - W_E^{NS}(u,0) \qquad 7.2$$

Similarly, the structured-noise along the *v*-axis can also be estimated. Figure 7.7 shows the estimated structured-noise along the *u* and *v*-axes. This plot confirms that the 'spikes' observed in Figure 6.27 at mid and high spatial frequencies along the *u*-axis, and at low spatial frequencies along the *v*-axis, were due to the structured (fixed-pattern) noise. Appropriate changes in the CCD design should be made to eliminate this noise source. Preliminary indications from the manufacturer of the CCD (Fairchild Imaging, Inc., Milpitas, CA) suggest that the source of this noise has been identified and changes in the CCD design could be made to eliminate this noise source.

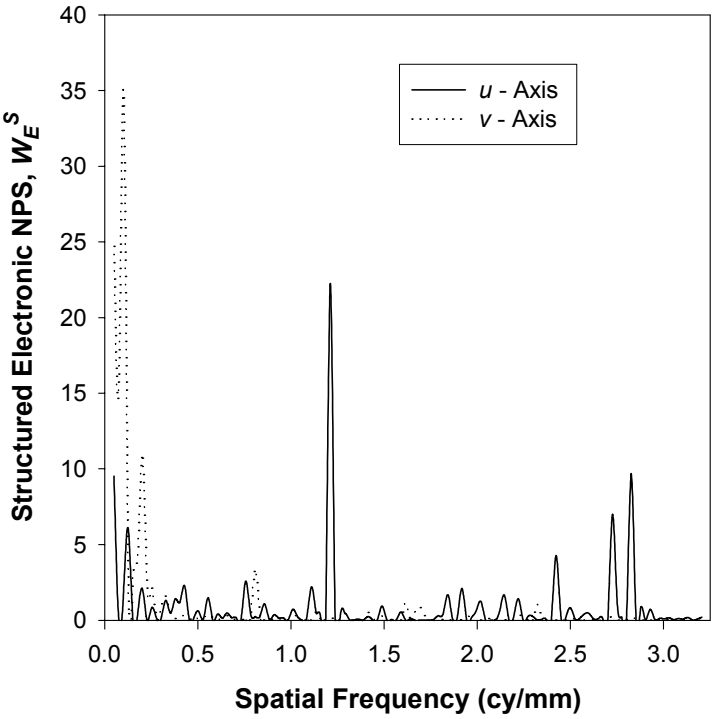


*Figure 7.7 Structured electronic noise along u and v-axes.*

Figure 6.29 showed the 2-D fluoroscopic NPS inclusive of the structured-noise component at four exposure rates. Similar measurement was also performed at 5.25-μR/frame, but is not reported, as there was no additional information. The plots indicate the presence of increased noise along the *u*-axis. Also, anisotropy at the low exposure rates of 0.99-μR/frame was observed. However, with increasing exposure the 2-D NPS indicated improved isotropy. While the source of this anisotropy is yet to be fully understood, one possible source might be the presence of pixel to interline channel cross-talk. Figure 7.8 shows an image of the slit, which indicates that there is spatial

correlation (smearing) along the interline channel indicating pixel to interline channel cross-talk.

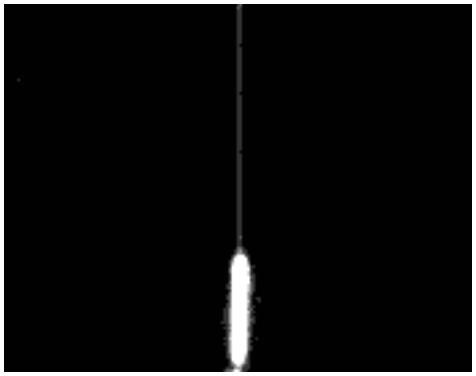

*Figure 7.8 Image of a slit showing the smearing along the interline channel.*

Figure 6.30 showed the 2-D fluoroscopic NPS excluding the structured-noise component. These plots showed that noise source seen along the *u*-axis is absent compared to Figure 6.29, indicative of fixed-pattern noise. Figure 6.31 showed the image lag characteristics of the system. The measured image lag was independent of signal. In image-intensifier-based systems image lag is signal dependent [21], which makes it more difficult to incorporate temporal filtering algorithms. The measured first-frame image lag was 0.9%, which illustrates excellent temporal imaging characteristics in comparison with image-intensifier-based systems, which exhibit a first-frame image lag of 21% at 2.5-μR/frame [21]. Figures 6.32 and 6.33 showed the lag-corrected fluoroscopic NPS along *u* and *v*-axes. The electronic NPS was also plotted, to facilitate direct comparison of electronic and fluoroscopic NPS. It is also of interest to determine the percentage of

the quantum-noise present in the fluoroscopic NPS. This can be determined by subtracting the electronic NPS from the fluoroscopic NPS as shown below.

$$W_X^Q(u,0) = \frac{W_X^{LC}(u,0) - W_E^{NS}(u,0)}{W_X^{LC}(u,0)} \times 100\% \qquad 7.3$$

Figure 7.9 shows the percentage of the quantum-noise present in the fluoroscopic NPS along *u* and *v*-axes. The plots show that more than 95% of the fluoroscopic noise is quantum-noise even at an exposure rate of 0.99-μR/frame, thus providing *strong experimental support* of the *first hypothesis* of quantum-noise-limited operation.

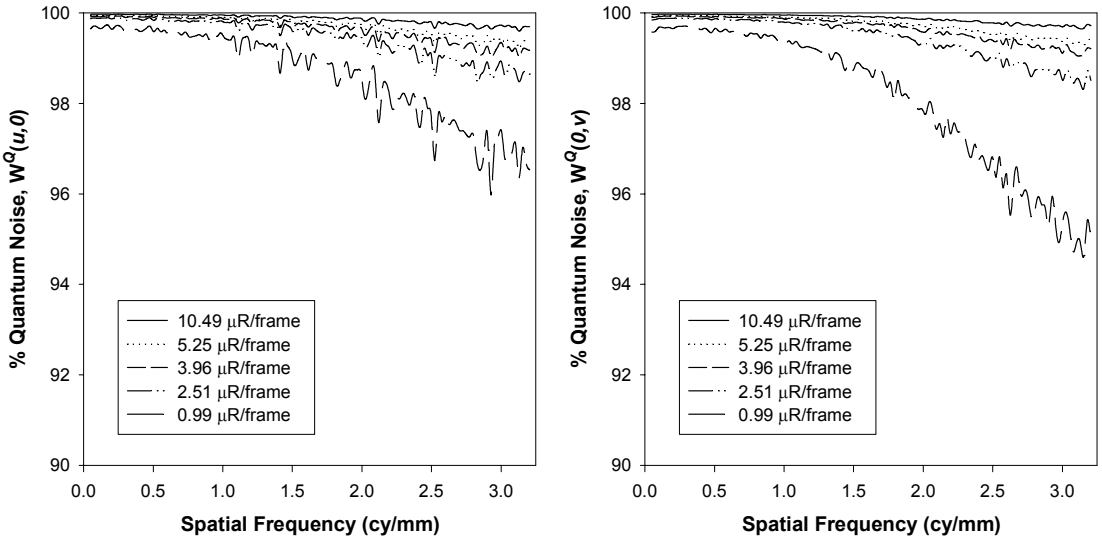


*Figure 7.9 Percentage of the quantum-noise present in the fluoroscopic NPS along u and v-axes.*

Figures 6.34 and 6.35 show the lag-corrected DQE along the *u* and *v*-axes. The plots indicate there was no significant dependence with exposure rate further validating the first hypothesis of quantum-noise-limited operation. The imager exhibited a DQE of

~0.61 at zero frequency and ~0.25 at the Nyquist limit along the *u*-axis. Figure 7.10 shows the comparison of the DQE performance with an image-intensifier-based system [21]. Significant improvement in DQE performance is observed providing *strong experimental support* for the *final hypothesis* of improved DQE.

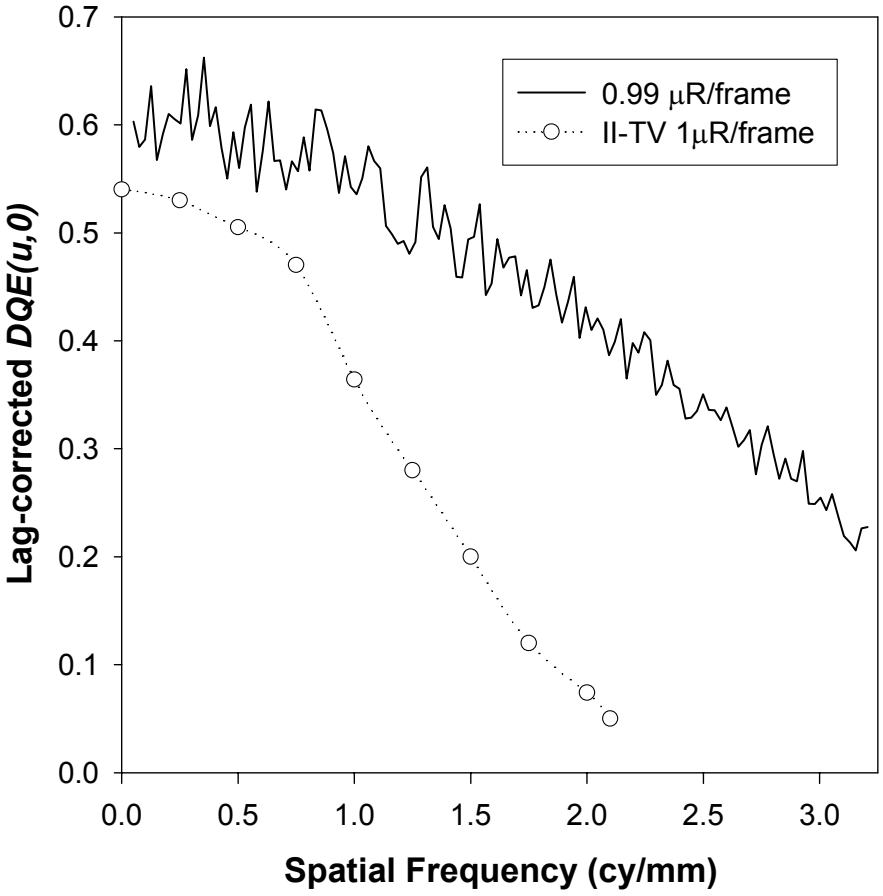


*Figure 7.10 Comparison of the DQE performance of the system with an image-intensifier-based system.*

### *7.5.1. DQE Comparison with Theoretical Models*

Figures 7.11 and 7.12 show the comparison of the measured DQE with the cascaded linear-systems-based models along the *u* and *v*-axes.

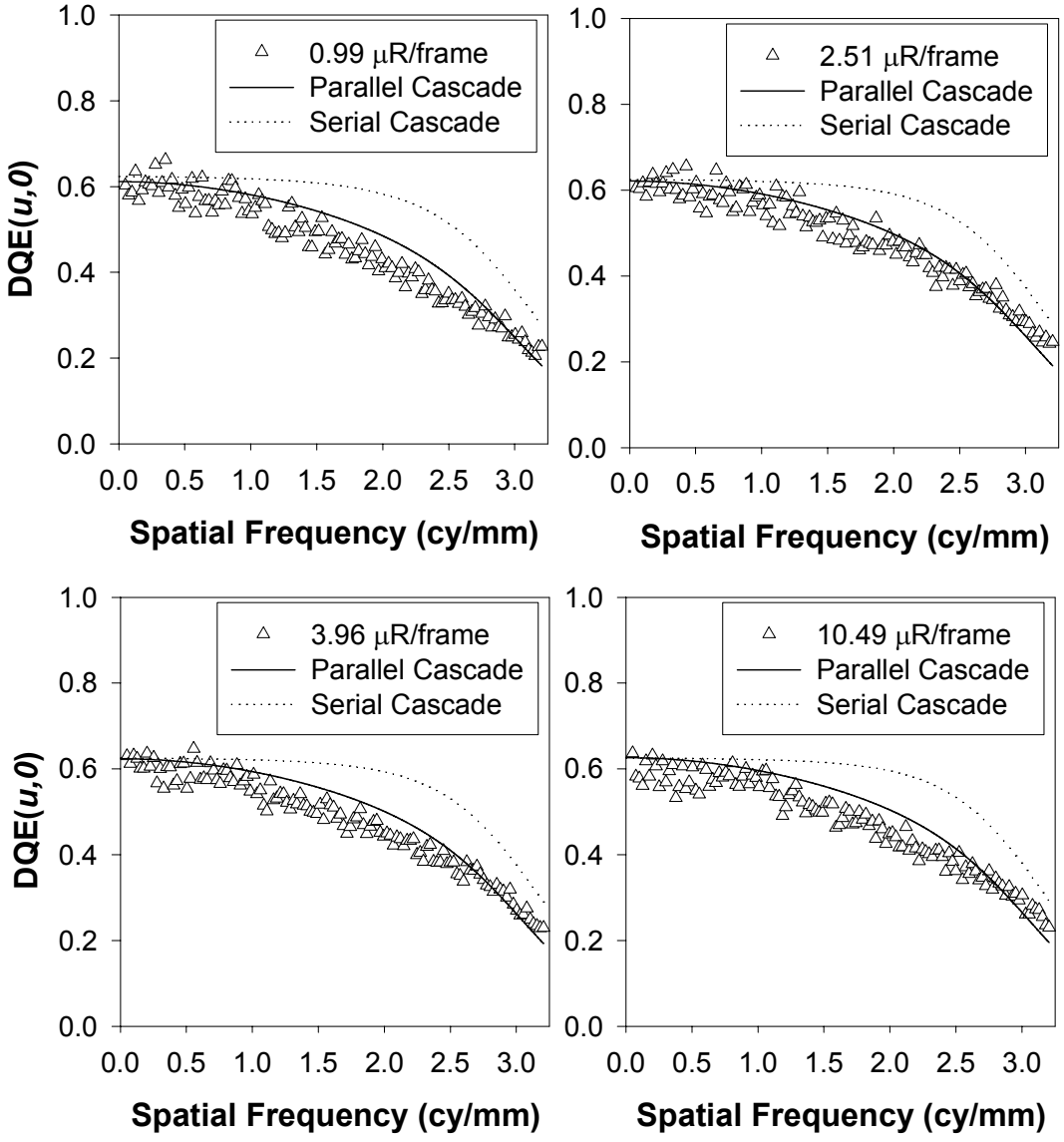


*Figure 7.11 Comparison of the measured DQE with the parallel and serial-cascaded linear-systems-based models along the u-axis.*

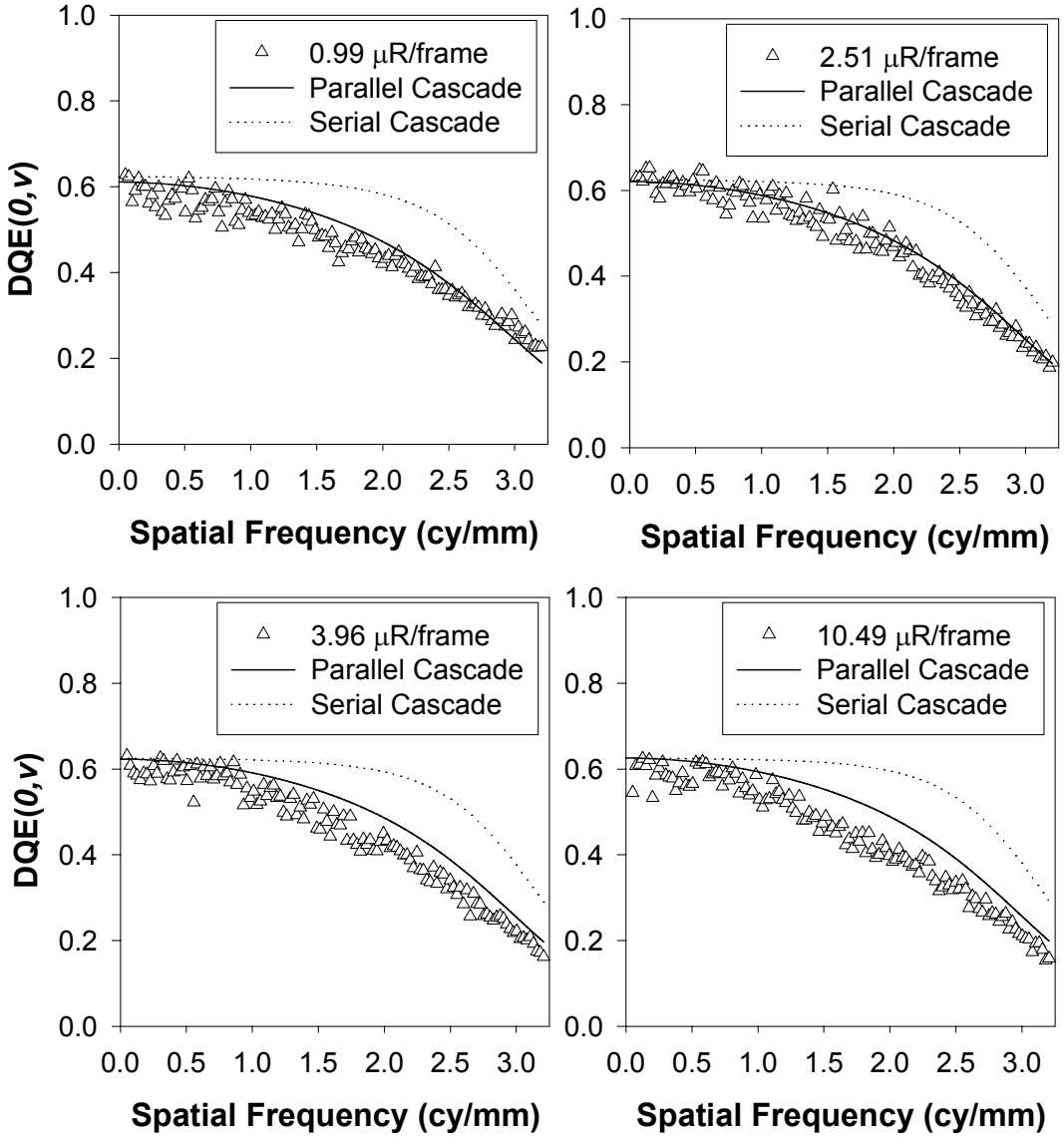


*Figure 7.12 Comparison of the measured DQE with the parallel and serial-cascaded linear-systems-based models along the v-axis.*

The linear-systems model using the parallel cascade for the quantum gain stage predicted the DQE performance better than the serial-cascaded linear-systems model.

## 7.6. QUALITATIVE MEASURES

Figure 6.36 showed an acquired image of the bar-pattern test tool. The image indicates resolvability of at least 3.19 line-pairs (lp)/mm. While 3.54 lp/mm could be resolved, it was affected by aliasing (Nyquist limit: 3.205 cy/mm). Figure 6.37 showed an acquired image of a wire-mesh phantom. The section of the image marked as '30' indicates 30 holes per inch (1.25 lp/mm) and the section of the image marked as '60' indicates 60 holes per inch (2.5 lp/mm). Rarely do image-intensifier-based systems show the ability of resolving greater than 30 holes per inch. Most importantly, the image indicated no apparent distortion and loss of resolution at the periphery, a common problem with image-intensifier-based systems. These images provide *strong experimental support* for the *second hypothesis* that the imager will be free of geometric distortion.

# 8. CONCLUSIONS

Theoretical and experimental results provide strong support for the specific hypotheses stated in chapter 3. Specifically, Table 6.1 and Figure 7.1 support the first hypothesis of improved quantum efficiency and quantum-noise-limited operation, respectively. Figure 6.37 supports the second hypothesis of lack of distortion. Lack of low-frequency drop in Figure 6.24 supports the third hypothesis that the system will be free of veiling glare effects. Comparison of the measured presampling MTF with that of an image-intensifier-based system shown in Figure 7.3 supports the fourth hypothesis of improved spatial resolution. Comparison of the measured DQE with that of an image-intensifier-based system shown in Figure 7.10 supports the fifth hypothesis of improved DQE.

The results demonstrate high and uniform spatial resolution at 30 fps fluoroscopy, while preserving and potentially improving on the DQE performance than that currently afforded by image-intensifier-based fluoroscopic systems. Results from DQE and image lag measurements at fluoroscopic exposure rates combined with the high spatial resolution observed from the measured presampling MTF provide strong support for potential adaptation of this type of imager for the low-dose requirements of cardiovascular and the low-lag, high-spatial resolution requirements of pediatric angiography.

# 9. FUTURE WORK

The future work is broadly classified into three sections, improving the design of the imager, improving the theoretical model, and additional experiments to be performed.

## 9.1. IMPROVING IMAGER DESIGN

While the imager showed excellent noise-performance characteristics, two sources of concern addressed below should be addressed. The noise arising from the readout that manifests as vertical lines seen in Figure 7.5 needs to be identified and eliminated. Preliminary indications from the manufacturer of the CCD (Fairchild Imaging, Inc., Milpitas, CA) suggest that the source of this noise has been identified and changes in the CCD design could be made to eliminate this noise source. The source of the pixel to interline channel cross-talk observed in Figure 7.8, which could be the source of anisotropy of the NPS at low exposure rates, needs to be identified and rectified. A four-module imager with these noise sources rectified should be manufactured, so that appropriate seam correction algorithm can be implemented. While one such algorithm was investigated in this work, several such algorithms have been published [76] and the effectiveness, suitability, and impact on image quality of these algorithms needs to be studied. While the DQE and MTF performance of the imager showed desirable characteristics, further optimization of the CsI:Tl thickness needs to be achieved such that optimal performance for the intended task can be attained.

## 9.2. IMPROVING THE MODEL

The parallel-cascaded linear-system-based model showed good agreement with theory and could serve as a valuable tool for improving the imager design such that optimal performance can be achieved. Appropriate Monte-Carlo simulation techniques need to be incorporated into the model to theoretically estimate the fraction of K-fluorescent x-rays reabsorbed by the CsI:Tl and the stochastic blur caused by this reabsorption process. While the model at present makes use of published results [83], incorporation of a similar Monte-Carlo simulation would provide the flexibility to investigate the potential performance of the imager for various system design parameters such as CsI:Tl thickness. Currently, the laboratory is in the process of acquiring appropriate Monte-Carlo simulation package. Further, the model can be expanded to include a task-specific approach to optimize the system design.

## 9.3. ADDITIONAL EXPERIMENTATION

Scintillator blur measurements of thicker (> 525-μm) CsI:Tl need to be performed, so that they could be incorporated into the theoretical model. Once an optimal design has been achieved through the theoretical model, and such an imager manufactured, experimental confirmation of the predicted performance through objective metrics such as presampling MTF, NPS and DQE need to be performed. Upon achievement of the desired performance of these objective metrics, task-dependent

quantitative performance parameters such as threshold contrast-detail characteristics, for static and dynamic objects need to be performed. The imager upon completion of these studies needs to incorporated into a clinical system, so that clinical trials can be performed.

## REFERENCES


1. R.A. Geise, N.E. Peters, A. Dunnigan and S. Milstein, "Radiation doses during pediatric radiofrequency catheter ablation procedures," PACE 19, 1605-1611 (1996).
2. D. Aliabadi, M.C. Pica, P.A. McCullough, C.L. Grines, R.D. Safian, W.W. O'Neill and J.A. Goldstein, "Rapid bedside coronary angiography with a portable fluoroscopic imaging system," Catheter and Cardiovascular Diagnosis 41, 449-455 (1997).
3. I. Langmuir, U.S. Patent No. 2,198,479 granted on April 23, 1940.
4. J.W. Coltman, "Fluoroscopic Image Brightening by Electronic Means," Radiology 51, 359-367 (1948).
5. W. Putten and S. Bouley, "Performance evaluation of Image-intensifier-TV Fluoroscopic Systems," Proc. SPIE 2432, 376-383 (1995).
6. G. Spekowius, H. Boerner, W. Eckenbach and P. Quadfleig, "Simulation of the imaging performance of x-ray image-intensifier/TV camera chains," Proc. SPIE 2432, 12-23 (1995).
7. H. Blume, J. Colditz, W. Eckenbach, P. Hoen, J. Meijer, R.M. Snoeren, W.E. Spaak and G. Spekowius, "Image-intensifier and X-ray Exposure Control Systems," RSNA categorical course in Physics, 87-103 (1995).
8. R.A. Close, K.C. Shah and J.S. Whitting, "Regularized method for scatter-glare correction in fluoroscopic images," Med. Phys. 26(9), 1794-1801 (1999).

9. J.M. Boone, J.A. Seibert, W.A. Barrett and E.A. Blood, "Analysis and correction of imperfections in the image-intensifier-TV-digitizer imaging chain," Med. Phys. 18(2), 236-242 (1991).
10. R.R. Liu, S. Rudin and D.R. Bednarek, "Super-global distortion correction for a rotational C-arm x-ray image-intensifier," Med. Phys. 26(9), 1802-1810 (1999).
11. H. Liu, H. Jiang, L.L. Fajardo, A. Karellas and W. Chen, "Lens distortion in optically coupled digital x-ray imaging," Med. Phys. 27(5), 906-912 (2000).
12. P.M. DeGroot, "Image-intensifier Design and Specifications," Med. Phys. Mono. 20, 429-460 (1994).
13. R.J. Moore, *Imaging Principles of Cardiac Angiography*, Aspen Publishers (1990).
14. U.S. Food and Drug Administration. FDA public health advisory: Avoidance of serious x-ray induced skin injuries to patients during fluoroscopically-guided procedures. September 30, 1994.
15. L.K. Wagner, P.J. Eifel and R.A. Geise, "Potential Biological Effects following High X-ray Dose Interventional Procedures," Journal of Vascular Interventional Radiology, 71-84 (1994).
16. W. Huda and K.R. Peters, "Radiation-induced Temporary Epilation after a Neuro-radiologically Guided Embolization Procedure," Radiology, 642-644 (1994).
17. L. Dehen, C. Vilmer, C. Humiliere, T. Corcos, D. Pentousis, L. Ollivaud, D. Chatelain and L. Dubertret, "Chronic radiodermatitis following cardiac catheterisation: a report of two cases and a brief review of literature," Heart 81, 308-312 (1999).

18. J.T. Cusma, M.R. Bell, M.A. Wondrow, J.P. Taubel and D.R. Holmes, "Real-time Measurement of Radiation Exposure to Patients during Diagnostic Coronary Angiography and Percutaneous Interventional Procedures," Journal of American College of Cardiology 33(2), 427-435 (1999).
19. B. Kazan, "A solid-state amplifying fluoroscope screen," American Journal of Roentgenology 79, 709-719 (1958).
20. L.E. Antonuk, J. Yorkston and W. Huang, "A Real Time, Flat-panel, Amorphous Silicon, Digital X-ray Imager," Radiographics 15, 993-1000 (1995).
21. P.R. Granfors, "Performance characteristics of an Amorphous Silicon Flat Panel X-ray Imaging Detector," Proc. SPIE 3659, 480-490 (1999).
22. W. Zhao, I. Blevis, S. Germann, J.A. Rowlands, D. Waechter and Z. Huang, "Digital radiology using active matrix readout of amorphous selenium: construction and evaluation of a prototype real-time detector," Med. Phys. 24(12), 1834-1843 (1997).
23. A. Tsukamoto, S. Yamada, T. Tomisaki, M. Tanaka, T. Sakaguchi, H. Asahina and M. Nishiki, "Development of a selenium-based flat-panel detector for real-time radiography and fluoroscopy," Proc. SPIE 3336, 388-395 (1998).
24. P.J. Papin and H.K. Huang, "A prototype amorphous selenium imaging plate system for digital radiography," Med. Phys. 14, 322-329 (1987).
25. U. Neitzel, I. Maack and S. Gunther-Kohfahl, "Image quality of a digital chest radiography system based on a selenium detector," Med. Phys. 21, 509-516 (1994).
26. W. Que and J.A. Rowlands, "X-ray imaging using amorphous selenium: inherent spatial resolution." Med. Phys. 22, 365-374 (1995).

27. J.A. Rowlands, W.G. Ji, W. Zhao and D.L. Lee, "Direct-conversion flat-panel x-ray imaging: reduction of noise by presampling filtration," *Proc. SPIE* 3977, 446-455 (2000).

28. A. Karellas, L.J. Harris, H. Liu, M.A. Davis and C.J. D'Orsi, "Charge-coupled device detector: Performance considerations and potential for small-field mammographic imaging applications," Med. Phys. 19(4), 1015-1023 (1992).

29. H. Liu, A. Karellas, L.J. Harris and C.J. D'Orsi, "Methods to calculate the lens efficiency in optically coupled CCD x-ray imaging systems," Med. Phys. 21(7), 1193-1195 (1994).

30. A.D.A. Maidment and M.J. Yaffe, "Analysis of the spatial-frequency-dependent DQE of optically coupled mammography detectors", Med. Phys. 21(6), 721-729 (1994).

31. S. Hejazi and D.P. Trauernicht, "System considerations in CCD-based x-ray imaging for digital chest radiography and digital mammography," Med. Phys. 24(2), 287-297 (1997).

32. S. Thunberg, H. Sklebitz, B. Ekdahl, L. Batz, A. Lundin, H. Moller, F. Fleischmann, G. Kreider and T. Weidner, "OPDIMA: Large-area CCD-based X-ray image sensor for spot imaging and biopsy control in mammography," Proc. SPIE 3659, 150-158 (1999).

33. S. Vedantham, A. Karellas, S. Suryanarayanan, I. Levis, M. Sayag, R. Kleehammer, R. Heidsieck and C.J. D'Orsi, "Mammographic imaging with a small format CCD-

based digital cassette: Physical characteristics of a clinical system," Med. Phys. 27(8), 1832-1840 (2000).

34. J.H. Siewerdsen, L.E. Antonuk, Y. El-Mohri, J. Yorkston, W. Huang, J.M. Boudry and I.A. Cunningham, "Empirical and theoretical investigation of the noise performance of indirect detection, active matrix flat-panel imagers (AMFPIs) for diagnostic radiology," Med. Phys. 24(1), 71-89 (1997).
35. J.P. Bissonette, I.A. Cunningham, D.A. Jaffray, A. Fenster and P. Munro, "A quantum accounting and detective quantum efficiency analysis for video-based portal imaging," Med. Phys. 24(6), 815-826 (1997).
36. W. Zhao and J.A. Rowlands, "Digital radiology using active matrix readout of amorphous selenium: theoretical analysis of detective quantum efficiency," Med. Phys. 24(12), 1819-1833 (1997).
37. J.H. Siewerdsen, L.E. Antonuk, Y. El-Mohri, J. Yorkston, W. Huang, and I.A. Cunningham, "Signal, noise power spectrum and detective quantum efficiency of indirect-detection flat-panel imagers for diagnostic radiology," Med. Phys. 25(5), 614-628 (1998).
38. G.M. Jenkins and D.G. Watts, *Spectral analysis and its applications* (Holden-Day, San Francisco, 1968).
39. J.C. Dainty and R. Shaw, *Image Science* (Academic, New York, 1974).
40. A. Papoulis, *Probability, Random Variables, and Stochastic Processes*, 3rd ed., (McGraw-Hill, New York, 1991).

41. “Medical Imaging – the assessment of image quality,” ICRU Report No. 54 (International Commission of Radiation Units and Measurements, Bethesda, Maryland, 1995).
42. M.J. Tapiovaara and R.F. Wagner, “SNR and DQE analysis of broad spectrum x-ray imaging,” Phys. Med. Biol. 30, 519-529 (1985).
43. C.E. Metz and K. Doi, “Transfer function analysis of radiographic imaging systems,” Phys. Med. Biol. 24, 1079-1106 (1979).
44. H.H. Barrett and W. Swindell, *Radiological Imaging – The Theory of Image Formation, Detection and Processing*, Revised Ed. (Academic Press, New York, 1981).
45. M. Rabbani, R. Shaw and R. Van Metter, “Detective quantum efficiency of imaging systems with amplifying and scattering mechanisms,” J. Opt. Sci. Am. A 4, 895-901 (1987).
46. M. Rabbani and R. Van Metter, “Analysis of signal and noise propagation for several imaging mechanisms,” J. Opt. Sci. Am. A **7**, 1156-1164 (1989).
47. I.A. Cunningham, M.S. Westmore and A. Fenster, “A spatial frequency-dependent quantum accounting diagram and detective quantum efficiency model of signal and noise propagation in cascaded imaging systems,” Med. Phys. 21(3), 417-427 (1994).
48. I.A. Cunningham, “Linear-systems Modeling of Parallel-cascaded Stochastic Processes: The NPS of Radiographic Screens with Reabsorption of Characteristic X Radiation,” Proc. SPIE 3336, Medical Imaging 1998: Physics of Medical Imaging, 220-230 (1998).

49. I.A. Cunningham, "Applied linear-systems theory," in *Handbook of Medical Imaging, Vol. 1: Physics and Psychophysics*, editors J. Beutel, H.L. Kundel and R. Van Metter (SPIE Press, Bellingham, 2000), pp. 79-160.

50. I.A. Cunningham, T. Moschandreou and V. Subotic, "The Detective Quantum Efficiency of Fluoroscopic Systems: The Case for a Spatial-Temporal Approach (Or, Does the Ideal Observer have Infinite Patience?)," Proc. SPIE 4320, Medical Imaging 2001: Physics of Medical Imaging, 479-488 (2001).

51. S. Vedantham, A. Karellas, S. Suryanarayanan, D. Albagli, S. Han, E.J. Tkaczyk, C.E. Landberg, B. Opsahl-Ong, P.R. Granfors, I. Levis, C.J. D'Orsi and R.E. Hendrick, "Full breast digital mammography with an amorphous silicon-based flat panel detector: Physical characteristics of a clinical prototype," Med. Phys. 27(3), 558-567 (2000).

52. S. Vedantham, A. Karellas, S. Suryanarayanan, C.J. D'Orsi, and R.E. Hendrick, "Breast Imaging using an Amorphous Silicon based Full-Field Digital Mammographic System: Stability of a clinical prototype," J Digital Imaging 13(4), 1191-1199 (2000).

53. P.R. Granfors and R. Aufrichtig, "Performance of a 41 x 41-$cm^2$ amorphous silicon flat-panel x-ray detector for radiographic imaging applications," Med. Phys. 27(6), 1324-1331 (2000).

54. T. Jing, C.A. Goodman, G. Cho, J. Drewery, W.S. Hong, H. Lee, S.N. Kaplan, A. Mireshghi, V. Perez-Mendez and D. Wildermuth, "Amorphous Silicon Pixel Layers

with Cesium Iodide Converters for Medical Radiography," IEEE Nuclear Science Symposium, San Francisco, California, November 2-5 (1993).

55. The Institute of Physics and Engineering in Medicine (IPEM), *Catalogue of Diagnostic X-ray Spectra and other Data*, CD-ROM, Report No. 78 (The Institute of Physics and Engineering in Medicine, United Kingdom, 1997).
56. J.H. Hubbell and S.M. Seltzer, *Tables of X-ray Mass Attenuation Coefficients and Mass-Energy Absorption Coefficients*, Physics Reference Data, (National Institutes of Standards and Technology, Gaithersburg, Maryland, 1996).
57. I. Holl, E. Lorenz and G. Mageras, "A Measurement of Light Yield of Common Inorganic Scintillators," IEEE Transactions on Nuclear Science 35(1), 105-109 (1988).
58. V. Perez-Mendez, G. Cho, J. Drewery, T. Jing, S.N. Kaplan, A. Mireshghi and D. Wildermuth, "Amorphous Silicon pixel radiation detectors and associated thin film transistor electronics readout," Lawrence Berkeley Lab Publication No. 32460.
59. J.A. Rowlands and K.W. Taylor, "Absorption and noise in cesium iodide x-ray image-intensifiers," Med. Phys. 10(6), 786-795 (1983).
60. D.R. Dance and G.J. Day, "Escape probabilities for fluorescent x-rays," Phys. Med. Biol. 30(3), 259-262 (1985).
61. R.K. Swank, "Absorption and noise in x-ray phosphors." J. Appl. Phys. 44(9), 4199-4203 (1973).
62. A.R. Lubinsky, J.F. Owen and D.M. Korn, "Storage phosphor system for computed radiography: screen optics," Proc. SPIE 626, 120-132 (1986).

63. T. Radcliffe, G. Barnea, B. Wowk, R. Rajapakshe and S. Shalev, "Monte-Carlo optimization of metal/phosphor screens at megavoltage energies," Med. Phys. 20(4), 1161-1169 (1993).

64. J.M. Sabol and J.M. Boone, "Monte-Carlo simulation of photon transport within a hybrid grid-detector system for digital mammography," Proc. SPIE 3032, 266-274 (1997).

65. W. Hillen, W. Eckenbach, P. Quadfleig and T. Zaengel, "Signal-to-noise performance in Cesium Iodide X-ray fluorescent screens," Proc. SPIE 1443, 120-131 (1991).

66. H. Fujita, D.Y. Tsai, T. Itoh, K. Doi, J. Morishita, K. Ueda and A. Ohtsuka, "A simple method for determining the modulation transfer function in digital radiography," IEEE Transactions on Medical Imaging MI-11, 34-39 (1992).

67. J.R. Janesick, T. Elliot and F. Pool, "Radiation damage in scientific charge coupled devices," IEEE Transactions on Nuclear Science 36(1), (1989).

68. P. Acton, G. Agnew, R. Cotton, S. Hedges, A.K. McKemey, M. Robbins, T. Roy and S.J. Watts, "Future potential of charge coupled devices as detectors of ionizing radiation," Nuclear Instruments and Methods in Physics Research A305, 504-511 (1991).

69. D.J. Burt, "Development of x-ray CCDs," Proc. ESA symposium on Photon Detectors for Space Instrumentation, ESA/ESTEC, Noordwijk, The Netherlands, November 10-12, 1992.

70. I. Levis, S. Vedantham and A. Karellas, "Attenuation characteristics of fiberoptic plates for digital mammography and other x-ray imaging applications," Med. Phys. 25(7), A110 (1998).

71. J.R. Janesick, *Scientific Charge-Coupled Devices*. (SPIE Press, 2001).

72. H. Ott, *Noise Reduction Techniques in Electronic Systems*. (John Wiley and Sons, 1976).

73. M.J. Yaffe and J.A. Rowlands, "X-ray detectors for digital radiography," Phys. Med. Biol. 42(1), 1-39 (1997).

74. A. Rose, "The sensitivity performance of the eye on an absolute scale," J. Opt. Soc. Am. 38, 196 (1948).

75. M.B. Williams, P.U. Simoni, L. Smilowitz, M. Stanton, W. Phillips and A. Stewart, "Analysis of the detective quantum efficiency of a developmental detector for digital mammography," Med. Phys. 26(11), 2273-2285 (1999).

76. H. Liu, G. Wang, J. Chen and L.L. Fajardo, "Interpolation algorithms for digital mammography systems with multiple detectors," Acad. Radiol. 6(3), 170-175 (1999).

77. H.E. Johns and J.R. Cunningham, *The Physics of Radiology*, 4$^{th}$ Ed., C.C. Thomas Publisher, Springfield, Illinois, 1983.

78. J.T. Dobbins, D.L. Ergun, L. Rutz, D.A. Hinshaw, H. Blume and D.C. Clark, "DQE(f) of four generation of computed radiography acquisition devices," Med. Phys. 22(10), 1581-1593 (1995).

79. J.D. Valentine, W.W. Moses, S.E. Derenzo, D.K. Wehe and G.F. Knoll, "Temperature Dependence of CsI(Tl) Gamma-ray Excited Scintillation Characterisitics," Nucl. Instrum. Meth. A325, 147-157 (1993).

80. Y. Matsunaga, F. Hatori, T. Hiroyuki and O. Yoshida, "Analysis of signal to noise ratio of photoconductive layered solid-state imaging device," IEEE Trans. Electron Devices 42, 38-42 (1995).

81. J. Yao and I.A. Cunningham, "Parallel Cascades: New ways to describe noise transfer in medical imaging systems," Med. Phys. 28(10), 2020-2038 (2001).

82. W. Zhao, W.G. Ji and J.A. Rowlands, "Effects of characteristic x-rays on the noise power spectra and detective quantum efficiency of photoconductive x-ray detectors," Med. Phys. 28(10), 2039-2049 (2001).

83. J.M. Boone, J.A. Seibert, J.M. Sabol and M. Tecotzky, "A Monte-Carlo study of x-ray fluorescence in x-ray detectors," Med. Phys. 26, 905-916 (1999).

84. Data sheet for AD9814 – Complete 14-Bit CCD/CIS Signal Processor. (Analog Devices, Inc., Norwood, MA, 1999).

85. P.R. Granfors, D. Albagli, E.J. Tkaczyk, R. Aufrichtig, H. Netel, G. Brunst, J.M. Boudry and D. Luo, "Performance of a flat-panel cardiac detector," Proc. SPIE 4320, 77-86 (2001).

86. H. Blume, J. Colditz, W. Eckenbach, P. Hoen, J. Meijer, R.M. Snoeren, W.E. Spaak, and G. Spekowius, "Image-intensifier and X-ray Exposure Control Systems", RSNA categorical course in Physics, 87-103 (1995).

## APPENDIX: SELECT PUBLICATIONS

- S. Vedantham, A. Karellas, S. Suryanarayanan, D. Albagli, S. Han, E.J. Tkaczyk, C.E. Landberg, B. Opsahl-Ong, P.R. Granfors, I. Levis, C.J. D'Orsi and R.E. Hendrick, "Full breast digital mammography with an amorphous silicon-based flat panel detector: Physical characteristics of a clinical prototype," Med. Phys. 27(3), 558-567 (2000) [Included with permission from the Medical Physics Journal, © 2000 American Association of Physicists in Medicine].

- S. Vedantham, A. Karellas, S. Suryanarayanan, I. Levis, M. Sayag, R. Kleehammer, R. Heidsieck and C.J. D'Orsi, "Mammographic imaging with a small format CCD-based digital cassette: Physical characteristics of a clinical system," Med. Phys. 27(8), 1832-1840 (2000) [Included with permission from the Medical Physics Journal, © 2000 American Association of Physicists in Medicine].

# Full breast digital mammography with an amorphous silicon-based flat panel detector: Physical characteristics of a clinical prototype

Srinivasan Vedantham, Andrew Karellas,[a] and Sankararaman Suryanarayanan
*Department of Radiology, UMass Memorial Health Care, University of Massachusetts Medical School, Worcester, Massachusetts 01655*

Douglas Albagli, Sung Han, Eric J. Tkaczyk, Cynthia E. Landberg, and Beale Opsahl-Ong
*G. E. Corporate Research and Development, Niskayuna, New York 12309*

Paul R. Granfors
*G. E. Medical Systems, Milwaukee, Wisconsin 53201*

Ilias Levis and Carl J. D'Orsi
*Department of Radiology, UMass Memorial Health Care, University of Massachusetts Medical School, Worcester, Massachusetts 01655*

R. Edward Hendrick[b]
*Radiology Department, University of Colorado Health Science Center, Denver, Colorado 80262*

(Received 28 June 1999; accepted for publication 28 December 1999)

The physical characteristics of a clinical prototype amorphous silicon-based flat panel imager for full-breast digital mammography have been investigated. The imager employs a thin thallium doped CsI scintillator on an amorphous silicon matrix of detector elements with a pixel pitch of 100 $\mu$m. Objective criteria such as modulation transfer function (MTF), noise power spectrum, detective quantum efficiency (DQE), and noise equivalent quanta were employed for this evaluation. The presampling MTF was found to be 0.73, 0.42, and 0.28 at 2, 4, and 5 cycles/mm, respectively. The measured DQE of the current prototype utilizing a 28 kVp, Mo–Mo spectrum beam hardened with 4.5 cm Lucite is ~55% at close to zero spatial frequency at an exposure of 32.8 mR, and decreases to ~40% at a low exposure of 1.3 mR. Detector element nonuniformity and electronic gain variations were not significant after appropriate calibration and software corrections. The response of the imager was linear and did not exhibit signal saturation under tested exposure conditions. © *2000 American Association of Physicists in Medicine.* [S0094-2405(00)01803-4]

Key words: breast imaging, digital mammography, physics, image quality, detective quantum efficiency (DQE)

## I. INTRODUCTION

The physical aspects of mammography have been the subject of many investigations which have addressed basic imaging characteristics such as x-ray scatter,[1–4] x-ray tube focal spot effects,[5] and x-ray spectra.[6,7] This knowledge has served as the basis for many technical improvements and regulatory standards of performance.[8]

Though film-screen mammography is currently the standard in breast imaging, it has well-known limitations with regard to dynamic range, contrast, and lack of convenient options for postprocessing of images. It is apparent that electronic detection has the theoretical capability of overcoming certain fundamental limitations of film-screen systems. The potential advantages of electronic detection include high detection efficiency, high dynamic range, capability of contrast enhancement,[9] and postprocessing capabilities including computer-aided diagnosis.[10–15] Further, direct electronic acquisition enables the exploration of novel imaging techniques such as tomosynthesis,[16,17] dual-energy mammography,[18,19] and digital subtraction imaging.[20] In the past, investigators have used different modes of electronic detection technology to gain insight into electronic mammography, commonly referred to as digital mammography.[21] Early evaluations have used image intensifiers and subsequently slot-scanned systems[22,23] with charge-coupled devices (CCDs) and CCDs with fiberoptic tapers.[24] Development of an electronic detector to cover the entire breast presents a formidable technical challenge. Currently, digital mammography is limited to small field devices for stereotactic localization, core biopsy, and spot compression views.[24,25] It is now feasible to manufacture large flat panel monolithic arrays of amorphous silicon photodiodes coupled to thin-film transistors on a glass substrate. These arrays utilize a scintillator as the primary detection layer to convert x rays to light, which is subsequently detected by the photosensing silicon elements. Several studies characterizing amorphous silicon[26–30] and amorphous selenium[31,32] based imagers for chest radiography and other applications have been reported in the recent past. However, detailed experimental characterization of amorphous silicon based flat panel imagers under realistic mammographic conditions have not been reported in the past.

This study characterizes the image quality parameters of

TABLE I. Amorphous silicon-based flat panel detector specifications.

| | |
|---|---|
| Flat panel image area | 18 cm×23 cm |
| Pixel matrix | 1800×2304 |
| Pixel size | 100 $\mu$m |
| Scintillator | CsI:T1 |

an amorphous silicon-based clinical prototype flat panel imager (GE Medical Systems, Milwaukee, WI) presently undergoing technical and clinical evaluation at the University of Massachusetts Medical School and the University of Colorado Health Sciences Center.

## II. METHODS AND MATERIALS

The full-breast digital mammography imager characterized in this study is composed of a thallium-doped CsI scintillator and an amorphous silicon photodiode array and incorporates special-purpose readout electronics. Light created from the interaction of x-ray photons in the scintillator travels down the columnar crystalline structure of the scintillator, which is in contact with a two-dimensional array of amorphous silicon photodiodes and thin-film transistors. Light exiting from the scintillator is detected by the monolithic thin film flat panel array, which consists of a matrix of 1800 ×2304 detector elements that are 100 $\mu$m in pitch. The specifications of the mammographic flat panel imager are presented in Table I. Each detector element (pixel) in the array is an individually addressable light detector. The electrical signals of all pixels are individually read out and digitized to 16 bit digital values in 300 ms by special-purpose low-noise electronics[33] which are located inside the image receptor assembly. The schematic of the detector is shown in Fig. 1. The imager is integrated into a prototype digital mammography system based on a multipulse high frequency x-ray generator (Senographe DMR, GE Medical Systems, Milwaukee, WI). This system uses a selectable dual track target, either molybdenum (Mo) or rhodium (Rh) with selectable filtration of Mo or Rh. All measurements were performed at 28 kVp with a Mo/Mo target/filter combination. This particular technique was chosen as it was found to be the median exposure technique used in a random sample of 100 breast exams from a population of 1400 patients performed with this flat panel imager.

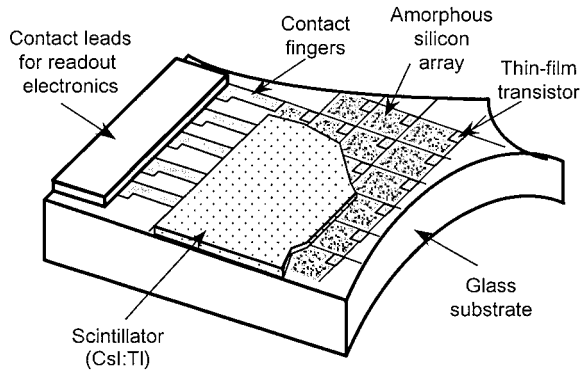


FIG. 1. Schematic of the amorphous silicon detector array.

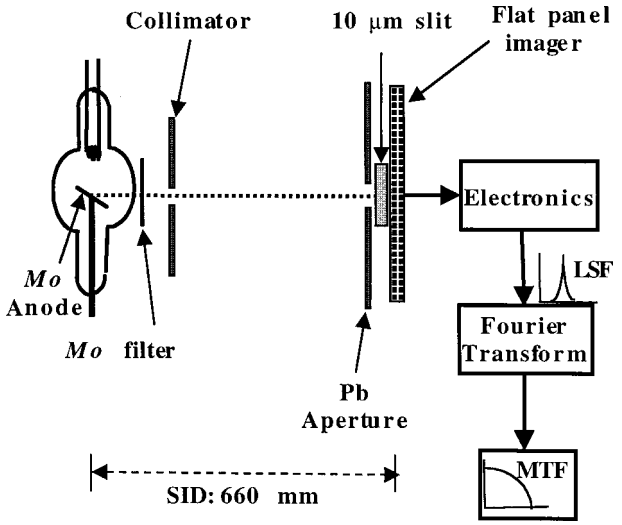


FIG. 2. Experimental setup for MTF measurement. The area surrounding the 10 $\mu$m slit was covered with Pb (0.5 cm thick).

### A. Presampling modulation transfer function measurement

The presampling modulation transfer function (MTF) was measured according to the technique described by Fujita *et al.*[34] The experimental procedure for measuring the same has also been described in detail by Dobbins *et al.*[35] The effects of undersampling have also been described in detail by Dobbins.[36] The experimental setup is shown in Fig. 2. An image of a 10-mm-long, 10 $\mu$m ($\pm$1 $\mu$m) slit made of 1.5-mm-thick tantalum placed at a slight angle (less than 4°) to the anode–cathode axis at the center of the detector was obtained. The area around the slit was covered with Pb (0.5 cm thick). The slit was placed about 5.5 mm (due to thickness of the breast support plate and the slit housing) from the surface of the imager. Since the magnification of the slit was about 1.0083, there was no appreciable spreading of the line spread function (LSF) due to focal spot blurring. The exposure technique was adjusted to ensure that the tails of the dark image subtracted LSF obtained had no significant electronic noise. The appropriate technique found to be 28 kVp, 160 mAs was used. The source-to-image distance was maintained at 660 mm during the study. The image of the slit was obtained without the antiscatter grid in place. The slit image obtained was corrected for variations along the edge of the slit. This was accomplished by normalizing the signal values along the horizontal direction (perpendicular to the anode–cathode axis) by dividing each pixel value by the sum of the pixel values in that particular row as illustrated in Fig. 3. This normalization method assumes that the slit width is approximately constant over the length used for obtaining the finely sampled LSF and that the signal spreading is approximately equal along each line of data. The validity of these assumptions was verified by calculating the MTF from sev-

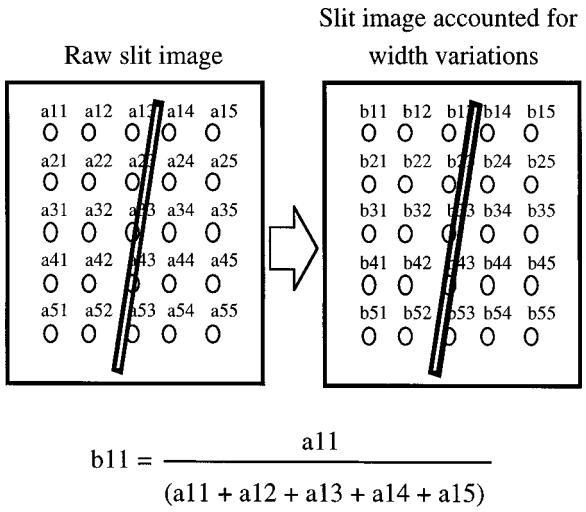


FIG. 3. Illustration of slit image correction for variations in slit width.

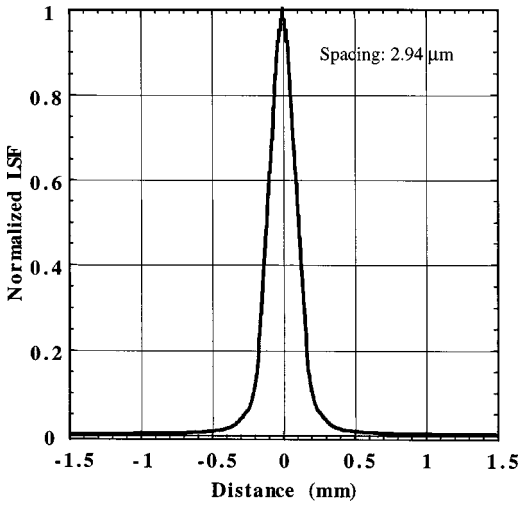


FIG. 5. Finely sampled LSF.

eral locations along the central region of the slit, and the MTF was found to vary by less than 1%. Before performing this normalization care was taken to avoid loss of information due to truncation by converting the pixel intensity values to 32 bit floating point numbers. The pixel amplitudes along the column or vertical direction (along the anode–cathode axis) were plotted as shown in Fig. 4. This provided the adequate number of individual LSFs needed to obtain a finely sampled LSF. Since each pixel represented a sample of the LSF at a distance equal to the distance between the center of the slit and the pixel center, the finely sampled LSF was obtained by plotting the pixel intensity from the center of the slit. The finely sampled LSF was synthesized by using 34 individual LSFs and normalized to a peak value of one (Fig. 5). The Fourier transform (FT) of the finely sampled LSF was performed and the resultant FT was deconvolved of the finite dimension of the slit by dividing the resultant FT by a sinc function in the frequency domain to provide the presampling MTF. The presampling MTF was measured along both the horizontal (perpendicular to the anode–cathode axis) and vertical (along the direction of the anode–cathode axis) directions.

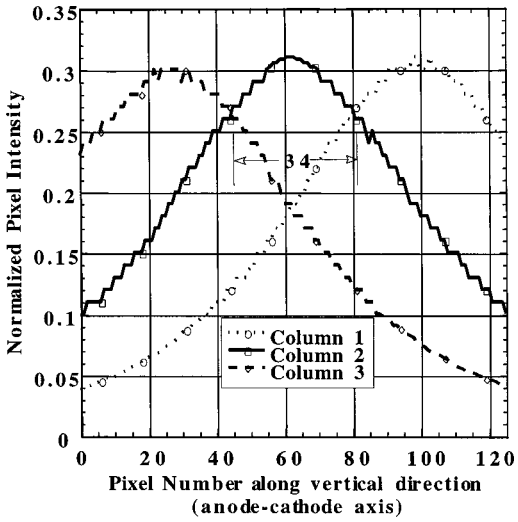


FIG. 4. The pixel amplitudes along the anode–cathode axis used for determining the number of rows of data needed to obtain a finely sampled LSF.

### B. Noise power spectrum measurement

There are many inherent difficulties in measuring the noise power spectrum (NPS) of digital systems.[35–38] Computing the two-dimensional (2D) NPS is important to study the presence or absence of any off-axis noise peaks. Since the computation time of computers is no longer a constraint,[35] computing the entire 2D NPS and estimating the one-dimensional (1D) NPS from the 2D NPS was used. The 1D NPS was estimated from the 2D NPS using the technique described by Dobbins *et al.*[35] This technique utilizes a thick cut parallel to and immediately adjacent to the axes for estimating the 1D NPS. We used the data in a thick slice comprised of eight lines on either side of both the axes (excluding the axes). For each data value at $(u,v)$ in this thick slice, the frequency value was computed as $\sqrt{u^2+v^2}$ for the 1D NPS estimate. The assumptions for utilizing this technique for estimating the 1D NPS are that the 2D NPS exhibit moderate radial symmetry and that the noise data are nominally uniform within the small annuli of spatial frequencies used for regrouping the noise data.

The next major difficulty was to determine the finite window of the noise data required to provide adequate resolution for proper representation of the NPS without the finite window overtly affecting the NPS estimate. Since the measured NPS is produced by convolving the ''true'' NPS with the $\mathrm{sinc}^2$ function in the frequency domain, due to the finite window of the noise data, the choice of region-of-interest (ROI) size has to be considered carefully. We estimated the NPS using ROI sizes of $512\times512$, $256\times256$, $128\times128$, and $64\times64$, and determined the $256\times256$ ROI to be the smallest ROI required for proper representation of the NPS with minimum spectral distortion (spectral deviation between $512\times512$ ROI and $256\times256$ ROI was less than 5% over the

entire frequency range and the spectral deviation increased with smaller ROI sizes). Hence, the 256×256 ROI was utilized for NPS estimations in the entire study.

The other difficulty was to determine the number of NPS realizations needed to be averaged in order to obtain a smooth and accurate curve depicting the noise spectrum. Ideally, we would need a large number of NPS realizations so that they can be averaged to obtain a smooth spectrum. We considered 10, 15, 20, 30, and 50 NPS realizations and found that the ensemble average of 15 NPS realizations taken from the same location through 15 images was sufficient to accurately characterize the NPS of the system. We were able to achieve a smooth spectrum by averaging eight lines of data on either side of the axes.

Problems associated with background trends such as from the heel effect can corrupt the noise spectrum and provide artificially inflated values[35,38] along the axes. However, techniques for suppression of such background trends have been described by various authors.[35,38] We surface (ramp) fitted each ROI and subtracted these background trends. Though this method was successful in suppressing these background trends, it did not completely eliminate them. Hence, we avoided using data values directly on the axes, as they were not representative in amplitude of the rest of the 2D NPS in the vicinity of the axes.

In order to measure the noise power spectra of the detector the detector has to be linear and shift invariant.[39] The linear response and sensitivity of the system was measured by averaging the pixel intensity over a 256×256 ROI centered at the 4 cm from the chest wall edge of the detector at various exposure levels. All images for the noise power spectral estimate used for calculation of detective quantum efficiency (DQE) were dark subtracted [Eq. (1)] and flat field corrected [Eq. (2)] resulting in a nominally uniform image,

$$\text{dark subtracted}_i(x,y) = \text{flood}_i(x,y) - \text{dark}_i(x,y), \tag{1}$$

$$\text{flat field}_i(x,y) = \frac{\text{dark subtracted}_i(x,y)}{(1/n)\sum_{i=1}^{n}\text{dark subtracted}_i(x,y)} \times \frac{1}{m^2}\sum_{y=1}^{m}\sum_{x=1}^{m}\left[\frac{1}{n}\sum_{i=1}^{n}\text{dark subtracted}_i(x,y)\right], \tag{2}$$

where $\text{flood}_i(x,y)$ and $\text{dark}_i(x,y)$ represent the flood and dark ROIs, respectively; $(1/n)\Sigma_{i=1}^{n}$ dark subtracted$_i(x,y)$ is the average of the dark subtracted ROIs; $1/m^2\Sigma_{v=1}^{m}\Sigma_{u=1}^{m}[(1/n)\Sigma_{i=1}^{n}\text{dark subtracted}_i \times(x,y)]$, is the mean of the average of the dark subtracted ROIs; and, in our case, $m=256$ and $n=15$. The ROIs (256×256) used for the NPS analysis were taken from the same location (centered at 4 cm from the chest wall edge of the detector) from multiple (15) images. Though the detector might not to be completely shift invariant, the process of flat field correcting and using the same ROI from multiple images for NPS analysis allows for the reasonable assumption of the ''shift-invariant'' property of the system.

The noise power spectra were determined at four exposure levels and were obtained with 4.5-cm-thick Lucite in the x-ray beam path. This thickness of Lucite was used as it was found to be the median thickness range (4.5–4.99 cm) of the compressed breast from a random sample of 100 breast exams obtained from a population of 1400 patients. The antiscatter grid was not used while obtaining the images as it might provide a possible noise source, which might corrupt the measurement. In order to minimize scattered radiation affecting the measurement due to the removal of the antiscatter grid, the 4.5-cm-thick Lucite block was mounted on to the tube housing. In addition, the x-ray beam was collimated both at the tube port and at the surface of the detector using Pb (0.5 cm) so that only a 4 cm×4 cm area of the detector was irradiated. This enabled us to obtain our objective of achieving a realistic clinical spectrum without the measurement being affected by either excessive scattered radiation or the presence of structure from an antiscatter grid. The setup for NPS measurement is shown in Fig. 6. Fifteen dark image subtracted, flat field corrected, 256×256 ROIs were acquired as described previously. Before performing dark image subtraction and flat field correction, care was taken to avoid information loss due to truncation by converting the pixel intensity values to 32 bit floating point numbers from the original 16 bit digital values. A surface fit (like a ramp) to suppress background trends like heel effect was performed on each ROI. The ensemble average of the squares of the magnitude of these 15 Fourier transformed 256×256 ROIs scaled as shown in Eq. (3) provided the 2D raw noise power spectrum, $\text{NPS}_{\text{raw}}(u,v)$.[35]

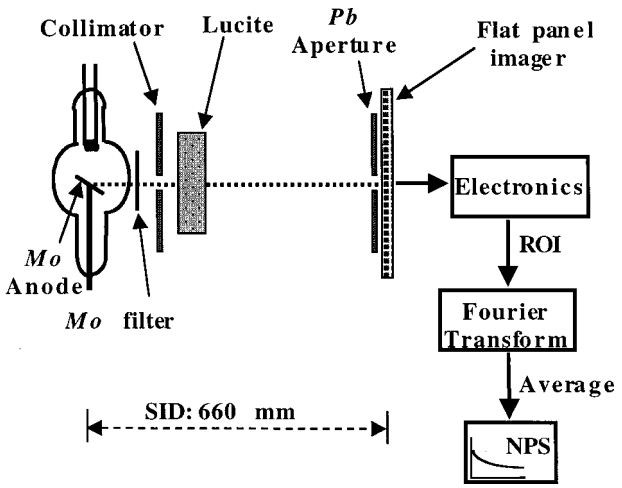


FIG. 6. Experimental setup for NPS measurement where a 4 cm×4 cm area of the detector centered at 4 cm from the chest wall edge was irradiated. Lead collimation at the tube port and at the detector surface reduced excessive scatter.

The $\text{NPS}_{\text{raw}}(u,v)$ was obtained by

$$\text{NPS}_{\text{raw}}(u,v) = \frac{\langle|\text{FT}[\text{flat field}(x,y)]|^2\rangle}{N_x N_y}\Delta_x\Delta_y, \tag{3}$$

where $\langle|\text{FT}[\text{flat field}(x,y)]|^2\rangle$ represents the ensemble average of the squares of the magnitude of the Fourier transformed 256×256 ROIs, $N_x$ and $N_y$ are the number of ele-

ments in the $x$ and $y$ directions, respectively (which are equal and is 256 in this case), and $\Delta_x$ and $\Delta_y$ are the pixel pitch in $x$ and $y$ directions, respectively (which are equal and is 100 $\mu$m with this imager).

To compute noise equivalent quanta (NEQ) and DQE a 1D NPS curve was required. This was achieved by using the data in a thick slice comprised of eight lines on either side of both the $u$ and $v$ axes (excluding the axes). For each data value at $(u,v)$ in this thick slice, the frequency value was computed as $\sqrt{u^2+v^2}$ for the 1D NPS estimate. The final 1D NPS at each exposure level is the average of 8 (lines) $\times 2$(sides) $\times 256$ data points (=4096 data values) grouped into frequency bins 0.04 mm$^{-1}$. The 1D $\mathrm{NPS}_{\mathrm{normalized}}(f)$ to be used for the DQE calculations was obtained by scaling the 1D $\mathrm{NPS}_{\mathrm{raw}}(f)$ for the mean signal by

$$\mathrm{NPS}_{\mathrm{normalized}}(f)=\frac{\mathrm{NPS}_{\mathrm{raw}}(f)}{(\text{mean signal of } 256\times 256\,\mathrm{ROI})^2}. \tag{4}$$

The mean signal of the $256\times 256$ ROI is expressed in digital values.

The electronic noise present in the system was also estimated. The entire detector was covered with Pb (2 cm) and 15 images were acquired using the minimum possible exposure technique. The 2D $\mathrm{NPS}_{\mathrm{electronic}}(u,v)$ was estimated as per Eq. (3) at this minimum possible exposure technique with Pb, and the 1D $\mathrm{NPS}_{\mathrm{electronic}}(f)$ estimated by using a thick slice as described earlier. From this measurement, the noise contribution due to the x rays, $\mathrm{NPS}_{\mathrm{x\ ray}}(f)$ was calculated at each exposure level as per Eq. (5), where $\mathrm{NPS}_{\mathrm{raw}}(f)$ is the raw NPS estimated as per Eq. (3) and $\mathrm{NPS}_{\mathrm{electronic}}(f)$ is the electronic noise of the system. The x-ray component of $\mathrm{NPS}_{\mathrm{raw}}(f)$ was computed as per Eq. (6)

$$\mathrm{NPS}_{\mathrm{x\ ray}}(f)=\mathrm{NPS}_{\mathrm{raw}}(f)-\mathrm{NPS}_{\mathrm{electronic}}(f), \tag{5}$$

$$\text{x-ray component of } \mathrm{NPS}_{\mathrm{raw}}(f)=\frac{\mathrm{NPS}_{\mathrm{x\ ray}}(f)}{\mathrm{NPS}_{\mathrm{raw}}(f)}\times 100\%. \tag{6}$$

In order to study the structured noise component or the presence of any varying nonstochastic noise, the 2D $\mathrm{NPS}_{\mathrm{subtracted}}(u,v)$ was estimated as per Eqs. (7) and (8). Background suppression (ramp fit) was not performed for estimation of $\mathrm{NPS}_{\mathrm{subtracted}}(u,v)$. The 1D $\mathrm{NPS}_{\mathrm{subtracted}}(f)$ was obtained by using a thick slice of eight lines of data on either side of the axes as described earlier,

$$\mathrm{residual}_i(x,y)=[\mathrm{flood}_i(x,y)-\mathrm{dark}_i(x,y)]-\frac{1}{n}\sum_{i=1}^{n}\text{flat field}_i(x,y), \tag{7}$$

$$\mathrm{NPS}_{\mathrm{subtracted}}(u,v)=\frac{\langle|\mathrm{FT}(\mathrm{residual}(x,y))|^2\rangle}{(\text{mean signal of } 256\times 256\,\mathrm{ROI})^2 N_x N_y}\Delta_x\Delta_y. \tag{8}$$

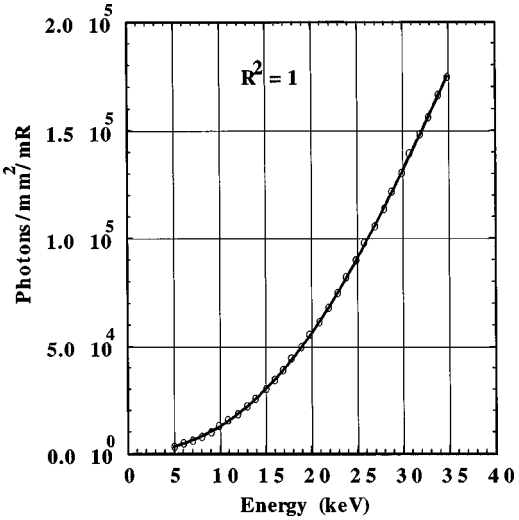


FIG. 7. Curve fitted x-ray photon fluence per mR between the energy range of 5 and 35 keV obtained from published values.

### C. NEQ and DQE measurement

The NEQ was computed as[35]

$$\mathrm{NEQ}(f)=\frac{\mathrm{MTF}^2(f)}{\mathrm{NPS}_{\mathrm{normalized}}(f)}. \tag{9}$$

The NEQ of the system was computed for the four exposure levels. For the purpose of calculating the DQE of the digital imager, Eqs. (10) and (11) were used:[35]

$$\mathrm{DQE}(f)=\frac{\mathrm{MTF}^2(f)}{\mathrm{NPS}_{\mathrm{normalized}}(f)q}. \tag{10}$$

and hence

$$\mathrm{DQE}(f)=\frac{\mathrm{NEQ}(f)}{q}, \tag{11}$$

where $\mathrm{MTF}(f)$ is the modulation transfer function of the system; $\mathrm{NPS}_{\mathrm{normalized}}(f)$ is the normalized noise power spectrum of the imaging system; $q$ is the number of x-ray photons incident on the detector per unit area; $\mathrm{NEQ}(f)$ is the noise equivalent quanta of the imaging system and $f$ is the spatial frequency. The only factor that needs to be determined is $q$.

*Determination of q.* Determination of $q$ was done in three stages. First, the x-ray photon fluence per mR was curve fitted between the energy range of 5 to 35 keV from already published values[40] and is shown in Fig. 7. The photon fluence per mR, $Y(e)$, at energy $(e)$ is best described by the polynomial:

$$Y(e)=2.2128+33.514e+89.23e^2+3.0588e^3-0.0239e^4-0.0006e^5-3\times 10^{-7}e^6. \tag{12}$$

The x-ray spectral distribution, $q(e)$, was characterized by averaging 15 spectra obtained using a cadmium zinc telluride (CZT) based high resolution spectrometer (XR-100T-CZT, Amptek, Inc., USA). The x-ray spectrum was corrected for dead time losses and pile-up.[41] Correction for the spectrometer energy response was not needed as the energy ab-

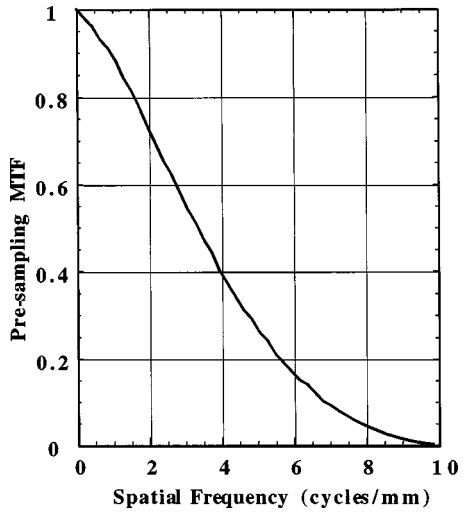


FIG. 8. The presampling MTF of the full field flat panel *a*:Si imager.

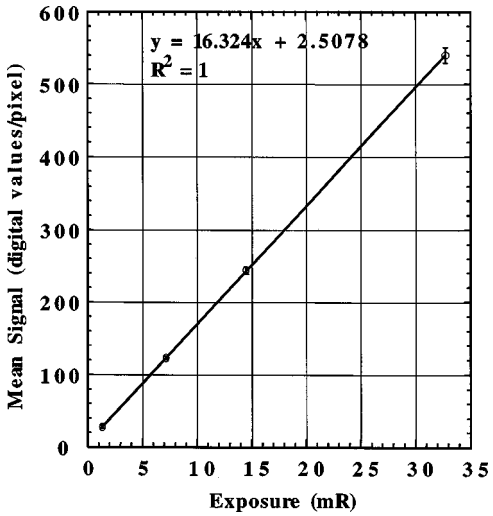


FIG. 9. Linearity of the system. The data points represent the mean intensity and the error bars represent the standard deviation from this mean value.

sorption efficiency of the 3-mm-thick CZT spectrometer is more than 99.9% for the energy range (5–35 keV) of the incident spectrum. The exposure ($X$) on the surface of the detector was measured under the same conditions as during the NPS measurement with a calibrated mammographic ionization chamber connected to MDH 1515 (RadCal Corp., USA) dosimeter. The precision at each exposure level was improved by averaging five measurements. The total number of photons incident per unit area of the detector at each exposure level was calculated as per Eq. (13). With the knowledge of $q$, the DQE($f$) was calculated,

$$q = X \frac{\int q(e) Y(e) de}{\int q(e) de}. \tag{13}$$

## III. RESULTS AND DISCUSSION

### A. Presampling MTF

The measured presampling MTF is shown in Fig. 8. The presampling MTF measured both along the vertical and horizontal directions were identical. The presampling MTF was found to be 0.73, 0.42 and 0.28 at 2, 4, and 5 cycles/mm, respectively. Although the MTF of an imaging system is an important objective measure of the spatial resolution, this parameter alone may not be predictive of the overall performance of the system. Other metrics such as DQE as a function of the spatial frequency provide additional insight.

### B. Noise power spectra

The linearity of the system was measured and is shown in Fig. 9. From the linearity measurements the sensitivity of the system was found to be 16.324 digital values/mR/pixel. The 2D NPS obtained at 1.3, 7.1, 14.5, and 32.8 mR are shown in Figs. 10(a), 10(b), 10(c), and 10(d), respectively. The noise power at the intersection of the $u$ and $v$ axes are much higher in magnitude and hence this point has been blanked for display purposes. The images are displayed in a black and white scheme where the transition point is set at the midpoint of the minimum and maximum of the 2D NPS images. The 2D NPS does not show the presence of any off-axis noise peaks. The 1D $NPS_{raw}$ at four exposure levels of 1.3, 7.1, 14.5, and 32.8 mR are shown in Fig. 11. The electronic noise present in the system is also shown in Fig. 11. The 1D $NPS_{raw}$ demonstrates an increase in noise with increasing exposure as the photon noise increases with increasing exposure. The integral of the NPS at each exposure was confirmed to be identical to the rms variance of the 256×256 ROI. Figure 12 shows the x-ray component of the total NPS calculated as

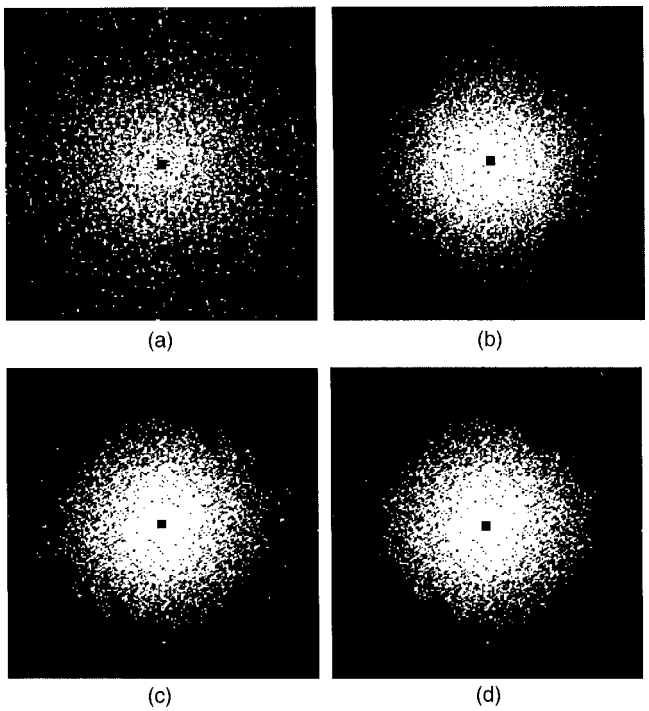


FIG. 10. The 2D NPS obtained at 1.3, 7.1, 14.5, and 32.8 mR are shown in (a), (b), (c), and (d), respectively. The intersection of the axes has been masked for display purposes. The images are displayed in a black and white scheme, with the transition point set at the mean of the ROI.

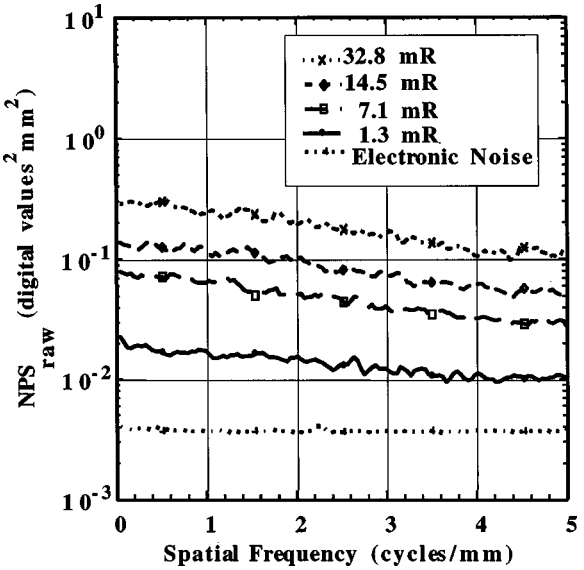


FIG. 11. The 1D noise power spectra ($NPS_{raw}$) at four exposure levels of 1.3, 7.1, 14.5, and 32.8 mR are shown. The electronic noise is also shown.

per Eq. (6) at the four exposure levels. Even at a low exposure of 1.3 mR, the x-ray component was dominant (greater than 60% of the total NPS at 5 cycles/mm and approximately 80% of the total NPS at ~0 cycle/mm). Figure 13 suggests that there is no appreciable structure noise or varying nonstochastic noise at exposures of 1.3 and 32.8 mR as the $NPS_{subtracted}$ and $NPS_{normalized}$ are identical.

### C. NEQ and DQE

The NEQ of the system at four exposure levels are shown in Fig. 14. The Mo–Mo spectrum incident on the detector transmitted through 4.5 cm of Lucite and the breast support plate recorded with a high resolution spectrometer is shown in Fig. 15. From this spectral distribution and Fig. 7, the photon flux incident on the detector was determined to be $0.533\times10^5$ photons/mm$^2$/mR. The DQE of the system at four exposure levels is shown in Fig. 16. To demonstrate the exposure dependence of the DQE of the system, DQE (0.2 cycle/mm), DQE(1 cycle/mm), DQE(2 cycles/mm), DQE(3 cycles/mm), and DQE(5 cycles/mm) are plotted as a function of the incident exposure in Fig. 17. The plot indicates that the DQE of the system increases with increasing exposure, and reaches a constant value at about 15 mR. The lower values of DQE at low exposures are primarily due to the contribution of electronic noise in the system. The DQE (~0 cycle/mm) was found to be 0.4, 0.48, 0.54, and 0.55 at incident exposures of 1.3, 7.1, 14.5, and 32.8 mR, respectively.

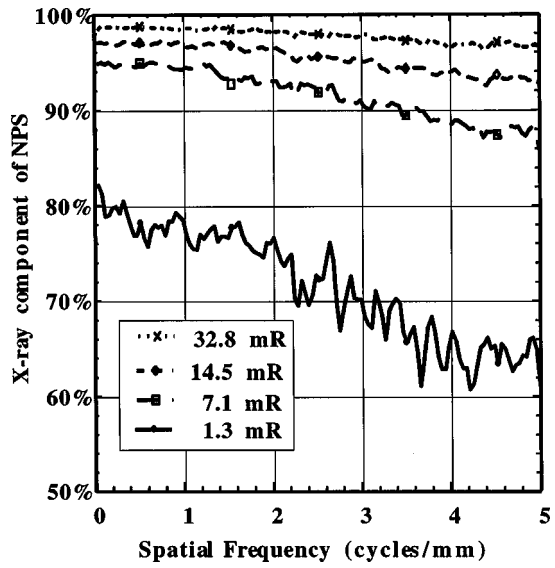


FIG. 12. The x-ray component of $NPS_{raw}$ at four exposure levels of 1.3, 7.1, 14.5, and 32.8 mR are shown.

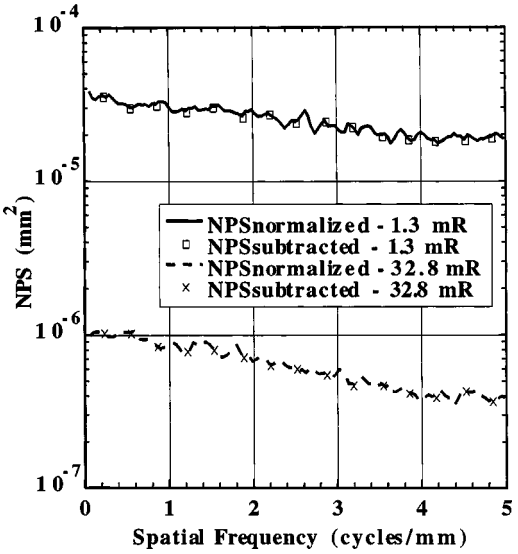


FIG. 13. The 1D $NPS_{normalized}$ and $NPS_{subtracted}$ obtained at 1.3 and 32.8 mR.

### D. Discussion

Metrics such as MTF and DQE have been widely used to describe the performance characteristics of imaging systems.

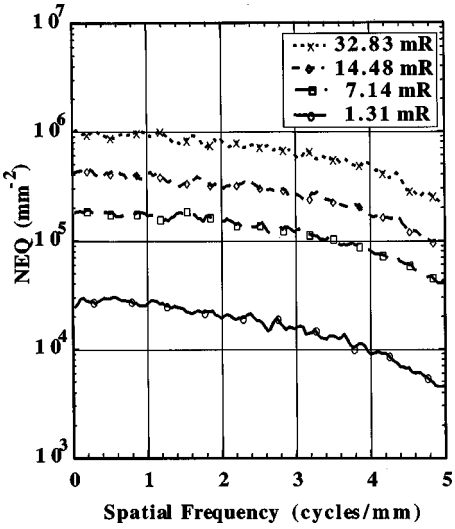


FIG. 14. The NEQ of the system at four exposure levels.

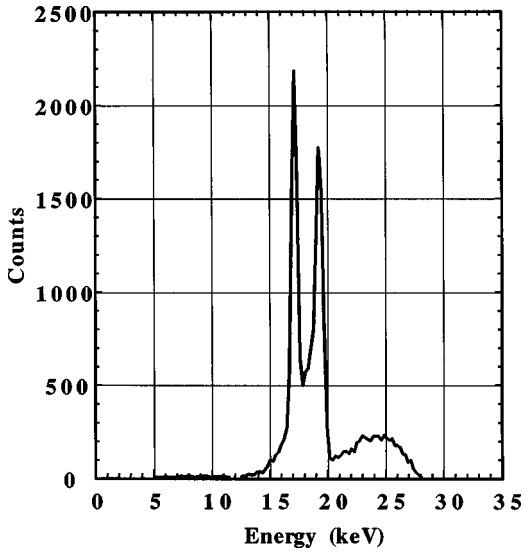


FIG. 15. The Mo–Mo spectra incident on the detector transmitted through 4.5 cm of Lucite and the breast support plate, recorded with a high resolution spectrometer for calculation of $q$.

A comparison of the flat-panel imager with other imaging systems such as screen-film systems to show the general trends could provide additional information as to the advantages and limitations of the flat-panel imager. Nishikawa and Yaffe[42] have evaluated various mammographic screen-film systems in the past. More recently, Bunch[43] has also evaluated the MTF and DQE of two widely used mammographic screen-film systems. Their results show a maximum DQB($\sim$0) of 0.35 compared with 0.55 measured with the flat panel imager. The improved DQE of the flat panel imager at low and midfrequencies can be particularly advantageous in the imaging of low-contrast soft tissue lesions.[44,45] Their results also indicate that the spatial resolution is much higher

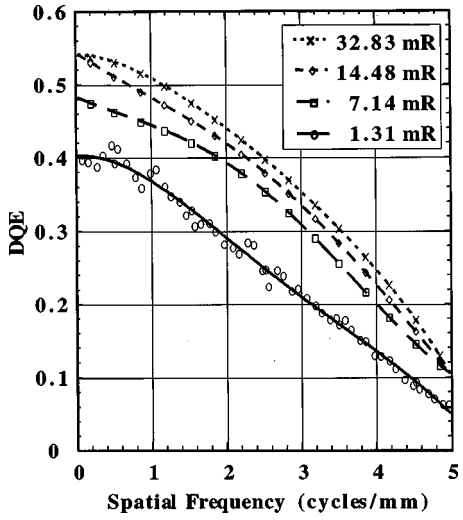


FIG. 16. The DQE of the system at four exposure levels. Data points are curve fitted with a sixth-order polynomial for clarity. To demonstrate the goodness of fit, data points at an exposure of 1.3 mR are shown.

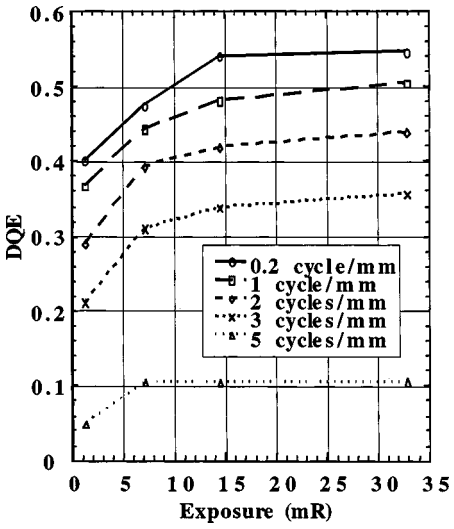


FIG. 17. DQE of the system plotted as a function of incident exposure.

with screen-film systems[42,43] compared to the flat-panel imager, but an increased film noise at high frequencies have also been observed.

Previous laboratory studies[23] in digital mammographic imaging using different technology have suggested that even with lower spatial resolution, lesion detectability, including microcalcifications can be improved by contrast enhancement of digital data. Prior work with this flat-panel imager has demonstrated a high dynamic range.[46] Clinical images with the current prototype demonstrate encouraging results for visualization of soft tissue anatomy and calcifications.[47–49] The clinical efficacy in terms of sensitivity and specificity is the subject of a different investigation, which is currently in progress.[47]

## IV. CONCLUSIONS

A consistent set of image quality measurements was performed characterizing the full field amorphous silicon-based flat panel imager for mammographic applications. The flat panel imager did not exhibit any appreciable structured noise or varying nonstochastic noise component at the tested exposure levels. The response of the imager was linear and exhibited high sensitivity under tested exposure conditions. The flat panel imager demonstrated good dose efficiency within the tested exposure range.

## ACKNOWLEDGMENTS

The authors would like to thank James T. Dobbins, Ph.D., Duke University Medical Center, Durham, NC27710 for useful scientific and technical discussions. The authors from GE Corporate Research and Development and GE Medical Systems acknowledge the invaluable assistance of many present and former colleagues. In particular, Gene Hilton, Ph.D., played a key role in the early development of the digital detector measurement technology. This work was supported in part by US Army Grant No DAMD17-96-C-6104 to the University of Colorado Health Sciences Center, and in part

by Grant No. R01CA59770 from the National Cancer Institute to the University of Massachusetts Medical School. The full-field digital mammography detector was developed independently by GE Corporate Research and Development with partial support from the National Cancer Institute Grant No. 5R01CA60183. The contents of this work are solely the responsibility of the authors and do not necessarily represent the official views of NCI, NIH, or US Army.

[a]Author to whom correspondence should be addressed; electronic mail: andrew.karellas@umassmed.edu

[b]Present address: Breast Imaging Section, Northwestern University, Chicago, Illinois 60611.

[1] D. P. Chakraborty, ''The effect of the antiscatter grid on full-field digital mammography phantom images,'' J. Digit. Imaging **12**, 12–22 (1999).

[2] Z. Jing, W. Huda, and J. K. Walker, ''Scattered radiation in scanning slot mammography,'' Med. Phys. **25**, 1111–1117 (1998).

[3] J. Persliden and G. A. Carlsson, ''Scatter rejection by air gaps in diagnostic radiology. Calculations using a Monte Carlo collision density method and consideration of molecular interference in coherent scattering,'' Phys. Med. Biol. **42**, 155–175 (1997).

[4] R. Fahrig, J. G. Mainprize, N. Robert, A. Rogers, and M. J. Yaffe, ''Performance of glass fiber antiscatter devices at mammographic energies,'' Med. Phys. **21**, 1277–1282 (1994).

[5] H. Roehrig, T. Yu, and E. Krupinski, ''Image quality control for digital mammographic systems: initial experience and outlook,'' J. Digit. Imaging **8**, 52–66 (1995).

[6] J. M. Boone, T. R. Fewell, and R. J. Jennings, ''Molybdenum, rhodium, and tungsten anode spectral models using interpolating polynomials with application to mammography,'' Med. Phys. **24**, 1863–1874 (1997).

[7] A. Karellas, I. Sechopoulos, I. Levis, A. C. Huber, and J. A. Pantazis, ''Measurement of the x-ray spectra and tube potential in mammographic units with a self-calibrating compact cadmium zinc telluride (CZT) detector,'' Radiology **205**, 301 (1997).

[8] Title 21, United States Code of Federal Regulations, Part 900, 1998.

[9] U. Bick, M. L. Giger, R. A. Schmidt, R. M. Nishikawa, and K. Doi, ''Density correction of peripheral breast tissue on digital mammograms,'' Radiographics **16**, 1403–1411 (1996).

[10] M. A. Kupinski and M. L. Giger, ''Automated seeded lesion segmentation on digital mammograms,'' IEEE Trans. Med. Imaging **17**, 510–517 (1998).

[11] S. S. Buchbinder, I. S. Leichter, P. N. Bamberger, B. Novak, R. Lederman, S. Fields, and D. J. Behar, ''Analysis of clustered microcalcifications by using a single numeric classifier extracted from mammographic digital images,'' Acad. Radiol. **5**, 779–784 (1998).

[12] M. A. Anastasio, H. Yoshida, R. Nagel, R. M. Nishikawa, and K. Doi, ''A genetic algorithm-based method for optimizing the performance of a computer-aided diagnosis scheme for detection of clustered microcalcifications in mammograms,'' Med. Phys. **25**, 1613–1620 (1998).

[13] D. Wei, H. P. Chan, N. Petrick, B. Sahiner, M. A. Helvie, D. D. Adler, and M. M. Goodsitt, ''False-positive reduction technique for detection of masses on digital mammograms: Global and local multiresolution texture analysis,'' Med. Phys. **24**, 903–914 (1997).

[14] H. Yoshida, K. Doi, R. M. Nishikawa, M. L. Giger, and R. A. Schmidt, ''An improved computer-assisted diagnostic scheme using wavelet transform for detecting clustered microcalcifications in digital mammograms,'' Acad. Radiol. **3**, 621–627 (1996).

[15] M. Kallergi, G. M. Carney, and J. Gaviria, ''Evaluating the performance of detection algorithms in digital mammography,'' Med. Phys. **26**, 267–275 (1999).

[16] L. T. Niklason *et al.*, ''Digital tomosynthesis in breast imaging,'' Radiology **205**, 399–406 (1997).

[17] U. E. Ruttimann, R. A. J. Groenhuis, and R. L. Webber, ''Restoration of digital multiplane tomosynthesis by a constrained iteration method,'' IEEE Trans. Med. Imaging **MI-3**, 141–148 (1984).

[18] D. P. Chakraborty and G. T. Barnes, ''An energy sensitive cassette for dual-energy mammography,'' Med. Phys. **16**, 7–13 (1989).

[19] T. Asaga, S. Chiyasu, S. Mastuda, H. Mastuura, H. Kato, M. Ishida, and T. Komaki, ''Breast imaging: Dual-energy projection radiography with digital radiography,'' Radiology **164**, 869–870 (1987).

[20] F. L. Flanagan, J. G. Murray, P. Gilligan, J. P. Stack, and J. T. Ennis, ''Digital subtraction in Gd-DTPA enhanced imaging of the breast,'' Clin. Radiol. **50**, 848–854 (1995).

[21] M. B. Williams and L. L. Fajardo, ''Digital mammography: Performance considerations and current detector designs,'' Acad. Radiol. **3**, 429–437 (1996).

[22] D. W. Holdsworth, R. K. Gerson, and A. Fenster, ''A time-delay integration charge-coupled device camera for slot-scanned digital radiography,'' Med. Phys. **17**, 876–886 (1990).

[23] R. M. Nishikawa, G. E. Mawdsley, A. Fenster, and M. J. Yaffe, ''Scanned-projection digital mammography,'' Med. Phys. **14**, 717–727 (1987).

[24] A. Karellas, L. J. Harris, H. Liu, M. A. Davis, and C. J. D'Orsi, ''Charge-coupled device detector: Performance considerations and potential for small-field mammographic imaging applications,'' Med. Phys. **19**, 1015–1023 (1992).

[25] S. Hejazi and D. P. Trauernicht, ''System considerations in CCD-based x-ray imaging for digital chest radiography and digital mammography,'' Med. Phys. **24**, 287–297 (1997).

[26] J. H. Siewerdsen, L. E. Antonuk, Y. El-Mohri, J. Yorkston, W. Huang, J. M. Boudry, and I. A. Cunningham, ''Empirical and theoretical investigation of the noise performance of indirect detection, active matrix flat-panel imagers (AMFPIs) for diagnostic radiology,'' Med. Phys. **24**, 71–89 (1997).

[27] L. E. Antonuk *et al.*, ''Performance evaluation of a large area, 97 $\mu$m pitch: Indirect detection active matrix flat-panel imager (AMFPI) for radiography and fluoroscopy,'' Radiology **209**, 357 (1998).

[28] L. E. Antonuk *et al.*, ''Performance limits of high resolution large area active matrix flat-panel imagers (AMFPIs),'' Radiology **209**, 581 (1998).

[29] L. E. Antonuk *et al.*, ''Strategies to significantly enhance performance of active matrix flat-panel imagers (AMFPIs),'' Radiology **209**, 358 (1998).

[30] H. M. Rougeot, B. Opsahl-Ong, D. E. Castleberry, C. E. Landberg, J. Q. Liu, and C. M. Kimme-Smith, ''Performance evaluation of a flat-panel filmless full-field digital mammography system,'' Radiology **201**, 190 (1996).

[31] U. Neitzel, I. Maack, and S. Gunther-Kohfahl, ''Image quality of a digital chest radiography system based on a selenium detector,'' Med. Phys. **21**, 509–516 (1994).

[32] W. Zhao and J. A. Rowlands, ''Digital radiology using active matrix readout of amorphous selenium: Theoretical analysis of detective quantum efficiency,'' Med. Phys. **24**, 1819–1833 (1997).

[33] S. L. Garverick, L. Skrenes, and R. D. Baertsch, ''A 32-channel charge readout IC for programmable, nonlinear quantization of multichannel detector data,'' IEEE J. Solid-State Circuits **30**, 533–541 (1995).

[34] H. Fujita, D. Y. Tsai, T. Itoh, K. Doi, J. Morishita, K. Ueda, and A. Ohtsuka, ''A simple method for determining the modulation transfer function in digital radiography,'' IEEE Trans. Med. Imaging **11**, 34–39 (1992).

[35] J. T. Dobbins, D. L. Ergun, L. Rutz, D. A. Hinshaw, H. Blume, and D. C. Clark, ''DQE($f$) of four generations of computed radiography acquisition devices,'' Med. Phys. **22**, 1581–1593 (1995).

[36] J. T. Dobbins, ''Effects of undersampling on the proper interpretation of modulation transfer function, noise power spectra, and noise equivalent quanta of digital imaging systems,'' Med. Phys. **22**, 171–181 (1995).

[37] M. L. Giger, K. Doi, and C. E. Metz, ''Investigation of basic imaging properties in digital radiography. II. Noise Weiner spectrum,'' Med. Phys. **11**, 797–805 (1984).

[38] C. D. Bradford, W. W. Peppler, and J. T. Dobbins, ''Performance characteristics of a Kodak computed radiography system,'' Med. Phys. **26**, 27–37 (1999).

[39] J. C. Dainty and R. Shaw, *Image Science* (Academic, New York, 1974).

[40] H. E. Johns and J. R. Cunningham, *The Physics of Radiology*, 4th ed. (Thomas, Springfield, IL, 1983).

[41] J. W. Byng, J. G. Mainprize, and M. J. Yaffe, ''X-ray characterization of breast phantom materials,'' Phys. Med. Biol. **43**, 1367–1377 (1998).

[42] R. M. Nishikawa and M. J. Yaffe, ''SNR properties of mammographic film-screen systems,'' Med. Phys. **12**, 32–39 (1985).

[43] P. Bunch, ''The effects of reduced film granularity on mammographic image quality,'' Proc. SPIE **3032**, 302–317 (1997).

[44] L. T. Niklason *et al.*, ''Improved detection of low contrast objects with full-field digital mammography versus film-screen mammography,'' Radiology **205**, 436 (1997).

[45] R. E. Hendrick *et al.*, ''Low-contrast lesion detection: Comparison of

screen-film and full-field digital mammography,'' Radiology **205**, 274 (1997).
[46] A. Karellas *et al.*, ''Evaluation of a full-field clinical prototype flat panel imager for digital mammography,'' Radiology **209**, 159 (1998).
[47] J. M. Lewin *et al.*, ''Clinical evaluation of a full-field digital mammography prototype for cancer detection in a screening setting—work in progress,'' Radiology **209**, 238 (1998).
[48] L. Moss, C. J. D'Orsi, A. Karellas, E. Hendrick, J. Lewin, and G. Sisney, ''Initial experience with a high resolution full field digital mammographic system,'' J. Digit. Imaging **11**, 110 (1998).
[49] R. H. Moore *et al.*, ''Initial clinical experience with full-field digital mammography,'' Radiology **205**, 274 (1997).

# Mammographic imaging with a small format CCD-based digital cassette: Physical characteristics of a clinical system[a)]

Srinivasan Vedantham, Andrew Karellas,[b)] Sankararaman Suryanarayanan, and Ilias Levis
*Department of Radiology, UMass Memorial Health Care, University of Massachusetts Medical School, Worcester, Massachusetts 01655*

Michel Sayag
*Lockheed Martin Fairchild Systems, Milpitas, California 95035*

Robert Kleehammer
*Lockheed Martin Fairchild Systems, Syosset, New York 11791*

Robert Heidsieck
*GE Medical Systems S.A, Buc Cedex, France*

Carl J. D'Orsi
*Department of Radiology, UMass Memorial Health Care, University of Massachusetts Medical School, Worcester, Massachusetts 01655*

(Received 2 February 2000; accepted for publication 9 May 2000)

The physical characteristics of a clinical charge coupled device (CCD)-based imager (Senovision, GE Medical Systems, Milwaukee, WI) for small-field digital mammography have been investigated. The imager employs a MinR 2000™ (Eastman Kodak Company, Rochester, NY) scintillator coupled by a 1:1 optical fiber to a front-illuminated $61\times61$ mm CCD operating at a pixel pitch of 30 microns. Objective criteria such as modulation transfer function (MTF), noise power spectrum (NPS), detective quantum efficiency (DQE), and noise equivalent quanta (NEQ) were employed for this evaluation. The results demonstrated a limiting spatial resolution (10% MTF) of 10 cy/mm. The measured DQE of the current prototype utilizing a 28 kVp, Mo–Mo spectrum beam hardened with 4.5 cm Lucite is ~40% at close to zero spatial frequency at an exposure of 8.2 mR, and decreases to ~28% at a low exposure of 1.1 mR. Detector element nonuniformity and electronic gain variations were not significant after appropriate calibration and software corrections. The response of the imager was linear and did not exhibit signal saturation under tested exposure conditions.  [S0094-2405(00)01308-0]

Key words: breast imaging, digital mammography, physics, image quality, detective quantum efficiency (DQE)

## I. INTRODUCTION

In recent years, advances in screen-film mammography and film processing techniques have contributed to significant improvements in mammographic image quality. While screen-film techniques provide a powerful tool for initial detection and subsequent follow-up of a suspicious area, they present significant limitations in detecting very subtle soft tissue lesions, especially in the presence of dense glandular tissue. Some of the fundamental limitations of screen-film mammography, particularly with respect to contrast and noise, have been discussed in several studies.[1,2] Consequently, attempts have been made to explore the potential of electronic detection as an alternate detection technique. Systems based on electronic detection have the theoretical capability of overcoming certain fundamental limitations of screen-film systems. The potential advantages of electronic detection include high detection efficiency, high dynamic range, capability for contrast enhancement,[3] and post processing capabilities including computer-aided diagnosis.[4–9] Further, direct electronic acquisition enables the exploration of novel imaging techniques such as tomosynthesis,[10,11] dual-energy mammography,[12,13] and digital subtraction imaging.[14] In the past, investigators have used different modes of electronic detection technology to gain insight into electronic mammography, commonly referred to as digital mammography.[15] Early evaluations have used image intensifiers and subsequently slot-scanned systems[1,2,16,17] with charge-coupled devices (CCDs) and CCDs with fiberoptic tapers.[18] The potential for utilizing CCD-based imagers for small-field digital mammography was described by Karellas *et al.*[18] and, now, the use of CCDs for core biopsies has become common practice. The use of core biopsies has been increasing in the past 10 years and a number of open surgical excisions are being replaced by these minimally invasive procedures. Although screen-film systems produce excellent image quality for these procedures, the film development process severely hinders fast display of acquired images, resulting in patient discomfort. The recent adaptation of CCD technology has enabled electronic acquisition of mammographic images during these procedures quickly and efficiently. Core biopsy procedures performed with an electronic

TABLE I. CCD-based mammographic detector specifications.

| | |
|---|---|
| CCD image area | 61×61 mm |
| Pixel matrix | 4096×4097 |
| Pixel size | 15 μm |
| Scintillator | MinR 2000™ [a] |
| Operating temperature | 12 °C |
| Pixel binning | 2×2 |
| Binned pixel size | 30 μm |
| Binned pixel matrix | 2048×2048 |

[a]™Eastman Kodak Company, Rochester, NY.

imaging device can reduce the duration of the procedure and patient discomfort. The study by Dershaw *et al.*[19] demonstrated the reduced duration for completion of needle localization studies when using digital technology. Moreover, digital imaging systems for mammographically guided digital stereotactic breast biopsy have an important advantage over screen-film systems in that they provide a digital output that can be used for quantitative analysis.[20] Observer performance comparison of digital radiograph systems for stereotactic breast needle biopsy has also been reported in the past.[21]

The first generation of these devices employed either a lens or a fiberoptic taper to couple the scintillator with the CCD. Field coverage of 5×5 cm to 6×6 cm is typical. Although this is a very restricted field of view, it is considered adequate for most localization and core biopsy procedures. The spatial resolution of these first generation devices was lower than that of the screen-film systems, and the limited optical coupling efficiency due to demagnification between the x-ray scintillator and CCD presented a significant challenge in attaining high detective quantum efficiency (DQE). The geometric demagnification between the scintillator and CCD reduces spatial resolution by virtue of the geometry of the optics. The light loss due to the demagnification reduces the optical signal to the CCD, and therefore contrast and dose efficiency are negatively affected. With the present day ability to manufacture large CCDs (6×6 cm, typically), the fiberoptic tapers or lens coupling which pose serious limitations can be overcome with a straight optical fiber. While this approach of coupling the CCD with the scintillator using a straight optical fiber provides the theoretical capability of improved optical efficiency, detailed experimental characterization of the physical properties of such imagers under realistic mammographic conditions have not been reported in the past. This study characterizes the image quality parameters of a CCD-based clinical imaging system (Senovision, GE Medical Systems, Milwaukee, WI) which employs a MinR 2000™ (Eastman Kodak Company, Rochester, NY) scintillator coupled by a 1:1 optical fiber to a front-illuminated 61×61 mm CCD.[22] See Table I.

## II. METHODS AND MATERIALS

The CCD used in this imager is a full-frame area image sensor with a matrix array of 4096 horizontal by 4097 vertical detector elements (pixels). The pixel pitch and spacing is 15μm. The imaging array is operated in the multipinned phase (MPP)[23] mode. In this mode, the dark current is decreased down to 25 pA/cm$^2$ at room temperature of 25 °C. The dark current is further minimized to ~10 pA/cm$^2$ by cooling the CCD to the operating temperature of 12 °C by a liquid circulation system. The CCD was manufactured using 2.5 micron design rules. The single-metal, triple-poly process allows a layout with small pixel geometries and few array blemishes. Incident photons pass through a transparent polycrystalline silicon gate structure, creating electron hole pairs. The resulting photoelectrons are collected in the pixels during the integration period. The amount of charge accumulated in each pixel is a linear function of the localized incident illumination density and integration period. The pixel structure is made up of contiguous CCD elements with no voids or inactive areas. In addition to sensing light photons, these elements are used to shift image data vertically. Consequently, x rays must not be detected during this transfer period. The full-frame architecture of the CCD provides image data as a sequential readout of 4097 lines, each containing 4096 pixels. At the end of the integration period, a three-phase clocking mechanism is utilized to transfer charge vertically through the CCD array to the horizontal readout register. A channel stop region between vertical columns separates the columns to prevent charge migration. The imaging area is divided into four quadrants and each quadrant may be clocked independently, if desired. The CCD may be clocked such that the full array is read out from any one of the four output amplifiers. The present readout mode utilizes only one amplifier and reads out the full array through this amplifier. The last clocked gate in the horizontal registers is larger than the other gates to facilitate binning (grouping of adjacent pixels prior to readout) the charge packets horizontally. The CCD has four, dual field-effect transistor (FET), floating diffusion output amplifiers, with a reset metal-oxide-semiconductor field-effect transistor (MOSFET) tied to the input gate. Charge packets are clocked to a precharged capacitor whose potential changes linearly in response to the number of electrons delivered. This potential is applied to the input gate of the amplifier producing a signal at the output. The capacitor is reset to a precharge level using the reset MOSFET, prior to the arrival of the next charge packet, except when horizontally binning. The output from the CCD is connected to an external load resistor to ground. The CCD array is operated in a 2×2 pixel binned mode to provide a full-frame image area of 2048×2048 pixels with a pixel pitch of 30 μm. Vertical binning is achieved by transferring two lines of charges from 4096 pixels onto the horizontal register. Horizontal binning is achieved by transferring two charge packets onto the last clocked, larger gate of the horizontal register and resetting the capacitor to the precharge level after the arrival of two charge packets. The charge packets' readout through the output amplifiers are digitized to 12 bits, providing digital values in the range of 0 to 4095. The schematic of the detector is shown in Fig. 1. The detector is also designed to fit the 18×24 cm cassette tray of mammographic systems providing an easy transition from a screen-film system to a digital system. The imager is integrated with a high-frequency x-ray generator (Senographe

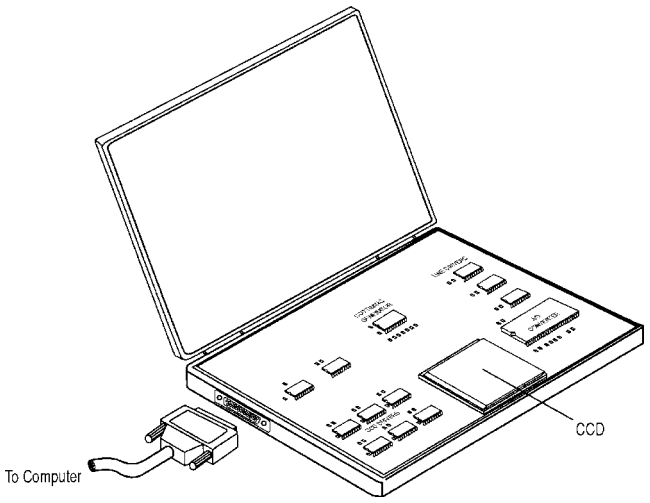


FIG. 1. Schematic of the CCD-based mammographic detector.

DMR, GE Medical Systems, Milwaukee, WI). This system uses a selectable dual track target, either molybdenum or rhodium, with selectable filtration of molybdenum or rhodium. All measurements were performed at 28 kVp with a Mo/Mo target/filter combination.

### A. Linearity

In order to study the signal and noise performance through Fourier components, the detector has to be linear and stationary.[24–26] The linear response of the system was measured by averaging the pixel intensity over the entire $2048\times2048$ image at various exposure levels. The images were obtained without the antiscatter grid in place, as the antiscatter grid is not used during clinical stereotactic localization studies. In order to measure the linearity with a clinically relevant spectrum, a 4.5 cm thick Lucite block was used in the x-ray beam path. The Lucite block was mounted onto the tube housing to reduce scattered radiation. The experimental setup for measuring the linear response is shown in Fig. 2. The sensitivity (signal per pixel/mR) of the system was calculated to be the slope of the linear response curve.

Under the condition of nominally uniform exposure to the detector, the stationary property can be reasonably assumed. Also, the assumption of ergodicity (which implies stationarity)[25,26] has been made to facilitate ensemble averaging of noise data.

### B. Presampling MTF measurement

The presampling modulation transfer function (MTF) was measured based on the slanted-slit technique described by Fujita *et al.*[27] The experimental procedure for measuring the same has also been described in detail by Dobbins *et al.*[28] Dobbins[29] has also described the effect of undersampling in detail. The specific methodology employed for measurement of the presampling MTF is identical to that used with the amorphous silicon-based imager, which was presented previously.[30] Hence, only specific attributes to the measurement procedure employed with this system alone would be addressed in this paper. The experimental setup is shown in Fig. 3. The presampling MTF was measured both along the anode–cathode axis and perpendicular to the anode–cathode axis. As an example, the methodology used for measuring the presampling MTF perpendicular to the anode–cathode axis is presented alone. A dark-subtracted image of a 10 micron slit oriented at a slight angle to the anode–cathode axis was acquired. Since imperfections along the edges of

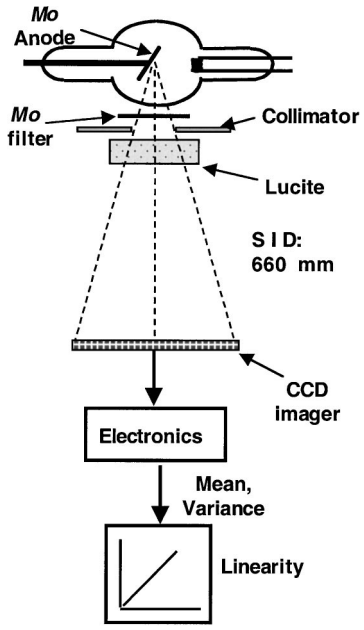


FIG. 2. Experimental setup for linearity measurement. The 4.5 cm thick Lucite block was mounted on to the tube housing to reduce excessive scatter.

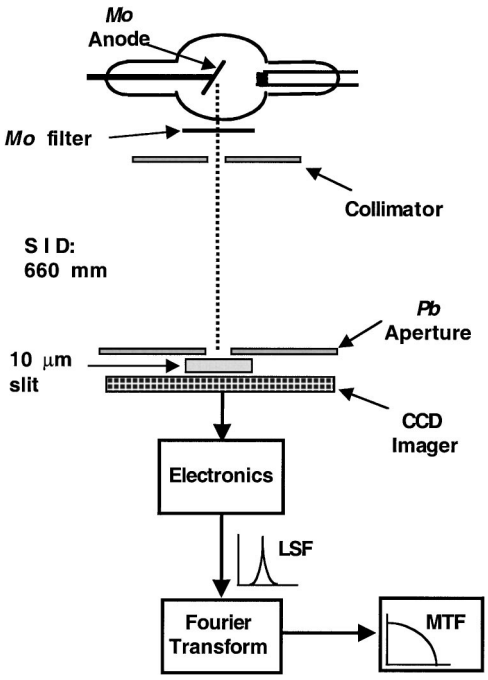


FIG. 3. Experimental setup for MTF measurement. The area surrounding the 10 micron slit was covered with Pb (0.5 cm thick).

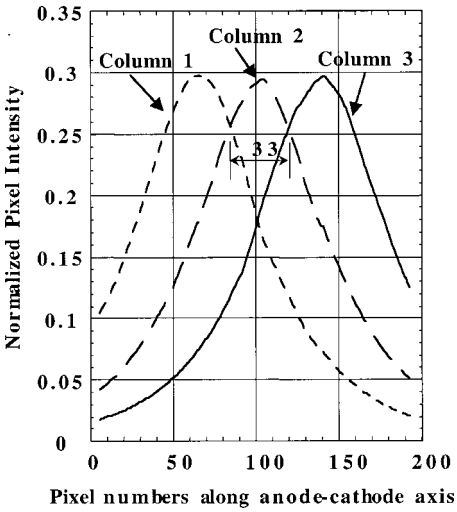


FIG. 4. The pixel amplitudes along the anode–cathode axis used for determining the adequate number of individual LSFs required for synthesizing a finely sampled LSF. Based on the separation between the two points of intersection, 33 individual LSFs were required for obtaining the finely sampled LSF.

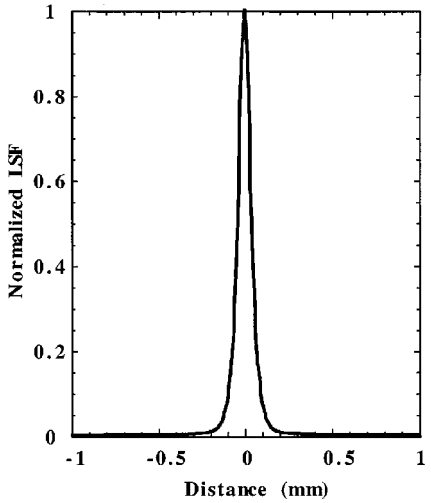


FIG. 5. Finely sampled composite LSF. The spacing between adjacent points is 0.91 microns.

the slit result in variations in slit width, a normalization scheme was used. In this scheme, the amplitude of each pixel ($x$) was divided by the sum of the amplitudes of all pixels in a line that is oriented perpendicular to the anode–cathode axis that includes the pixel ''$x$.'' This normalization scheme is feasible only if the assumptions that the slit width is approximately constant over the region used for obtaining the line spread function (LSF) and that the signal spreading is approximately equal along each line are made. These assumptions were verified by measuring the presampling MTF from several locations of the slit, the presampling MTF varied by less than 0.5%. In order to synthesize a finely sampled LSF, the adequate number of individual LSFs needs to be determined. This was achieved by plotting adjacent lines of pixel amplitudes along the anode–cathode axis as shown in Fig. 4. The separation between the two points of intersection determines the adequate number of LSFs required for obtaining a finely sampled LSF. The composite LSF was synthesized by using 33 individual LSFs. The composite LSF was normalized to a peak value of 1 and is shown in Fig. 5. The Fourier transform (FT) of the composite LSF was performed and the resultant FT was deconvolved of the finite dimension of the slit by dividing the resultant FT by a *sinc* function in the frequency domain to provide the presampling MTF.

### C. NPS measurement

The difficulties in measuring the noise power spectrum (NPS) of digital systems[24–26,28–32] have been described. The NPS can be calculated via the auto correlation function (indirect method) or by the Fourier transform of the image (direct method). With the advent of the fast Fourier transform and fast computers, the indirect method has largely been replaced with the direct method.[26] The NPS measurements reported in this paper were performed with the direct method. The typical assumption of ergodicity, usually made with radiographic images, has been made to facilitate this analysis. The presampling NPS cannot be directly measured using fine sampling techniques such as those employed to measure the presampling MTF, because the phases of the Fourier components of the image noise are random[27] and hence the measured NPS is inherently aliased. The experimental methodology used for NPS measurement is similar to that presented earlier.[30] The noise power spectra were determined at five exposure levels and were obtained with 4.5 cm thick Lucite block mounted on to the tube housing and without the antiscatter grid. In order to minimize scattered radiation, the x-ray beam was restricted both at the tube port and at the detector surface using Pb (0.5 cm), so that only a central 4 $\times$4 cm area of the detector is irradiated. This enabled us to obtain our objective of achieving a realistic clinical spectrum without the measurement being affected by either excessive scattered radiation or the presence of structure from an antiscatter grid. The setup for NPS measurement is shown in Fig. 6.

Ten dark image subtracted, flat-field corrected images of $2048\times2048$ pixels were acquired at each exposure level. The central $512\times512$ pixel matrix was obtained from each image. The $512\times512$ pixel matrix obtained was subdivided into four $256\times256$ ROIs for estimation of the noise power spectrum. Hence, a total of 40 ($=4\times10$ images) regions of interest (ROIs) at each exposure level was used to determine the NPS. Problems associated with background trends such as from the heel effect can corrupt the noise spectrum and provide artificially inflated values,[28,32] along the axes. Hence, we surface (ramp) fitted each ROI and subtracted these background trends. The 2D Fourier transform of each of the 40 ROIs was performed. The ensemble average of the squares of the magnitude of these 40 Fourier transformed ROIs were scaled as shown in Eq. (1) to obtain the two-dimensional (2D) raw noise power spectrum, $\mathrm{NPS}_{\mathrm{raw}}(u,v)$.

The $\mathrm{NPS}_{\mathrm{raw}}(u,v)$[28] was obtained by

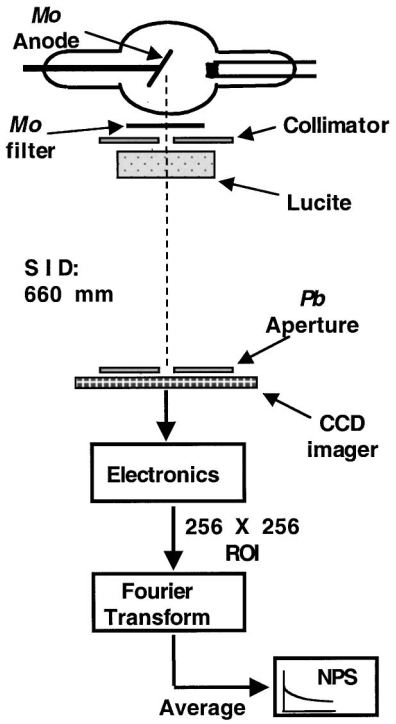


FIG. 6. Experimental setup for NPS measurement, where a central 4 $\times$4 cm area of the detector was irradiated. Lead collimation at the tube port and at the detector surface reduced excessive scatter.

$$\mathrm{NPS}_{\mathrm{raw}}(u,\nu)=\frac{\langle|\mathrm{FT}(u,\nu)|^2\rangle}{\mathrm{N}_x\cdot\mathrm{N}_y}\cdot\Delta_x\cdot\Delta_y, \tag{1}$$

where $\langle|\mathrm{FT}(u,\nu)|^2\rangle$ is the ensemble average of the squares of the magnitude of the Fourier-transformed 256 $\times$256 ROIs, $\mathrm{N}_x$ and $\mathrm{N}_y$ are the number of elements in the $x$ and $y$ directions, respectively (which are equal and are 256 in this case), and $\Delta_x$ and $\Delta_y$ are the pixel pitch in the $x$ and $y$ directions, respectively (which are equal and are 30 $\mu$m in this imager).

Although the ramp fit was successful in suppressing these background trends, it did not completely eliminate them. Hence, the data values directly on the axes were avoided while estimating the 1D NPS from the 2D NPS.

For the exposure levels, which demonstrated a nominal radial symmetry, the assumption of radial symmetry has been made. The 1D NPS curve required for estimation of NEQ and DQE was obtained by radially averaging the data in a thin slice comprised of eight lines on either side of both the $u$ and $\nu$ axes (excluding the axes). For each data value at ($u$, $\nu$) in this slice, the frequency value ($f$) was computed as $\sqrt{u^2+\nu^2}$ for the 1D NPS estimate.[28] The final 1D NPS at each exposure level is the average of 8(lines)$\times$2(axes) $\times$256 data points (= 4096 data values) grouped into frequency bins of 0.13 $\mathrm{mm}^{-1}$.

For the exposure levels at which the 2D NPS did not demonstrate radial symmetry, the NPS along the $u$ and $\nu$ axes were extracted separately. For these exposure levels, although the 2D NPS does not demonstrate radial symmetry, a nominal radial symmetry has been assumed within the thin slice used along either of the axes, to facilitate radial averaging of the data within this thin slice, with the frequency value computed as $\sqrt{u^2+\nu^2}$. For these exposure levels, the 1D NPS at each exposure level is obtained as the average of 8(lines)$\times$1(axis)$\times$256 data points (= 2048 data values) grouped into frequency bins of 0.13 $\mathrm{mm}^{-1}$.

The 1D $\mathrm{NPS}_{\mathrm{normalized}}(f)$ used for the estimating the DQE was obtained by dividing the 1D $\mathrm{NPS}_{\mathrm{raw}}(f)$ by the mean signal as shown in Eq. (2).

$$\mathrm{NPS}_{\mathrm{normalized}}(f)=\frac{\mathrm{NPS}_{\mathrm{raw}}(f)}{(\mathrm{Mean\ signal\ of\ 256}\times\mathrm{256\ ROI})^2}, \tag{2}$$

where the mean signal of the 256$\times$256 ROI is expressed in digital values.

### D. NEQ and DQE measurement

The NEQ was computed as

$$\mathrm{NEQ}(f)=\frac{\mathrm{MTF}^2(f)}{\mathrm{NPS}_{\mathrm{normalized}}(f)}. \tag{3}$$

The NEQ of the system was computed for the five exposure levels. For the purpose of calculating the DQE of the digital imager, the equation below was used:

$$\mathrm{DQE}(f)=\frac{\mathrm{MTF}^2(f)}{\mathrm{NPS}_{\mathrm{normalized}}(f)\cdot q}, \tag{4}$$

and, hence

$$\mathrm{DQE}(f)=\frac{\mathrm{NEQ}(f)}{q}, \tag{5}$$

where $\mathrm{MTF}(f)$ is the modulation transfer function of the system, $\mathrm{NPS}_{\mathrm{normalized}}(f)$ is the normalized noise power spectrum of the imaging system, $q$ is the number of x-ray photons per unit area incident on the detector, $\mathrm{NEQ}(f)$ is the noise equivalent quanta of the imaging system, and $f$ is the spatial frequency.

For the exposure levels that did not demonstrate radial symmetry, there were two 1D noise spectra, one along each of the two axes. The noise spectra used to represent the noise power at a particular exposure level for calculation of the $\mathrm{DQE}(f)$ was selected based on (i) the area under the noise spectra closest to the measured rms variance of the ROI, and (ii) the noise spectra that demonstrates the falloff trend of $\mathrm{NPS}(\sim 0)\times\mathrm{MTF}^2(f)$. As noted by Lubberts,[33] the $\mathrm{NPS}(f)$ does not follow this trend at higher spatial frequencies. Hence, the selection between NPS obtained along the $u$ and $\nu$ axes was based on the falloff trend up to the midfrequency of 6 cycles/mm.

#### 1. Determination of q

Determination of $q$ was performed using the recorded x-ray spectral shape, curve fit of the published values of photons incident per mR at each energy bin,[34] and the measured exposure onto the detector.[30] The incident x-ray spectra were recorded using a collimated, high-resolution, cadmium zinc telluride (CZT) based spectrometer.[35] The

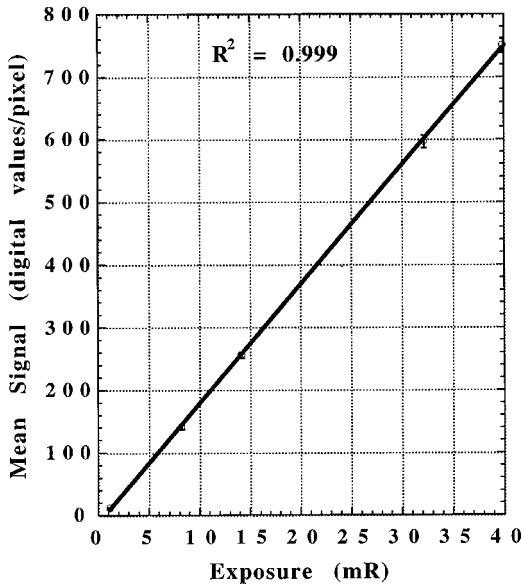


FIG. 7. Linearity of the system. The data points represent the mean intensity of 2048×2048 image. The error bars represent ±1 standard deviation from this mean value.

Mo–Mo spectrum was obtained by averaging 15 acquisitions of 100 mAs each. The spectrum was corrected for dead time losses and peak pileup.[36] With the knowledge of $q$, the spatial frequency dependent DQE($f$) was estimated.

## III. RESULTS AND DISCUSSION

The measured linear response of the system is shown in Fig. 7. The error bars represent ±1 standard deviation from the mean of the 2048×2048 image. From the slope of this linear response curve, the sensitivity was determined to be 19.06 digital values per pixel/mR.

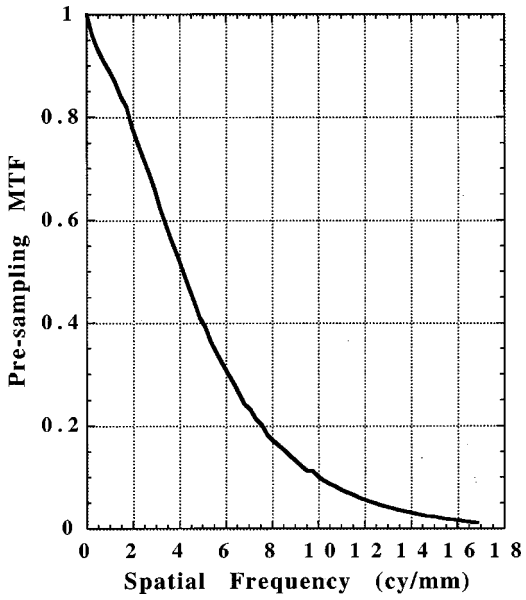


FIG. 8. The presampling MTF($f$) of the small-field CCD-based digital cassette.

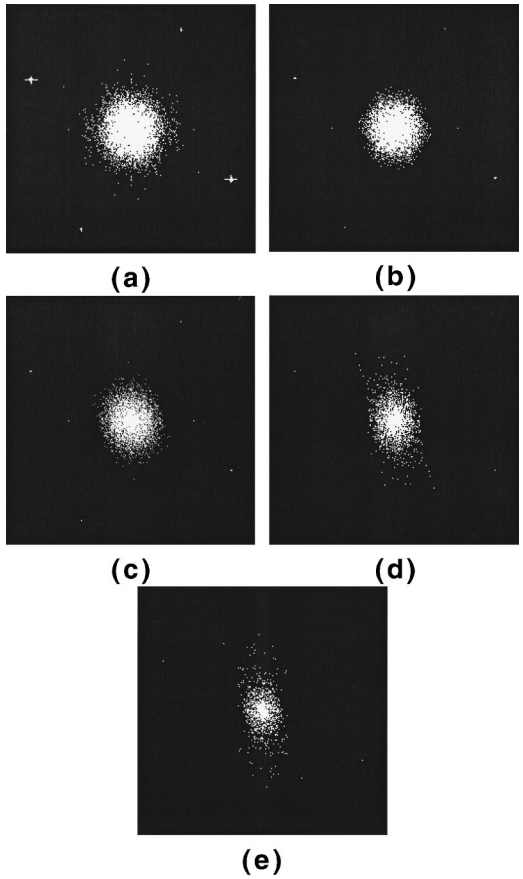


FIG. 9. The 2D NPS obtained at 1.1, 8.2, 14.2, 32.2, and 39.9 mR are shown in (a), (b), (c), (d), and (e) respectively.

### A. Modulation transfer function

The measured presampling MTF is shown in Fig. 8. The presampling MTF measured along the anode–cathode axis and perpendicular to the anode–cathode axis were identical. Although the MTF of an imaging system is an important objective measure of the spatial resolution and the signal transfer characteristics, this parameter alone may not be predictive of the overall performance of the system. Other metrics such as DQE as a function of the spatial frequency provide additional insight.

### B. Noise power spectra

The 2D NPS obtained at 1.1, 8.2, 14.2, 32.2, and 39.9 mR are shown in Figs. 9(a), 9(b), 9(c), 9(d), and 9(e), respectively. Each 2D NPS has been individually adjusted to provide maximum perceptibility. The 2D NPS are displayed in a black–white scheme with the transition point set at the mean intensity value of each 2D NPS. The noise power attributable to the off-axis noise peaks is small relative to overall noise power, and is increasingly true at higher exposures as the contribution of the x-ray quantum noise increases. While the 2D NPS at low to mid exposures demonstrate reasonable radial symmetry, at high exposures the 2D NPS demonstrate increasingly elliptical shape with increased exposures. The noise power at high exposures along the $\nu$ axis is signifi-

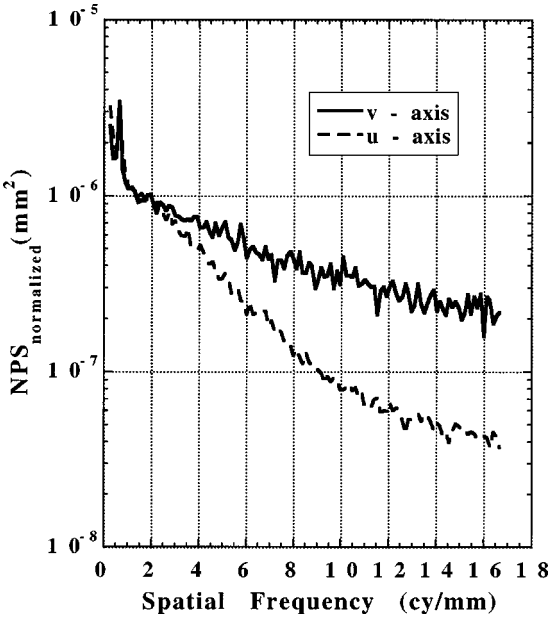


FIG. 10. As an example, the 1D $NPS_{normalized}$ at a high exposure of 39.9 mR obtained along the $u$ axis and $v$ axis are shown. The noise power along the $v$ axis is significantly higher than the noise power along the $u$ axis.

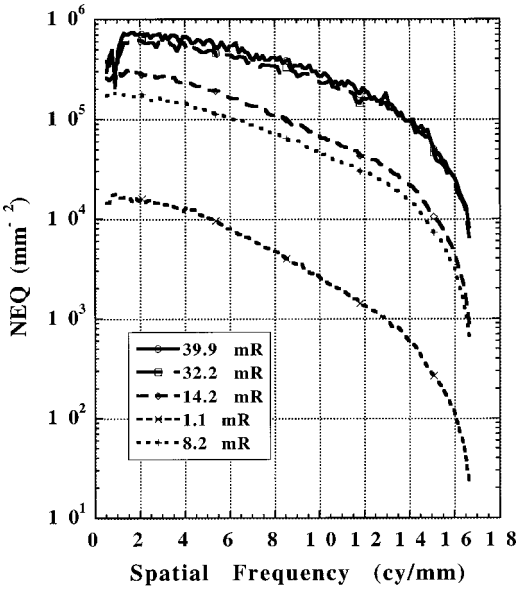


FIG. 12. The NEQ of the system at five exposure levels. NEQ($f$) at 1.1, 8.2, and 14.2 mR were obtained from the NPS($f$) extracted along both the $u$ and $v$ axes and the NEQ($f$) at 32.2 and 39.9 mR were obtained from the NPS($f$) extracted along the $u$ axis only.

cantly higher than the noise power along the $u$ axis, as shown in Figure 10 for an example exposure level of 39.9 mR. The increased noise power is along the vertical direction (parallel shift) of the CCD and may be associated with the charge transport properties of the CCD at high signal amplitudes. The normalized 1D noise power spectra ($NPS_{normalized}$) obtained from a thin slice of the 2D NPS at five exposure levels of 1.1, 8.2, 14.2, 32.2, and 39.9 mR are shown in Fig. 11. For the exposure levels of 1.1, 8.2, and 14.2 mR, the 1D NPS represent the average of thin slices located immediately adjacent and parallel to both the $u$ and $v$ axes. The integral of the NPS at each of these three exposures was confirmed to be identical to the rms variance of the $256\times256$ ROI. The 1D NPS also demonstrated an $MTF^2(f)$ falloff trend up to 6 cycles/mm.

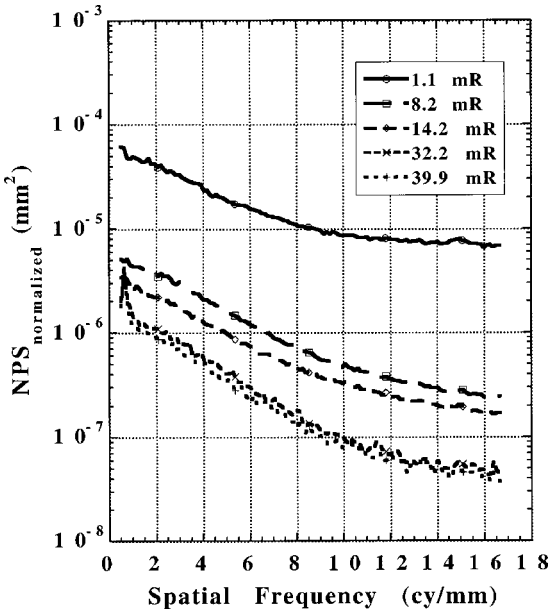


FIG. 11. The 1D normalized noise power spectra ($NPS_{normalized}$) at five exposure levels are shown. The 1D $NPS_{normalized}$ at 1.1, 8.2, and 14.2 mR were extracted from thin slices immediately adjacent and parallel to both the $u$ and $v$ axes. The 1D $NPS_{normalized}$ at 32.2 and 39.9 mR were extracted from thin slices immediately adjacent and parallel to the $u$ axis only.

For the exposure levels of 32.2 and 39.9 mR, the 1D NPS represent the average of thin slices located immediately adjacent and parallel to the $u$ axis only, due to lack of radial symmetry. The 1D NPS along the $u$ axis was selected to represent the noise spectra at 32.2 and 39.9 mR, as the integral of the NPS was within 2% of the rms variance of the $256\times256$ ROI and demonstrated an $MTF^2(f)$ falloff trend up to 6 cycles/mm.

### C. NEQ and DQE

The NEQs of the system at five exposure levels are shown in Fig. 12. The Mo–Mo spectrum incident on the detector after transmitting through 4.5 cm of Lucite is shown in Fig. 13. From the spectral shape, the photon fluence incident on the detector was determined to be $5.34\times10^4$ photons/mm$^2$/mR. The DQE of the system at five exposure levels is shown in Fig. 14. For the exposure levels of 32.2 and 39.9 mR, which did not demonstrate a radially symmetric 2D NPS, the DQE($f$) was computed with the NPS($f$) extracted along the $u$ axis, while at the other exposure levels the DQE($f$) was computed with the NPS($f$) extracted along both the $u$- and $v$ axes. To demonstrate the exposure dependence of the DQE of the system, DQE(0.2 cy/mm), DQE(2 cy/mm), DQE(5 cy/mm), DQE(10 cy/mm), and DQE(15 cy/mm) are plotted as a function of the incident exposure in Fig.

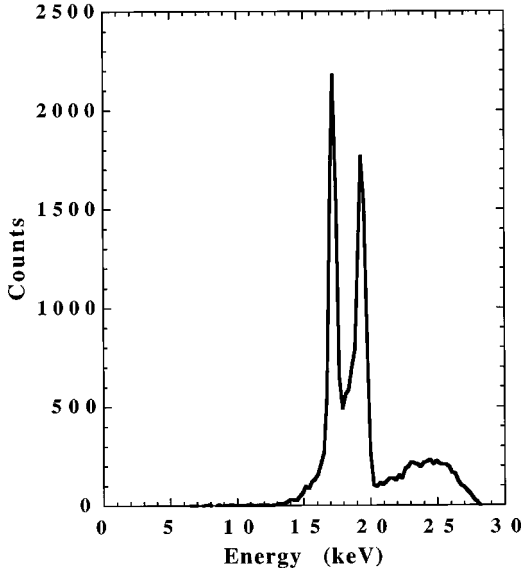


FIG. 13. The Mo–Mo spectrum incident on the detector after transmission through 4.5 cm of Lucite, recorded with a cadmium zinc telluride-based high-resolution spectrometer, for calculation of $q$.

15. The slight decrease in DQE at high exposures can probably be associated with the granular noise[37] due to the scintillator.

## IV. CONCLUSION

A consistent set of image quality measurements was performed characterizing the small-field CCD-based digital cassette for mammographic applications. The DQE($\sim$0) was measured to be 0.29, 0.40, 0.40, 0.37, and 0.36 at incident exposures of 1.1, 8.2, 14.2, 32.2, and 39.9 mR, respectively. The presampling MTF was found to be 0.78, 0.40, and 0.10 at 2, 5, and 10 cy/mm, respectively. The DQE of the CCD imager was found to be comparable to existing screen-film systems in the frequency range of zero to 10 cy/mm.[38]

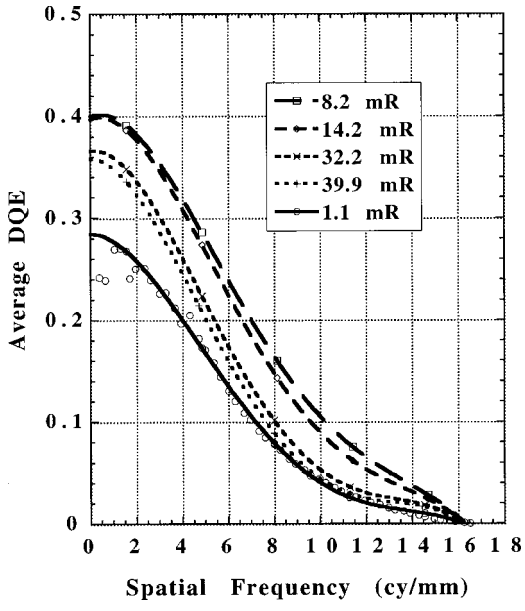


FIG. 14. The DQE of the system at five exposure levels. Data points are curve fitted with a fourth-order polynomial for clarity. To demonstrate the goodness of fit, data points at an exposure of 1.1 mR are shown. DQE($f$) at 1.1, 8.2, and 14.2 mR were obtained from the NPS($f$) extracted along both the $u$ and $v$ axes, and the DQE($f$) at 32.2 and 39.9 mR were obtained from the NPS($f$) extracted along the $u$ axis only.

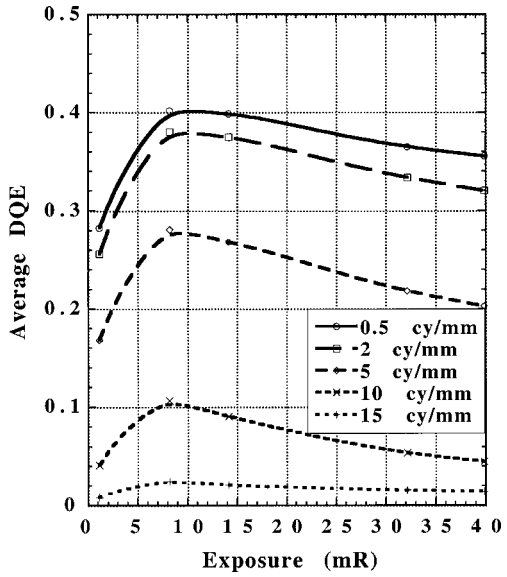


FIG. 15. DQE of the system plotted as a function of incident exposure.

## ACKNOWLEDGMENTS

The authors would like to thank James T. Dobbins, Ph.D., Duke University Medical Center, Durham, NC for useful scientific and technical discussions. This work was supported in part by Grant No. R01CA59770 from the National Cancer Institute to the University of Massachusetts Medical School. The contents of this work are solely the responsibility of the authors and do not necessarily represent the official views of NCI or NIH.

[a]Some of the contents of this work were earlier presented at the 84th Scientific Assembly and Annual Meeting of the Radiological Society of North America, 29 November–4 December, 1998.
[b]Author to whom correspondence should be addressed. Electronic mail: Andrew.Karellas@umassmed.edu

[1] A. D. Maidment and M. J. Yaffe, ''Scanned-slot digital mammography,'' Proc. SPIE **1231**, 316–326 (1990).
[2] R. M. Nishikawa, G. E. Mawdsley, A. Fenster, and M. J. Yaffe, ''Scanned-projection digital mammography,'' Med. Phys. **14**, 717–727 (1987).
[3] U. Bick, M. L. Giger, R. A. Schmidt, R. M. Nishikawa, and K. Doi, ''Density correction of peripheral breast tissue on digital mammograms,'' Radiographics **16**, 1403–1411 (1996).
[4] M. A. Kupinski and M. L. Giger, ''Automated seeded lesion segmentation on digital mammograms,'' IEEE Trans. Med. Imaging **17**, 510–517 (1998).
[5] S. S. Buchbinder, I. S. Leichter, P. N. Bamberger, B. Novak, R. Lederman, S. Fields, and D. J. Behar, ''Analysis of clustered microcalcifications by using a single numeric classifier extracted from mammographic digital images,'' Acad. Radiol. **5**, 779–784 (1998).
[6] M. A. Anastasio, H. Yoshida, R. Nagel, R. M. Nishikawa, and K. Doi, ''A genetic algorithm-based method for optimizing the performance of a computer-aided diagnosis scheme for detection of clustered microcalcifications in mammograms,'' Med. Phys. **25**, 1613–1620 (1998).

[7] D. Wei, H. P. Chan, N. Petrick, B. Sahiner, M. A. Helvie, D. D. Adler, and M. M. Goodsitt, ''False-positive reduction technique for detection of masses on digital mammograms: Global and local multiresolution texture analysis,'' Med. Phys. **24**, 903–914 (1997).
[8] H. Yoshida, K. Doi, R. M. Nishikawa, M. L. Giger, and R. A. Schmidt, ''An improved computer-assisted diagnostic scheme using wavelet transform for detecting clustered microcalcifications in digital mammograms,'' Acad. Radiol. **3**, 621–627 (1996).
[9] M. Kallergi, G. M. Carney, and J. Gaviria, ''Evaluating the performance of detection algorithms in digital mammography,'' Med. Phys. **26**, 267–275 (1999).
[10] L. T. Niklason *et al.*, ''Digital tomosynthesis in breast imaging,'' Radiology **205**, 399–406 (1997).
[11] U. E. Ruttimann, R. A. J. Groenhuis, and R. L. Webber, ''Restoration of digital multiplane tomosynthesis by a constrained iteration method,'' IEEE Trans. Med. Imaging **MI-3**, 141–148 (1984).
[12] D. P. Chakraborty and G. T. Barnes, ''An energy sensitive cassette for dual-energy mammography,'' Med. Phys. **16**, 7–13 (1989).
[13] T. Asaga, S. Chiyasu, S. Mastuda, H. Mastuura, H. Kato, M. Ishida, and T. Komaki, ''Breast imaging: Dual-energy projection radiography with digital radiography,'' Radiology **164**, 869–870 (1987).
[14] F. L. Flanagan, J. G. Murray, P. Gilligan, J. P. Stack, and J. T. Ennis, ''Digital subtraction in Gd-DTPA enhanced imaging of the breast,'' Clin. Radiol. **50**, 848–854 (1995).
[15] M. B. Williams and L. L. Fajardo, ''Digital Mammography: Performance considerations and current detector designs,'' Acad. Radiol. **3**, 429–437 (1996).
[16] Z. Jing, W. Huda, and J. K. Walker, ''Scattered radiation in scanning slot mammography,'' Med. Phys. **25**(7 Pt 1), 1111–1117 (1998).
[17] D. W. Holdsworth, R. K. Gerson, and A. Fenster, ''A time-delay integration charge-coupled device camera for slot-scanned digital radiography,'' Med. Phys. **17**, 876–886 (1990).
[18] A. Karellas, L. J. Harris, H. Liu, M. A. Davis, and C. J. D'Orsi, ''Charge-coupled device detector: Performance considerations and potential for small-field mammographic imaging applications,'' Med. Phys. **19**, 1015–1023 (1992).
[19] D. D. Dershaw, R. C. Fleischman, L. Liberman, B. Deutch, A. F. Abramson, and L. Hann, ''Use of digital mamography in needle localization procedures,'' Am. J. Roentgenol. **161**, 559–562 (1993).
[20] H. Roehrig, T. Yu, and E. A. Krupinski, ''Image quality control for digital mammographic systems: initial experience and outlook,'' J. Digit. Imaging **8**, 52–66 (1995).
[21] E. A. Krupinski, H. Roehrig, and T. Yu, ''Observer performance comparison of digital radiography systems for sterotactic breast needle biospsy,'' Acad. Radiol. **2**, 116–122 (1995).
[22] M. Sayag and A. Karellas, ''Digital sensor cassette for mammography,'' Patent No. 5, 715, 292 (1998).
[23] Loral Fairchild Imaging Sensors, Loral Fairchild CCD Databook, 144 (1994).
[24] J. C. Dainty and R. Shaw, *Image Science* (Academic, San Diego, 1974).
[25] H. H. Barrett and W. Swindell, *Radiological Imaging: The Theory of Image Formation, Detection and Processing*, revised ed. (Academic, San Diego, 1981).
[26] M. B. Williams, P. A. Mangiafico, and P. U. Simoni, ''Noise power spectra of images from digital mammography detectors,'' Med. Phys. **26**, 1279–1293 (1999).
[27] H. Fujita, D. Y. Tsai, T. Itoh, K. Doi, J. Morishita, K. Ueda, and A. Ohtsuka, ''A simple method for determining the modulation transfer function in digital radiography,'' IEEE Trans. Med. Imaging **MI-11**, 34–39 (1992).
[28] J. T. Dobbins, D. L. Ergun, L. Rutz, D. A. Hinshaw, H. Blume, and D. C. Clark, ''DQE($f$) of four generations of computed radiography acquisition devices,'' Med. Phys. **22**, 1581–1593 (1995).
[29] J. T. Dobbins, ''Effects of undersampling on the proper interpretation of modulation transfer function, noise power spectra, and noise equivalent quanta of digital imaging systems,'' Med. Phys. **22**, 171–181 (1995).
[30] S. Vedantham, A. Karellas, S. Suryanarayanan, D. Albagli, S. Han, J. E. Tkaczyk, C. E. Landberg, B. Opsahl-Ong, P. R. Granfors, I. Levis, C. J. D'Orsi, and R. E. Hendrick, ''Full breast digital mammographic imaging with an amorphous silicon-based flat panel detector: Evaluation of the physical characteristics of a clinical prototype,'' Med. Phys. **27**, 558–567 (2000).
[31] M. L. Giger, K. Doi, and C. E. Metz, ''Investigation of basic imaging properties in digital radiography. II. Noise Weiner spectrum,'' Med. Phys. **11**, 797–805 (1984).
[32] C. D. Bradford, W. W. Peppler, and J. T. Dobbins, ''Performance characteristics of a Kodak computed radiography system,'' Med. Phys. **26**, 27–37 (1999).
[33] G. Luberts, ''Random noise produced by x-ray fluorescent screens,'' J. Opt. Soc. Am. **58**, 1475 (1968).
[34] H. E. Johns and J. R. Cunningham, *The Physics of Radiology*, 4th ed. (Thomas, Springfield, IL, 1983).
[35] A. Karellas, I. Sechopoulos, I. Levis, A. C. Huber, and J. A. Pantazis, ''Measurement of the x-ray spectra and tube potential in mammographic units with a self-calibrating compact cadmium zinc telluride (CZT) detector,'' Radiology **205**(P), 301 (1997).
[36] J. W. Byng, J. G. Mainprize, and M. J. Yaffe, ''X-ray characterization of breast phantom materials,'' Phys. Med. Biol. **43**, 1367–1377 (1998).
[37] W. Hillen, U. Schiebel, and T. Zaengel, ''Imaging performance of a storage phosphor system,'' Med. Phys. **14**, 744–751 (1987).
[38] P. Bunch, ''The effects of reduced film granularity on mammographic image quality,'' Proc. SPIE **3032**, 302–317 (1997).